

**Search for higgsinos with compressed mass
spectra using low-momentum mildly-displaced
tracks with the ATLAS detector**

Yuya Mino

*High Energy Physics Group
Division of Physics and Astronomy
Graduate School of Science
Kyoto University*



Abstract

The Standard Model is an effective theory that accurately describes nature and has successfully explained most of the experimental results. However, some questions remain unresolved in the Standard Model, such as the existence of the dark matter and the quadratic divergence of the Higgs boson mass. Supersymmetry, a symmetry between fermions and bosons, is a theoretical extension of the Standard Model that may resolve these problems by introducing a new superpartner for each Standard Model particle. In particular, it can solve the hierarchy problem when the mass of the higgsinos, superpartners of the Higgs boson, is close to the electroweak scale. Collider experiments have attempted searches for light higgsinos in the region where the mass difference between charged and neutral higgsinos is $O(100)$ MeV, but a sensitivity gap remains. The mass difference between higgsinos depends strongly on the masses of wino and bino, which are superpartners of the electroweak gauge bosons. The sensitivity gap corresponds to wino and bino masses between 10 and 100 TeV and is difficult to probe by existing collider searches.

This thesis describes a search for higgsinos with compressed mass spectra of $O(100)$ MeV using 140 fb^{-1} of $\sqrt{s} = 13$ TeV proton-proton collision data collected by the ATLAS detector. In the compressed mass region, the charged higgsino (“chargino”) has the largest branching ratio for decaying to a single pion and the lightest neutral higgsino (“neutralino”). Neutralinos do not interact with the detector and are identified as missing transverse momentum. Tracks produced by charged particles are characterized by low momentum. However, they are produced at a small distance from the interaction point due to the relatively long lifetime of the chargino in the compressed mass region. Therefore, requiring tracks with significant impact parameters can reduce background events and significantly increase sensitivity.

A dedicated event selection is applied to define two regions, maximizing the signal-to-noise ratio to conduct the counting experiment. The number of data observed in the two signal regions, with 35 and 15 events, and the number predicted from the Standard Model were consistent within the uncertainty. This search sets a 95% CL limit on the higgsino mass as a function of the mass difference. In the mass difference region of 0.3–1.0 GeV, the higgsino mass was excluded up to approximately 170 GeV, extending the mass reach significantly beyond the LEP results of approximately 90 GeV. As a result, this analysis excluded a range of wino and bino masses between 10 and 100 TeV, with a higgsino mass of 100 GeV.

Acknowledgements

Throughout my extensive research journey for around six years, I faced many challenges. However, with the support of many individuals, I was able to reach this point. In the following, I would like to express my gratitude to those who have provided invaluable guidance and support.

I would like to express my sincere gratitude to Prof. Tsuyoshi Nakaya for his guidance and support throughout my doctoral program. Not only did he provide insightful comments on my dissertation, but he also offered invaluable guidance on my future career path. Thanks to his assistance, I was able to fully commit myself to writing the doctoral thesis.

A special thank you goes to Dr. Toshi Sumida for his consistent guidance and support over the extended period of nine years. Whenever my research faced challenges, he promptly made time to engage in discussions that enabled me to work diligently until the very end. These discussions taught me the value of collaborating with others.

My immense gratitude goes to Prof. Kunihiro Nagano for consistently posing insightful questions and steering the direction of my analysis. Without his leadership in the Kyoto ATLAS group after the departure of Dr. Toshi Sumida, I believe the group might not have remained intact up to this point. Thank you for your generosity and support, even in moments of unworthiness.

I would like to extend my heartfelt appreciation to Prof. Shion Chen for his invaluable support in the analysis, dedicated role as the contact editor for the paper, effective coordination within the group, and insightful comments on my doctoral thesis. Without his efforts, I believe achieving graduation at this point would not have been possible. After arriving at Kyoto University, he not only led the Kyoto ATLAS team as the institute representative but also guided me into the fascinating field of quantum computing and sensing technologies. His guidance and mentorship, deeply rooted in extensive knowledge and inquisitiveness, have enabled me to maintain my motivation and successfully complete my research.

My gratitude extends to Prof. Hidetoshi Otono and Prof. Hideyuki Oide for proposing such a fascinating research topic that I was able to be passionate about over the past four years. This research has been a significant source of inspiration for me, and I appreciate the chance to have contributed to it. I apologize for the time it took to achieve the results of this analysis despite the strong foundation you provided. I am deeply grateful for your patience and insightful advice while awaiting the outcomes.

I am profoundly grateful to everyone in the Displaced Track (Cut-and-Count based) analysis team who contributed tirelessly to the progress of the analysis in this dissertation. In particular, I extend my deepest appreciation to Dr. Jeffrey David Shahinian and Dr. Michael Holzbock, who demonstrated leadership throughout the extensive four-year period, bringing this analysis to its impressive completion. Additionally, the quick responses and collaborative efforts of Alessandro Sala, who worked diligently alongside me, played a crucial role in smoothly concluding the analysis. Despite the split in the analysis group midway, I would like to express my gratitude to everyone in the Displaced Track (Neural-Network based), 1Lepton 1Track, Vector Boson Fusion, and ISR Slepton analysis teams for engaging in various discussions.

The Kyoto High-energy Physics Lab has been the most prolonged community in which I have been involved throughout my life. The warm atmosphere in the research lab provided the support needed to persist through the long journey of my research. I am particularly grateful to Prof. Atsuko Ichikawa, Prof. Osamu Tajima, Prof. Roger Wendell, Dr. Tatsuya Kikawa, Dr. Junya Suzuki, and Dr. Syunsuke Adachi, who, despite being in different experimental groups, have educated me in physics during my master's and doctoral program. While it is not possible to mention everyone by name here, I would like to express my sincere gratitude to all the students who spent time with me in the research lab. During our breaks for coffee, lunch, and dinner, you all shared valuable insights, not only in physics but in a wide range of topics, making them highly informative and exciting. I am especially grateful for progressing through the doctoral program alongside Dr. Takahiro Odagawa and Dr. Soichiro Kuribayashi. Despite our completely different research topics, being able to hear about each other's work provided me with valuable inspiration and motivation. I would also like to express my appreciation to Tomofumi Abe, Takuji Ikemitsu, Masanori Tajima, and Masayuki Hatano, with whom I completed the master's program. Not only did we overcome the challenging times of writing our master's theses together, but they also provided assistance and support even before joining the research lab. I would also like to extend my gratitude to the former and current Kyoto ATLAS group members: Dr. Takuya Tashiro, Dr. Takuto Kunigo, Dr. Shunichi Akatsuka, Dr. Yohei Noguchi, Dr. Yuta Okazaki, Koichiro Kuniyoshi, Yoshiaki Tsujikawa, Ren Kobayashi, Takane Sano, Nobuyuki Yoshimura, Chihiro Kawamoto, and Tetsuro Nakagawa. I am sincerely thankful for their support. Engaging in discussions with everyone who enthusiastically worked on their research was not only informative but also enjoyable. I would like to express my heartfelt thanks to the secretaries, Tanizawa-san, Sekiguchi-san, Sasaki-san, and Tsuzuki-san, for their invaluable assistance during my research at CERN. Their support enabled me to conduct my research comfortably and successfully complete it.

During my analysis at CERN, I received tremendous support from various staff and students. I am deeply grateful to Dr. Takuya Nobe, Dr. Tomoya Iizawa, and Dr. Tomohiro Inada, fellow residents of Ferney House, who, not only as neighbors but also as experienced seniors in the field, generously provided guidance on future prospects and fruitful discussions on my analysis. Moreover, their support extended beyond professional matters as they often took me out for meals and assisted with personal aspects of my life. I would like to express my sincere appreciation to Prof. Junichi Tanaka, Prof. Ryu Sawada, Prof. Yuji Enari, and Dr. Masahiko Saito for promptly addressing issues with the computing resources, which was immensely helpful for my research in

CERN. Additionally, Prof. Yuji Enari not only provided support for my personal life based on his extensive experience of living around CERN but also offered guidance on my future career. I also received invaluable advice from Dr. Minori Fujimoto and Dr. Reiyu Oishi, not only as friends but also as excellent advisors with advanced expertise in the field. Their guidance played a crucial role in overcoming the challenges I faced in my own analysis. I am immensely grateful to my ATLAS colleagues Arisa Kubota, Dr. Gen Tateno, Haruka Asada, Dr. Moe Wakida, Dr. Reiyu Oishi, Ushioda Risa, and Dr. Yunjian He, whose simultaneous efforts in starting and advancing their analyses provided me with great inspiration and valuable advice. A special thanks goes to Kaito Sugizaki, a colleague in the same research group who has offered support and listened to various discussions regarding our analyses. Additionally, I would like to express my gratitude to Aoto Tanaka for assisting with technical issues despite the differences in our analyses. Both of them have been great friends who frequently invited me to play tennis together, which allowed me to clear my mind about the challenges of my research life.

Throughout my master's and doctoral programs, I am deeply grateful to everyone in the ATLAS Japan TGC group for their significant support in the muon trigger upgrade for HL-LHC and the commissioning towards Run 3. The guidance provided in advancing the research on the muon trigger has laid the foundation for progressing in physics analyses. I express my gratitude to Prof. Masaya Ishino, who served as my technical supervisor during the two years of the master's program, providing guidance and support for the muon trigger upgrade towards HL-LHC. I would also like to thank Prof. Osamu Sasaki, Prof. Makoto Tomoto, Prof. Yasuyuki Okumura, and Prof. Yasuyuki Horii for consistently offering insightful comments during the Phase-II meetings. Thanks to their guidance, I was able to complete my research successfully throughout my master's studies. For the commissioning towards Run 3, a special thanks goes to Prof. Tatsuya Masubuchi, who provided valuable guidance regarding a part of the muon trigger system in which I was involved briefly, and Dr. Masato Aoki and Dr. Junpei Maeda, who provided hands-on instruction on the operation of the muon trigger system. I would like to express my sincere appreciation to the AJ SUSY group for their invaluable support and guidance throughout my physics analysis. I am particularly grateful to Prof. Shion Chen and Dr. Tomoyuki Saito for their insightful comments and guidance from the early stages of the analysis. Their extensive experience and expertise offered insight into the details of my analysis and provided guidance on scheduling toward graduation.

Finally, I am deeply grateful to my parents, Takayuki Mino and Mariko Mino, for their unwavering understanding and support in all phases of my life. Their encouragement was crucial to my success, and I am grateful for their affection and guidance. Without their assistance, I would not have been able to reach the goal of my research journey, and I owe all of my achievements to them.

Contents

1	Introduction	13
2	Theoretical Background	17
2.1	The Standard Model	17
2.1.1	Overview	17
2.1.2	Remaining problems of the Standard Model	19
2.2	The Minimal Supersymmetric Standard Model	20
2.2.1	Overview	20
2.2.2	Solutions to the problems of the Standard Model	23
2.3	Phenomenology of the electroweak sector of the MSSM	24
2.3.1	Electroweakinos	24
2.3.2	Light Higgsino Scenario	25
2.3.3	Mass difference between the higgsino-like mass eigenstates	25
2.4	Experimental constraints on the Higgsino LSP scenario	26
2.4.1	Collider Experiments	27
2.4.2	Direct dark matter detection	29
2.4.3	Indirect dark matter detection	30
2.4.4	Electron Electric Dipole Moment (EDM)	30
2.5	Definition of the Target Signal Models	32
3	The ATLAS Experiment at the LHC	34
3.1	Large Hadron Collider	34
3.2	ATLAS detector	34
3.2.1	Coordinate system	36
3.2.2	Magnet system	37
3.2.3	Inner detectors	37
3.2.4	Calorimeters	40
3.2.5	Muon spectrometers	41
3.3	Trigger and Data Acquisition	42
3.3.1	Overview of the trigger system	43
3.3.2	Missing Transverse Momentum Trigger	43
3.4	Future Upgrades	44

4	Data and Monte Carlo Simulation	45
4.1	ATLAS Run 2 data	45
4.2	Monte Carlo Simulation	45
4.2.1	General description	46
4.2.2	SM Background Simulation Samples	48
4.2.3	Signal Simulation Samples	49
4.2.4	Summary of Simulation Samples	50
5	Event Reconstruction	52
5.1	Overview of Event Reconstruction	52
5.2	Low-level objects	54
5.2.1	Tracks and Vertices	54
5.2.2	Topo-clusters	56
5.3	Physics objects	56
5.3.1	Jets	56
5.3.2	Muons, Electrons, and Photons	59
5.3.3	Overlap removal	59
5.3.4	Missing Transverse Energy	60
5.4	Summary of Object Selections	60
6	Analysis Strategy and Event Selections	63
6.1	Analysis Strategy	63
6.2	Trigger Selections	64
6.3	Event Cleaning	66
6.4	Signal track definition	67
6.5	Event selection	73
6.5.1	Preselections	73
6.5.2	Signal Region Selection	76
7	Background Estimation	81
7.1	Origin of the background events and the estimation strategy	81
7.2	Semi data-driven background estimation for τ decay tracks	85
7.2.1	Overview	85
7.2.2	Control Regions and Validation Regions	88
7.2.3	Fit results in Validation Regions	90
7.3	Full data-driven background estimation for QCD tracks	92
7.3.1	Overview	92
7.3.2	Preselection	95
7.3.3	Control Regions and Validation Regions	97
7.3.4	Fit results in Validation Regions	100
7.4	Validation of the combined estimation	105
7.5	Summary	108

8	Systematic Uncertainties	109
8.1	Theoretical Uncertainty	109
8.2	Experimental Uncertainty	110
8.2.1	Jets	110
8.2.2	Tracks	111
8.2.3	Pileup	112
8.2.4	Other experimental uncertainties	112
8.3	Uncertainty of Data-driven background estimation	112
8.4	Summary of Systematic Uncertainties	113
9	Results	115
9.1	Background-only fit results in signal regions	115
9.2	Model-independent search	121
9.3	Model-dependent interpretation	123
10	Discussion	125
10.1	Limit on the Electroweakino masses	125
10.2	Implication to Electroweak Naturalness	127
10.3	Future Prospects	127
10.3.1	Soft Lepton and Disappearing Track analysis	127
10.3.2	Displaced Track analysis	129
11	Conclusion	134
	Bibliography	136
	List of Figures	147
	List of Tables	152
	Appendices	155
A	Supplements of Theoretical Background	155
A.1	Muon Anomalous Magnetic Moment	155
A.2	Mechanisms to enhance the annihilation cross-section of bino-like LSP	156
A.3	Limits to electroweakinos as a dark matter candidate	157
B	Muon Trigger Upgrade for the HL-LHC	160
B.1	Overview of the Thin Gap Chamber	160
B.2	Trigger Logic using Muon Detectors inside the Magnetic Field	162
B.3	Upgrade of the Endcap Muon Trigger System	162
B.4	Development of the New Endcap Trigger Logic	163
B.4.1	Muon Segment Reconstruction in the TGC BW	164
B.4.2	Coincidence with detectors inside the magnetic field	167

B.4.3	Summary of the Endcap Muon Trigger Logic	170
C	Supplements of Event Reconstructions	171
C.1	Jets	171
C.2	Muons	172
C.3	Electrons and Photons	174
D	Expected yields and efficiency for each selection	180
E	Composition of Background Events	185
F	Full data-driven estimation of Non-collision background	189
G	Validation of τ decay track estimation with $t\bar{t}$ process	192
G.1	Overview	192
G.2	Control Regions and Validation Regions	193
G.3	Fit results in Validation Regions	196
H	Minor Experimental Uncertainties	200
I	Auxiliary Materials	202
I.1	Acceptance and Efficiency	202
I.2	Cross-section Upper Limits	206
I.3	Limit on Electroweakino masses	207

Acronyms

p_T^{miss}	missing transverse momentum
E_T^{miss}	missing transverse energy
p_T	transverse momentum
CL_s	confidence level
m_T	transverse mass
$m_{\ell\ell}$	invariant mass
BEH	Brout-Englert-Higgs
BSM	beyond the Standard Model
CB muon	combined muon
corrJVF	corrected Jet Vertex Fraction
CR	control region
CSC	Cathode Strip Chamber
DGLAP	Dokshitser-Gribov-Lipatov-Altarelli-Parisi
EDM	Electric Dipole Moment
EMTopo	Electromagnetic Topo-cluster
FCal	forward calorimeters
HEC	hadronic endcap calorimeters
HL-LHC	High-Luminosity LHC
HLT	High-Level Trigger
IBL	Insertable B-Layer
ID	Inner Detector
ISR	initial state radiation
ITk	Inner Tracker

JER	Jet Energy Resolution
JES	Jet Energy Scale
JVT	Jet Vertex Tagger
L1Calo	Level-1 Calo
L1Muon	Level-1 Muon
L1 Trigger	Level-1 Trigger
LEP	Large Electron-Positron Collider
LHC	Large Hadron Collider
LINAC 2	linear accelerator 2
LO	leading order
LSP	lightest SUSY particle
MC	Monte Carlo
MDT	Monitored Drift Tube
ME	Matrix Element
MS	Muon spectrometer
MSSM	Minimal Supersymmetric Standard Model
MWPC	Multi Wire Proportional Chamber
NF	Normalization Factor
NLO	next-to-leading order
NNLO	next-to-next-to leading order
NSW	New Small Wheel
pdf	probability density function
PDF	Parton Density Function
PFlow	Particle Flow
pMSSM	phenomenological MSSM
PS	Proton Synchrotron
PSB	Proton Synchrotron Booster
QCD	Quantum Chromodynamics
RGE	renormalization group equation
RoI	Region of Interest
RPC	Resistive Plate Chamber
SA muon	standalone muon
SCT	Semiconductor Tracker
SI	spin independent
SM	Standard Model
SPS	Super Proton Synchrotron

SR	signal region
SUSY	supersymmetry
TF	Transfer Factor
TGC	Thin Gap Chamber
TGC BW	TGC Big Wheel
TileCal	Tile Calorimeter
TRT	Transition Radiation Tracker
VBF	Vector Boson Fusion
VR	validation region

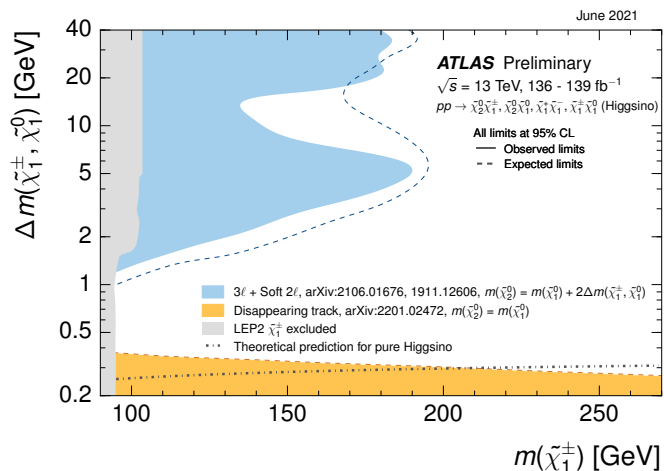
Chapter 1

Introduction

The Standard Model (SM) of particle physics is the best theory we have to date describing the elementary particles that constitute matter, as well as their interactions. Despite its remarkable success, the SM suffers from some outstanding problems, such as the quadratic divergence of the Higgs boson mass [1, 2] and the existence of dark matter [3–6]. While a number of theories attempt to address these problems, supersymmetry (SUSY) [7–12] is a highly attractive theoretical framework that has the potential to solve multiple problems simultaneously. In addition, SUSY has the advantageous feature of unifying interactions at high-energy scales, making it a compelling candidate for the theory of everything among various theoretical frameworks.

The SUSY theory introduces new particles called “superpartners” that differ in spin by 1/2 from each SM particle. Thanks to the opposite polarity of the loop contribution, this successfully eliminates the quadratic divergence term of the Higgs boson mass. Since higgsinos, superpartners of the Higgs bosons, are closely related to the electroweak symmetry breaking scale, they can be probed within the mass reach of the Large Hadron Collider (LHC). If R -parity [13] is conserved, a light higgsino can be a candidate for dark matter because it is an electromagnetically neutral and stable particle. In the SUSY theory, superpartners of electroweak gauge bosons are referred to as electroweak gauginos. Higgsinos and electroweak gauginos are mixed as a result of electroweak symmetry breaking, forming mass eigenstates called “electroweakinos”. Electroweakinos with neutral charge are referred to as “neutralinos” denoted as $\tilde{\chi}_i^0$ ($i = 1, 2, 3, 4$) which arise from the mixing of neutral higgsinos ($\tilde{H}_u^0, \tilde{H}_d^0$) and gauginos (\tilde{B}^0, \tilde{W}^0). Similarly, “charginos” denoted as $\tilde{\chi}_i^\pm$ ($i = 1, 2$) are charged electroweakinos that result from the mixing of charged higgsinos ($\tilde{H}_u^+, \tilde{H}_d^-$) and gauginos (\tilde{W}^\pm). The masses of higgsinos and electroweak gauginos before the mixing determine the mass spectrum of charginos and neutralinos [14]. When higgsinos are sufficiently lighter than electroweak gauginos, they have a mass spectrum where the lightest chargino and two neutralinos are nearly degenerate. When the electroweak gauginos are sufficiently massive ($> \mathcal{O}(10)$ TeV), the mass difference between the two neutralinos, $\Delta m(\tilde{\chi}_2^0, \tilde{\chi}_1^0)$, vanishes. To the contrary, the mass difference between the lightest chargino and neutralino, $\Delta m(\tilde{\chi}_1^\pm, \tilde{\chi}_1^0)$, maintains a mass difference of 250–400 MeV through the radiative corrections. When the electroweak gaugino mass is as light as $< \mathcal{O}(1)$ TeV, the mass difference can run up to $\mathcal{O}(1)$ GeV.

Figure 1.1: Existing experimental constraints on the higgsino states with compressed mass spectra, established by the ATLAS experiment. The dashed gray line shows the mass difference caused by the radiation in the case of pure higgsino. The exclusion limit is established for mass differences larger than 1.5 GeV through the soft lepton analysis [17, 18] (blue). The disappearing track analysis [15] (orange) has set a limit to the regime with mass differences below 400 MeV. There exists a sensitivity gap between the two analyses, which has been covered up to 90 GeV by LEP experiments [20]. The figure is taken from Ref. [22].



At the LHC, electroweakinos are produced in pairs if R -parity is conserved. The pair-produced electroweakinos decay into two neutralinos and additional decay products depending on the mass spectrum of electroweakinos. The LHC has explored regions with compressed mass spectra using two methods based on the type of additional decay products and the chargino lifetime. As the mass difference decreases, the chargino lifetime increases because the available phase space for the chargino decay becomes limited. For regions with small mass differences ($\Delta m(\tilde{\chi}_1^\pm, \tilde{\chi}_1^0) \approx 250 - 400$ MeV), the disappearing track signature has been used to search for regions with long chargino lifetimes of $\mathcal{O}(0.1 - 10)$ ns [15, 16]. On the other hand, regions with large mass differences ($\Delta m(\tilde{\chi}_2^0, \tilde{\chi}_1^0) \gtrsim 2$ GeV) have been searched by identifying the two prompt leptons produced by the decay of the second lightest neutralino [17–19]. Although these two analyses provide strong constraints on higgsinos with compressed mass spectra, there is an evident sensitivity “gap” for higgsinos in the range of $\Delta m(\tilde{\chi}_1^\pm, \tilde{\chi}_1^0) \approx 0.3 - 1.0$ GeV, where the most stringent constraints still originate from the Large Electron-Positron Collider (LEP) experiments [20]. Figure 1.1 illustrates exclusion limits set by analyses targeting the compressed higgsino states in the ATLAS and LEP experiments. In this mass difference region, the electroweak gaugino mass is relatively heavy, which results in very small couplings of higgsinos to nuclei. As a result, this region is challenging to search even through the direct dark matter detection experiments [21].

The primary objective of this thesis is to explore this previously unprobed model space at the LHC through a novel analysis approach. As illustrated in Figure 1.2, in the $\Delta m(\tilde{\chi}_1^\pm, \tilde{\chi}_1^0) \approx 0.3 - 1.0$ GeV region where the sensitivity gap remains, chargino has a relatively long lifetime of $\mathcal{O}(1 - 10)$ ps and decays mainly to pions at a distance of about $\mathcal{O}(0.1 - 1)$ mm from the interaction point. This results in tracks characterized by finite displacements from the hard-scattering vertex, as illustrated in Figure 1.3. The displacement of tracks is measured accurately with the ATLAS detector. Therefore, although prompt decays in proton-proton collisions generate many low-momentum tracks, we can identify pion tracks originating from the chargino decays by requiring significant

Figure 1.2: The masses and lifetimes of metastable particles in the SM. The gray region indicates the lifetime range of detector-prompt and detector-stable particles. Detector-prompt particles are defined as those that decay near the interaction point. In contrast, detector-stable particles do not decay until they reach the outside of the detector. The red region represents the chargino lifetime at the mass differences we intend to investigate in this thesis.

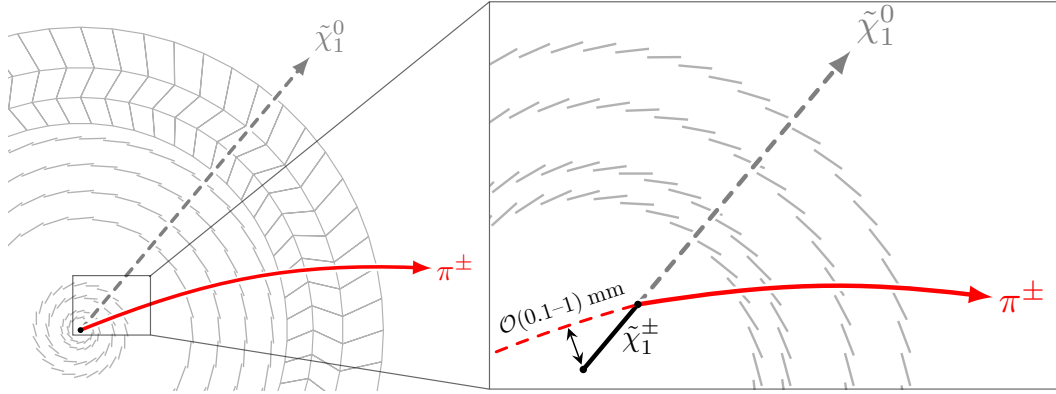
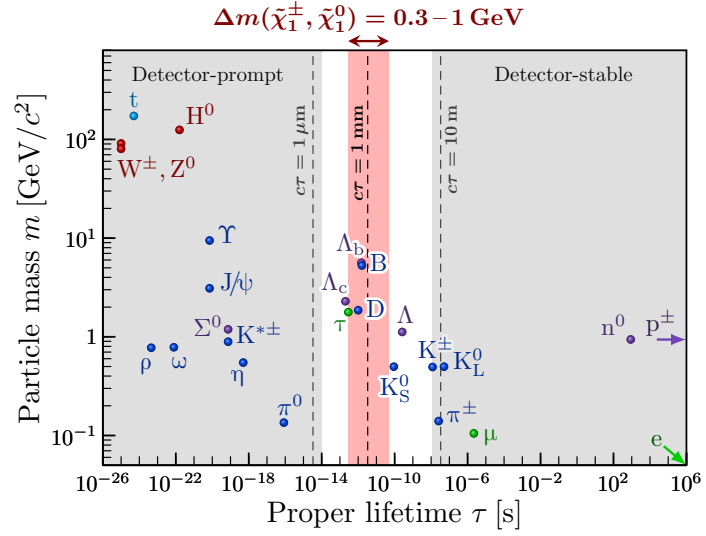


Figure 1.3: Schematics of the mildly-displaced track signature. The schematic on the left-hand side illustrates a neutralino and pion passing through the tracking detector, which is shown in gray. The neutralino, indicated by a dotted gray line, has only weak interactions and cannot be detected. The right side is a magnified view of the center of the detector, showing the reconstruction of the pion as a track with significant displacement due to the relatively long lifetime of the chargino.

displacement. On the other hand, the lifetime of the chargino is so short that it decays before reaching the innermost layer of the ATLAS detector in the target mass difference region. Therefore, the impact parameter of pion tracks is relatively mild compared to that of the pion track in the mass difference region targeted by the disappearing track analysis. Throughout this thesis, tracks with significant displacement are referred to as “mildly-displaced tracks”. As can be seen in Figure 1.2, some of the SM particles have lifetimes similar to those of the chargino, and methods for reducing and estimating these backgrounds are crucial for extending the sensitivity. This thesis describes a search method using a “mildly-displaced track” signature, followed by methods to estimate SM particles with relatively long lifetimes that appear as background events.

In Chapter 2, we will provide the details of the theoretical aspects of the SM and SUSY. We examine the underlying principles and concepts behind both theories, including their implications for particle physics. In addition, we will discuss the phenomenology of SUSY and explore the constraints imposed by various experiments.

Chapter 3 provides an overview of the LHC and the ATLAS detector, followed by a detailed description of the data collected and the Monte Carlo (MC) simulations in Chapter 4. Chapter 5 describes the algorithms for reconstructing the particles generated from the proton-proton collisions.

In Chapter 6, the analysis strategy for this search is first described. The selection applied to the reconstructed particles is then discussed, which aims to maximize the sensitivity. This selection includes the criteria used to define mildly-displaced tracks, which is essential to this analysis. As measuring particle displacement with accuracy is crucial to this study, an examination of relevant parameters and resolutions related to displacement is also addressed.

Chapter 7 provides detailed information on the primary background and the strategy used to estimate background yields. Different estimation methods have been used for different background processes, and this chapter discusses them in detail. In addition, the methods used to validate these estimation strategies are presented, followed by the results of the validation procedure.

The estimation of background yields must also consider systematic uncertainties associated with the reconstruction algorithms and the estimation strategies. Therefore, Chapter 8 discusses the systematic uncertainties considered for the background and the signal processes.

In Chapter 9, we present the results of this analysis obtained by comparing the estimated number of background events with the actual data observed. The absence of anomalous data excess allows one to set constraints on the electroweakino masses, which will be discussed in Chapter 10. Furthermore, we explore possible future sensitivity improvements in this analysis while considering detector upgrades planned for the future data-taking periods. Finally, Chapter 11 presents a summary of the conclusions derived from the results of this analysis.

Chapter 2

Theoretical Background

This chapter describes the theoretical background of the Standard Model (SM) and the supersymmetry (SUSY). A brief overview of the SM is provided in Section 2.1, followed by the description of its inherent problems in Section 2.1.2. Section 2.2 briefly describes SUSY and with a particular focus on the Minimal Supersymmetric Standard Model (MSSM) [23, 24], the minimal SUSY extension of the SM. Section 2.3 describes the phenomenology relevant to higgsinos, and Section 2.4 summarizes the limits imposed by various experiments. Finally, details of the target signal models are provided in Section 2.5.

2.1 The Standard Model

2.1.1 Overview

The SM consists of 17 types of elementary particles, categorized into fermions and bosons, as shown in Figure 2.1. Fermions, with half-integer spins, consist of six types of quarks and leptons in three generations. In contrast, bosons, characterized by integer spins, can be classified into two categories: gauge bosons with spin 1, serving as mediators of interaction, and the Higgs boson (H) with spin 0, responsible for giving mass to particles. The SM particles and interactions are described by the quantum field theory, and the Lagrangian in which the SM structure is encoded is invariant under Lorentz and gauge transformations. The three interactions described in the following appear from the gauge invariance of the SM under the $SU(3)_C \times SU(2)_L \times U(1)_Y$ gauge transformation.

Gluons (g) mediate the strong interaction within Quantum Chromodynamics (QCD), described by the $SU(3)_C$ gauge group. The interaction takes place between particles that carry color charges. The QCD theory has been established through the thorough studies of the deep inelastic scattering of electrons and protons in electron-proton colliders such as the HERA accelerator at DESY [25–27].

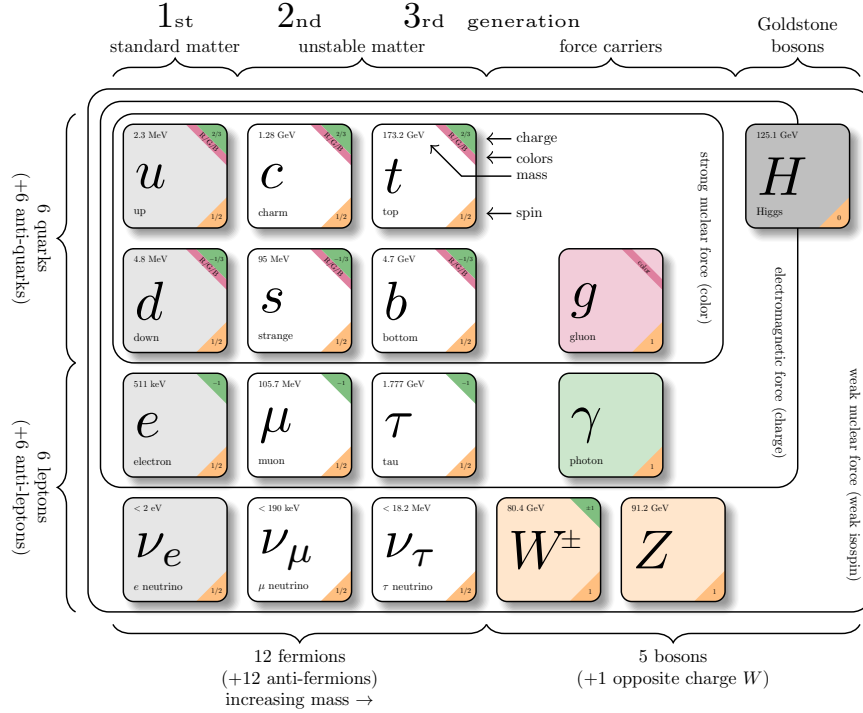


Figure 2.1: Particles constituting the SM. The figure summarizes the spin-1/2 fermions that constitute matter, the spin-1 gauge bosons that mediate interactions between fermions and gauge bosons, and the spin-0 Higgs bosons that give mass to particles. The figure is taken from Ref. [35].

Weak bosons (W , Z) and photons (γ) mediate weak and electromagnetic interactions, described by the $SU(2)_L \times U(1)_Y$ gauge group. The weak interaction is characterized by short-distance interactions due to the heavy mass of the weak bosons. The electroweak theory was experimentally verified through the precision measurement of Z and W bosons at the SLC [28], LEP [29], and Tevatron [30].

As described above, the interactions are successfully described by gauge invariance and agree well with experimental results. However, the mass terms of gauge bosons and fermions violate the gauge invariance and, therefore, are required to be precisely zero. The Brout-Englert-Higgs (BEH) mechanism [31, 32] was proposed to solve this problem. This mechanism introduces the kinetic energy and potential terms of the $SU(2)$ doublet composed of complex scalar fields into the SM Lagrangian. While the gauge invariance is preserved at the Lagrangian level, the non-zero vacuum expectation value in the group state allows the gauge bosons and fermions to gain mass through the interactions with the Higgs field.

In 2012, the Higgs boson was discovered by ATLAS [33] and CMS [34], bringing together all the particles that are predicted by the SM. While the SM has been a successful and elegant theory that has explained many experimental observations, some problems remain unresolved by the SM, as described in the following section.

2.1.2 Remaining problems of the Standard Model

Quadratic Divergence of the Higgs boson mass The bare mass of spin-0 particles (the Higgs boson in the SM) undergo significant quantum corrections from particles that couple directly or indirectly. The contribution from the loops involving a Dirac fermion f is expressed by

$$\Delta m_H^2 = -\frac{|\lambda_f|^2}{8\pi^2} \Lambda_{\text{UV}}^2 + \dots, \quad (2.1)$$

where the Lagrangian term is written as $-\lambda_f H \bar{f} f$. The m_H^2 is the Higgs boson mass, Λ_{UV} is an ultraviolet cutoff scale, interpreted as the energy scale where new physics starts to modify the behavior of the theory. When Λ_{UV} reaches the Planck scale ($M_P \sim 10^{18}$ GeV), Δm_H^2 reaches $\sim \mathcal{O}(10^{36})$ GeV and a precise cancelation must occur for all orders of perturbation to achieve the electroweak scale mass. In the case of fermions and gauge bosons, only logarithmic divergence arises, whereas quadratic divergence is absent because of the chiral and gauge symmetries.

Dark matter Numerous astrophysical observations have suggested the existence of dark matter: measurement of the galaxy rotation curves [3, 4], gravitational lensing effects [5], bullet clusters [6] and so on. The Λ -CDM model introduces dark matter with negligible velocity compared to the speed of light in terms of galaxy structure formation. Observations suggest that dark matter must be electromagnetically close-to-neutral and only interact with ordinary matter weakly through weak interaction and gravity. In order to produce dark matter of this nature, the ‘‘freeze-out’’ mechanism is commonly considered. During the early universe, dark matter was in thermal equilibrium with the particles in the SM. As the universe expanded and reached the energy scale less than the mass of dark matter, the production of dark matter became kinematically forbidden. With the continued expansion of the universe, the number density of dark matter decreased, resulting in small annihilation rates. At the freeze-out temperature, when the annihilation rate becomes lower than the expansion rate of the universe, the number of dark matter particles no longer changes. The dark matter density at the freeze-out temperature is called the ‘‘relic density’’. The latest measured relic density reported by Planck [36] is

$$\Omega_c h^2 = 0.1200 \pm 0.0012, \quad (2.2)$$

where h is the reduced Hubble constant and Ω_c is the dark matter density. Note that neutrinos cannot be a good dark matter candidate in spite of their charge-neutrality and non-zero mass since their light mass means they are relativistic and cannot form the large-scale structures of galaxies. Therefore, no SM particle is eligible as a good candidate for dark matter.

2.2 The Minimal Supersymmetric Standard Model

2.2.1 Overview

SUSY is an attractive theoretical framework that addresses unresolved phenomena not explained by the SM. It introduces a symmetry between fermions and bosons that transforms SM particles into new particles with a spin differing by $1/2$, referred to as “superpartners”. The fields of the SM particles and their superpartners form multiplets, referred to as “supermultiplets”, which are the irreducible representation of the SUSY algebra.

The MSSM is derived from the minimal extension of the SM by adding one superpartner to each SM particle and two Higgs doublets. To ensure the cancelation of gauge anomalies arising from fermion loops, the sum of the $U(1)_Y$ hypercharge of fermions must be zero. A single Higgs doublet would introduce new fermion superpartners, breaking the cancelation. Therefore, two Higgs doublets with opposite $U(1)_Y$ hypercharge need to be introduced to maintain the cancelation of gauge anomalies. Each Higgs doublet provides mass to up- and down-type quarks, known as up- and down-type Higgs. The up-type and down-type Higgs acquire vacuum expectation values after the spontaneous symmetry breaking. The ratio of the vacuum expectation value is defined as

$$\tan \beta \equiv \langle H_u^0 \rangle / \langle H_d^0 \rangle. \quad (2.3)$$

The extension introduces a minimal number of new particles and interactions, which will be described below. Furthermore, we will explain how the introduction of MSSM resolves the issues in the SM, as mentioned in Section 2.1.2.

Particles in the MSSM Each SUSY particle is denoted by an additional tilde (\sim) to the corresponding SM particle. The superpartners of fermions, “sfermions”, are indicated by adding “s (scalar)” in front of each SM particle. Sfermions include “squarks” and “sleptons”, which are superpartners of quarks and leptons, respectively. Each left-handed fermion (f_L) and right-handed fermion (f_R) form a supermultiplet, resulting in the superpartners for both chiralities, denoted as \tilde{f}_L and \tilde{f}_R . The subscripts L and R for the sfermions indicate the chirality of the corresponding fermion, while the sfermions themselves are spin-0 particles. The superpartners of bosons, referred to as “gauginos”, are denoted by adding “-ino” as a suffix to each SM particle.

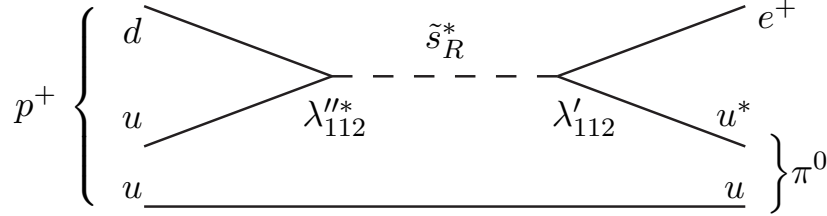
The SM particles and their superpartners are organized into two types of supermultiplets: “chiral supermultiplets” and “vector supermultiplets”. Chiral supermultiplets consist of spin- $1/2$ fermions or spin-0 Higgs bosons along with their superpartners, as presented in Table 2.1. Vector supermultiplets, on the other hand, comprise spin-1 gauge bosons and their superpartners, as given in Table 2.2.

Table 2.1: Chiral supermultiplets in the MSSM.

Names		spin 0	spin 1/2	$SU(3)_C, SU(2)_L, U(1)_Y$
squarks, quarks ($\times 3$ generations)	Q	$(\tilde{u}_L \tilde{d}_L)$	$(u_L d_L)$	$(\mathbf{3}, \mathbf{2}, \frac{1}{6})$
	\tilde{u}	\tilde{u}_R^*	u_R^\dagger	$(\bar{\mathbf{3}}, \mathbf{1}, -\frac{2}{3})$
	\tilde{d}	\tilde{d}_R^*	d_R^\dagger	$(\bar{\mathbf{3}}, \mathbf{1}, \frac{1}{3})$
sleptons, leptons ($\times 3$ generations)	L	$(\tilde{\nu} \tilde{e}_L)$	(νe_L)	$(\mathbf{1}, \mathbf{2}, -\frac{1}{2})$
	\tilde{e}	\tilde{e}_R^*	e_R^\dagger	$(\mathbf{1}, \mathbf{1}, 1)$
Higgs, higgsinos	H_u	$(H_u^+ H_u^0)$	$(\tilde{H}_u^+ \tilde{H}_u^0)$	$(\mathbf{1}, \mathbf{2}, +\frac{1}{2})$
	H_d	$(H_d^0 H_d^-)$	$(\tilde{H}_d^0 \tilde{H}_d^-)$	$(\mathbf{1}, \mathbf{2}, -\frac{1}{2})$

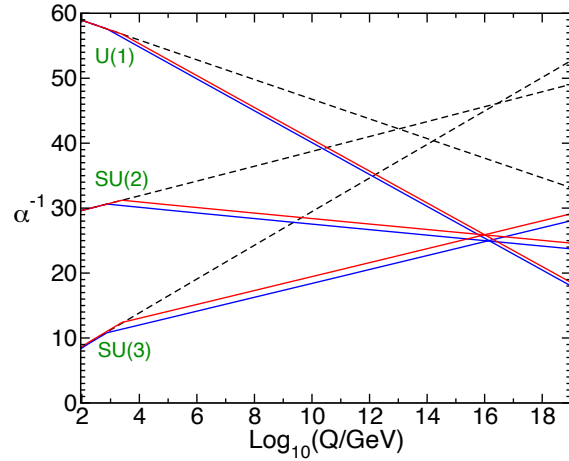
Table 2.2: Vector supermultiplets in the MSSM.

Names	spin 1/2	spin 1	$SU(3)_C, SU(2)_L, U(1)_Y$
Gluino, gluon	\tilde{g}	g	$(\mathbf{8}, \mathbf{1}, 0)$
Wino, W bosons	$\tilde{W}^\pm, \tilde{W}^0$	W^\pm, W^0	$(\mathbf{1}, \mathbf{3}, 0)$
Bino, B boson	\tilde{B}^0	B^0	$(\mathbf{1}, \mathbf{1}, 0)$


 Figure 2.2: Diagram of a proton decay mediated by a strange squark. The diagram is induced by R -parity violating couplings. The figure is taken from Ref. [14].

R -parity When constructing the Lagrangian of the MSSM, it is possible to include terms that violate a discrete symmetry called “ R -parity”. The R -parity is defined as $R = (-1)^{3(B-L)+2s}$, where B and L are the baryon and lepton numbers, and s is the spin of the particle. The R -parity of SM particles is +1, while the SUSY particles have an R -parity of -1. If the R -parity is conserved, an even number of SUSY particles is produced by collision of SM particles. In general, R -parity violating terms are not prohibited but lead to rapid proton decays, as shown in Figure 2.2. This tends to be in tension with the limit set by experiments. Another consequence of the conservation of R -parity is that the lightest SUSY particle (LSP) cannot decay and remains stable, making it a viable candidate for dark matter. In this thesis, we assume that R -parity is conserved.

Figure 2.3: Renormalization group evolution of the inverse gauge couplings $\alpha_a^{-1}(Q)$ ($a = 1, 2, 3$), calculated up to two-loop effects. The dotted (solid) lines show the evolution in the SM (MSSM). In the MSSM case, the sparticle masses are treated as a common threshold varied between 750 GeV and 2.5 TeV, and $\alpha_3(m_Z)$ is varied between 0.117 and 0.120. The figure is taken from Ref. [14].



Grand Unification The introduction of SUSY brings a significant advantage of unifying the coupling constants of strong, weak, and electromagnetic interactions at high-energy scales. The coupling constant varies with the energy scale due to the running effect from the renormalization, which is described by the renormalization group equation (RGE). When SUSY is introduced, the number of particles coupled to the gauge boson increases, which enhances the contribution of the loop effects to the couplings. While there is no energy scale at which the three coupling constants have the same value in the SM, the introduction of superpartners changes the coefficients of the RGE and unifies the coupling constant at a scale of $M_U \sim 1.5 \times 10^{16}$ GeV in the presence of SUSY particles of around $O(1)$ TeV, as shown in Figure 2.3.

Soft SUSY breaking SUSY must be broken, since no SUSY particles are discovered at the mass of the SM partners. Additional terms are introduced to the MSSM Lagrangian to break SUSY explicitly. Only soft terms, which do not involve terms with dimensionless couplings, are introduced to maintain the cancellation of the quadratic divergences of the Higgs boson mass. The most general soft terms are described as [14]

$$\begin{aligned}
\mathcal{L}_{\text{soft}}^{\text{MSSM}} = & -\frac{1}{2} (M_3 \tilde{g} \tilde{g} + M_2 \tilde{W} \tilde{W} + M_1 \tilde{B} \tilde{B} + \text{c.c.}) \\
& - (\tilde{u} \mathbf{a}_u \tilde{Q} H_u - \tilde{d} \mathbf{a}_d \tilde{Q} H_d - \tilde{e} \mathbf{a}_e \tilde{L} H_d + \text{c.c.}) \\
& - \tilde{Q}^\dagger \mathbf{m}_Q^2 \tilde{Q} - \tilde{L}^\dagger \mathbf{m}_L^2 \tilde{L} - \tilde{u} \mathbf{m}_u^2 \tilde{u}^\dagger - \tilde{d} \mathbf{m}_d^2 \tilde{d}^\dagger - \tilde{e} \mathbf{m}_e^2 \tilde{e}^\dagger \\
& - m_{H_u}^2 H_u^* H_u - m_{H_d}^2 H_d^* H_d - (b H_u H_d + \text{c.c.}) .
\end{aligned} \tag{2.4}$$

The first line consists of the terms of the gaugino mass where M_1 , M_2 , and M_3 represent the bino, wino, and gluino mass, respectively. The second line introduces trilinear scalar couplings, which correspond to the Yukawa couplings in the MSSM, where \mathbf{a}_i ($i = u, d, e$) is a 3×3 matrix in family space. The remaining lines represent the scalar mass terms, where \mathbf{m}_i^2 ($i = Q, L, \bar{u}, \bar{d}, \bar{e}$) is a 3×3 matrix in family space and b is the bilinear scalar coupling.

2.2.2 Solutions to the problems of the Standard Model

Quadratic Divergence of the Higgs boson mass If the Lagrangian includes a heavy complex scalar particle S , where the Lagrangian term is described as $-\lambda_S |H|^2 |S|^2$, the Higgs boson receives additional quantum corrections described as

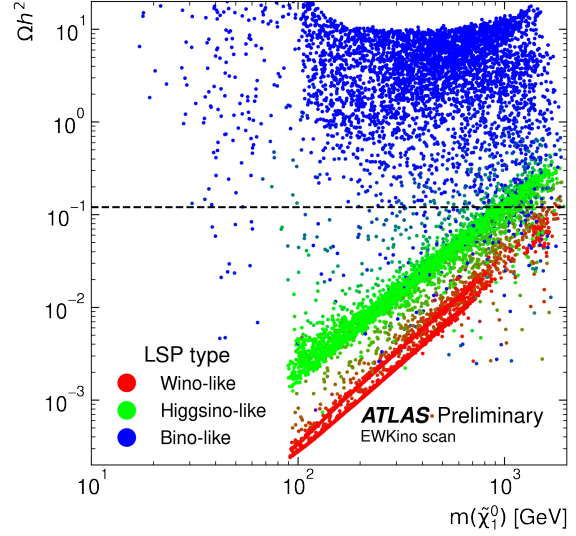
$$\Delta m_H^2 = \frac{\lambda_S}{16\pi^2} [\Lambda_{\text{UV}}^2 - 2m_S^2 \ln(\Lambda_{\text{UV}}/m_S) + \dots], \quad (2.5)$$

where m_S^2 is the mass of the scalar particles. In the MSSM, Equations 2.1 and 2.5 cancel, leaving the $\mathcal{O}(\log \Lambda_{\text{UV}})$ term by the introduction of two scalar partners (\tilde{f}_L and \tilde{f}_R) for each SM fermion (f).

At the tree level, the Higgs boson mass is bounded by $m_{h^0} < m_Z |\cos(2\beta)|$ [14] and a radiative correction of a total of a few hundred of GeV is required to elevate the Higgs boson mass to 125 GeV. The most significant one-loop level quantum correction to the Higgs boson mass arises from loops with top and stop particles. A large value of $\tan \beta$ ($\tan \beta \gg 1$) is preferred to resolve the problem of the quadratic divergence of the Higgs boson mass without precise tuning of the parameters in the MSSM. If $\tan \beta \sim 1$, the Higgs boson mass, expressed as $m_Z |\cos(2\beta)|$ at the tree level, requires significant radiative corrections to explain the observed Higgs boson mass. The stop mass must be larger to achieve the required radiative correction, requiring a more precise tuning of the stop mass to satisfy the necessary correction. A small value of $\tan \beta$ ($\tan \beta \ll 1$) raises the Higgs boson mass to the Z boson mass at the tree level. However, the up-type Yukawa couplings become non-perturbatively large since the couplings are inversely proportional to the vacuum expectation value of the up-type Higgs from the relation $m_t = y_t v_u = y_t v \sin \beta$.

Dark matter In the MSSM, the LSP is a stable and weakly interacting particle, making it a viable candidate for dark matter. In most cases, we consider the neutralino as the LSP. The masses that can explain the relic density significantly vary based on the combination of bino, wino, and higgsinos. To realize the observed relic density, the mass of the Higgsino (Wino)-like LSP need to be around 1(3) TeV. Figure 2.4 illustrates the relation between the neutralino mass and the relic density for each LSP type obtained from the phenomenological MSSM (pMSSM) scan. If the Higgsino (Wino)-like LSP does not make up all of dark matter, its mass can be below 1(3) TeV. The annihilation cross-section of Bino-like LSP tends to be too small due to the helicity-suppressed annihilation of Majorana particles into fermions [37, 38] and the vanishing interaction with the SM particles when sleptons and squarks are heavy, resulting in an overabundant relic density. Therefore, models with a realistic Bino-like LSP dark matter must have additional mechanisms to enhance the annihilation cross-section, as discussed in Appendix A.2.

Figure 2.4: Scatter plot of the neutralino mass points that pass through the pMSSM scan and the resulting relic density. The pMSSM reduces the number of parameters in the MSSM to 19 parameters through phenomenological constraints. A scan on the parameters of the pMSSM has been performed using external constraints, such as electroweak precision measurements, flavour physics searches, and direct dark matter detection searches. The horizontal dashed line corresponds to the observed relic density. The color of each point corresponds to the type of particle that constitutes the neutralino. The figure is taken from Ref. [39].



2.3 Phenomenology of the electroweak sector of the MSSM

2.3.1 Electroweakinos

As discussed in Chapter 1, higgsinos (\tilde{H}), bino (\tilde{B}), and wino (\tilde{W}) are mixed to form mass eigenstates called electroweakinos. The neutralino mass term in the MSSM Lagrangian is described as

$$\mathcal{L}_{\text{neutralino mass}} = -\frac{1}{2} (\psi^0)^T \mathbf{M}_{\tilde{N}} \psi^0 + \text{c.c.}, \quad (2.6)$$

where $\psi^0 = (\tilde{B}, \tilde{W}^0, \tilde{H}_d^0, \tilde{H}_u^0)$ is the gauge-eigenstate basis. The neutralino mixing matrix $\mathbf{M}_{\tilde{N}}$ describes the mixing between the neutral gauginos and higgsinos, defined as

$$\mathbf{M}_{\tilde{N}} = \begin{pmatrix} M_1 & 0 & -c_\beta s_W m_Z & s_\beta s_W m_Z \\ 0 & M_2 & c_\beta c_W m_Z & -s_\beta c_W m_Z \\ -c_\beta s_W m_Z & c_\beta c_W m_Z & 0 & -\mu \\ s_\beta s_W m_Z & -s_\beta c_W m_Z & -\mu & 0 \end{pmatrix}, \quad (2.7)$$

where μ represents the higgsino mass parameter, θ_W is the Weinberg angle ($c_W \equiv \cos \theta_W$, $s_W \equiv \sin \theta_W$), and β is defined by the ratio of the two vacuum expectation values of the up- and down-type Higgs ($c_\beta \equiv \cos \beta$, $s_\beta \equiv \sin \beta$).

The chargino mass term in the MSSM Lagrangian is described as

$$\mathcal{L}_{\text{chargino mass}} = -\frac{1}{2} (\psi^\pm)^T \mathbf{M}_{\tilde{C}} \psi^\pm + \text{c.c.}, \quad (2.8)$$

where $\psi^\pm = (\tilde{W}^+, \tilde{H}_u^+, \tilde{W}^-, \tilde{H}_d^-)$ is the gauge-eigenstate basis. The chargino mixing matrix $\mathbf{M}_{\tilde{C}}$ describes the mixing between charged gauginos and higgsinos, defined as

$$\mathbf{M}_{\tilde{C}} = \begin{pmatrix} \mathbf{0} & \mathbf{X}^T \\ \mathbf{X} & \mathbf{0} \end{pmatrix}, \text{ with } \mathbf{X} = \begin{pmatrix} M_2 & \sqrt{2}s_\beta m_W \\ \sqrt{2}c_\beta m_W & \mu \end{pmatrix}. \quad (2.9)$$

2.3.2 Light Higgsino Scenario

In the MSSM, the following equation holds by requiring minimization of the Higgs potential [40].

$$-\frac{m_Z^2}{2} = |\mu|^2 - \frac{m_{H_d}^2 - m_{H_u}^2 \tan^2 \beta}{\tan^2 \beta - 1} \quad (2.10)$$

It is evident from this equation that μ must not be too large in comparison to the electroweak scale, which we refer to as ‘‘electroweak naturalness’’ [40, 41]. In this thesis, we consider the higgsino LSP scenario, where $|\mu|$ is close to the electroweak scale motivated by naturalness.

2.3.3 Mass difference between the higgsino-like mass eigenstates

Motivated by electroweak naturalness and dark matter, this thesis targets a higgsino LSP with a mass approximately at the electroweak scale. When the wino and bino mass is decoupled with the higgsino mass ($|\mu| \ll M_1, M_2$), the lightest chargino and neutralinos form compressed mass spectra, as illustrated in Figure 2.5. The mass difference between the two light neutralinos, denoted as $\Delta m_0 \equiv m(\tilde{\chi}_2^0) - m(\tilde{\chi}_1^0)$, is induced by mixing with bino or wino [42–45] and can be expressed as

$$\Delta m_0 \simeq m_Z^2 \left| \frac{c_W^2}{M_2} + \frac{s_W^2}{M_1} \right|. \quad (2.11)$$

The mass difference between the lightest chargino and neutralino, denoted as $\Delta m_\pm \equiv m(\tilde{\chi}_1^\pm) - m(\tilde{\chi}_1^0)$ can be divided into two terms: tree-level term ($\Delta m_\pm^{\text{tree}}$) and radiation correction term ($\Delta m_\pm^{\text{rad}}$). The $\Delta m_\pm^{\text{tree}}$ is induced by mixing with bino and wino, and the $\Delta m_\pm^{\text{rad}}$ is induced by electroweak gauge-boson loops. The two terms $\Delta m_\pm^{\text{tree}}$ and $\Delta m_\pm^{\text{rad}}$ are described as [42–45]

$$\begin{aligned} \Delta m_\pm^{\text{rad}} &\simeq \frac{\alpha_2 s_W^2 \mu}{2\pi} \int_0^1 dt (1+t) \ln \left[1 + \frac{m_Z^2 (1-t)}{\mu^2 t^2} \right], \\ \Delta m_\pm^{\text{tree}} &\simeq \frac{\Delta m_0}{2} - \frac{1}{2} m_Z^2 \sin 2\beta \left(\frac{c_W^2}{M_2} - \frac{s_W^2}{M_1} \right), \end{aligned} \quad (2.12)$$

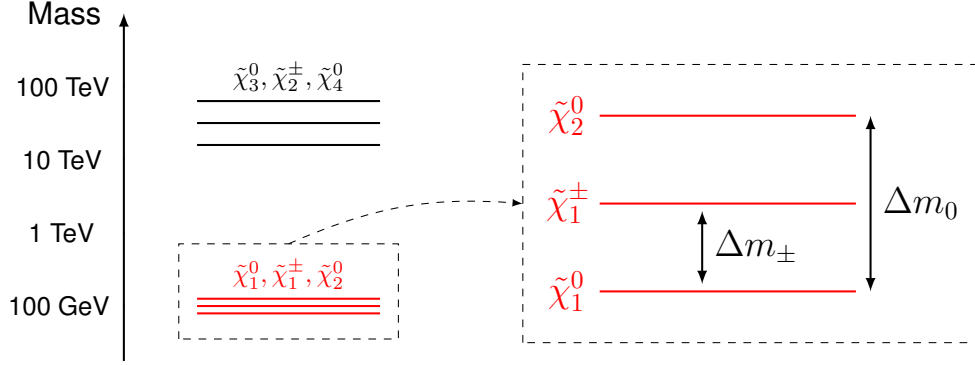


Figure 2.5: Schematic of the mass spectra of electroweakinos in the higgsino LSP scenario with the gauginos decoupled in mass. Since the higgsino and gaugino masses are sufficiently decoupled, the particles $\tilde{\chi}_1^0, \tilde{\chi}_1^\pm$, and $\tilde{\chi}_2^0$ consist mainly of higgsinos, while $\tilde{\chi}_3^0, \tilde{\chi}_2^\pm$, and $\tilde{\chi}_4^0$ are mainly composed of bino and wino. The light higgsinos shown in red are targeted in this search. As illustrated on the right side, the mass difference between $\tilde{\chi}_2^0$ and $\tilde{\chi}_1^0$ is denoted as Δm_0 , while the mass difference between $\tilde{\chi}_1^\pm$ and $\tilde{\chi}_1^0$ is denoted as Δm_\pm .

where α_2 is the fine structure constant for the $SU(2)_L$ gauge interaction. For $\mu \gg m_Z$ [42],

$$\Delta m_\pm^{\text{rad}} \simeq \frac{\alpha_2 m_Z}{2} \sin^2 \theta_W \simeq 354 \text{ MeV}. \quad (2.13)$$

The higgsino mass difference becomes smaller as the gaugino masses become decoupled from the higgsino mass, but Δm_\pm is always larger than $O(200 - 300)$ MeV due to radiation corrections.

In the target mass difference region, the decay length of the lightest chargino is approximately given as [42]

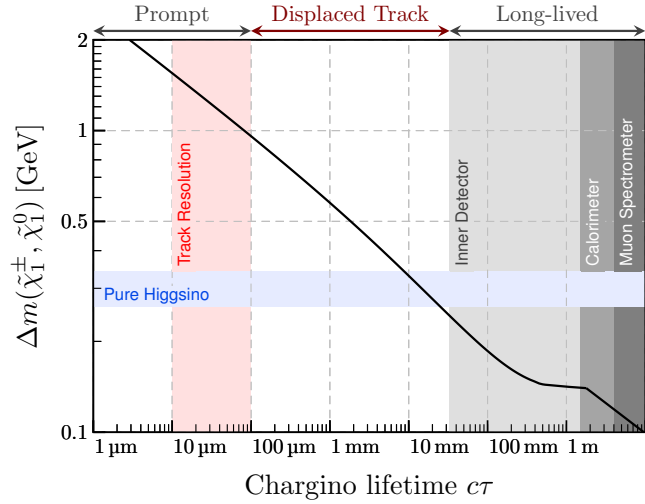
$$\Gamma^{-1} \simeq \Gamma_{\tilde{\chi}_1^\pm \rightarrow \tilde{\chi}_1^0 \pi^\pm}^{-1} \simeq \frac{14 \text{ mm}}{\hbar c} \times \left[\left(\frac{\Delta m_\pm}{340 \text{ MeV}} \right)^3 \sqrt{1 - \frac{m_{\pi^\pm}^2}{\Delta m_\pm^2}} \right]^{-1}, \quad (2.14)$$

where Γ , $\Gamma_{\tilde{\chi}_1^\pm \rightarrow \tilde{\chi}_1^0 \pi^\pm}$, and m_{π^\pm} represent the total decay width of the chargino decay, the partial decay width of the chargino decay to pions, and the pion mass, respectively. Figure 2.6 shows the dependence of the chargino lifetime on the higgsino mass difference. In the higgsino mass difference range we are interested in ($\Delta m_\pm \approx 0.3 - 1.0$ GeV), the lifetime of the chargino extends to $c\tau \approx O(0.1 - 1)$ mm, which is long enough to be distinguished from prompt decay particles.

2.4 Experimental constraints on the Higgsino LSP scenario

Searches for higgsino LSP have been conducted using various techniques, including collider experiments, the direct dark matter searches using nuclear recoil signals, and the indirect dark

Figure 2.6: Dependence of the chargino lifetime ($c\tau$) on the mass difference between the chargino and neutralino (Δm_{\pm}). The gray area indicates the location of the ATLAS detector. The blue area indicates the range of mass difference, where the gaugino mass is sufficiently decoupled from the higgsino mass. The red region represents the impact parameter resolution of tracks reconstructed in the ATLAS detector. If a particle's lifetime is longer than this red region, it can be distinguished from particles produced promptly.



matter searches aiming to detect annihilation signals through astronomical observations. Limits from collider experiments are provided in Section 2.4.1, followed by the limits from direct and indirect dark matter detections in Sections 2.4.2 and 2.4.3, respectively. Section 2.4.4 discusses the limits imposed by electron Electric Dipole Moment (EDM) experiments, as the presence of higgsinos affects the electron EDM. Generally, the direct and indirect searches have imposed strong constraints on the existence of higgsinos. However, these suffer from substantial model uncertainties on dark matter profiles in the galaxy center or around the Earth, as well as the signal propagation in space. Collider searches, on the other hand, are entirely free from these uncertainties, which makes them no less important.

2.4.1 Collider Experiments

Higgsinos in compressed mass spectra have been the focus of numerous search efforts at the Large Hadron Collider (LHC). Given the soft visible decay products of the SUSY states, the primary signature suitable for triggering is the missing transverse energy (E_T^{miss}) arising from the neutralinos. To obtain a large E_T^{miss} above the trigger threshold, an initial state radiation (ISR) topology must be exploited, requiring the SUSY system to recoil against hadronic activities. This results in a “jets+ E_T^{miss} ” signature, enabling the higgsino sensitivity independent of the decay signature [46, 47]. The signal-to-background ratio in searches for electroweak SUSY production is relatively low due to the low cross-sections and significant irreducible background. Consequently, these searches have not been sensitive to direct higgsino production. Therefore, in addition to the “jets+ E_T^{miss} ” signature, an additional decay signature is required to suppress the SM backgrounds in the searches introduced below. The diagrams that illustrate electroweakino pair production and their decays, targeted by the searches described below, are shown in Figure 2.7.

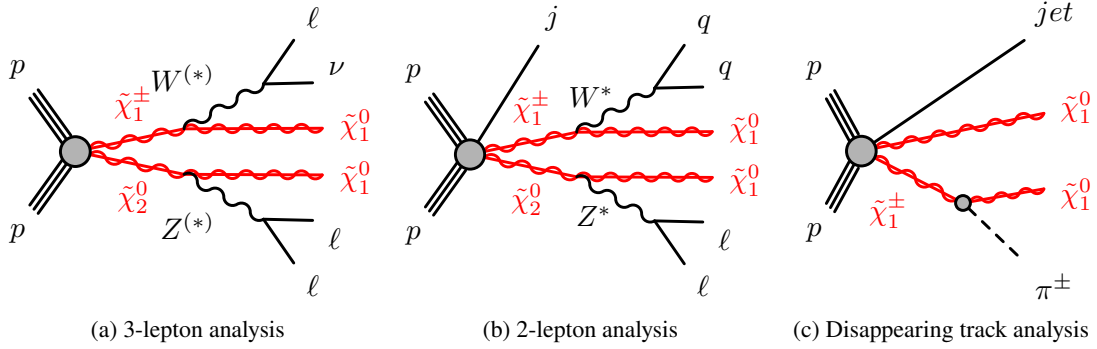


Figure 2.7: Diagrams of processes targeted by the existing searches for electroweakino-pair production with compressed mass spectra of higgsinos. The diagrams are arranged in descending order of higgsino mass difference from left to right.

Limits from the soft lepton search For larger higgsino mass differences above approximately 1.5 GeV, the final-state leptons from higgsino decays acquire large enough transverse momentum (p_T) to be reconstructed with reasonable efficiency in the ATLAS detector, which is about 3 GeV for muons and 4.5 GeV for electrons. In the ATLAS soft 2-lepton search, a pair of soft leptons from a neutral higgsino decay with a small invariant mass is required, in addition to the “jets+ E_T^{miss} ” signature. The ATLAS soft 3-lepton search also considers the case where the charged higgsino decays leptonically. Their statistical combination is depicted in the summary plot in Figure 1.1, probing the higgsino mass up to 180 GeV and the mass difference between the lightest charged higgsino and neutral higgsino down to 1.5 GeV. CMS has performed a similar analysis, and similar results have been obtained [48].

Limits from the disappearing track search For very small higgsino mass differences of only several hundred MeV, the chargino becomes long-lived and can traverse the first layers of the tracking detector before decaying into a charged pion with extremely low p_T ($\mathcal{O}(100)$ MeV). The charged pion is not reconstructed due to the limitation of the threshold of track reconstruction. This results in a distinct signature known as a “disappearing track”, serving as the additional decay signature to the “jets+ E_T^{miss} ” signature: the track of the chargino is visible in the first few tracking layers before it vanishes, and no matching hits can be found in the outer tracking layers. The results from the latest iteration of this analysis are shown in Figure 1.1. The analysis probes higgsino mass differences up to 400 MeV and is sensitive to pure higgsino states of approximately 200 GeV. CMS has performed a similar analysis, and similar results have been obtained [16].

Limits from the Large Electron-Positron Collider (LEP) Limits on compressed higgsino states are established by combining results from the four experiments from the Large Electron-Positron Collider (LEP): ALEPH, DELPHI, L3, and OPAL [20]. In regions with sufficient mass difference ($\Delta m(\tilde{\chi}_1^\pm, \tilde{\chi}_1^0) > 3$ GeV), the large missing energy with jet or lepton topology is utilized to set a limit up to 100 GeV in the higgsino mass. In the small mass difference region

($\Delta m(\tilde{\chi}_1^\pm, \tilde{\chi}_1^0) < 3 \text{ GeV}$), an ISR photon is required to boost the SUSY system, generating a large missing energy and suppressing background. In this case, the exclusion limit extends to about 90 GeV in the higgsino mass. The combined exclusion limit by LEP experiments is presented in Figure 1.1.

2.4.2 Direct dark matter detection

The process of Higgs boson exchange between neutralinos and nuclei induces the spin independent (SI) elastic scattering, as illustrated in Figure 2.8(a). The most stringent limits to the SI dark matter-nucleon cross-section, denoted as σ_{SI} , have been set by the LUX-ZEPLIN (LZ) experiment [21]:

$$\sigma_{\text{SI}} = 9.2 \times 10^{-48} \text{ cm}^2 \text{ (at } m_\chi = 36 \text{ GeV)}. \quad (2.15)$$

Limits from the SI elastic scattering If either wino or bino has a relatively light mass, the Higgs boson-mediated process is enhanced through the increased higgsino-gaugino mixing, leading to a larger SI elastic scattering cross-section. Since the mixing of higgsinos and gauginos is related to the mass difference, the scattering cross-section can be approximately related to the higgsino mass difference. For $\tan\beta \gg 1$ [42],

$$\Delta m_\pm \sim \Delta m_\pm^{\text{rad}} + 170 \text{ MeV} \left(\frac{\sigma_{\text{SI}}}{10^{-48} \text{ cm}^2} \right)^{1/2}. \quad (2.16)$$

The strongest limit to the SI elastic scattering cross-section at $m_\chi = 100 \text{ GeV}$ imposed by the experiments is $\sim 3 \times 10^{-47} \text{ cm}^2$. Figure 2.9 shows the dependence of the SI elastic scattering cross-section on the gaugino mass. The limit indicates that direct dark matter detection experiments are capable of finding a higgsino mass difference of more than 1 GeV, derived from Equation 2.16.

Limits from the inelastic scattering If the gauginos are decoupled from the higgsino mass, the inelastic scattering process is enabled through the exchange of a Z boson, as illustrated in Figure 2.8(b). The direct dark matter detection experiments are also sensitive to the inelastic scattering process and exclude regions with $\Delta m_0 < \mathcal{O}(200) \text{ keV}$ [49]. The region with a higgsino mass difference of $\Delta m_0 > \mathcal{O}(200) \text{ keV}$ is challenging to search in the future. This is because it falls within the range of sensitivity restricted by irreducible backgrounds from coherent neutrino scattering, also known as the “neutrino floor”. Even with a significant increase in the sensitivity of future direct dark matter detection experiments, this region would remain challenging to investigate.

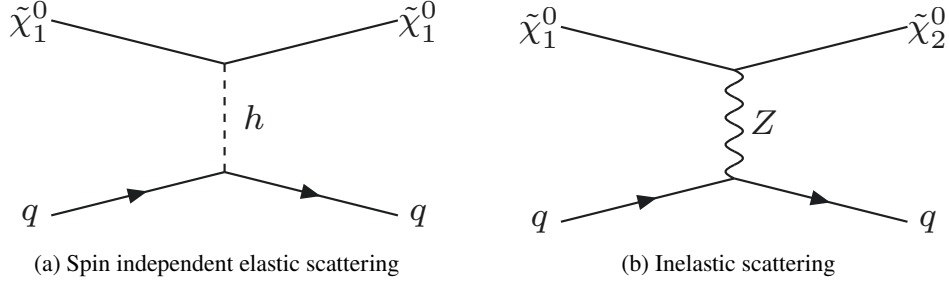
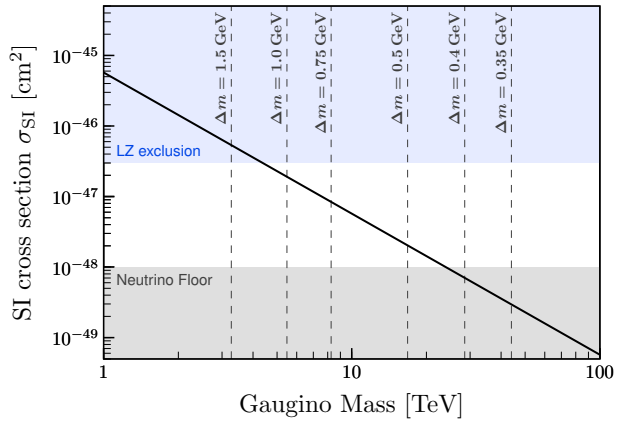


Figure 2.8: Diagrams inducing elastic and inelastic scattering between neutralinos and quarks. The figures are taken from Ref. [49].

Figure 2.9: Dependence of the SI elastic scattering cross-section on the gaugino mass derived from Equation 2.16 with $M_1 = M_2$, $\mu = 100$ GeV, and $\tan\beta = 50$. The blue area indicates the region excluded by the LZ experiment at $m_\chi = 100$ GeV [21]. The gray region represents the range where the sensitivity is restricted by irreducible backgrounds from coherent neutrino scattering. This region is referred to as the “neutrino floor”. The vertical gray dashed lines illustrate the mass differences between the lightest chargino and neutralino for the given gaugino mass ($M_1 = M_2$).



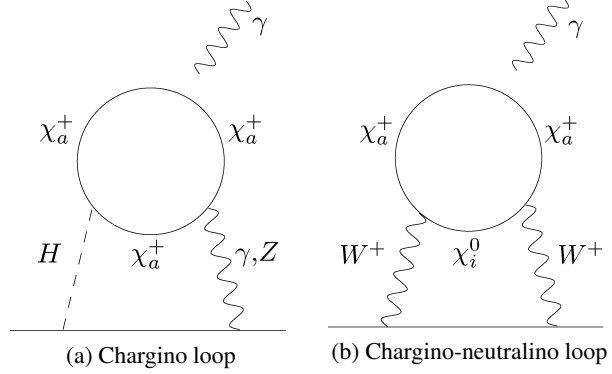
2.4.3 Indirect dark matter detection

The indirect dark matter detection of anti-protons and gamma-rays produced from the annihilation of neutralinos is also very effective in the search for higgsinos. The most stringent limit to the annihilation cross-section of higgsino-like LSPs is $\mathcal{O}(10^{-25})$ $\text{cm}^3 \text{s}^{-1}$, set by the Fermi-LAT experiment [50] through the observation of gamma-ray spectrum from W^+W^- and ZZ final states. The annihilation cross-section of higgsino-like LSPs at $m_\chi \approx 1.0$ TeV is expected to be $\langle\sigma v\rangle \approx 1.3 \times 10^{-26}$ $\text{cm}^3 \text{s}^{-1}$.

2.4.4 Electron Electric Dipole Moment (EDM)

The electron EDM is a very powerful probe for measuring the CP violation induced by electroweakinos in the MSSM. The loop corrections to the electron EDM induced by charginos and neutralinos are illustrated in Figure 2.10.

Figure 2.10: Barr-Zee diagrams induced by charginos contributing to the electron EDM. (a) Diagram illustrating a chargino loop connected to the fermion line with a photon (Z boson) and a Higgs boson. (b) Diagram illustrating a chargino-neutralino loop connected to the fermion line with two W bosons. The external photon line can be attached to any charged internal line in the diagram. The figures are taken and revised from Ref. [51].



The contribution to the electron EDM, denoted as $|d_e|$, is given by the loop mediated by γH , ZH , and WW :

$$d_e = d_{\gamma H} + d_{ZH} + d_{WW}, \quad (2.17)$$

where subscripts indicate the mediating particles. Each contribution can be described as [49]

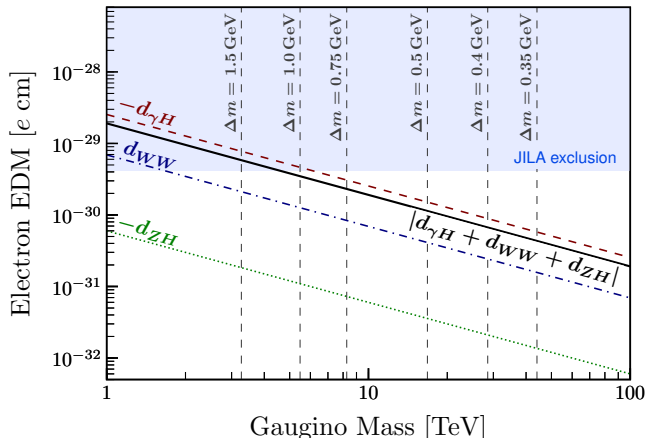
$$\begin{aligned} d_{\gamma H} &= -\frac{2e\alpha m_e}{(4\pi)^3} \frac{g^2 \sin 2\beta}{\mu M_2} \sin \phi_2 \times f_0 \left(\frac{|\mu|^2}{m_H^2} \right), \\ d_{ZH} &= -\frac{eg^2 m_e}{4(4\pi)^4} (1 - 4 \sin^2 \theta_W) (1 - \tan^2 \theta_W) \frac{g^2 \sin 2\beta}{\mu M_2} \sin \phi_2 \times f_1 \left(\frac{m_Z^2}{m_H^2}, \frac{|\mu|^2}{m_H^2} \right), \\ d_{WW} &= \frac{eg^2 m_e}{8(4\pi)^4} \frac{\sin 2\beta}{\mu} \left(\frac{g^2}{M_2} \sin \phi_2 - \frac{g'^2}{M_1} \sin \phi_1 \right) \times f_0 \left(\frac{|\mu|^2}{m_W^2} \right), \end{aligned} \quad (2.18)$$

where e , α , m_e , and θ_W represent the electric charge, the fine structure constant, the electron mass, and the Weinberg angle, respectively. In each equation, g and g' represent the $SU(2)_L$ and $U(1)_Y$ gauge coupling constants in the SM, respectively. The mass parameters μ , M_1 , and M_2 represent the higgsino, bino, and wino mass before the mixing with ϕ_1 and ϕ_2 defined as the angle of the complex phase on M_1 and M_2 , respectively. The loop functions mentioned in the above equations are defined as [49]

$$\begin{aligned} f_0(r) &= r \int_0^1 dx \frac{1}{r-x(1-x)} \ln \left(\frac{r}{x(1-x)} \right), \\ f_1(r_1, r_2) &= \frac{1}{1-r_1} \left[f_0(r_2) - r_1 f_0 \left(\frac{r_2}{r_1} \right) \right]. \end{aligned} \quad (2.19)$$

The most stringent limit to $|d_e|$ is established by the JILA experiment [52]:

Figure 2.11: Dependence of the electron EDM on the gaugino mass derived from Equation 2.18 with $M_1 = M_2$, $\mu = 100$ GeV, $\phi_1 = \phi_2 = \pi/2$, and $\tan\beta = 50$. The blue area indicates the region excluded by the JILA experiment [52]. The dashed or dotted lines represent the contribution from each loop illustrated in Figure 2.10. The solid line represents the total electron EDM. The vertical gray dashed lines illustrate the mass differences between the lightest chargino and neutralino.



$$|d_e| < 4.1 \times 10^{-30} e \text{ cm}. \quad (2.20)$$

Figure 2.11 shows the dependence of the electron EDM on the gaugino mass. When a large $\tan\beta$ ($\tan\beta = 50$) and maximum CP violation ($\phi_1 = \phi_2 = \pi/2$) are assumed, this is interpreted into an exclusion limit on the gaugino masses up to $\mathcal{O}(10)$ TeV, or on the higgsino mass difference down to $\mathcal{O}(1)$ GeV.

2.5 Definition of the Target Signal Models

This thesis considers a benchmark model in which model parameters other than mass are fixed for convenience. This model, also called the “simplified model”, serves as a benchmark model, allowing one to establish the criteria for selecting events in this analysis and for comparing the search sensitivity with the other previous searches. Although certain assumptions, such as the branching ratio, are necessary for constructing the model, the resultant simplified model is considered realistic enough in this case. This section outlines the configuration for building the simplified model in this thesis.

Production mode This thesis considers the direct production of charginos and neutralinos mediated by the off-shell W and Z bosons. The compressed mass spectra of the higgsino states emerge when the wino and bino masses are decoupled, resulting in a significant mass for $\tilde{\chi}_2^\pm$, $\tilde{\chi}_3^0$, and $\tilde{\chi}_4^0$. Given the negligible production cross-section of electroweakinos with large masses, the focus is on the following production modes:

$$pp \rightarrow \tilde{\chi}_1^0 \tilde{\chi}_2^0, \quad \tilde{\chi}_1^0 \tilde{\chi}_1^\pm, \quad \tilde{\chi}_2^0 \tilde{\chi}_1^\pm, \quad \tilde{\chi}_1^+ \tilde{\chi}_1^-. \quad (2.21)$$

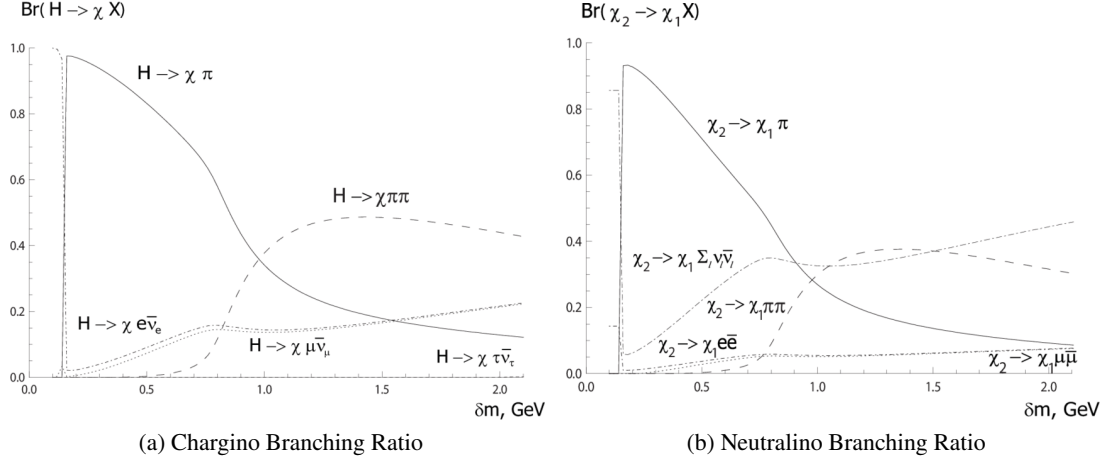


Figure 2.12: Branching ratio and higgsino mass difference dependence for $\tilde{\chi}_1^\pm$ and $\tilde{\chi}_2^0$. The figures are taken from Ref. [53].

Decay mode Charginos and neutralinos produced with compressed mass spectra decay via off-shell W and Z bosons:

$$\tilde{\chi}_1^\pm \rightarrow W^* \tilde{\chi}_1^0, \quad \tilde{\chi}_2^0 \rightarrow Z^* \tilde{\chi}_1^0. \quad (2.22)$$

Properties such as the mass and decay of higgsinos are determined by several model parameters in the MSSM. However, a benchmark model with these parameters fixed is selected for this analysis. In this thesis, the masses of SUSY particles other than $\tilde{\chi}_2^0$, $\tilde{\chi}_1^\pm$, and $\tilde{\chi}_1^0$ are decoupled and set at 45 TeV. Although the higgsino mass difference and branching ratio vary depending on the gaugino mass, the values are given by hand when creating simulation samples.

The mass hierarchy considered is $m(\tilde{\chi}_2^0) > m(\tilde{\chi}_1^\pm) > m(\tilde{\chi}_1^0)$, with the electroweakino masses equally spaced: $\Delta m(\tilde{\chi}_2^0, \tilde{\chi}_1^\pm) = \Delta m(\tilde{\chi}_1^\pm, \tilde{\chi}_1^0)$. The decay branching ratio of $\tilde{\chi}_1^\pm$ and $\tilde{\chi}_2^0$ to $\tilde{\chi}_1^0$ is assumed to be 100%. Only the mass difference ($\Delta m(\tilde{\chi}_1^\pm, \tilde{\chi}_1^0)$) and $\tilde{\chi}_1^0$ mass ($m(\tilde{\chi}_1^0)$) are considered as free model parameters. The branching ratio of $\tilde{\chi}_1^\pm$ and $\tilde{\chi}_2^0$ in the target higgsino mass difference region is calculated theoretically [53], which largely depends on the mass difference only, as illustrated in Figure 2.12. Since the final state topology targeted in this analysis depends only on the higgsino mass difference, fixing the model parameters as above does not lose generality.

Chapter 3

The ATLAS Experiment at the LHC

3.1 Large Hadron Collider

The Large Hadron Collider (LHC) is a proton-proton collider situated on the Swiss-French border with a circumference of approximately 27 km. Figure 3.1 provides an overall view of the LHC accelerator system. In the initial stage of the acceleration system, protons extracted from hydrogen gas are accelerated to 50 MeV in the linear accelerator 2 (LINAC 2). The protons progress through further acceleration stages, reaching energies of 1.4 GeV in the Proton Synchrotron Booster (PSB), 26 GeV in the Proton Synchrotron (PS), and finally, 450 GeV in the Super Proton Synchrotron (SPS). Protons entering the LHC are divided into two beam pipes, accelerated to 7 TeV in opposite directions, before colliding at four collision points, where detectors reside: ATLAS (A Toroidal LHC ApparatuS) [54], CMS (Compact Muon Solenoid) [55], ALICE (A Large Ion Collider Experiment) [56], and LHCb (Large Hadron Collider beauty) [57].

Each proton bunch contains approximately 10^{11} protons, and collisions between bunches occur at 25 ns intervals in the LHC. The LHC is designed to fill 2808 proton bunches in a single orbit and achieve an instantaneous luminosity of $1 \times 10^{34} \text{ cm}^{-2} \text{ s}^{-1}$. During 2015–2018, when the data used in this thesis were obtained, the instantaneous luminosity of the beam reached $2 \times 10^{34} \text{ cm}^{-2} \text{ s}^{-1}$, about twice the designed value. The LHC parameters selected during Run 2, along with the beam spot size for each year, are summarized in Table 3.1.

3.2 ATLAS detector

The ATLAS detector [54], positioned at one of the four collision points of the LHC, is a cylindrical apparatus with a diameter of 25 m, a length of 44 m, and a weight of approximately 7000 tons. The overall view of the ATLAS detector is provided in Figure 3.2(a). The ATLAS detector consists of, from the inside, inner detectors, a solenoid magnet, calorimeters, a toroidal magnet, and muon spectrometers.

The CERN accelerator complex *Complexe des accélérateurs du CERN*

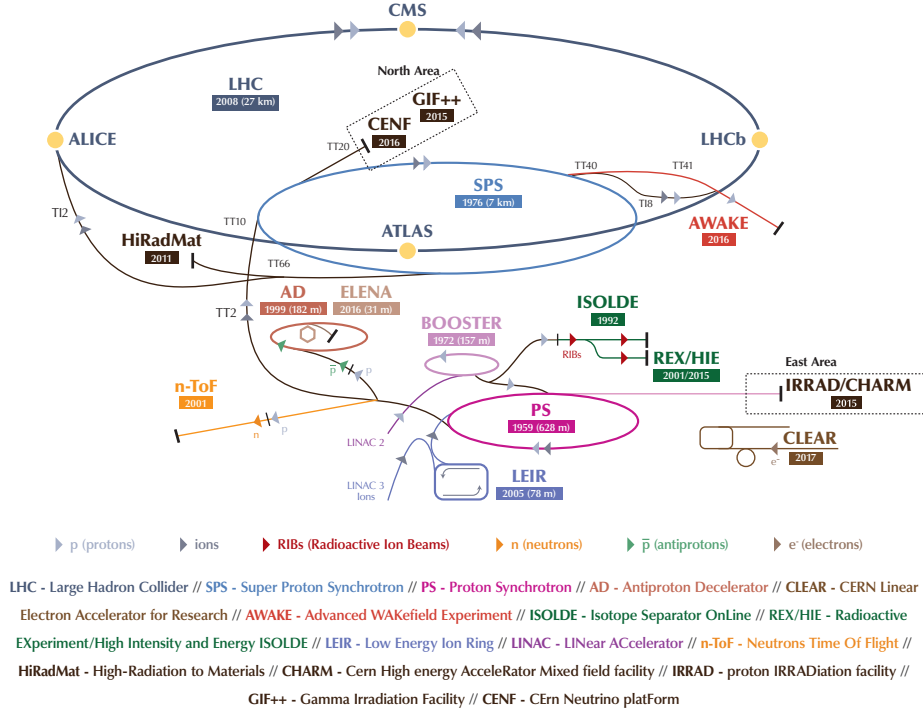


Figure 3.1: Overall view of the LHC accelerator system. The LHC beams intersect at the four collision points (ATLAS, CMS, ALICE, LHCb). The figure is taken from Ref. [58].

Table 3.1: Selected LHC parameters of $\sqrt{s} = 13$ TeV proton-proton collision during 2015–2018 [59]. In 2017, a vacuum incident caused a major heat load problem due to electron clouds, making it difficult to operate with the usual 25 ns bunch scheme. To cope with the heat load, the “8b4e” scheme was used, in which eight bunches are filled at 25 ns intervals followed by four bunch-slot gaps.

Parameter	2015	2016	2017	2018
Maximum number of colliding bunch pairs (n_b)	2232	2208	2544/1909	2544
Bunch spacing [ns]	25	25	25/8b4e	25
Typical bunch population [10^{11} protons]	1.1	1.1	1.1/1.2	1.1
Peak luminosity $\mathcal{L}_{\text{peak}}$ [10^{33} cm ⁻² s ⁻¹]	5	13	16	19
Average beam spot size in x - y plane [μm]	14.0–13.4	9.0–8.5	8.1–7.9	7.3–7.1
Average beam spot size along the beam axis [mm]	43.63	34.02	36.94	33.90

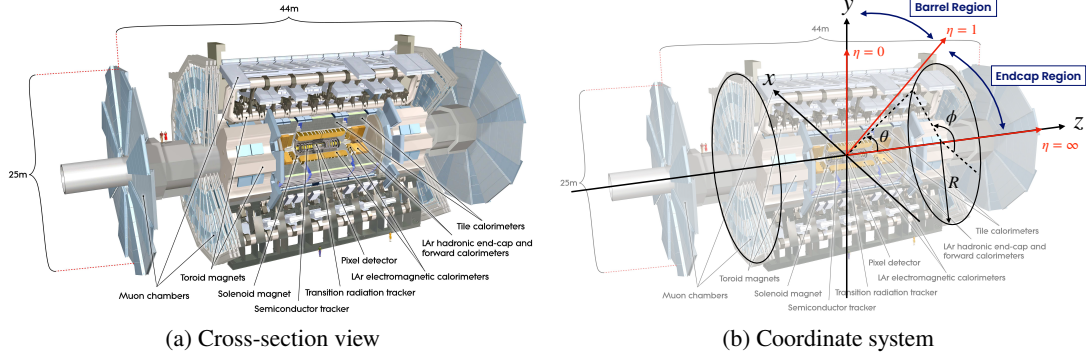


Figure 3.2: Cross-section view and coordinate system of the ATLAS detector. The ATLAS detector is a cylindrical detector with a diameter of 25 m, a length of 44 m, and a weight of about 7000 tons. The cartesian and cylindrical coordinate systems are employed in the ATLAS experiment. The figures are taken from Ref. [54].

3.2.1 Coordinate system

In the ATLAS experiment, the cartesian and cylindrical coordinate systems are used to represent the positions of the detector and particles, as illustrated in Figure 3.2(b). The coordinate system has its origin at the center of the detector, designating the z -axis as the direction of the beam axis and defining the x - y plane as the plane perpendicular to the beam axis. The x -axis is defined as positive in the direction from the impact point to the center of the LHC ring, and the y -axis is considered positive in the upward vertical direction toward the ground. Within the ATLAS detector, the side with positive (negative) z axis is called the A-side (C-side). The azimuthal angle ϕ and the polar angle θ denote the angle around the beam axis and the angle from the beam axis, respectively.

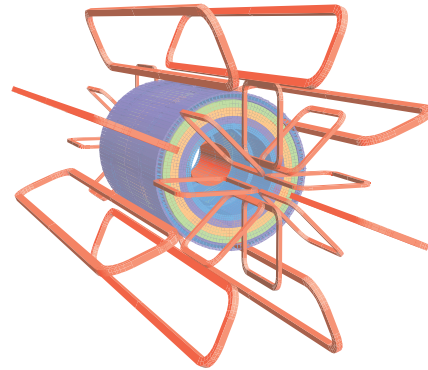
The variable pseudo-rapidity η is introduced and used in the ATLAS experiment. Pseudo-rapidity η is defined as the high energy limit of the rapidity $y = \frac{1}{2} \ln \left(\frac{E+p_z c}{E-p_z c} \right)$ and is expressed solely using the azimuthal angle θ , described as

$$\eta = \lim_{E, |p| \rightarrow \infty} \frac{1}{2} \ln \left(\frac{E + p_z c}{E - p_z c} \right) = \frac{1}{2} \ln \left(\frac{1 + \cos \theta}{1 - \cos \theta} \right) = \frac{1}{2} \ln \left(\frac{\cos(\theta/2)}{\sin(\theta/2)} \right) = -\ln \tan(\theta/2). \quad (3.1)$$

The distance between particles is defined as $\Delta R = \sqrt{\Delta\eta^2 + \Delta\phi^2}$, which is determined by the difference in pseudo-rapidity η and azimuthal angle ϕ of the particles.

Since the ATLAS detector has different types of detector in its cylindrical structure, the side part with $|\eta| < 1.0$ is called the barrel region, and the bottom part with $|\eta| > 1.0$ is known as the endcap region.

Figure 3.3: Layout of the superconducting magnets in the ATLAS detector. The superconducting magnets are drawn in red. A calorimeter surrounds the center solenoid magnet, and the return yoke is located outside the solenoid magnet. The figure is taken from Ref. [54].



3.2.2 Magnet system

The magnet system bends the trajectories of charged particles and plays an essential role in measuring their momentum and charge. The magnet system consists of one superconducting solenoid magnet and three superconducting toroidal magnets, as shown in Figure 3.3.

Solenoid magnet The superconducting solenoid magnet is installed between the inner detectors and electromagnetic calorimeters in the barrel region, generating a magnetic field of 2 T along the beam axis. Charged particles passing through the inner detector are bent in the ϕ direction to measure the transverse momentum.

Toroidal magnet The superconducting toroidal magnets are installed in the endcap and barrel region, generating a magnetic field of 1 T and 0.5 T to measure the transverse momentum of charged particles passing through the muon spectrometers. The toroidal magnet consists of eight equally spaced coils in the ϕ direction. Considering the interference of magnetic fields between the endcap and barrel regions, the endcap toroidal magnets are placed at 22.5 degrees rotated from the barrel region.

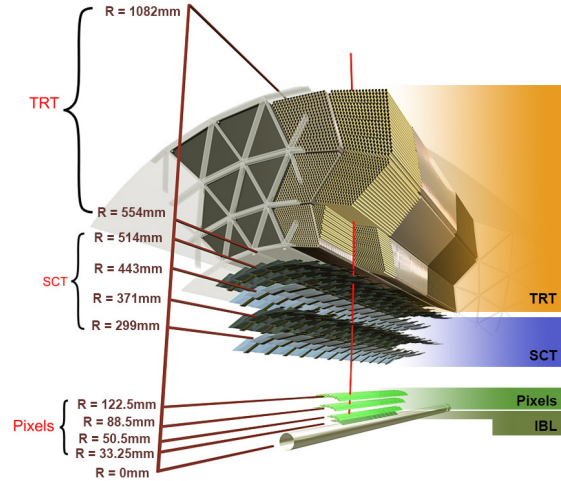
3.2.3 Inner detectors

Inner Detectors (IDs) are installed in the innermost part of the ATLAS detector. The momentum of charged particles passing through the solenoid magnet field is measured with the IDs. The ID consists of semiconductor-based trackers, the Insertable B-Layer (IBL), pixel detector, Semiconductor Tracker (SCT), and is complemented by a gaseous detector, the Transition Radiation Tracker (TRT) from the inside. Charged particles incident on the depletion layer of a semiconductor detector produce electron-hole pairs that are read as a signal. Semiconductor-based trackers are sensitive to small energy deposits due to their small gap energy and are placed in a liquid argon cryostat to reduce thermal noise. The layout of the ID in the barrel and endcap

Table 3.2: Coverage and performance of the beam pipe and each ID [54, 60].

Item	Region	Coverage		Resolution		
		R	z	$R-\phi$	R	z
Beam Pipe	-	23.5 mm	-	-	-	-
IBL	Barrel	33.25 mm	0–330.15 mm	0–3 μm	10 μm	60 μm
Pixel Detector	Barrel	50.5–122.5 mm	0–400.5 mm	10 μm	-	115 μm
	Endcap	88.8–149.6 mm	495–650 mm	10 μm	115 μm	-
SCT	Barrel	299–514 mm	0–749 mm	17 μm	-	580 μm
	Endcap	275–560 mm	839–2735 mm	17 μm	580 μm	-
TRT	Barrel	563–1066 mm	0–712 mm	130 μm	-	-
	Endcap	644–1004 mm	848–2710 mm	130 μm	-	-

Figure 3.4: Schematic of the IDs in the barrel region. The red line shows the trajectory of a charged particle with p_T of 10 GeV traversing the ID. The charged particle passes through the beryllium beam pipe, three layers of pixel detectors, four layers of SCTs, and 36 tubes of the TRT detector. The figure is taken from Ref. [61].



region is shown in Figures 3.4 and 3.5, respectively. The coverage and performance of each ID and beam pipe are summarized in Table 3.2.

Insertable B-Layer (IBL) and Pixel detector The innermost layer of the ID, called the Insertable B-Layer (IBL), was installed during the long shutdown period (2013–2015) before Run 2. The beam pipe was also replaced with a smaller radius to provide enough space for the IBL. The pixel size of IBL is $\Delta\phi \times \Delta z = 50 \mu\text{m} \times 250 \mu\text{m}$. The IBL covers the entire ϕ region by shifting the modules by about 26 degrees in the ϕ direction relative to the beam axis. The IBL provides hit information near the beam pipe ($R = 33.25 \text{ mm}$), which improves the tracking and vertexing performance. B hadrons have relatively long lifetimes and produce secondary vertices slightly distant from the interaction point. The IBL was introduced to enhance the precision of the reconstruction of these secondary vertices. The IBL has played an essential role in improving

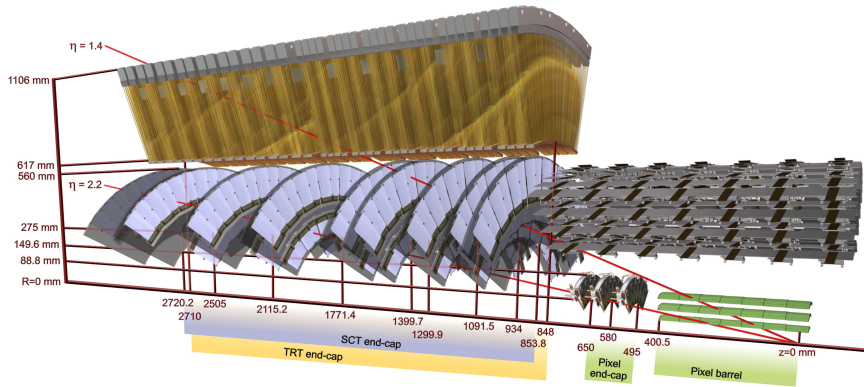


Figure 3.5: Schematic of the IDs in the endcap region. The two red lines show the trajectory of charged particles with p_T of 10 GeV traversing the ID. The charged particle passing through $\eta = 1.4$ penetrates the beryllium beam pipe, three layers of pixel detectors, four layers of SCTs, and about 40 tubes of the TRT detector. Since the TRT coverage area is up to $\eta = 2$, the charged particle passing through $\eta = 2.2$ does not cross the TRT detector. The IBL is omitted from this picture. The figure is taken from Ref. [54].

the performance of the reconstruction of jets from B hadrons, referred to as “ b -jets”. Three pixel layers are installed in the barrel and endcap region. The pixel size of the pixel detector is $\Delta\phi \times \Delta z = 50 \mu\text{m} \times 600 \mu\text{m}$.

Semiconductor Tracker (SCT) The Semiconductor Tracker (SCT) module consists of two strips with a pitch of $80 \mu\text{m}$, mounted at an angle of 40 mrad . The two-dimensional position information of an incident particle can be measured from the intersection of two readout strips. The barrel region has four layers of SCT modules, and the endcap region has nine layers of SCT modules.

Transition Radiation Tracker (TRT) The Transition Radiation Tracker (TRT) consists of 73 (160) layers of drift tubes, with 4 mm diameter aligned along the beam axis in the barrel (endcap) region. The drift tubes are filled with Xe(or Ar)-rich gas and operated as drift chambers. The space between the tubes is filled with polypropylene fibers, and transition radiation occurs when a charged particle traverses the tubes. The photons produced by the transition radiation are typically $5 - 7 \text{ keV}$, which is sufficiently larger than the ionization loss energy of $1 - 2 \text{ keV}$ to determine if transition radiation has occurred. Since electrons have an average probability of transition emission of 20% per tube, transition emission is used to distinguish between electrons and pions.

A single charged particle leaves an average of one hit in the IBL detector, four hits in the Pixel detector, and eight hits in the SCT detector. Although the resolution of the TRT detector is lower than other IDs, it makes a significant contribution to the determination of the track momentum since charged particles leave an average of 32 hits when they pass through the TRT detector.

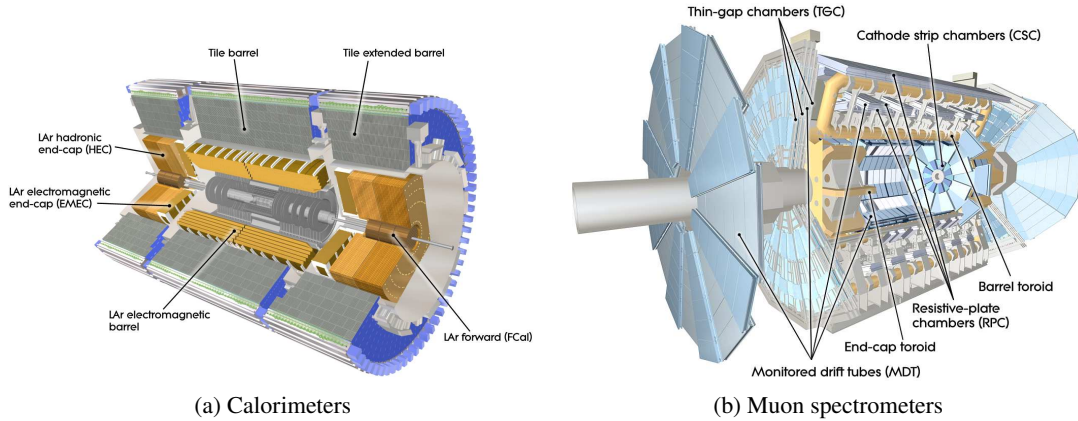


Figure 3.6: Layout of the calorimeters and Muon spectrometers (MSs) in the ATLAS detector. The figures are taken from Ref. [54].

3.2.4 Calorimeters

Calorimeters are installed outside the IDs and consist of electromagnetic and hadronic calorimeters. Electromagnetic calorimeters measure the energy of electrons and photons using electromagnetic showers, while hadronic calorimeters measure the energy of hadrons using hadron showers. The layout of the calorimeters is illustrated in Figure 3.6(a).

Electromagnetic calorimeter The electromagnetic calorimeter is a sampling calorimeter with a lead absorber, filling its gap with liquid argon. Charged particles entering the liquid argon cause ionization, and free electrons drift to the electrodes by the electric field. The drift time is very slow (600 ns), leading to significant contributions from other bunch crossings. However, the triangular-shaped pulse is sampled by bipolar pulse shaping [62] to cancel contributions from other bunch crossings. The ATLAS electromagnetic calorimeter has an excellent granularity, especially in the η direction of the first layer (0.003), which enables discrimination between a shower produced from a single photon and two photons from the decay of a neutral pion. This granularity also provides a more accurate measurement of the direction of the photon (“photon pointing”), which contributed to the measurement of the invariant mass with high precision in the $H \rightarrow \gamma\gamma$ measurement.

Hadronic calorimeter Hadron calorimeters consist of different absorbers and active materials depending on their location. The Tile Calorimeter (TileCal), installed in the barrel region ($|\eta| < 1.7$), is a sampling calorimeter composed of layers alternating between steel absorbers and scintillating tiles as active materials. The hadronic endcap calorimeters (HEC), installed in the endcap region ($1.5 < |\eta| < 3.2$), utilizes copper as the absorber to improve compactness and liquid argon as the active material. The forward calorimeters (FCal), installed in the forward region ($3.1 < |\eta| < 4.9$), use tungsten as absorbers to suppress the spread of hadronic showers.

Table 3.3: Coverage and performance of each MS [54]. Due to the higher rate in the forward direction, the TGC and CSC with greater rate tolerance are positioned.

Detector	Type	Coverage	Resolution		
			z/R	ϕ	Time
MDT	Precise measurement	$0 < \eta < 2.7$	$30 \mu\text{m} (z)$	–	–
CSC	Precise measurement	$2.0 < \eta < 2.7$	$40 \mu\text{m} (R)$	5 mm	7 ns
RPC	Triggering events	$0 < \eta < 1.05$	10 mm (z)	10 mm	1.5 ns
TGC	Triggering events	$1.05 < \eta < 2.7$	2–6 mm (R)	3–7 mm	4 ns

3.2.5 Muon spectrometers

MSs are installed at the outermost layer of the ATLAS detector as shown in Figure 3.6(b). MSs consist of four types of detectors: Resistive Plate Chamber (RPC), Thin Gap Chamber (TGC), Monitored Drift Tube (MDT), and Cathode Strip Chamber (CSC). MSs are classified into two types: RPC and TGC for triggering events, and MDT and CSC for precise measurements. The RPC and MDT detectors are installed in the barrel region, while the TGC, MDT, and CSC detectors are installed in the endcap region. The coverage and performance of each MS are summarized in Table 3.3.

Resistive Plate Chamber (RPC) The RPC consists of two high resistive plates with a 2 mm insulator inserted. The gas volume between the two plates is filled with $\text{C}_2\text{H}_2\text{F}_4$ based gas mixture. The high voltage application of 9.8 kV and thin gap widths produce a sharp signal rise. Strips are placed orthogonally to calculate positions in the η and ϕ coordinates.

Thin Gap Chamber (TGC) The TGC is a Multi Wire Proportional Chamber (MWPC) filled with $\text{CO}_2/n\text{-C}_5\text{H}_{12}$ mixture gas, which determines the R and ϕ position from a two-dimensional readout by wires and strips. The wires and strips are placed with a pitch of 1.4 mm, shorter than the pitch between the wires, resulting in a high detector time response and rate tolerance.

Monitored Drift Tube (MDT) The MDT consists of six or eight layers of drift tubes of 30 mm diameter filled with Ar/CO_2 mixture gas. Electrons produced by ionization are collected by the anode wire placed at the center of the drift tube. The MDT measures the position of tracks based on the drift time of the electrons.

Cathode Strip Chamber (CSC) The CSC is a MWPC placed in the $|\eta| > 2$ region, where hit rates are expected to be too high for the MDTs to be sufficiently tolerant. The detector is filled with Ar/CO_2 mixture gas. Two cathode strips are placed orthogonally, allowing for the measurement of the R and ϕ coordinates.

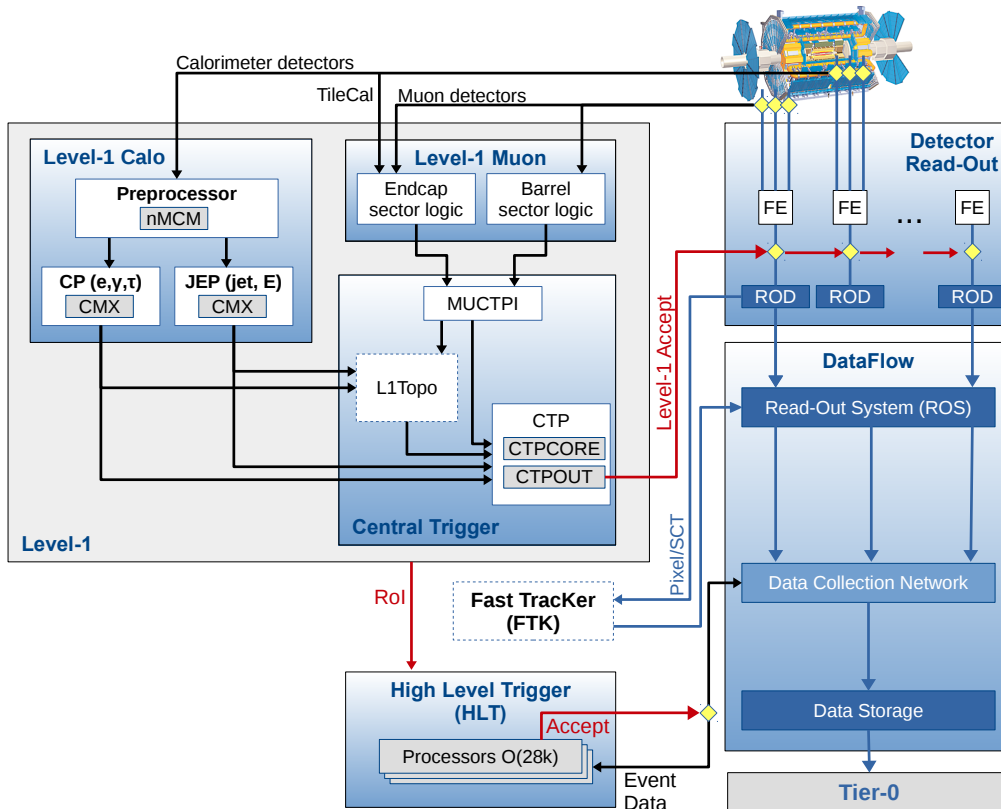


Figure 3.7: Overview of the trigger and data acquisition system in Run 2. The left side illustrates the trigger system, while the right side shows the data acquisition system. The trigger system consists of the Level-1 Trigger and the High-Level Trigger. The figure is taken from Ref. [63].

3.3 Trigger and Data Acquisition

In the ATLAS detector, beam collisions occur at 40 MHz, resulting in a data acquisition rate of up to $O(1)$ PB per second to acquire every event. On the other hand, the cross-section of events that produce weak bosons, Higgs bosons, or top quarks of our interest is 6–8 orders of magnitude smaller compared to the total inelastic scattering cross-section that occurs in proton-proton collisions. Therefore, in the ATLAS experiment, the detector signals are used to quickly determine whether a collision event is of interest before recording the data. The system that determines the events of our interest to be recorded is called the “trigger system”, and the system that temporarily holds the data and records them when an event is triggered is called the “data acquisition system”. Figure 3.7 illustrates the trigger and data acquisition system in Run 2. Details of the trigger system will be discussed in Section 3.3.1. Section 3.3.2 describes the missing transverse momentum trigger, which is essential to acquire data for this analysis.

3.3.1 Overview of the trigger system

The trigger system of the ATLAS detector consists of the Level-1 Trigger (L1 Trigger) for hardware-based fast trigger decision and the High-Level Trigger (HLT) for software-based precise trigger decision.

Level-1 Trigger (L1 Trigger) The L1 Trigger consists of calorimeter-based Level-1 Calo (L1Calo), muon-spectrometer-based Level-1 Muon (L1Muon), and Central Trigger, which combines trigger decision from L1Calo and L1Muon. The L1 Trigger sends the η and ϕ information of issued triggers, called Region of Interest (RoI), to the HLT for more precise trigger decisions.

High-Level Trigger (HLT) The HLT uses the detector information around the RoI to reconstruct objects with an algorithm similar to an offline algorithm to perform more precise trigger decisions. The trigger rate is reduced to 1 kHz by the HLT.

3.3.2 Missing Transverse Momentum Trigger

As discussed in Chapter 2, this analysis utilizes the “jets+ E_T^{miss} ” signature to search for SUSY particles. Since the missing transverse momentum trigger (E_T^{miss} trigger) is the most effective way to obtain such data, this section briefly describes the algorithm of the E_T^{miss} trigger in the L1 Trigger and HLT. Due to time constraints, only the calorimeter information is used in both algorithms. More details are given in Ref. [64].

L1 Trigger algorithm The analog sum of signals from calorimeter cells is taken to form “towers”, with a size of approximately $\Delta\eta \times \Delta\phi = 0.1 \times 0.1$, and thresholds are set to the digitized signal to reduce calorimeter noise. The towers are combined to form larger towers, with a size of approximately $\Delta\eta \times \Delta\phi = 0.2 \times 0.2$, known as “jet elements”. The missing transverse momentum is calculated by taking the negative vector sum of the jet elements.

HLT algorithm The calibrated energy information obtained from the calorimeter is used when calculating the missing transverse momentum in the HLT. During 2015–2016, E_T^{miss} was calculated using jets since the reconstructed jet energy was corrected for the pileup effect, referred to as the “Jet-based” algorithm. In 2017, when the number of simultaneous proton-proton collisions increased, a new algorithm called the “Pileup-fit” algorithm was used. Calorimeter signals are divided into those with low and high energy deposits, and the former is used to estimate the contribution from collisions of non-interest, event by event. This allowed the performance of the trigger to be maintained despite the increased number of proton-proton collisions.

3.4 Future Upgrades

The LHC Run 3 period has started in 2022, increasing the center-of-mass energy to 13.6 TeV and is expected to obtain about 400 fb^{-1} data, including the data acquired in previous runs, by the end of 2025. After a three-year shutdown period, the center-of-mass energy will be increased to 14 TeV and is expected to obtain about $3000 - 4000 \text{ fb}^{-1}$ of data in about ten years. This period is called the High-Luminosity LHC (HL-LHC), and the high statistics will be utilized to detect new particles with small production cross-sections and to make precise measurements of the Higgs boson. The HL-LHC increases the instantaneous luminosity by a factor of 5 to 7.5 relative to the nominal value to achieve high statistics. However, this increase in luminosity will also result in a significant rise in radiation levels due to an increase in the mean number of interactions per crossing. The IDs located in the innermost part of the detector will be upgraded to address the situation. The trigger rate will increase significantly, necessitating upgrades to the trigger system, the data acquisition system, and the electronics. Specifically, the muon system will install a new muon chamber, and the trigger system will be substantially upgraded.

Inner Detector Upgrade In the HL-LHC, all IDs, including the TRT, are replaced by an all-silicon tracker, composed of pixel and strip detectors, referred to as the Inner Tracker (ITk). The ITk offers more forward coverage, which improves the acceptance range from $|\eta| = 2.5$ to $|\eta| = 4.0$. This results in better sensitivity to physics that generates particles in the forward direction, for example, the Vector Boson Fusion (VBF) process. The innermost layer will be placed at 34 mm, which is slightly farther away compared to the IBL, but the pixel size will be reduced to $\Delta\phi \times \Delta z = 25 \mu\text{m} \times 100 \mu\text{m}$, finer than the current $\Delta\phi \times \Delta z = 50 \mu\text{m} \times 250 \mu\text{m}$ pitch size. The pixel size for pixel detectors other than the innermost layer is designed to be $\Delta\phi \times \Delta z = 50 \mu\text{m} \times 50 \mu\text{m}$. The proposed upgrade to the ITk significantly increases the number of channels for both strips and pixels. Specifically, the upgrade increases the number of channels by a factor of ten for strips and sixty for pixels.

Muon System Upgrade The current detector layout has an area in the center of the barrel region that the RPC does not cover due to the presence of the toroidal magnet and the supporting feet. As a result, the detector acceptance is limited to approximately 70%. Furthermore, the transition region between the endcap and the barrel region ($1.0 < |\eta| < 1.3$) is not fully covered by the New Small Wheel (NSW) detector recently introduced in Run 3. New RPC detectors will be added to the innermost layer to cover the dead zone. The two-layer TGC chamber located in the barrel-endcap transition area will be upgraded to a three-layer TGC chamber to accommodate higher trigger rates in the TGC chamber. Some MDT chambers located in the innermost layer of the barrel area will be replaced by MDT chambers consisting of tubes with smaller radii. To cope with higher trigger rates, the HL-LHC plans to upgrade the electronics of the muon system and introduce more complex algorithms by increasing the circuit size and processing time. Additional information about the upgrade to the muon system, along with my personal contributions, can be found in Appendix B.

Chapter 4

Data and Monte Carlo Simulation

This thesis uses data collected by the ATLAS detector in proton-proton collisions in the LHC. SM background and signal yields are estimated using Monte Carlo (MC) simulation samples. Details of the data and MC simulations are discussed in this chapter.

4.1 ATLAS Run 2 data

During Run 2 (2015–2018), LHC has delivered $\sqrt{s} = 13$ TeV proton-proton collision data with integrated luminosity of 156 fb^{-1} , of which 147 fb^{-1} were recorded by the ATLAS detector. As physics analyses require that the recorded data pass standard data quality requirements in ATLAS [65], the actual data used in the physical analysis is $140.1 \pm 1.2 \text{ fb}^{-1}$ with uncertainty of 0.83% [59], measured by the LUCID-2 (LUminosity Cherenkov Integrating Detector) detector [66]. The integrated luminosity of the data for physics analyses during 2015, 2016, 2017, and 2018 is 3.24, 33.40, 44.63, and 58.79 fb^{-1} , respectively [59].

During Run 2, the mean number of interactions per crossing drastically changed due to increased instantaneous luminosity, as illustrated in Figure 4.1. This phenomenon in which multiple proton-proton collisions occur in a single proton bunch collision is called “pileup”.

4.2 Monte Carlo Simulation

At the LHC, multiple proton-proton collisions occur in a single proton-bunch collision. Also, depending on the time resolution of the detector, signals from other bunch collisions may affect the measurement. To accurately estimate the number of SM background and signal yields, it is necessary to simulate all the physical processes that occur in proton-proton collisions. Section 4.2.1 briefly overviews the simulated physics processes in proton-proton collisions. Sections 4.2.2 and 4.2.3 provide details of the configurations to generate simulation samples for SM backgrounds and signals, respectively. Finally, the cross-sections of the SM backgrounds and signals are

Figure 4.1: Mean number of interactions per crossing for each data-taking year. The blue histogram shows the distribution throughout the period, with a mean of 33.7. The figure is taken from Ref. [67].

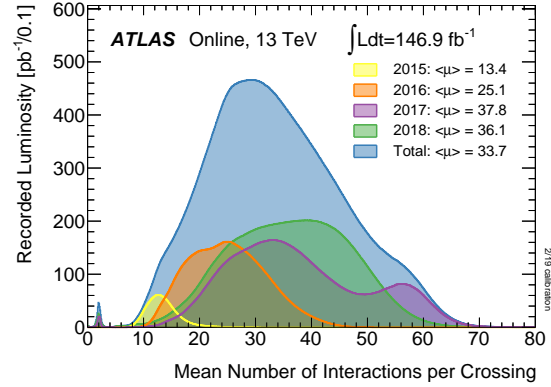
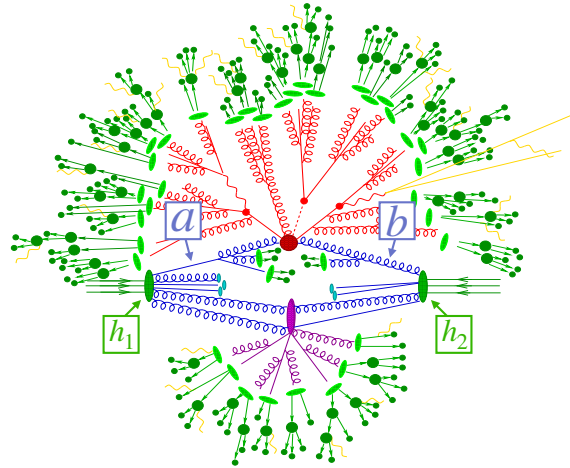


Figure 4.2: Illustration of the event generation step of a $t\bar{t}h$ event. h_1, h_2 represent the colliding hadrons, and a, b denote the hard-scattering partons within each hadron. The prominent red blob in the center represents the hard-scattering process, followed by smaller red blobs depicting the decay of the top quarks and the Higgs boson. The purple blob represents the interaction between other partons of the same proton contributing to the hard-scattering process, referred to as “Underlying events” (denoted as “UE”). The light-green blobs represent the hadronization step, followed by dark-green blobs, illustrating the decay of hadrons. The yellow line represents the radiation of photons. The figure is taken and revised from Ref. [68].



summarized in Section 4.2.4. In addition to estimating SM background and signal yields, samples generated by MC simulations are used to assess the impact of systematic uncertainties. The systematic uncertainties considered in this thesis are further discussed in Section 8.

4.2.1 General description

Hard-scatter Event Generation Figure 4.2 illustrates the event generation step of a $t\bar{t}h$ event. The hard-scattering process from proton-proton collisions can be estimated by factorizing the calculation into two components: the perturbatively calculable part, corresponding to the Matrix Element (ME), and the perturbatively non-calculable part, corresponding to the parton shower and fragmentation. Parton shower and fragmentation are predicted by phenomenological models with parameters tuned to match observations. In proton-proton collisions, interactions between other partons of the same proton also contribute to the hard-scattering process, referred to as “underlying events”, which can be modeled using data. The differential cross-section of an observable O can be described as [69]

$$\frac{d\sigma}{d\mathcal{O}} = \sum_{a,b} \int_0^1 dx_a dx_b \sum_F \int d\Phi_F f_a^{h_1}(x_a, \mu_F) f_b^{h_2}(x_b, \mu_F) \frac{d\hat{\sigma}_{ab \rightarrow F}}{d\hat{\mathcal{O}}} D_F(\hat{\mathcal{O}} \rightarrow \mathcal{O}, \mu_F), \quad (4.1)$$

where a, b represents the partonic constituents in the colliding hadrons h_1, h_2 , and $d\Phi_F$ is the standard phase space differential in the final state. The energy scale at which the perturbatively calculable and non-calculable parts are separated is called the ‘‘factorization scale’’ and is denoted as μ_F . The Parton Density Function (PDF) $f_j^h(x_j, \mu_F)$ describes the momentum fraction that a parton of type j carries within the hadron h at the factorization scale. The partonic scattering cross-section $d\hat{\sigma}_{ab \rightarrow F}$ can be calculated as

$$d\hat{\sigma}_{ab \rightarrow F} = \frac{1}{2\hat{s}_{ab}} |\mathcal{M}_{ab \rightarrow F}|^2(\Phi_F; \mu_F, \mu_R), \quad (4.2)$$

where $1/2\hat{s}_{ab}$ represents the parton flux factor. \mathcal{M} is the matrix element, summed over all possible intermediate states and phase space of $ab \rightarrow F$ at the factorization scale μ_F and the renormalization scale μ_R . The strong coupling constant in the matrix element is subject to quantum corrections, such as corrections to the quark and gluon self-energies, with values varying with the energy scale, referred to as the renormalization scale. The evolution of the parton emission from the matrix element is complemented by the parton shower approximation. Since the probability of one parton splitting into two can be calculated using the Dokshitzer-Gribov-Lipatov-Altarelli-Parisi (DGLAP) evolution equations [70–72], the parton shower approximation predicts the partonic final state by repeating the parton splitting process until the momentum of the parton reaches $\mathcal{O}(1)$ GeV.

The final part of the equation is the fragmentation function D_F , which represents the evolution from the partonic final state to the color-neutral final state, and $\hat{\mathcal{O}}$ represents an observable at the partonic final state. The fragmentation process is modeled by the Lund string model [73].

Pileup Simulation Pileup arises from the same proton-proton collision as the hard-scattering or from surrounding bunch crossings, which is complex and requires intensive CPU consumption for simulation. The pileup events produced with PYTHIA 8.186, A3 tune, and MSTW2008LO PDF set are overlaid with the hard-scattering MC simulation samples until the pileup distribution matches the distribution in Figure 4.1.

Detector Simulation The particles produced in the event generation step are passed to the ATLAS simulation framework [74], based on GEANT4 [75], to emulate the detector response. Signal samples undergo simulation using the Atfast-II (AFII) [76] fast simulation package. This package effectively reduces simulation time by parameterizing the detector response against shower activities.

4.2.2 SM Background Simulation Samples

This section outlines the configuration details for generating background processes in this thesis. Background processes are classified into three categories: vector boson production, top production, and QCD multijet production. The QCD multijet production is characterized by multiple jets appearing in the final state.

Vector boson production At the LHC, the production of single and two vector bosons, known as single boson and di-boson productions, have relatively large production cross-sections. Feynman diagrams for single boson and di-boson productions are illustrated in Figure 4.3. For single boson production, the t -channel production dominates over the s -channel production induced by pure electroweak interactions. In the t -channel production, jets are produced via strong interactions. Although di-boson production is usually initiated by quarks, it can also occur through triple and quadratic gauge-boson couplings, as well as loop-induced gluon-initiated di-boson production.

For single boson (di-boson) production, the event generation, including the matrix element, parton shower, and hadronization step, is performed using SHERPA 2.2.11/2.2.2 (SHERPA 2.2.2/2.2.1) [68], depending on the process, with NNPDF3.0_{NNLO} [77]. Since the cross-section is calculated at next-to-next-to leading order (NNLO) accuracy for single boson productions, the total cross-section calculated by SHERPA is normalized to NNLO accuracy by applying scale factors given in Ref. [78].

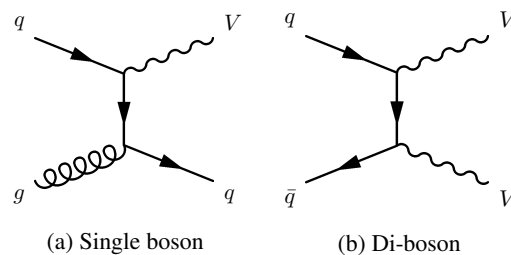


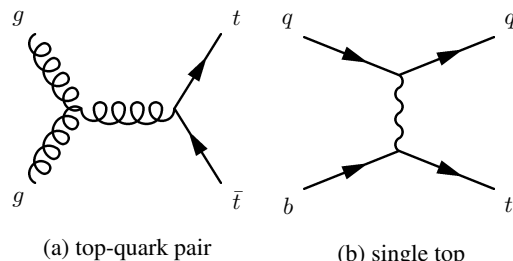
Figure 4.3: Feynman diagrams illustrating (a) single boson and (b) di-boson productions. (a) The quark in the final state is observed as a hadron jet after parton shower and hadronization. (b) The diagram represents quark-initiated di-boson production.

Top production Due to its high energy, the LHC is often called a top quark factory. This energy results in a high production cross-section of top quarks. About 90% of the top-quark production is generated by gluon-initiated production, and the remaining 10% is generated by quark-initiated production. Single top production can be classified into three processes: dominant t -channel production, associated tW -channel, and s -channel production. Feynman diagrams for top-quark pair and single top productions are illustrated in Figure 4.4.

The matrix element part is simulated by POWHEG [79–82] at next-to-leading order (NLO) accuracy with NNPDF3.0_{NNLO}. The output from POWHEG is passed to PYTHIA 8.230 [83] to simulate the parton shower and hadronization step, using the A14 tune [84]. The A14 tune is a set of parameters tuned to match observables sensitive to underlying events, jet structure, and additional jet emissions. Parameters are tuned using data measured by ATLAS during the LHC Run 1

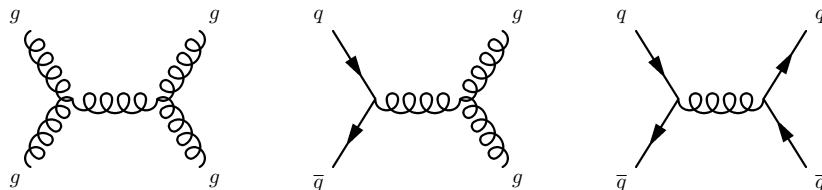
period. The decay of heavy-flavour particles is simulated with EVTGEN 1.6.0 [85]. Since the cross-section is calculated at NNLO+NNLL accuracy, the total cross-section calculated by POWHEG is normalized to the NNLO+NNLL accuracy by applying the scale factors given in Ref. [86].

Figure 4.4: Feynman diagrams illustrating (a) top-quark pair and (b) single top productions. (a) The diagram represents gluon-initiated top-quark pair production. (b) The t -channel production is the dominant production mode for single top production.



QCD multijet production Feynman diagrams for QCD multijet productions are illustrated in Figure 4.5. The multijet process has the highest production cross-section, characterized by multiple jets but no leptons in the final state. The event generation, including the matrix element, parton shower, and hadronization step, is performed using PYTHIA 8.235 with NNPDF2.3NLO. The matrix element is calculated at leading order (LO) accuracy. The A14 tune is used to simulate the parton shower and the underlying events. The decay of heavy-flavour particles is simulated with EVTGEN 1.6.0.

Figure 4.5: Feynman diagrams illustrating QCD multijet productions.

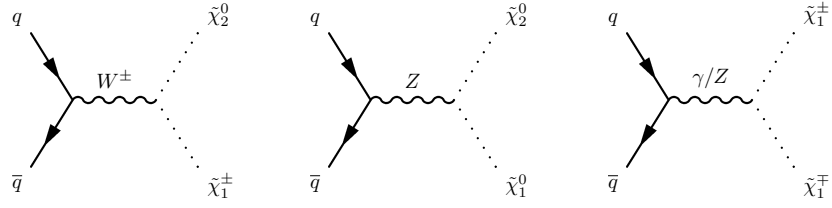


4.2.3 Signal Simulation Samples

The following section describes the details of the signal model simulation samples described in Section 2.5. Feynman diagrams for the pair production of electroweakinos are illustrated in Figure 4.6. Signal simulation samples with pure higgsino-like states are produced for each production mode: $\tilde{\chi}_2^0 \tilde{\chi}_1^0$, $\tilde{\chi}_2^0 \tilde{\chi}_1^\pm$, $\tilde{\chi}_1^0 \tilde{\chi}_1^\pm$, $\tilde{\chi}_1^\pm \tilde{\chi}_1^\mp$. The mass difference $\Delta m(\tilde{\chi}_1^\pm, \tilde{\chi}_1^0)$ and LSP mass $m(\tilde{\chi}_1^0)$ considered are 0.25 – 1.5 GeV and 85 – 225 GeV, respectively.

The samples are generated with MADGRAPH v2.9.5 [87] for the matrix element and PYTHIA 8.306 for showering. The cross-sections and their uncertainties are calculated to NLO+NLL accuracy using the RESUMMINO [88] package. Since the decay of electroweakinos is calculated by PYTHIA, the polarization of the W/Z boson produced by the chargino or neutralino decay is not considered. As MADSPIN [89, 90] takes spin into account in event generation, a comparison of the MADSPIN

Figure 4.6: Feynman diagrams illustrating pair productions of electroweakinos.



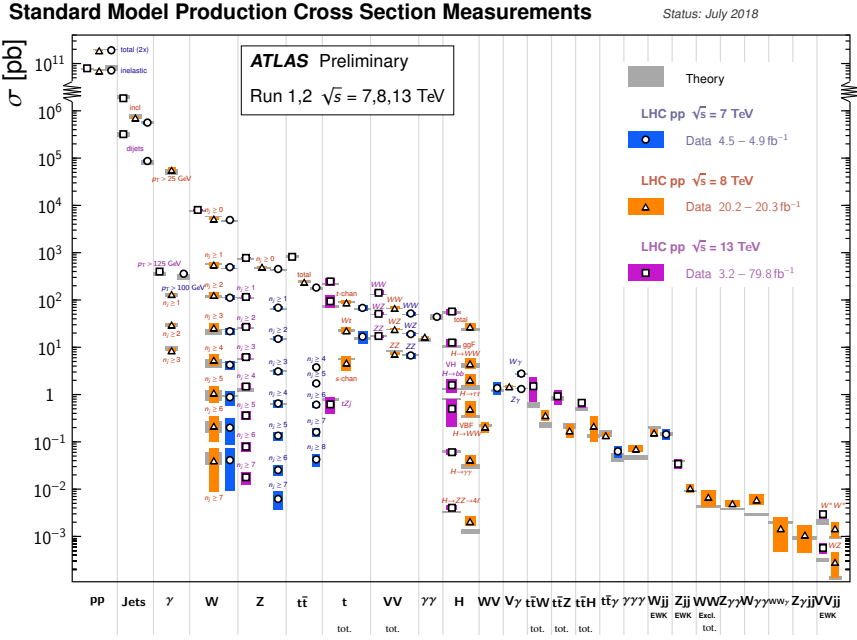
and PYTHIA distributions shows that there is no significant difference in the kinematics of the final state particles due to the polarization of the W/Z boson.

4.2.4 Summary of Simulation Samples

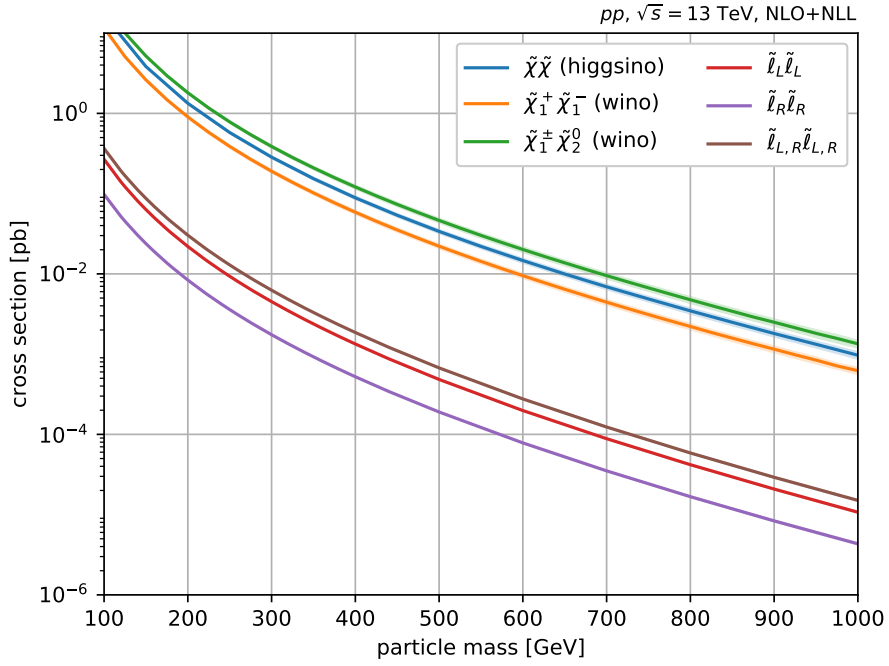
The MC generator setup for SM background and signal samples used in this thesis is summarized in Table 4.1. As discussed in Chapter 1, achieving the “jets+ E_T^{miss} ” signature in this thesis requires a large E_T^{miss} . Background processes with sufficient cross-section and neutrinos in the final state, considered as potential backgrounds, include the production of single bosons (W, Z), top quarks, and di-bosons (WW, WZ, ZZ), as depicted in Figure 4.7(a). The production cross-sections of these backgrounds range from about $10^1 - 10^3$ pb. In contrast, the production cross-sections of signal processes typically reach up to 10^1 pb, as illustrated in Figure 4.7(b).

Table 4.1: Summary of generator setup for SM background and signal samples.

Process	Matrix element	Parton shower	Tune	PDF set	Cross-section
<i>V = (W, Z, γ) production</i>					
V+jets	SHERPA 2.2.11/2.2.2		SHERPA standard	NNPDF3.0 _{NNLO}	NNLO
VV	SHERPA 2.2.2/2.2.1		SHERPA standard	NNPDF3.0 _{NNLO}	Generator NLO
<i>Top production</i>					
$t\bar{t}$	POWHEG BOX	PYTHIA 8.230	A14	NNPDF3.0 _{NLO}	NNLO+NNLL
single top	POWHEG BOX	PYTHIA 8.230	A14	NNPDF3.0 _{NLO}	NNLO+NNLL
<i>Other</i>					
QCD multijet		PYTHIA 8.235	A14	NNPDF2.3 _{LO}	Generator LO
<i>BSM production</i>					
Signal	MADGRAPH v2.9.5	PYTHIA 8.306	A14	NNPDF2.3 _{LO}	NLO+NLL



(a) Cross-section of SM processes



(b) Cross-section of signal processes

Figure 4.7: Production cross-section of (a) SM background processes and (b) signal processes. (a) The total and fiducial production cross-sections measured in the LHC are illustrated in blue, orange, and purple filled areas, corresponding to measurements with a different center-of-mass energy. The gray filled area shows the cross-section calculated at NLO or higher. (b) Production cross-sections of charginos, neutralinos, and sleptons. The production cross-section of higgsinos is plotted as the sum of all possible production modes. The figures are taken from Ref. [91] and Ref. [92].

Chapter 5

Event Reconstruction

Particles produced in proton-proton collisions leave characteristic signals in the detector unique to their respective particle types, as illustrated in Figure 5.1. These signals are used to reconstruct four vectors representing the produced particles, referred to as “objects”. In the first step, tracks, vertices, and calorimeter clusters (Topo-clusters) are reconstructed as fragmentary information of the produced particles. These objects are further combined to reconstruct objects that closely resemble the true information of the produced particles. These reconstructed objects are called “physics objects” and include jets, leptons, photons, and missing transverse momentum. This chapter describes the reconstruction algorithm used in the analysis.

5.1 Overview of Event Reconstruction

Figure 5.2 illustrates the event reconstruction flow used in this thesis. Raw detector information is combined to form tracks, vertices, and topo-clusters, referred to as “low-level objects”. Section 5.2 discusses the algorithms for reconstructing low-level objects. The low-level objects are combined to reconstruct physics objects, such as jets, muons, electrons, and photons. These physics objects must meet specific “identification” criteria and kinematic selections to form “baseline” objects, which is further discussed in Section 5.3. To resolve the potential ambiguity arising from the reconstruction of multiple baseline objects from a single particle, a procedure called “overlap removal” is implemented and further discussed in Section 5.3.3. The missing transverse momentum is calculated using all baseline objects, which is described in Section 5.3.4. The baseline objects are subject to more stringent quality and “isolation” requirements to ensure a higher purity of the objects, referred to as “signal” objects.

In this thesis, charged particles produced by the decay of charginos and neutralinos have very low momentum and can only be reconstructed as tracks. Therefore, we require a more stringent selection for low-level tracks and consider them physics objects in this analysis. Since the selection of signal tracks is not standard but rather unique to this analysis, it will be described in Chapter 6. The definitions of the baseline and signal objects used in this analysis are summarized in Section 5.4.

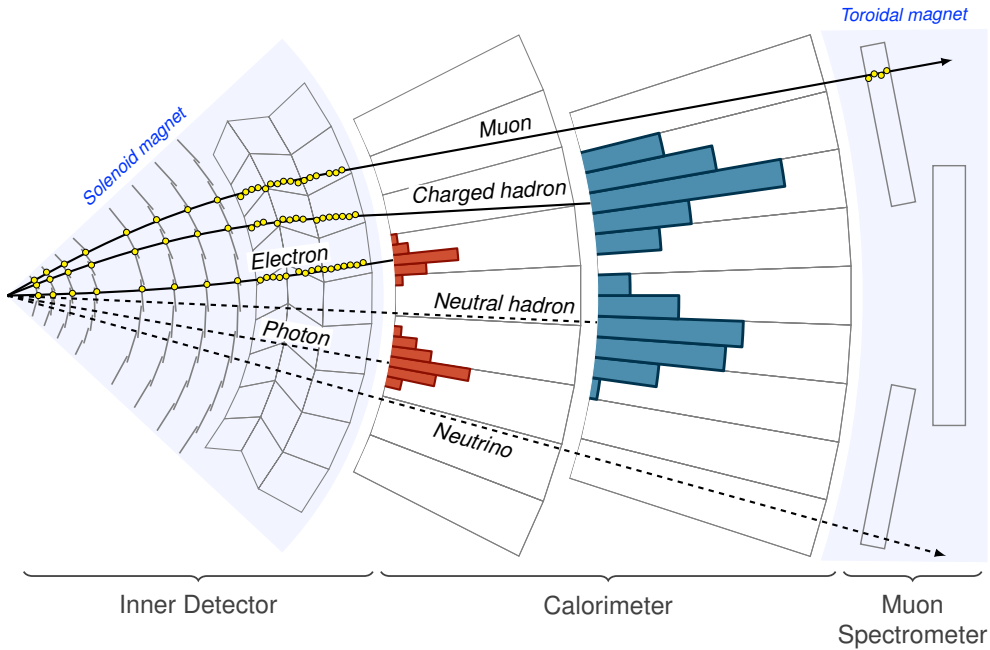


Figure 5.1: Schematic view of various particles passing through the ATLAS detector, leaving characteristic signals in the detector. The figure shows hit information represented by yellow dots and energy deposits displayed through red and blue bars in the electromagnetic and hadronic calorimeters, respectively.

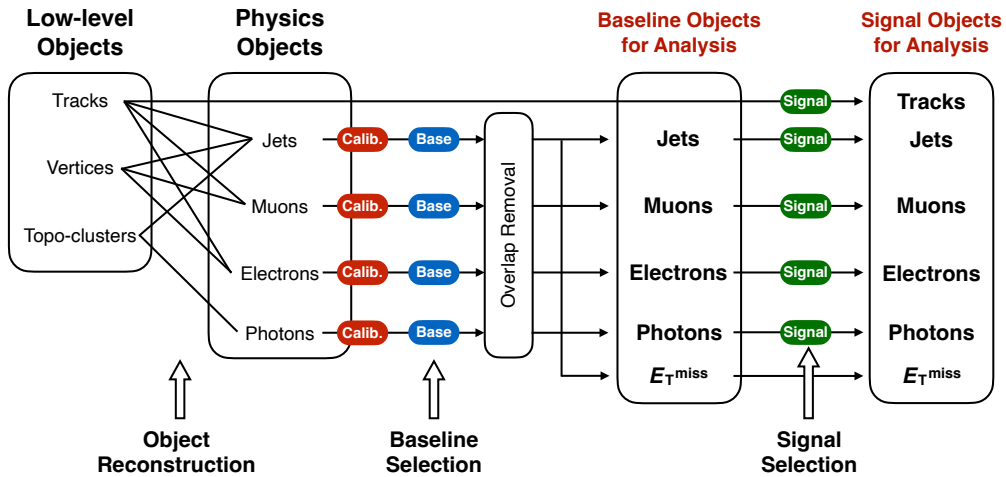


Figure 5.2: Schematic of the event reconstruction flow utilized in this thesis. The low-level objects are combined to form physics objects. The energy or momentum of physics objects is calibrated and required to pass baseline selections to form baseline objects. The overlap removal step resolves the ambiguity of baseline objects. The missing transverse momentum is calculated using all baseline objects. Finally, all physics objects must pass more stringent quality and isolation requirements to form signal objects. In this thesis, signal selections are also required for tracks, and these tracks are considered physics objects.

5.2 Low-level objects

5.2.1 Tracks and Vertices

Tracks The energy deposits of the charged particles left in the IDs are combined to form “tracks”, which are used to identify the trajectory of the charged particles. The tracking algorithm is briefly described below, and a schematic of it is presented in Figure 5.3. More details can be found in Ref. [93].

The tracks are reconstructed through the following steps.

1. **Space Point Creation** : Adjacent hits in the pixel and SCT detectors are merged to form “clusters”. The clusters are then converted to three-dimensional position information called “space points”.
2. **Pixel & Strip Seed Finding** : Track seeds are formed by combining three space points from the pixel or the SCT detector. Selections on longitudinal impact parameters are applied at this point to suppress low-quality track seeds and reduce computational time. From Run 2, fake track seeds are further suppressed by requiring an additional space point in another layer called the “confirmation space point”.
3. **Track Finding** : Track seeds are extrapolated by the combinatorial Kalman filter [94] to determine the pixel and SCT modules through which the track could pass.
4. **Ambiguity Resolving** : During the track finding step, multiple track candidates are reconstructed with overlap, and ambiguity among them must be resolved. To resolve the overlap between tracks, “track scores” are calculated based on the number of hits and holes, the track p_T , and other criteria. Tracks with low scores are considered fake and discarded at this point. When multiple tracks share the same clusters, called “shared hits”, they are assigned to the track with lower scores. Tracks with multiple shared hits are also considered fake tracks and are discarded.
5. **TRT Extended Track Refit** : Tracks are extended to the TRT detector, and if hits are found successfully, the fitting procedure and track scoring are repeated. If the track score is higher than the pixel and SCT detector only fit, the TRT hit is added to the track. If the track score is lower, the TRT hit is recorded as an “outlier” of the track.

The reconstructed tracks are described with five parameters ($d_0, z_0, \phi, \theta, q/p$), as illustrated in Figure 5.4. The transverse impact parameter, denoted by d_0 , refers to the closest transverse distance between the beam position and the tracks. On the other hand, the longitudinal impact parameter, denoted by z_0 , refers to the distance between the primary vertex and the nearest point of contact between the beam position and the tracks along the longitudinal axis. ϕ and θ are the azimuthal and polar angles of the tracks. q/p is the ratio between the charge and the momentum of the track.

Figure 5.3: Schematics of the track reconstruction process. The dotted line represents a charged particle passing through the ID. The track reconstruction begins with forming space points depicted as yellow dots. A track seed is created from three space points, and a confirmation space point is required to suppress fake tracks. Tracks are reconstructed by connecting space points in other layers. In the final step, tracks are extended to the TRT detector to determine the track momentum with higher precision.

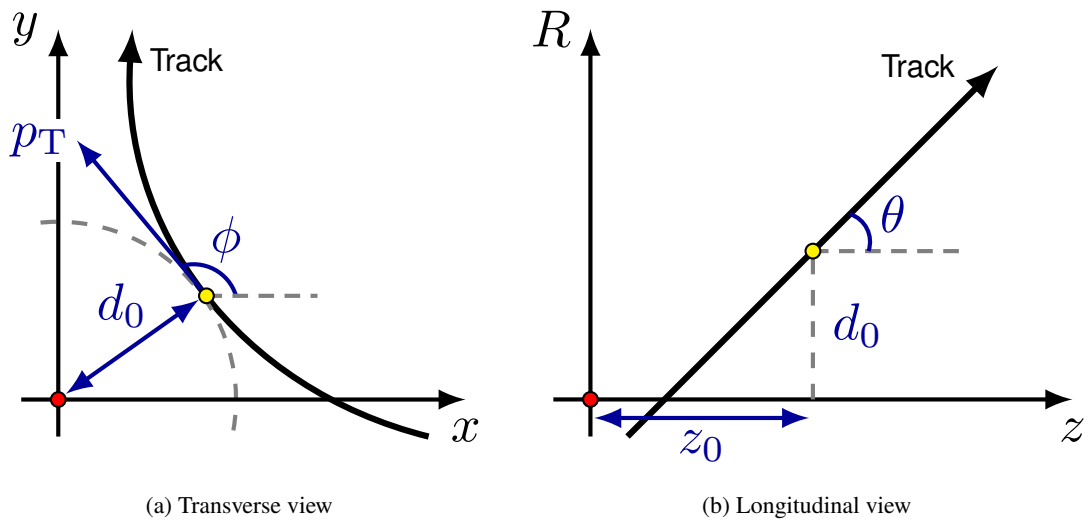
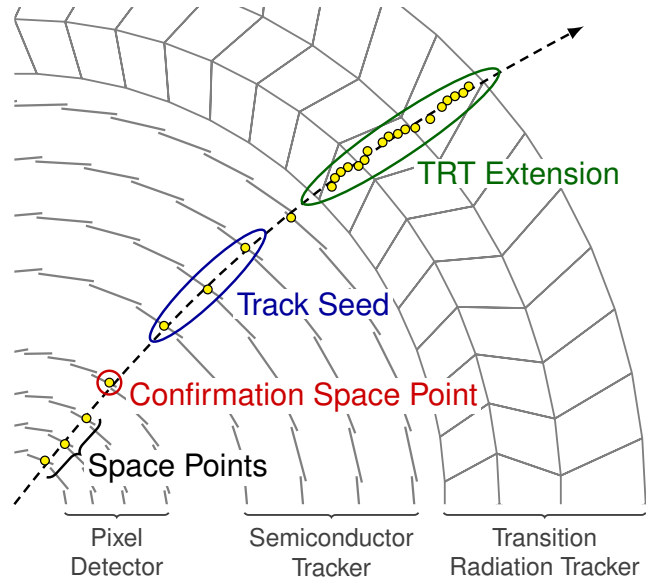


Figure 5.4: Schematics of the track parameters viewed from both the beam axis and a viewpoint perpendicular to the beam axis. The track parameters are calculated based on the closest point of the track to the beam axis in the x - y plane, referred to as the “perigee” point. All track parameters indicated by blue lines or symbols are calculated with respect to the perigee point. Red and yellow dots represent the hard-scattering vertex and perigee point, respectively.

Primary Vertices Vertices are reconstructed by calculating the intersection of reconstructed tracks. Tracks used to reconstruct the vertices along the beam axis must pass the selection criteria in Ref. [95]. The vertices are reconstructed through the following steps.

1. **Vertex Finding** : A vertex seed is defined by taking the beam spot position as the x, y position and the closest point between the track and the beam spot as the z position.
2. **Vertex Fitting** : After defining a vertex seed, the seed and the tracks are used as inputs to the adaptive vertex fitting algorithm [96]. After each fit, the tracks are reweighted depending on the compatibility with the vertex position, and the fitting procedure is repeated. After reaching the minima of the fit, tracks incompatible with the final vertex position are used as inputs for the new vertex reconstruction procedure.

The above two steps are repeated until all input tracks are associated with vertices or no additional vertices are reconstructed. The vertex associated with tracks with the most significant Σp_T^2 is defined as the “primary vertex” and considered the hard-scattering point of the event.

5.2.2 Topo-clusters

Energy deposits in the calorimeter cells are combined to form “topo-clusters”. Topo-clusters are used to reconstruct jets and quantify hadron activity around muons, electrons, and photons. To discriminate energy deposits from noise (electronic noise, pileup, etc.) in the calorimeter cells, the calorimeter cell significance is defined by dividing the measured energy deposit by the average noise level in the electromagnetic scale. Topo-clusters are reconstructed by finding a seed cell with 4σ significance and merging neighboring cells with 2σ significance. The above process is repeated, and once no more cells can be merged, all adjacent cells are merged to define the boundary. If two seed cells are adjacent to each other with cells with 2σ significance, they are merged to form a single topo-cluster.

5.3 Physics objects

5.3.1 Jets

Hadron jets emerge as focused clusters of particles originating from the hadronization process of quarks and gluons produced in high-energy proton-proton collisions. Tracks and topo-clusters are combined to form hadron jets following the procedures described briefly below. In the following, hadron jets will be abbreviated as “jets”. More details can be found in Ref. [97].

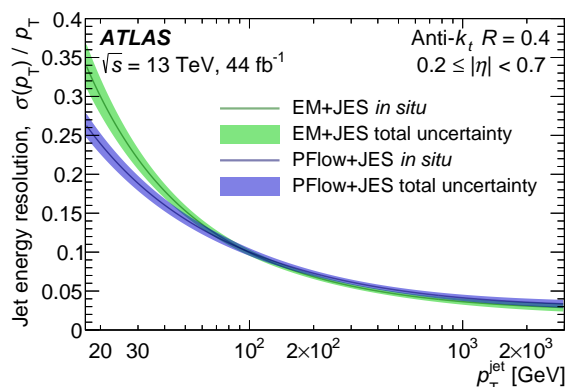
Particle Flow (PFlow) algorithm Individual hadrons in a jet generally have an energy of less than 10 GeV. In this low-energy range, the resolution of tracks is much better than that of calorimeter clusters. Therefore, the energy resolution of reconstructed jets is improved by prioritizing the use of track information for the energies from charged hadrons. However, since charged hadrons interact with both the ID and the calorimeters, it is essential to remove the overlap. The Particle Flow (PFlow) algorithm [97] can identify clusters, whether associated with a track or not, based on the position and momentum (energy) information of both tracks and topo-clusters. Details of the PFlow algorithm are described in Appendix C.

Reconstruction A new set of tracks and topo-clusters, provided by the PFlow algorithm, is combined by the Anti- k_t algorithm [98] to form jets. Tracks must be associated with the primary vertex, and positions of the topo-clusters are recalculated relative to the primary vertex.

Jet Vertex Tagger (JVT) Jets can originate not only from the primary vertex but also from pileup vertices. However, our focus lies solely on jets from the primary vertex. Therefore, we need to mitigate the pileup jets. A practical method is to use the track information to extract the vertex structure of the jets. The initial step is to classify tracks in the jet as either originating from the primary vertex or pileup vertices. Subsequently, the ratio of the total momentum of the tracks to the jet energy is computed for each classification and used for discrimination. The sum of the track p_T from the pileup vertices is proportional to the number of proton-proton collisions in each event. The sum of the track p_T is divided by the number of tracks to eliminate the dependency. The ratio between the sum of the track p_T from the primary vertex and pileup vertices is called the corrected Jet Vertex Fraction (corrJVF). Since the corrJVF becomes smaller when the number of tracks from the primary vertex is small, the selection for the corrJVF is adjusted according to the sum of the p_T of the tracks relative to the jet energy. The final discriminant is called the Jet Vertex Tagger (JVT). The JVT is exclusively applied to jets with $p_T < 60$ GeV and those within the acceptance of the ID ($|\eta| < 2.4$). More details can be found in Ref. [99].

Flavour tagging Jets containing b -hadrons, referred to as b -jets, are characterized by the long lifetime and multiplicity of decay objects from b -hadrons. Identifying b -jets involves a two-stage approach: low-level algorithms that produce discriminants based on track inputs and a high-level algorithm that combines the output from low-level algorithms to maximize performance. The low-level algorithm is broadly categorized into two methods: one utilizes the impact parameters of individual tracks associated with jets, while the other reconstructs secondary vertices using tracks. In this thesis, the *DL1rFixedCutBeff85%* working point is used for b -jet flavour tagging. This working point employs deep learning classifiers to combine outputs from the low-level algorithms, and the threshold for the discriminant is set to achieve an 85% efficiency for b -jet identification. More details can be found in Ref. [100].

Figure 5.5: Dependence of the calibrated jet relative energy resolution on jet p_T . The blue curve shows the resolution of the PFlow jet, and the green curve shows the resolution of the previously used Electromagnetic Topo-cluster (EMTopo) jet. The figure is taken from Ref. [101].



Calibration The measurement from reconstructed jets in sampling calorimeters represents only a fraction of the total energy. To obtain the complete energy, it is necessary to scale the measured energy and calibrate the measured energy resolution. The energy scale and resolution of the jets, referred to as Jet Energy Scale (JES) and Jet Energy Resolution (JER), are calibrated through the following steps.

- **Pileup correction** : The energy deposit from pileup contributions is subtracted from the measured energy in the first step. The median transverse energy density ρ is measured and multiplied by the “area” of the jet for subtraction.
- **MC-based calibration** : The energy response in simulations is corrected to match the response measured in the data. The energy response, denoted as $R = E_{\text{reco}}/E_{\text{truth}}$, is measured as a function of η and the energy of the jets and applied to the simulations.
- **Global sequential calibration** : The energy response between the truth jet and the reconstructed jet may differ depending on other sources, such as the flavour of the jets. To account for these variations, additional variables that characterize the jets are used to correct the energy response, such as the fraction of the measured energy from tracks associated with the jet.
- **In-situ calibration** : The final calibration step is applied exclusively to the data to address the residual difference between the reconstructed jets in the data and the truth jets in the simulations. The energy ratio between jets and well-measured reference objects, such as Z bosons, photons, and low- p_T jets, is measured in both the data and the simulation. The calibration process consists of three steps. In the first step, using the multijet process, the “ η intercalibration” is applied to calibrate the jets in the forward regions ($0.8 \leq |\eta| \leq 4.5$). The second step involves using Z +jets and γ +jets processes to calibrate jets with p_T in the range of $17 < p_T < 1000$ GeV and $25 < p_T < 1200$ GeV, respectively. Finally, the calibration step using the multijet process is applied to calibrate jets with high p_T up to 2.4 TeV.

Figure 5.5 shows the relative energy resolution of the calibrated jet. It can be seen that the PFlow algorithm improves the resolution in the low energy range.

5.3.2 Muons, Electrons, and Photons

This section briefly describes the reconstruction method and performance of muons, electrons, and photons. Muons, electrons, and photons are defined through three processes: “reconstruction”, “identification”, and “isolation”. In physical analyses, prompt leptons and photons from the hard-scattering vertex are particularly interesting. In contrast, leptons from semi-leptonic decays of hadronic sources and jets misidentified as leptons and photons constitute a significant fraction of the background events. These objects are called “non-prompt” leptons and photons and can be reduced by the isolation step. The reconstructed object in MC simulation is further scaled to match the data through a step called “momentum calibration” for muons and “energy calibration” for electrons and photons. For electrons and photons, corrections are also applied to the data to obtain the complete energy. Since electrons and photons are reconstructed using a similar algorithm, they will be discussed together in this section. More details are given in Appendix C.

Muons Muons are reconstructed using the ID and MS information. In the forward region, due to the acceptance of the ID, muons are reconstructed with only the information of the ID. In the identification step, the presence of a kink topology is determined to reduce muons from in-flight pion and strange meson decays. In addition, the quality of the muon is determined by the number of hits on the MS. In the isolation step, the magnitude of hadron activity around the muon is quantified using track and calorimeter information, and a selection is applied to suppress non-prompt muons. Muons that have passed through the above steps are calibrated using the invariant mass ($m_{\ell\ell}$) of $J/\psi \rightarrow \mu\mu$ and $Z \rightarrow \mu\mu$ processes for low and high p_T , respectively. The scale factors are calculated by taking the ratio of the efficiency measured in MC simulation and data.

Electrons and Photons Electrons and photons are reconstructed by forming “superclusters” from topo-clusters only using energy measured in the electromagnetic calorimeter, tracks matched to the topo-clusters, and conversion vertices. Electron identification uses a likelihood discriminant with inputs from track and electromagnetic calorimeter information. The likelihood discriminant is formed by probability density functions (pdfs) measured in the $Z \rightarrow ee$ (for $E_T > 15$ GeV) and $J/\psi \rightarrow ee$ (for $E_T > 15$ GeV) processes for signals and backgrounds. Photon identification is performed by applying cuts to the shower-shape variables of the photons to suppress the hadronic jet background. In the electron and photon isolation step, hadron activity is quantified using track and calorimeter information around the reconstructed objects, and a selection is applied to both variables to reduce non-prompt electrons and photons.

5.3.3 Overlap removal

The overlap removal procedure utilizes collections of electrons, muons, jets, and photons to eliminate overlapping objects based on the ΔR between two objects or whether the objects share ID tracks. When high-momentum hadronic sources undergo semi-leptonic decays, the alignment

Table 5.1: The order of overlaps removed between reconstructed objects. Target refers to the object that will either be discarded or kept based on each criterion. ΔR is calculated as the positional difference between the reference and target object.

Reference	Target	Criterion
Electron	Muon	Reject muon if associated ID track is shared with electron
Electron	Photon	Reject photon if $\Delta R < 0.4$
Muon	Photon	Reject photon if $\Delta R < 0.4$
Jet	Electron	Reject electron if $\Delta R < \min(0.4, 0.04 + 10 \text{ GeV}/p_T(e))$
Muon	Jet	Reject non b -jet with $\Delta R < 0.2$
Jet	Muon	Reject muon if $\Delta R < \min(0.4, 0.04 + 10 \text{ GeV}/p_T(\mu))$
Jet	Photon	Reject photon if $\Delta R < 0.4$

between jets and leptons becomes very close. The ΔR is adjusted with the lepton p_T to avoid overlap between these objects. The sequence of removing overlap between the reconstructed objects is detailed in Table 5.1.

5.3.4 Missing Transverse Energy

In the LHC, the transverse energy of particles produced from the proton-proton collision is conserved and equal to zero. The total transverse momentum of particles that do not leave signals in the detector, such as neutrinos or neutralinos, can be calculated by taking the negative vector sum of the transverse momentum of the reconstructed physics objects and the “soft term”. The soft term consists of tracks associated with the primary vertex but not with the baseline objects [102]. The vector sum is called the missing transverse momentum ($\mathbf{p}_T^{\text{miss}}$), and its magnitude is called the missing transverse energy (E_T^{miss}). This thesis uses the *Tight* working point for the E_T^{miss} to ensure performance in high pileup environments. The *Tight* working point calculates the E_T^{miss} without forward jets with $|\eta| > 2.4$ and $20 < p_T < 30 \text{ GeV}$, where more pileup jets occur. Modeling of the E_T^{miss} and soft term has been verified by comparing distributions in data and simulation for $Z \rightarrow \mu\mu$ events, as given in Figures 5.6(a) and 5.6(b), respectively. The distributions of the data and the simulation agree well within the assigned systematic uncertainties.

5.4 Summary of Object Selections

The selection criteria for kinematics, identification, and isolation of physics objects are summarized in Table 5.2. Specific criteria for selecting prompt leptons are used regarding their transverse distance from the beam axis and longitudinal distance from the primary vertex. Electrons and muons must fulfill these requirements to be considered for selection.

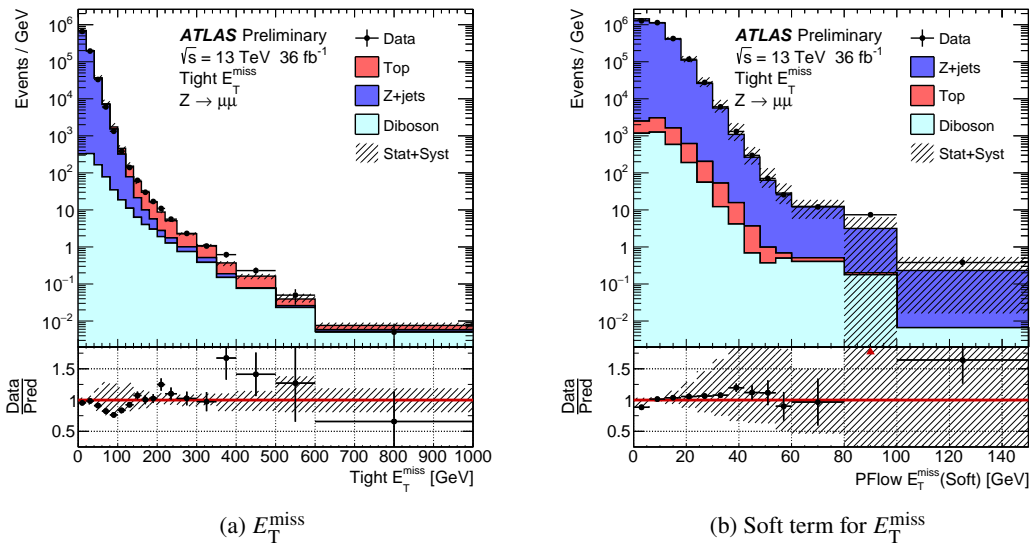


Figure 5.6: E_T^{miss} and soft term distributions in data and simulation for $Z \rightarrow \mu\mu$ events. The bottom panel shows the ratio of data and simulation. The hatched area corresponds to the combined systematic and MC statistical uncertainties. The figures are taken from Ref. [103].

Table 5.2: Summary of object definitions utilized in this thesis.

Property	Signal	Baseline
Jets		
Kinematic	$p_T > 20 \text{ GeV}, \eta < 2.8$	$p_T > 20 \text{ GeV}, \eta < 4.5$
Pileup mitigation	JVT Tight for $p_T < 60 \text{ GeV}, \eta < 2.4$	
b -tagging	DL1r FixedCutBeff 85% for $p_T > 20 \text{ GeV}, \eta < 2.5$	
Muons		
Kinematic	$p_T > 3 \text{ GeV}, \eta < 2.5$	$p_T > 3 \text{ GeV}, \eta < 2.7$
Identification	Medium	Medium
Isolation	PflowLoose_VarRad	–
Impact parameter	$ d_0/\sigma(d_0) < 3 \ \& \ z_0 < 0.5 \text{ mm}$	$ z_0 < 0.5 \text{ mm}$
Electrons		
Kinematic	$p_T > 4.5 \text{ GeV}, \eta < 2.47$	
Identification	MediumLLH	LooseAndBLayerLLH
Isolation	Loose_VarRad	–
Impact parameter	$ d_0/\sigma(d_0) < 5, z_0 < 0.5 \text{ mm}$	$ z_0 < 0.5 \text{ mm}$
Photons		
Kinematic	$p_T > 130 \text{ GeV}, \eta < 2.37$	$p_T > 25 \text{ GeV}, \eta < 2.37$
Identification	Tight	Tight
Isolation	FixedCutTight	–

Chapter 6

Analysis Strategy and Event Selections

This chapter outlines the analysis strategy and the selections applied to define signal regions (SRs), regions with sufficient signal events relative to background events.

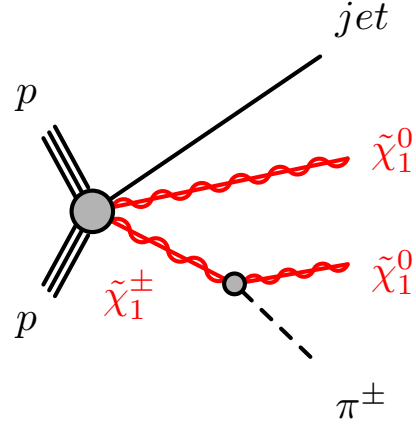
Section 6.1 provides a concise overview of the analysis strategy. Section 6.2 explains the triggers employed to collect the data in this thesis, while Section 6.3 outlines the fundamental event cleaning process used to ensure the data quality and reduce beam-induced background. Section 6.4 provides detailed information on the stringent criteria applied to the tracks to identify those originating from the chargino decay. Section 6.5 summarizes the selection criteria used for the physics objects and tracks in this analysis to minimize background events and retain signal events. Moreover, additional selections used to enhance the analysis sensitivity are also presented.

6.1 Analysis Strategy

As outlined in Chapters 1 and 2, this analysis extends the sensitivity to regions with small mass differences between the higgsinos by requiring a “jets+ E_T^{miss} ” and “mildly-displaced track” signature. Figure 6.1 depicts the Feynman diagram targeted in this analysis. Other production modes, which generate a chargino, also contribute to leaving a signature of a mildly-displaced track.

jets+ E_T^{miss} signature In regions with a small mass difference, visible decay products are typically very soft, and signal events can only be detected using the E_T^{miss} object. To obtain a high E_T^{miss} value in the plateau region of the trigger efficiency and minimize the SM backgrounds, a highly energetic initial state radiation (ISR) jet is required. This jet is necessary to boost the kinematics of the SUSY system and align the two lightest neutralinos.

Figure 6.1: Feynman diagram of the higgsino pair-production process targeted by this analysis. The chargino decays via an off-shell W boson to the LSP. In the diagram, the term *jet* refers to an ISR jet. After the off-shell W boson decays, the resulting pion or lepton leaves a low- p_T track in the final state. The two lightest neutralinos are aligned in the ϕ direction because they are boosted in the opposite direction of the ISR jet, leading to a large E_T^{miss} .



Mildly-displaced track signature In high-energy particle collisions, an enormous number of low- p_T tracks are produced by particles in the SM, which have a wide range of lifetimes. Due to the small mass difference, the lightest chargino and next-to-lightest neutralino have a mean lifetime long enough to travel a certain distance in the detector before decaying into visible pions. The distance can range from millimeters to centimeters. The produced pions have enough momentum to be reconstructed as tracks and are characterized by their transverse impact parameter (d_0), the distance between the interaction point and the track. The typical value of d_0 for these tracks is $O(0.1 - 1)$ mm. When the track p_T is $O(1)$ GeV, the d_0 resolution of a track, indicated by $\sigma(d_0)$, is typically around $O(0.01 - 0.1)$ mm as shown in Figure 6.2. Most low- p_T tracks originating from SM particles can be reduced by requiring significant displacements, defined as $S(d_0) \equiv |d_0|/\sigma(d_0)$. This allows for high sensitivity even when requiring low- p_T tracks around the reconstruction threshold. While the chargino has a relatively long lifetime, it is still short enough to decay before reaching the innermost layer of the tracking detector. Therefore, the standard algorithm is sufficient to reconstruct mildly-displaced tracks. Figure 6.3 shows a schematic of the analysis strategy.

6.2 Trigger Selections

In this thesis, $\sqrt{s} = 13$ TeV proton-proton collision data collected by E_T^{miss} triggers are used to define the SRs. These triggers are designed to target high E_T^{miss} originating from neutralinos recoiling against the ISR jet. Figure 6.4 shows that the E_T^{miss} trigger efficiency fluctuates across data-taking periods, reflecting different configurations optimized for varying pileup conditions. The configuration of the E_T^{miss} triggers for each data-taking period is summarized in Table 6.1, with the algorithms described in Section 3.3.2. In this thesis, a lower cut of $E_T^{\text{miss}} > 300$ GeV is applied to the data collected by the E_T^{miss} trigger, where the E_T^{miss} trigger is fully efficient. Data collected by single-muon, single-electron, and single-photon triggers are additionally used to estimate background yields of the SM, as discussed in Chapter 7.

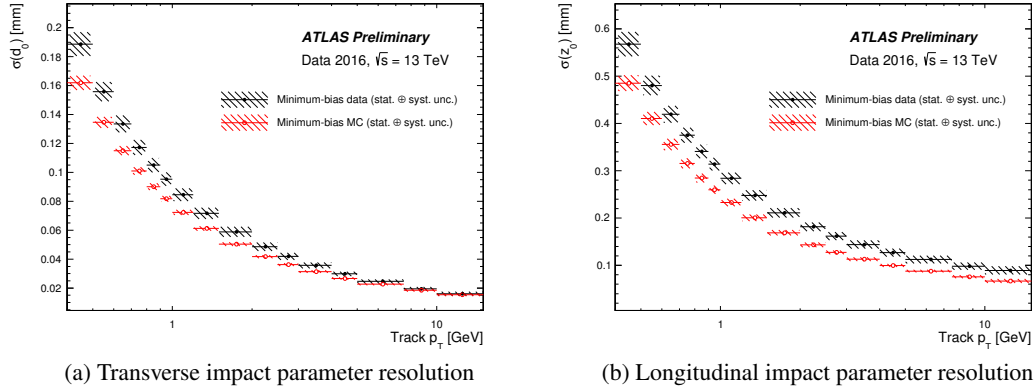


Figure 6.2: Resolution of transverse and longitudinal impact parameters measured in simulation and data as a function of track p_T . The resolutions were measured in minimum-bias simulation and in 2016 data. The figures are taken from Ref. [104].

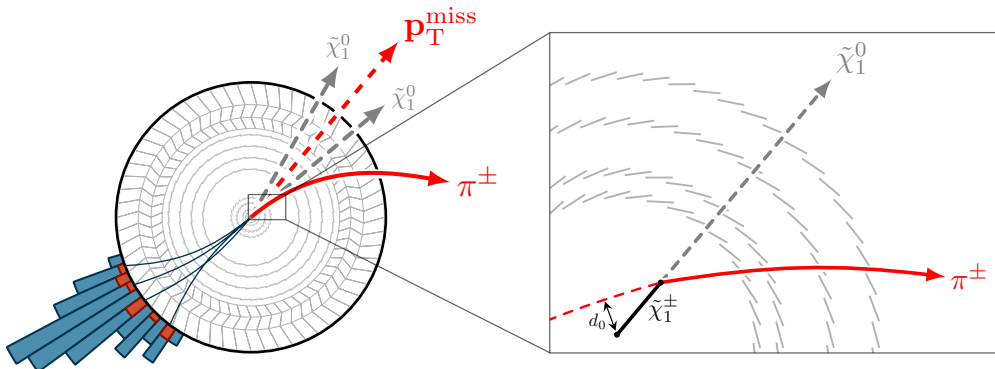


Figure 6.3: Schematic of the analysis strategy. The left side shows the cross-section of the ID and the calorimeter of the ATLAS detector. The pair-produced neutralinos are boosted in the opposite direction of the ISR jet, producing a large $\mathbf{p}_T^{\text{miss}}$. The right side shows a magnified view of the ID, illustrating a pion track with a relatively large impact parameter due to the relatively long lifetime of the chargedino.

Figure 6.4: E_T^{miss} trigger efficiency for each data-taking period during Run 2. The data is collected by reconstructing a Z boson from two muons. Since muons are not included in the calculation of the E_T^{miss} for triggers, the transverse momentum of the reconstructed Z boson ($p_T(Z)$) is used as a proxy for the E_T^{miss} . The figure is taken from Ref. [64].

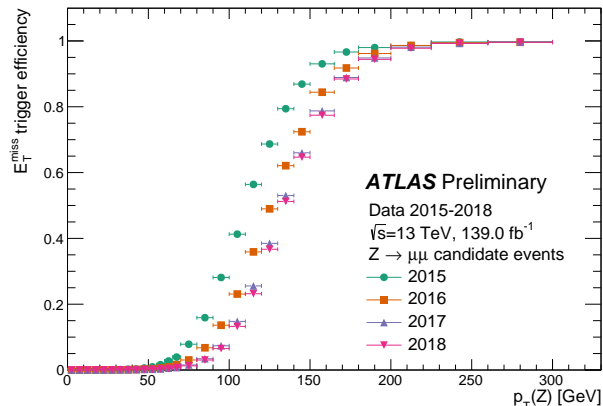


Table 6.1: Summary of the E_T^{miss} trigger configuration for each data-taking period. In 2018, a pre-threshold was applied to E_T^{miss} before applying the pileup-fit algorithm.

Year	L1 Threshold	HLT Threshold	E_T^{miss} algorithm
2015	50 GeV	70 GeV	Jet-based
2016	50 GeV	90 GeV	Jet-based
	50 GeV	100 GeV	Jet-based
	50 GeV	110 GeV	Jet-based
2017	55 GeV	100 GeV	Pileup-fit
2018	50 GeV	110 GeV	Pileup-fit, pre-threshold 70 GeV
	50 GeV	110 GeV	Pileup-fit, pre-threshold 65 GeV

6.3 Event Cleaning

Data used for physics analyses must pass several conditions to guarantee that the detector was in good condition. While this analysis requires a large E_T^{miss} , some fake E_T^{miss} is produced in the data by background events not originating from the LHC beam collisions, referred to as “non-collision backgrounds”. Non-collision backgrounds can be classified into beam-induced background and cosmic-ray shower-induced background. The beam-induced background refers to particles produced by the interaction of protons with the collimator or residual gas in the beam pipe that reaches the ATLAS detector. In particular, the beam-induced background does not conserve transverse momentum, resulting in a large E_T^{miss} in the opposite direction of the particles interacting with the ATLAS detector. Jets from non-collision backgrounds can be identified by checking the shower shape and direction of the jet relative to the interaction point. Moreover, jets generated by non-collision backgrounds do not have associated tracks and can be distinguished by considering the ratio of the total p_T of the associated tracks to the total energy of the jet. This analysis requires the leading jet to pass the *tight* jet cleaning working point [105] to mitigate jets

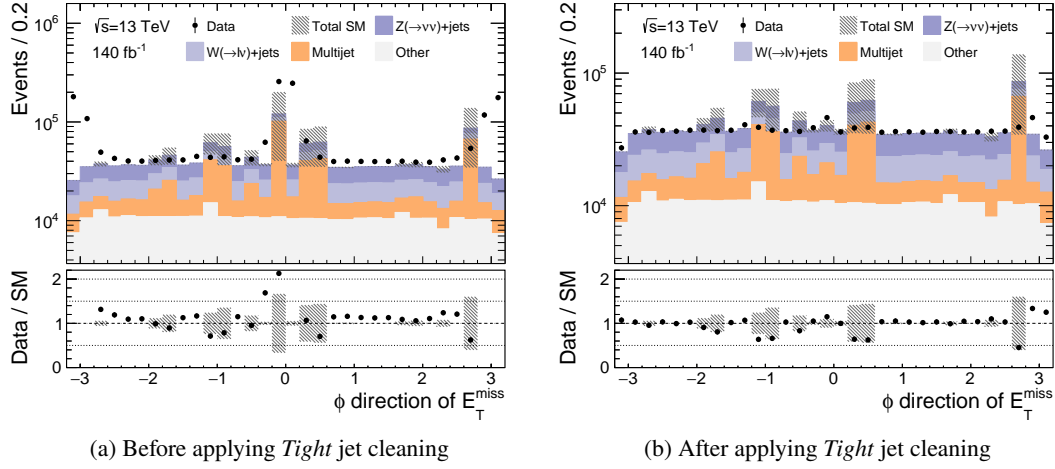


Figure 6.5: Distribution of ϕ direction of E_T^{miss} before and after applying the *Tight* jet cleaning. Before applying the *Tight* jet cleaning, there are peaks from the non-collision background in the direction of $|\phi| = 0, \pi$. These peaks disappear after applying the *Tight* jet cleaning, and the data and MC are in good agreement. The “Other” category includes contributions from $Z(\rightarrow \tau\tau)$ +jets, $W(\rightarrow \tau\nu)$ +jets, di-boson, single top, $t\bar{t}$, and γ +jets processes.

from non-collision backgrounds. Figure 6.5 shows the ϕ distribution of E_T^{miss} before and after applying the *Tight* jet cleaning. The beam-induced background is bent in the $|\phi| = 0, \pi$ direction by the recombination dipole, resulting in two peaks in the data distribution. The figure shows that the two peaks in the data disappear by applying the *Tight* jet cleaning, and the data and MC simulations show good agreement.

Although the *tight* jet cleaning is applied to the leading jet to suppress the non-collision background, it is not considered in MC simulations, and its contribution may not be negligible in this analysis. Using a full data-driven approach outlined in Appendix F, it has been confirmed that the contribution of the non-collision background can be sufficiently suppressed and neglected using the *tight* jet cleaning.

6.4 Signal track definition

In this analysis, pions and leptons produced by the decay of charginos and neutralinos have very low momentum. Therefore, low-momentum tracks are the only probes that can discriminate between signal and background events. The tracks discussed in Section 5.2 only satisfy the relatively loose requirements for reconstructing physics objects. Therefore, a more stringent selection is applied to identify tracks from the chargino and neutralino decays. This section discusses the criteria applied to the quality and kinematic variables of tracks to define signal tracks.

When two beams collide in the ATLAS detector, a large number of proton-proton collisions can occur. This often leads to an increase in the number of hits on the ID, which can result in the reconstruction of a track by random combinations. These tracks are known as “fake tracks” and lead to tracks with a significant impact parameter. Applying the following track quality selections is particularly effective in reducing the number of fake tracks.

Track quality

The *Tight Primary* working point [106] is required for the candidate track to achieve the highest reduction in fake tracks. The following selections are applied to the reconstructed tracks with $p_T > 500$ MeV and $|\eta| < 2.5$ to pass the *Tight Primary* working point.

- Less than or equal to one Pixel/SCT hit assigned to multiple tracks
- Less than or equal to two Pixel/SCT hits missing
- If $|\eta| < 1.65$ ($|\eta| > 1.65$), at least nine (eleven) hits in the silicon detectors
- At least one hit in either of the IBL or the B-Layer
- No Pixel hits missing

Figure 6.6(a) shows the efficiency of track reconstruction with respect to the track p_T . The efficiency remains high around 80%, even when the *Tight Primary* working point is required. The number of reconstructed tracks from beam collisions is proportional to the mean number of interactions per crossing. Therefore, Figure 6.6(b) indicates that the requirement of the *Tight Primary* working point significantly reduces the number of fake tracks. In this thesis, the chargino lifetime is expected to be short enough to decay before the IBL detector. As a result, requiring at least one hit on the IBL detector further reduces the occurrence of fake tracks.

Since we are interested in tracks produced from the primary vertex, reducing low- p_T tracks produced from pileup vertices is crucial, commonly known as “pileup tracks”. The following variables are effective in reducing pileup tracks.

Track η direction

Particles produced from the pileup vertices are emitted in the forward direction and can be reduced using the direction of the track, as shown in Figure 6.8(a). This analysis requires tracks with $|\eta| < 1.5$ to mitigate the contribution of pileup tracks.

Track impact parameter

As shown in Figure 6.7, pileup vertices are generated along the beam axis. Therefore, it is difficult to distinguish between tracks from the primary vertex and pileup vertices in the direction of the beam axis. However, since pileup vertices are generated at random z -positions relative to the primary vertex, they can be identified using the longitudinal impact parameter z_0 and the track direction θ . z_0 is the distance between the z -position of the closest point on the track to the primary vertex and the primary vertex. The $|\Delta z_0 \sin \theta|$ distribution is shown in Figure 6.8(b). To reduce pileup tracks, we require tracks to have

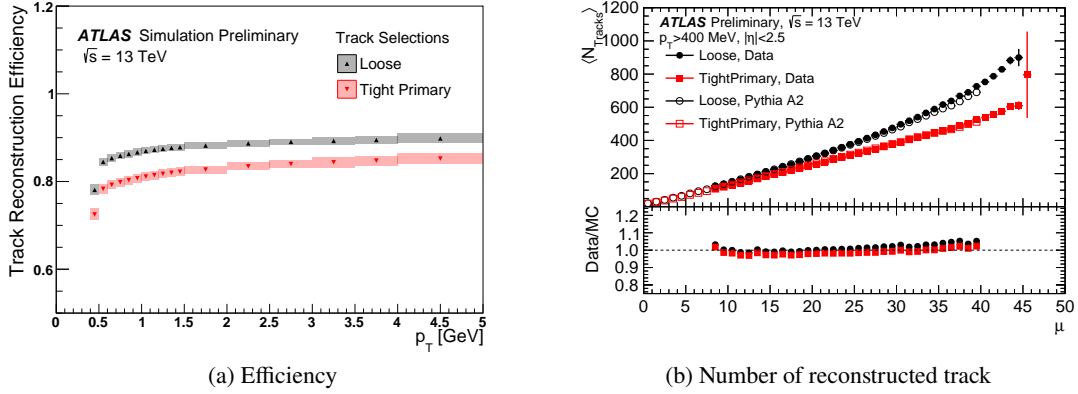


Figure 6.6: (a) Track reconstruction efficiency as a function of track p_T , evaluated by MC simulation samples. (b) Number of reconstructed tracks as a function of mean number of interactions per crossing (μ), evaluated in data and MC simulation samples. The bottom panel shows the ratio of data and MC simulation. Since the number of tracks from the beam collision is proportional to μ , the deviation from linearity indicates contributions from fake tracks. Figures (a) and (b) are taken from Ref. [106] and Ref. [107], respectively.

$|\Delta z_0 \sin \theta| < 1.5$ mm. The impact parameter in the transverse direction is used to select tracks with displacements compatible with higgsinos with mass differences less than 1 GeV. As the lifetime of the chargino in the area targeted in this analysis is $\mathcal{O}(0.1 - 1)$ mm, tracks are required to have $|d_0| < 10$ mm. Since the transverse impact parameter is crucial to distinguish between background and signal events, the lower limits are determined in Section 6.5.2.

As discussed in Section 6.1, the lifetime of the chargino in the region targeted in this analysis is $\mathcal{O}(0.1 - 1)$ mm. Among the metastable particles in the SM, τ leptons, strange hadrons, and B/D mesons are relatively long-lived, leaving tracks similar to those from the chargino decay. Since the 1-prong decay of τ leptons is very difficult to distinguish from the chargino decay, the number of background events is estimated by the method described in Section 7.2. On the other hand, the 3-prong decay of τ leptons and the decay of strange hadrons and B/D mesons produce multiple charged particles. These backgrounds can be reduced by measuring the hadron activity around the signal track. The decay topology of each particle is illustrated in Figure 6.9.

Track-based Isolation

The background tracks are reduced by requiring that there are no other tracks passing the *Tight Primary* selection with $p_T > 1$ GeV, $|z_0 \sin \theta| < 1.5$ mm, and $|d_0| < 1.5$ mm around the candidate track within $\Delta R = 0.4$.

Secondary vertex veto

Neutral strange hadrons, such as K_S^0 and Λ^0 , produce two charged particles after traveling a short distance. Although most of these backgrounds are suppressed by the track-based isolation, they remain when the signal candidate track's counterpart has a p_T lower than

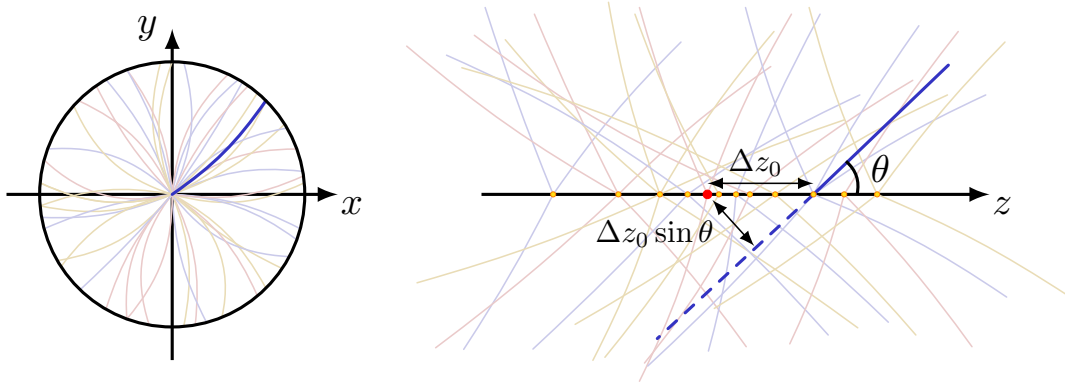


Figure 6.7: Schematic of tracks from the primary vertex and pileup vertices in an event, illustrated as solid colored lines. The left figure is a cross-section of the ATLAS detector, showing that the tracks from the primary vertex and pileup vertices are indistinguishable when viewed from the beam axis. The figure on the right is a view perpendicular to the beam axis direction, indicating that the z -position of tracks can be used as a discriminant to separate tracks from pileup vertices (indicated by orange dots) and tracks from the primary vertex (indicated by the red dot).

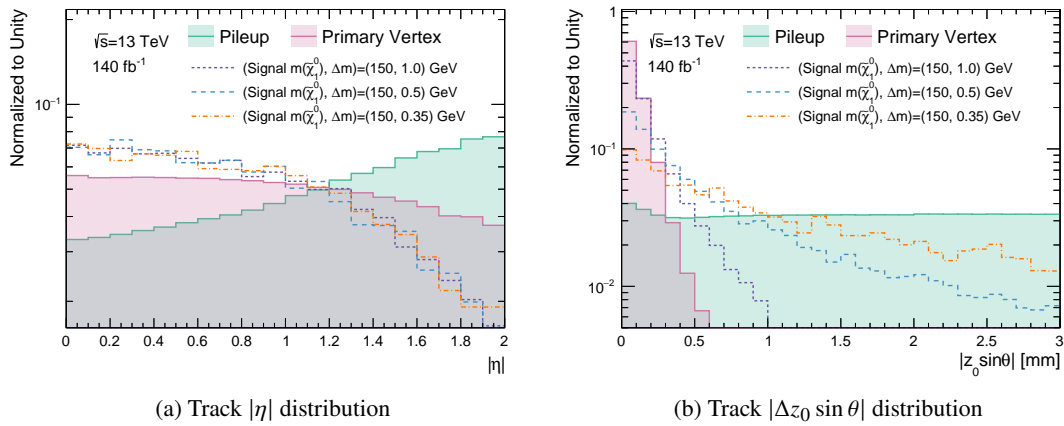


Figure 6.8: Shape comparison of track $|\eta|$ and $|\Delta z_0 \sin \theta|$ distributions after requiring the *Tight Primary* working point. Tracks are classified into tracks from the primary vertex and tracks from the pileup vertex. The dashed line illustrates signal simulation samples with different mass differences.

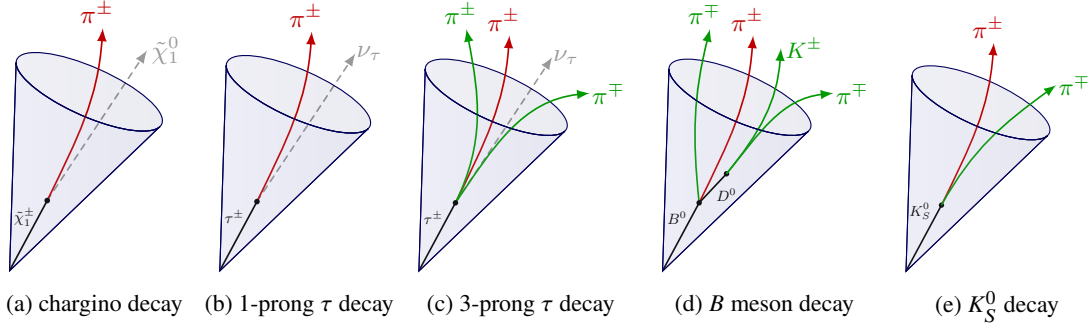


Figure 6.9: Decay topology of (a) chargino decay, (b) 1-prong τ decay, (c) 3-prong τ decay, (d) B meson decay, and (e) K_S^0 decay. The red line represents the signal candidate track. The blue cone is defined to have a radius of $\Delta R = 0.4$ around the signal candidate track and passes through the selection only if none of the tracks indicated by the green line are included.

1 GeV. To reduce this remaining background, mass-constrained fits are performed by assuming that the vertices are due to the decays of $\Lambda^0 \rightarrow p\pi^-$, $\bar{\Lambda}^0 \rightarrow \bar{p}\pi^+$, or $K_S^0 \rightarrow \pi^+\pi^-$. In the fit, the charge of the track is used to assign the corresponding mass of the decay product. A three-dimensional vertex fit is performed to reconstruct secondary vertices by looping over pairs of oppositely charged tracks in each event. Tracks associated with the reconstructed secondary vertices are vetoed to suppress the remaining strange hadron background. More details of the secondary vertex reconstruction are given in Ref. [108, 109].

The selections described above effectively reduce the number of low- p_T background tracks. However, there are still a considerable number of them, as seen in Figure 6.10. To address the issue of excessive low- p_T background tracks, we have implemented a lower threshold for the track p_T . This selection suppresses the number of background tracks before selecting one of several signal tracks in an event.

Track p_T

Setting a reasonable lower threshold for the track p_T of signal tracks is crucial, as chargino decays generate low- p_T tracks. As illustrated in the figure, τ decay tracks have a higher p_T compared to non- τ decay tracks, particularly those from pileup vertices. Since non- τ decay tracks, such as tracks from strange hadrons and B/D mesons, are mainly generated through QCD interaction, they are referred to as “QCD tracks” in the following. We can significantly reduce the number of QCD tracks by setting a lower threshold of 1 GeV to the track p_T . The track p_T selection is further optimized when defining the SRs in Section 6.5.2.

The definition of signal tracks is summarized in Table 6.2.

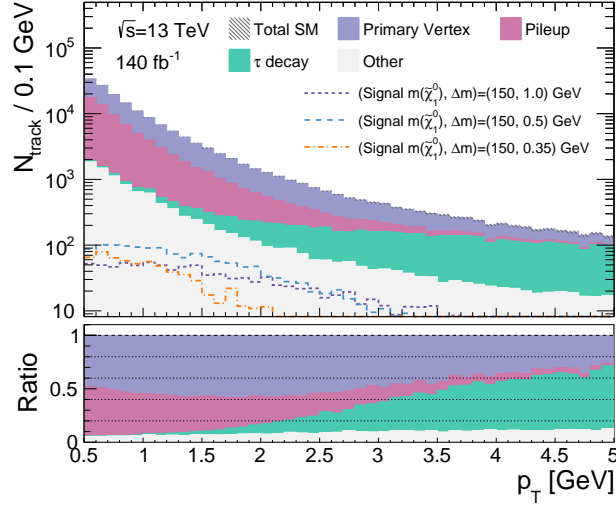


Figure 6.10: Distribution of track p_T after requiring the “jets+ E_T^{miss} ” signature and signal track selections. We apply the selection $S(d_0) > 3$ to signal tracks to emphasize the effect of mildly-displaced tracks. Tracks from the Z +jets and W +jets processes are classified into two categories: tracks resulting from τ decay and those resulting from non- τ decay. The latter are further classified into two subcategories: tracks from the primary vertex and those from pileup vertices. The dashed line illustrates signal simulation samples with different mass differences. The “Other” category includes contributions from di-boson, $t\bar{t}$, single top, γ +jets, and multijet processes.

Table 6.2: The selection criteria to define signal track objects.

Variable	Selection	Reduced Background
Track quality	<i>Tight Primary</i>	Fake tracks
Track $ \eta $	< 1.5	
Track $ d_0 $ [mm]	< 10	Pileup tracks
Track $ \Delta z_0 \sin \theta $ [mm]	< 1.5	
Track-based isolation	Pass	Tracks from τ leptons,
Secondary vertex veto	Pass	B/D mesons, and strange hadrons
Track p_T [GeV]	> 1	Pileup tracks and tracks from B/D mesons and strange hadrons

6.5 Event selection

This section outlines the primary selections applied to the physics objects. To reduce potential background processes and select events with the “jets+ E_T^{miss} ” signature, we apply preselections to the kinematic variables and the number of physics objects mentioned in Section 5.3. Section 6.5.1 details the variables used to select physics objects and the applied criteria. A single track is chosen for each event, using the displacement as a proxy for signal candidate tracks. Section 6.5.2 describes tighter selections applied to define the SRs.

6.5.1 Preselections

First, the following two are the primary variables to achieve the “jets+ E_T^{miss} ” signature.

Leading jet transverse momentum : $p_T(j_1)$

The leading jet is the reconstructed jet with the most significant transverse momentum. This variable plays a crucial role in this thesis in identifying events with an ISR jet. A requirement of $p_T(j_1) > 250$ GeV is imposed to enhance the momentum of the SUSY system, generating sufficient E_T^{miss} to pass the E_T^{miss} trigger.

Missing transverse momentum : E_T^{miss}

For signal events, two neutralinos are boosted to the same direction by requiring a large ISR jet, leading to significant E_T^{miss} . A requirement of $E_T^{\text{miss}} > 300$ GeV is imposed where the efficiency of the E_T^{miss} trigger is sufficiently large.

Since E_T^{miss} is defined as the negative vector sum of physics objects, “fake E_T^{miss} ” is reconstructed by mis-reconstruction or mis-calibration of the physics objects. Especially in the QCD multijet process, E_T^{miss} is easily generated by mis-measurement of the jet momentum. These background processes that produce “fake E_T^{miss} ” can be efficiently discarded by the requirement of $E_T^{\text{miss}} > 300$ GeV, since these processes typically produce lower E_T^{miss} . Further event reduction can be achieved by applying selection criteria to the following variables.

Number of jets : $N(j)$

$N(j)$ indicates the number of jets satisfying $p_T > 30$ GeV. Each event must have a maximum of four jets to reduce the hadronic activities originating from the multijet background process. While signal events typically have lower hadronic activity, the signal acceptance from events with two or three jets remains non-negligible.

Minimum $\Delta\phi$ between jets and E_T^{miss} : $\min(\Delta\phi(\mathbf{p}_T^{\text{jets}}, \mathbf{p}_T^{\text{miss}}))$

The separation in the azimuthal angle between the E_T^{miss} and the transverse momentum direction of the jets with $p_T > 30$ GeV. Inaccurate jet energy reconstruction results in mis-measured E_T^{miss} , often aligned with one of the reconstructed jets, as shown in Figure 6.11. To reduce the impact of this particular effect, we require that the separation between the jets and E_T^{miss} in the ϕ direction is greater than 0.4: $\min(\Delta\phi(\mathbf{p}_T^{\text{jets}}, \mathbf{p}_T^{\text{miss}})) > 0.4$.

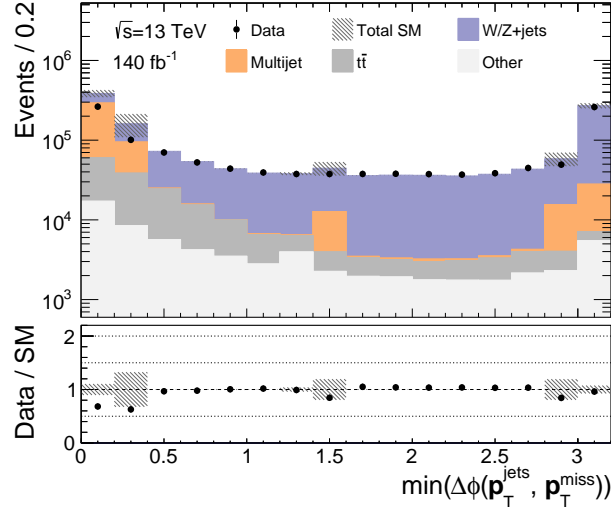


Figure 6.11: Distribution of $\min(\Delta\phi(\mathbf{p}_T^{\text{jets}}, \mathbf{p}_T^{\text{miss}}))$ after requiring the “jets+ E_T^{miss} ” signature: $p_T(j_1) > 250 \text{ GeV}$ and $E_T^{\text{miss}} > 300 \text{ GeV}$. Multijet events have a larger $N(j)$ than other background events, and the generated E_T^{miss} is aligned with a jet, resulting in $\min(\Delta\phi(\mathbf{p}_T^{\text{jets}}, \mathbf{p}_T^{\text{miss}}))$ close to zero. The “Other” category includes contributions from di-boson, single top, and γ +jets processes.

Several background processes produce neutrinos in the final state, including $Z(\rightarrow \nu\bar{\nu})$ +jets, $W(\rightarrow \ell\nu)$ +jets, di-boson, $t\bar{t}$, and single top processes. As a result, these processes produce significant E_T^{miss} . Among these processes, the $Z(\rightarrow \nu\bar{\nu})$ +jets process is challenging to distinguish from the signal process because it does not produce other particles than neutrinos in the final state. In contrast, other background processes result in leptons in the final state, which can be reduced using the following variable.

Number of leptons : $N(\ell_{\text{base}})$

$N(\ell_{\text{base}})$ indicates the number of leptons that meet the baseline criteria. Events containing reconstructed baseline leptons are excluded to mitigate contributions from W +jets, di-boson, $t\bar{t}$, and single top processes. While the chargino decays to a charged pion with the highest branching ratio, a non-negligible contribution arises from the chargino decaying to leptons in cases of larger mass differences. However, the resulting leptons are very soft for the mass differences of interest and are not excluded by the lepton veto.

After applying the lepton veto, the Z +jets and W +jets processes become the main background with a “jets+ E_T^{miss} ” signature. As explained in Section 6.4, the SM particles in the Z +jets and W +jets processes that have sufficient lifetimes to leave a mildly-displaced track consist of τ leptons, strange hadrons, and B/D mesons. By requiring a “jets+ E_T^{miss} ” signature, the system opposite to the jet is boosted, which causes charged particles from the chargino decay in the same direction as the neutralino in signal events. In the case of the Z +jets and W +jets processes, τ leptons produced by W/Z boson decays appear in the same direction as the neutrinos. On the other hand, the strange hadrons and B/D mesons produced in the Z +jets and W +jets processes

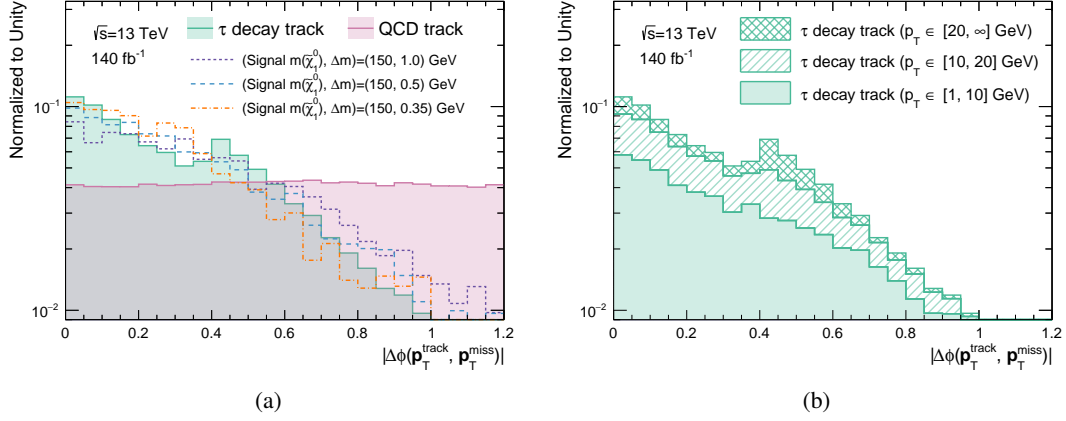


Figure 6.12: (a) Shape comparison of $|\Delta\phi(\mathbf{p}_T^{\text{track}}, \mathbf{p}_T^{\text{miss}})|$ distributions after requiring all preselections and displacement for signal tracks: $p_T(j_1) > 250 \text{ GeV}$, $E_T^{\text{miss}} > 300 \text{ GeV}$, $N(j) \leq 4$, $\min(\Delta\phi(\mathbf{p}_T^{\text{jets}}, \mathbf{p}_T^{\text{miss}})) > 0.4$, $N_\ell = 0$, and $S(d_0) > 3$. The classification of tracks in the Z +jets and W +jets processes is based on the origin of the track and can be divided into two categories: τ decay tracks and QCD tracks. The dashed line illustrates signal simulation samples with different mass differences. The τ decay tracks show a peak around 0.4, originating from one of the preselections: $\min(\Delta\phi(\mathbf{p}_T^{\text{jets}}, \mathbf{p}_T^{\text{miss}})) > 0.4$. (b) Shape comparison of τ decay tracks in different p_T ranges. The peak of the distribution in (a) originates from τ decay tracks with relatively high p_T . The decay of τ leptons can produce multiple particles that can be reconstructed as a jet, particularly when the decay products have enough energy to surpass the reconstruction threshold. However, we require separation between jets and E_T^{miss} in the preselection. Therefore, high- p_T tracks from τ decay near the E_T^{miss} are excluded. This analysis primarily focuses on low- p_T tracks. The peak observed in (a) is eliminated by the track p_T criteria of the SR selection, which is further discussed in Section 6.5.2.

are not produced from W/Z bosons. Consequently, these particles are randomly distributed with respect to the neutrinos. Therefore, the following variable can effectively suppress QCD tracks in the Z +jets and W +jets processes.

Alignment of track and E_T^{miss} in the ϕ direction : $|\Delta\phi(\mathbf{p}_T^{\text{track}}, \mathbf{p}_T^{\text{miss}})|$

The angular difference between the signal candidate track and E_T^{miss} in the ϕ direction. Figure 6.12 shows the $|\Delta\phi(\mathbf{p}_T^{\text{track}}, \mathbf{p}_T^{\text{miss}})|$ distribution. The strange hadrons and B/D mesons produced at the primary vertex and pileup vertices are produced randomly in the ϕ direction, leading to high suppression by requiring $|\Delta\phi(\mathbf{p}_T^{\text{track}}, \mathbf{p}_T^{\text{miss}})| < 0.4$.

When multiple tracks pass the above track selections, one track with the most significant track $S(d_0)$ is selected for each event. Preselections applied to the physics objects and tracks are summarized in Table 6.3.

6.5.2 Signal Region Selection

Additional selections are imposed to define the regions enriched in signals compared to SM backgrounds. These regions are called signal regions (SRs). The SRs are designed to optimize the significance (Z) while assigning a total uncertainty of 10% to the background yields. This level of background uncertainty is reasonable based on the background estimation strategy outlined in Chapter 7. The significance (Z) is defined as [110]

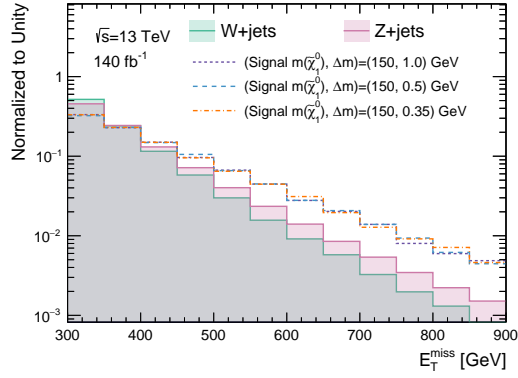
$$Z = \begin{cases} +\sqrt{2 \left(n \ln \left[\frac{n(b+\sigma^2)}{b^2+n\sigma^2} \right] - \frac{b^2}{\sigma^2} \ln \left[1 + \frac{\sigma^2(n-b)}{b(b+\sigma^2)} \right] \right)} & \text{if } n \geq b \\ -\sqrt{2 \left(n \ln \left[\frac{n(b+\sigma^2)}{b^2+n\sigma^2} \right] - \frac{b^2}{\sigma^2} \ln \left[1 + \frac{\sigma^2(n-b)}{b(b+\sigma^2)} \right] \right)} & \text{if } n < b, \end{cases} \quad (6.1)$$

where b is the number of expected background events with uncertainty σ and n is the number of signal events plus the number of background events. The variables E_T^{miss} , track p_T , and track $S(d_0)$ effectively distinguish between signal and background events, as highlighted in Figure 6.13. The figure indicates that QCD and chargino decay tracks have low p_T , while a significant proportion of τ decay tracks have relatively high p_T . To reduce the number of τ decay tracks with minimal loss of tracks from the chargino decay, an upper limit of 5 GeV is imposed on the track p_T .

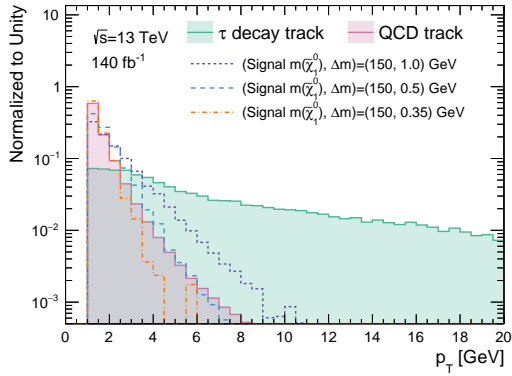
Raising the lower limits of these variables was optimized to efficiently reduce background tracks while maximizing sensitivity to signal tracks from the chargino decay. The applied selections are listed below.

- $E_T^{\text{miss}} > 600 \text{ GeV}$
- Track $p_T \in [2, 5] \text{ GeV}$
- Track $S(d_0) > 8$

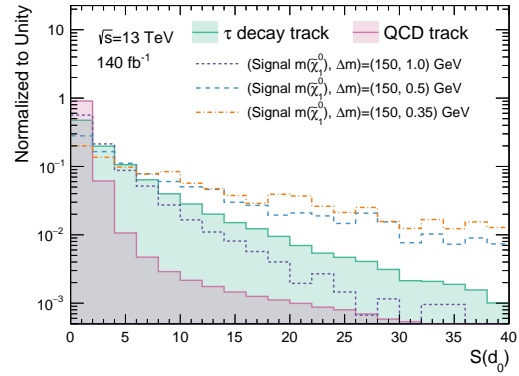
To enhance sensitivity to signals with different mass differences, we divided the track $S(d_0)$ into two regions. In regions where the mass difference between the chargino and neutralino is small, a significant $S(d_0)$ value is required. Specifically, the lower bound of $S(d_0)$ can be raised to 20 since the lifetime of the chargino is particularly long in these regions. On the contrary, in regions with a high mass difference, the lifetime of the chargino is short. As a result, the tracks produced by the chargino decays have a small $S(d_0)$ value, as illustrated in Figure 6.14. Therefore, we define a separate SR, which requires $8 < S(d_0) < 20$. This SR with smaller $S(d_0)$ values is named SR-Low, while the SR with larger $S(d_0)$ values is called SR-High. Figure 6.15 illustrates the ratio of neutralino and chargino decay tracks along with the cut efficiency for the track p_T and $S(d_0)$ selection. Although the track p_T selection has low efficiency in regions with small mass differences, the $S(d_0)$ selection has better efficiency than regions with large mass differences. Before the $S(d_0)$ selection, SM tracks account for a large proportion of the signal tracks, especially in regions where the mass difference is small. However, by applying the $S(d_0)$ selection, signal candidate tracks in the SRs are dominated by tracks from the neutralino or chargino decay.



(a) E_T^{miss} distribution



(b) Track p_T distribution



(c) Track $S(d_0)$ distribution

Figure 6.13: (a) Shape comparison of the E_T^{miss} distribution after requiring all preselections, except for requiring signal tracks. (b)(c) Shape comparison of the track p_T and $S(d_0)$ distribution after requiring all preselections. Tracks in the Z +jets and W +jets processes are classified into τ decay tracks and QCD tracks, depending on the origin of the track. The dashed line illustrates signal simulation samples with different mass differences.

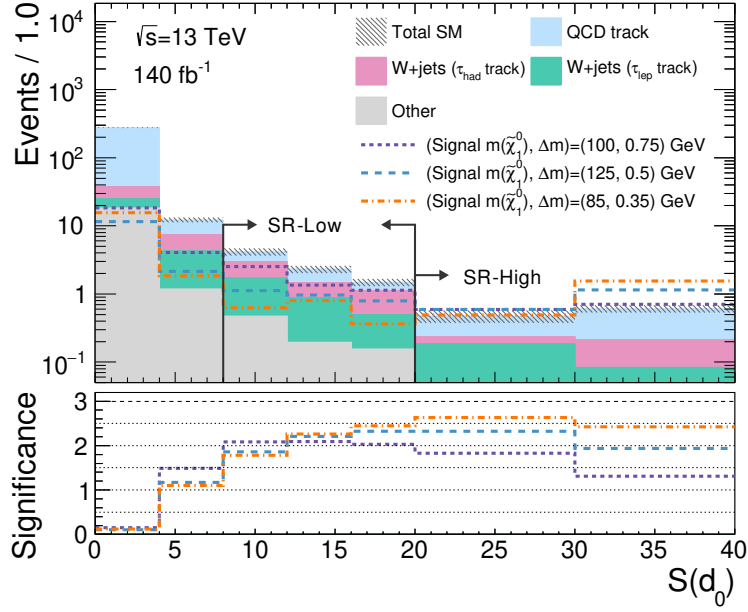


Figure 6.14: Track $S(d_0)$ distribution after applying $E_T^{\text{miss}} > 600$ GeV and track $p_T \in [2, 5]$ GeV. The dashed line illustrates signal simulation samples with different mass and mass differences. The arrows labeled SR-Low and SR-High correspond to the selections applied in each region. The hatched area corresponds to the MC statistical uncertainties. The bottom panel shows the significance (Z) calculated by accumulating the yields of the bins on the right side. A total uncertainty of 10% is assumed for the background yields. The “Other” category includes contributions from $Z(\rightarrow \tau\tau)$ +jets, di-boson, single top, $t\bar{t}$, γ +jets, and multijet processes.

Table 6.3 summarizes the additional selections applied to the preselections for each SR bin. The distributions and significance of E_T^{miss} and track p_T are given in Figure 6.16. The expected yields and the efficiency for each selection are summarized in Appendix D.

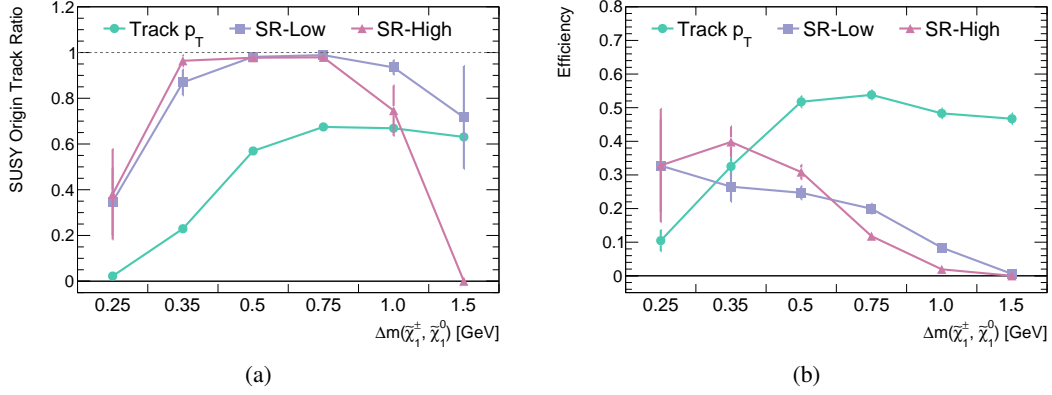
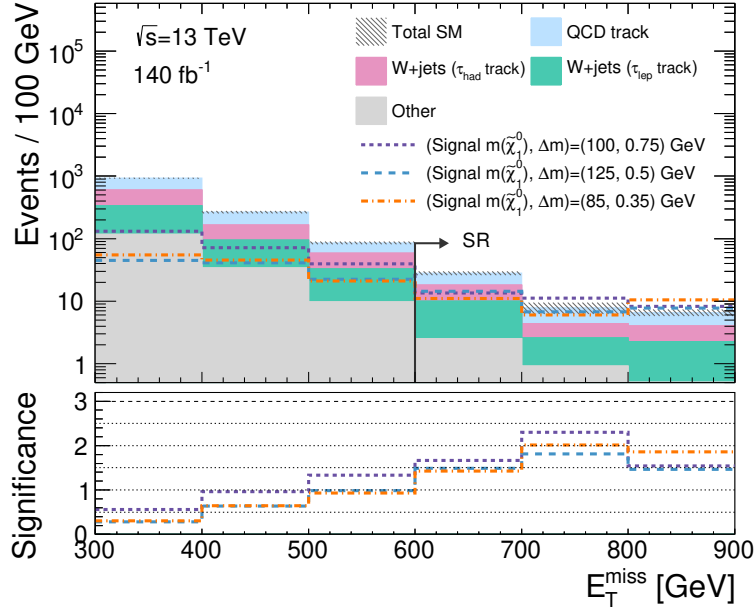


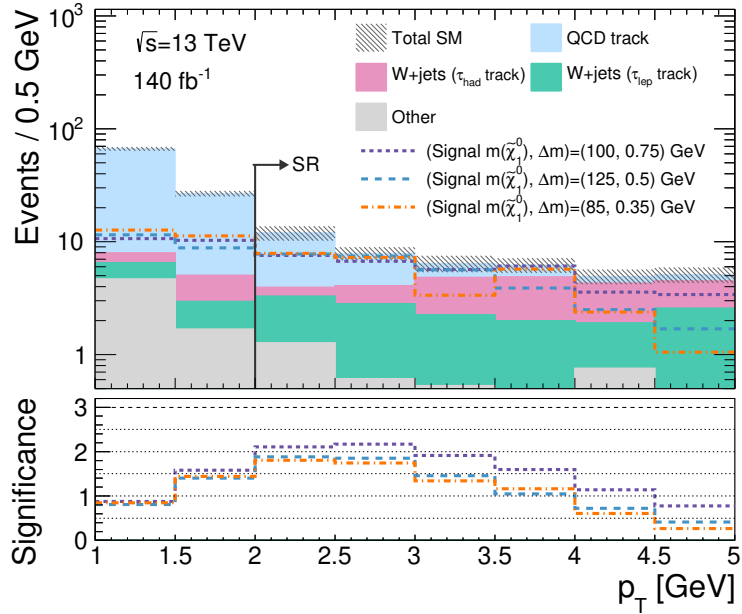
Figure 6.15: (a) Proportion of signal tracks originating from neutralino and chargino decay after each selection. (b) The efficiency of each selection is calculated with the yields before applying the selection as the denominator and the yields after applying the selection as the numerator. All selections, except the track p_T and track $S(d_0)$ selections to define the SRs, are already applied to the signal track objects before the track p_T selection. The efficiency is calculated using only tracks from neutralino and chargino as the denominator and numerator.

Table 6.3: Selections applied to define the 0ℓ category and SRs.

Category	0ℓ	
<i>Preselections</i>		
$p_T(j_1)$ [GeV]	> 250	
$ \eta(j_1) $	< 2	
E_T^{miss} [GeV]	> 300	
$N(\ell_{\text{base}})$	= 0	
$N(j)$	≤ 4	
$\min(\Delta\phi(\mathbf{p}_T^{\text{jets}}, \mathbf{p}_T^{\text{miss}}))$	> 0.4	
$ \Delta\phi(\mathbf{p}_T^{\text{track}}, \mathbf{p}_T^{\text{miss}}) $	< 0.4	
Region groups	SR-Low	SR-High
<i>Additional selections to define Signal Regions</i>		
E_T^{miss} [GeV]	> 600	
Track p_T [GeV]	[2, 5]	
Track $S(d_0)$	[8, 20]	> 20



(a) E_T^{miss} distribution



(b) Track p_T distribution

Figure 6.16: E_T^{miss} and track p_T distributions. Each plot is drawn without applying selections to the variable illustrated. The dashed line illustrates signal simulation samples with different mass and mass differences. The hatched area corresponds to the MC statistical uncertainties. The bottom panel shows the significance (Z) calculated by accumulating the yields of the bins on the right side. A total uncertainty of 10% is assumed for background yields. The “Other” category includes contributions from $Z(\rightarrow \tau\tau)$ +jets, di-boson, single top, $t\bar{t}$, γ +jets, and multijet processes.

Chapter 7

Background Estimation

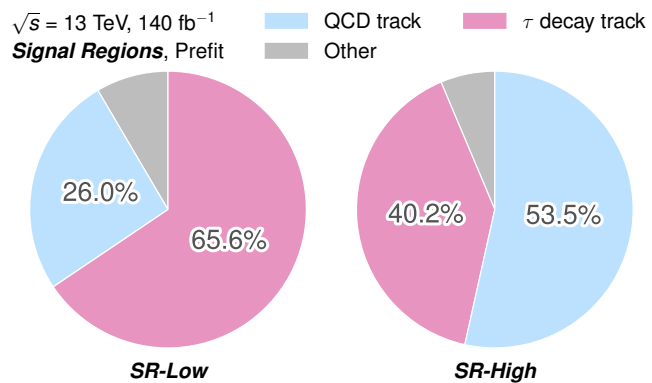
This chapter outlines the strategy used to estimate the yields of background processes that contribute significantly to the signal regions (SRs), followed by the strategy to validate this estimation approach. The regions defined to constrain the yields are called control regions (CRs), while the regions for validation are called validation regions (VRs).

Section 7.1 provides an overview of the main backgrounds and briefly describes the estimation methods. Details of the estimation and validation strategy for each background are described in Sections 7.2 and 7.3. Section 7.4 outlines an additional VR designed to validate the background estimation strategy in the proximity of the SRs. Finally, Section 7.5 summarizes the consistency between the data and the estimates in VRs defined for each background estimation procedure.

7.1 Origin of the background events and the estimation strategy

The background composition in the two SRs (SR-Low and SR-High), estimated directly from the simulation samples, is illustrated in Figure 7.1. Details of the background yields for each background process are presented in Appendix E.

Figure 7.1: Pie-charts showing the background composition in each SR, estimated directly from MC simulation samples. Events from the Z +jets and W +jets processes are classified according to the origin of the signal candidate track; we define tracks generated by τ decay as “ τ decay” tracks and other tracks as “QCD tracks”. The “Other” category includes contributions from $Z(\rightarrow \tau\tau)$ +jets, di-boson, γ +jets, multijet, single top, and $t\bar{t}$ processes.



The main background consists of tracks in $Z(\rightarrow \nu\bar{\nu})+\text{jets}$ and $W(\rightarrow \ell\nu)+\text{jets}$ processes, generating significant $E_{\text{T}}^{\text{miss}}$ to satisfy the SR selections. The composition of the background varies depending on the $S(d_0)$ cuts. The origin of these tracks can be categorized into two groups:

“ τ decay tracks” : estimated by semi data-driven method

τ leptons produced from W bosons are a significant background process that contaminate the SRs. This contamination occurs due to the long lifetime of τ leptons, which results in final states with displaced pions and leptons. Since this analysis requires a large $E_{\text{T}}^{\text{miss}}$, neutrinos from the W boson decay must be produced and boosted in the same direction as the W boson’s motion. On the other hand, τ leptons are generated in the opposite direction to the W boson’s motion, resulting in relatively low momentum. Although the lepton veto can help suppress leptons from τ decays, it is not completely effective due to the p_{T} threshold and the efficiency of lepton reconstruction. Figures 7.2(a) and 7.2(b) illustrate the composition of τ decay tracks in SR-Low and SR-High, respectively. Further details can be found in Appendix E.

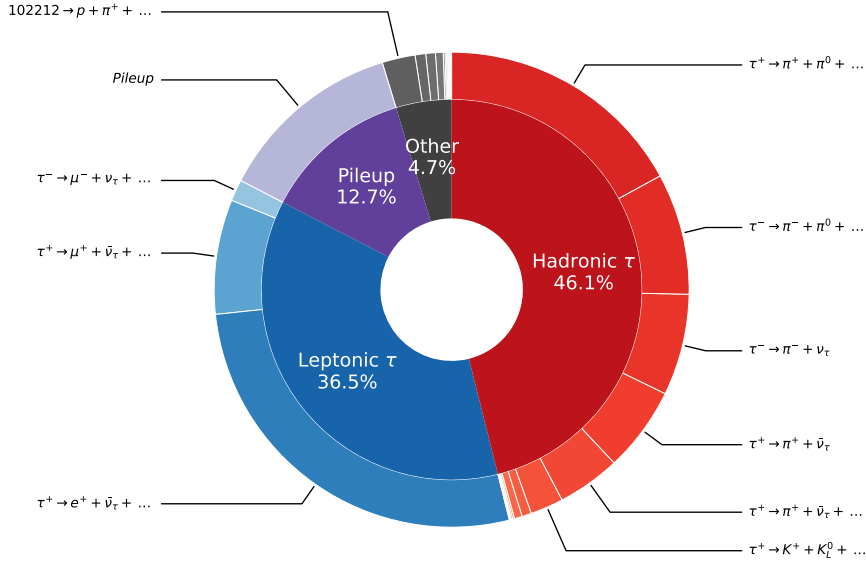
The method used to estimate τ decay tracks follows a semi data-driven approach, explained in Section 7.2. This approach relies on the fact that τ decay occurs mainly through the electroweak interaction and can be accurately simulated using MC simulations.

“QCD tracks” : estimated by full data-driven method

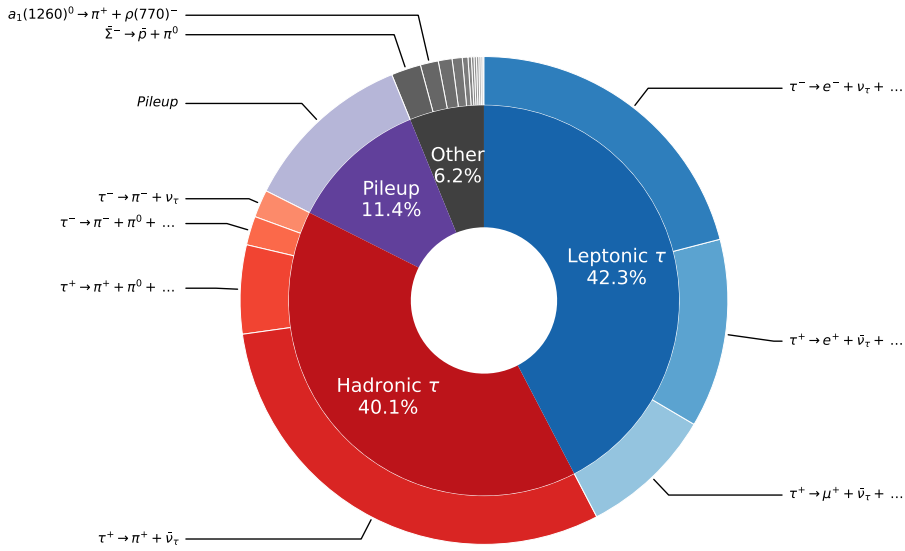
Tracks originating from soft initial- or final-state radiation, or interaction between partons other than those causing the hard-scattering process (“underlying events”), are the source of mildly-displaced tracks with low momentum in the $Z+\text{jets}$ and $W+\text{jets}$ processes. In the following, tracks not from τ decays are referred to as “QCD tracks”. The primary source of these tracks is long-lived strange hadrons from the hard-scattering process. Another source is charged particles produced from pileup vertices, resulting in significant impact parameters. Figures 7.3(a) and 7.3(b) illustrate the composition of QCD tracks in SR-Low and SR-High, respectively. Further details can be found in Appendix E.

It is challenging to accurately model the particles generated by QCD interactions, making it difficult to estimate the contribution of QCD tracks through MC simulations. Therefore, a more reliable approach is directly extracting the distribution from data in specific regions. QCD tracks are estimated using a full data-driven approach outlined in Section 7.3.

The $Z+\text{jets}$ and $W+\text{jets}$ processes have two types of events categorized by the signal candidate track: “ τ decay track” events, with a track from τ decays, and “QCD track” events, with a track not from τ decays. CRs are defined to estimate the number of events in the SRs of τ decay tracks and QCD tracks. VRs are defined in the phase space between SRs and CRs. The number of events in VRs is estimated using the same methodology as that used for CRs. The accuracy of the estimation method and the systematic uncertainty, as described in Chapter 8, is verified by comparing the estimated number of events with the observed data. Other background processes have a negligible impact on SR-Low and SR-High and are estimated directly from simulation samples.

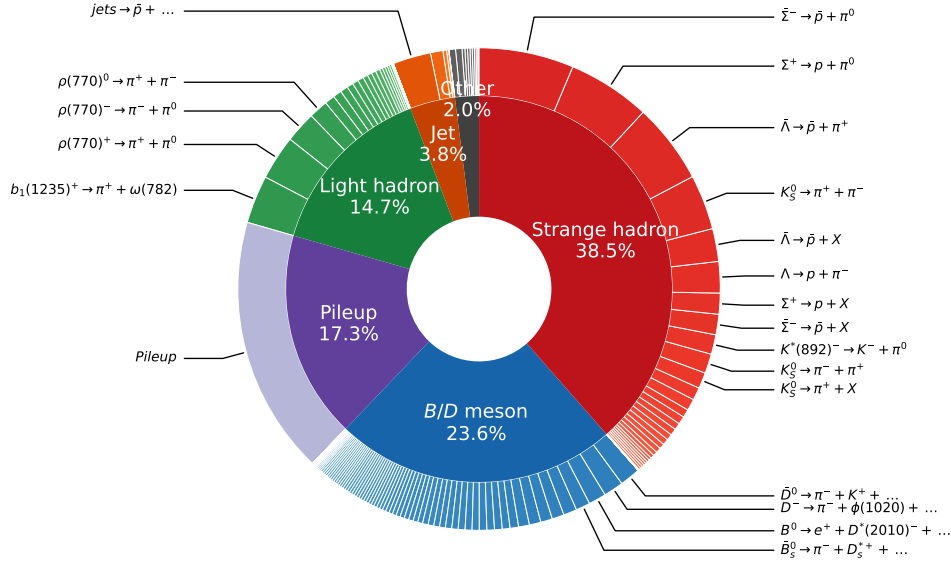


(a) SR-Low

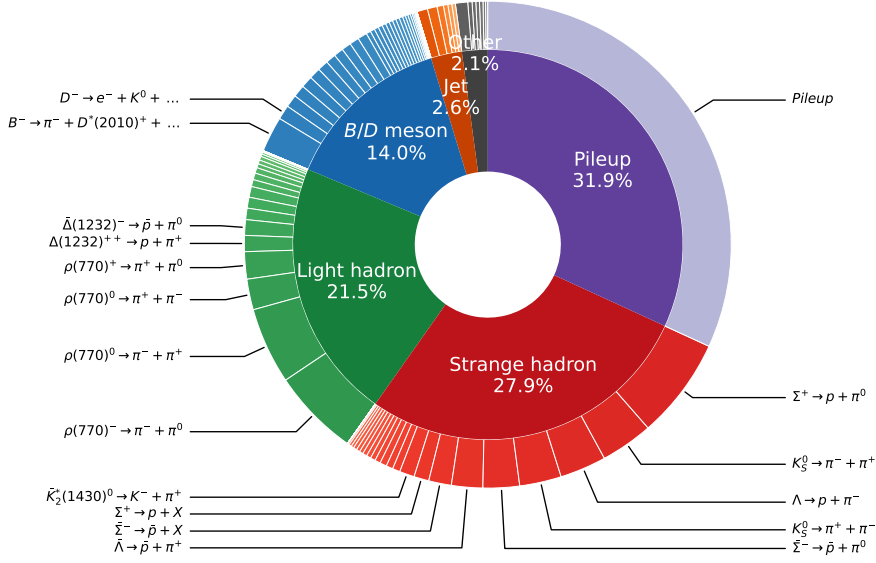


(b) SR-High

Figure 7.2: The figure presents the breakdown of signal candidate tracks in SR-Low and SR-High, estimated from the $W(\rightarrow \tau\nu)+\text{jets}$ sample and sorted by their decay mode. If there are multiple signal track candidates, the one with the most significant $S(d_0)$ is the signal track. However, this table refers to all signal track candidates. After sufficient selection criteria are applied, the number of tracks per event is significantly reduced. As a result, the discussion of the composition is not significantly affected. The item on the right side of the arrow shows information on the truth particle associated with the reconstructed signal track. The left side of the arrow indicates the parent particle identified from the truth particle above. If the decay of the parent particle generates multiple particles, the remaining particles are listed in the second and subsequent items on the right side of the arrow.



(a) SR-Low



(b) SR-High

Figure 7.3: The figure presents the breakdown of signal candidate tracks in SR-Low and SR-High, estimated from the $Z(\rightarrow \nu\bar{\nu})+\text{jets}$ sample and sorted by their decay mode. If there are multiple signal track candidates, the one with the most significant $S(d_0)$ is the signal track. However, this table refers to all signal track candidates. After sufficient selection criteria are applied, the number of tracks per event is significantly reduced. As a result, the discussion of the composition is not significantly affected. The item on the right side of the arrow shows information on the truth particle associated with the reconstructed signal track. The left side of the arrow indicates the parent particle identified from the truth particle above. If the decay of the parent particle generates multiple particles, the remaining particles are listed in the second and subsequent items on the right side of the arrow. X corresponds to particles with missing information due to too low p_T . The notation “jets” indicates that the tracks are from jets and are classified according to the type of particle reconstructed as the track.

7.2 Semi data-driven background estimation for τ decay tracks

7.2.1 Overview

In this analysis, the $W(\rightarrow \tau\nu)$ +jets process is considered one of the significant background. As discussed in Section 7.1, two types of signal candidate tracks are observed from the $W(\rightarrow \tau\nu)$ +jets process: τ decay tracks and QCD tracks. The QCD tracks are estimated inclusively with the Z+jets process and are further explained in Section 7.3.

Backgrounds originating from τ decay tracks are constrained in CRs that are kinematically close to the SRs. Both data and simulation samples are used to constrain them. Normalization Factors (NFs) for τ decay tracks are measured in these CRs, defined as

$$\text{NF} = \frac{N_{\text{data}} - N_{\text{non-}\tau\text{decay}}}{N_{\tau\text{decay}}}, \quad (7.1)$$

where N_{data} and $N_{\tau\text{decay}}$ represent the observed data and the expected yield for τ decay tracks in the CRs, respectively. $N_{\text{non-}\tau\text{decay}}$ represents the total expected yield from non- τ decay track background, including the signal process. To obtain the expected yields, the measured NF is applied to the predicted yield from MC simulation for τ decay tracks in the SRs.

As discussed in Section 6.5.2, the SRs focus on identifying low- p_T tracks with $2 < p_T < 5$ GeV. However, by increasing the track p_T selection to $8 < p_T < 20$ GeV, we can define a region where hadronic and leptonic τ decay tracks dominate, as illustrated in Figure 7.4. The lower limit of 8 GeV is set to reduce contamination from signal models with large mass differences, which could produce high- p_T tracks.

To improve the accuracy of the normalization of τ decay tracks, we have defined an additional region predominantly consisting of leptonic τ decay tracks. In cases where only one signal muon is required, the $W(\rightarrow \mu\nu)$ +jets process is dominant because signal muons must be produced promptly ($S(d_0) < 3$), as we have discussed in Section 5.3. However, when a baseline muon is required, which does not pass the signal selection, muons with high $S(d_0)$ ($S(d_0) > 3$) are included. Muons from the leptonic τ decay typically have slightly higher $S(d_0)$ as illustrated in Figure 7.5. Therefore, a region enriched in the $W(\rightarrow \tau\nu)$ +jets process can be defined by requiring exactly one baseline muon with a significant impact parameter, which we refer to as the “1-baseline muon category” (denoted as “ $1\mu_{\text{base}}$ ”).

Accurate modeling of the τ decay through electroweak interaction simplifies the extrapolation of the NF across different track p_T ranges. However, it is challenging to model the \mathbf{p}_T of the W bosons due to the hadron activities in the opposite direction. Therefore, the extrapolation of the NF is limited within the same p_T range of the W boson. Event selections must be performed based on the \mathbf{p}_T of the W bosons to extract events with the same hadron activities. For this, a variable called $\mathbf{p}_T^{\text{recoil}}$ is defined that represents the \mathbf{p}_T of the weak boson. $\mathbf{p}_T^{\text{recoil}}$ is calculated by adding the \mathbf{p}_T of leptons to the $\mathbf{p}_T^{\text{miss}}$. In the SRs, the magnitude of $\mathbf{p}_T^{\text{recoil}}$ (p_T^{recoil}) is equivalent to

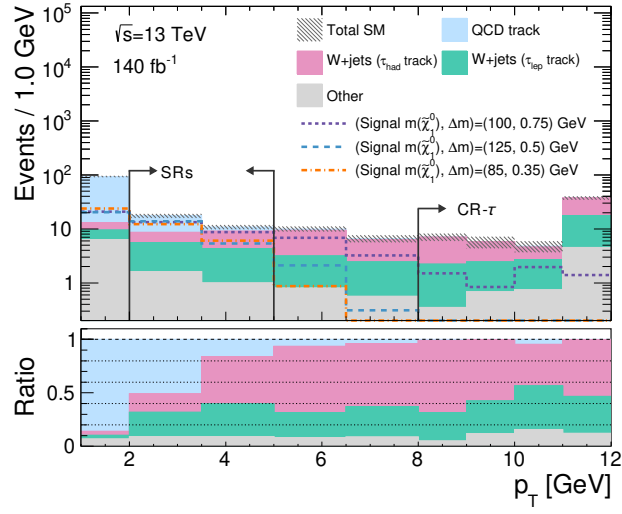


Figure 7.4: Pre-fit track p_T distribution without applying the track p_T selection. The dashed line illustrates signal simulation samples with different mass and mass differences. The hatched area corresponds to the combined systematic and MC statistical uncertainties. The bottom plot shows the background composition in each bin. The “Other” category includes contributions from $Z(\rightarrow \tau\tau)$ +jets, di-boson, single top, $t\bar{t}$, γ +jets, and multijet processes.

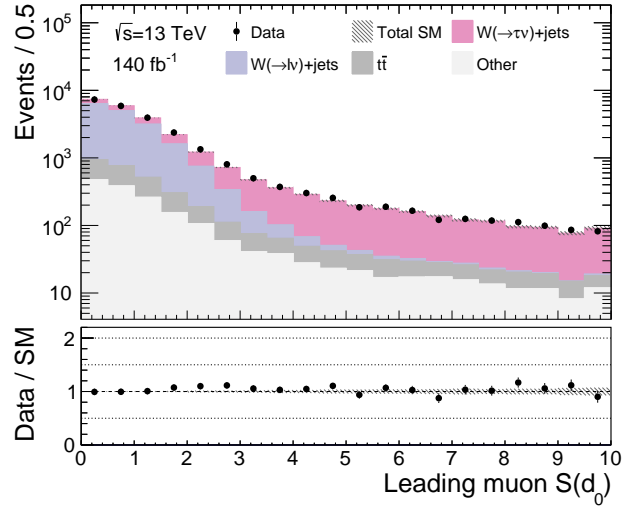


Figure 7.5: Distribution of $S(d_0)$ of the leading muon. Selections to signal tracks are not applied. The bottom panel shows the ratio of the observed data and background yield estimated directly from simulation samples. The “Other” category includes contributions from $Z(\rightarrow \nu\bar{\nu})$ +jets, $Z(\rightarrow \tau\tau)$ +jets, di-boson, single top, γ +jets, and multijet processes.

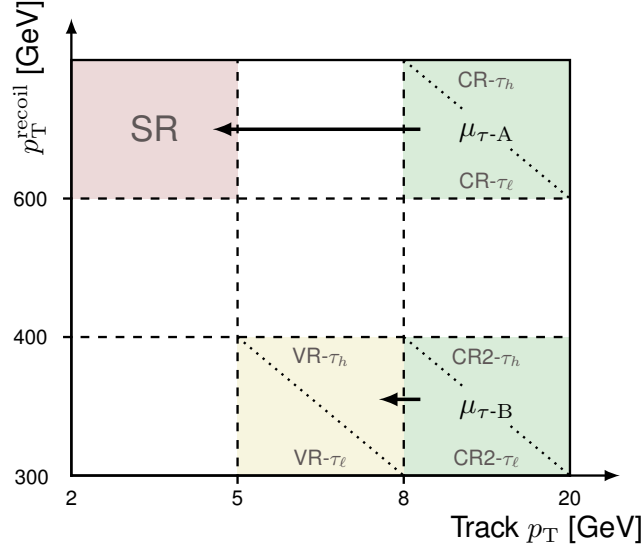


Figure 7.6: Schematic views of region definition for τ decay track background estimation. The red, green, and yellow areas show the SRs, CRs, and VRs used for the estimation of τ decay tracks. A single NF is constrained by two CRs in the high- p_T range of the 0ℓ and $1\mu_{\text{base}}$ categories. The NF is extrapolated to the low- p_T range and multiplied to the τ decay track yields in the SRs, indicated by two arrows. The VRs to validate the extrapolation of the NF is defined in the medium- p_T and low- p_T^{recoil} range in the 0ℓ and $1\mu_{\text{base}}$ categories. The NF for τ decay tracks are calculated in the low- p_T^{recoil} range and applied to the yields in the VRs, indicated by an arrow.

E_T^{miss} since there are no leptons in the event. Applying selections to $\mathbf{p}_T^{\text{recoil}}$ ensures equivalent hadron activities between the 0ℓ and $1\mu_{\text{base}}$ categories.

In the low- p_T range ($2 < p_T < 5$ GeV), QCD tracks are dominant. Therefore, the accuracy of the extrapolation of the measured NF from the high- p_T range ($8 < p_T < 20$ GeV) to the low- p_T range ($2 < p_T < 5$ GeV) is verified in the medium- p_T range ($5 < p_T < 8$ GeV). The p_T^{recoil} range is lowered to $300 < p_T^{\text{recoil}} < 400$ GeV in the 0ℓ and $1\mu_{\text{base}}$ categories to reduce signal contamination. The NF is calculated in the high- p_T range with $300 < p_T^{\text{recoil}} < 400$ GeV and applied to the adjacent medium- p_T range to validate the extrapolation. Figure 7.6 presents a schematic diagram of the estimation and validation strategy for the NF.

The background estimation strategy for τ decay tracks is summarized below.

- A single NF is defined for the τ decay tracks. The NF is measured in the high- p_T range of the 0ℓ and $1\mu_{\text{base}}$ categories. The 0ℓ category is enriched in hadronic τ decay tracks, while the $1\mu_{\text{base}}$ category is enriched in leptonic τ decay tracks.
- To validate the extrapolation of the NF from the high- p_T range ($8 < p_T < 20$ GeV) to the low- p_T range ($2 < p_T < 5$ GeV), the low- p_T^{recoil} region is utilized to avoid signal contamination.

The contribution of QCD tracks is relatively small in the CRs and VRs designated for estimating the τ decay tracks. Therefore, the QCD track yield is obtained directly from the MC simulations. The definition of each region used to measure and validate the NF is described below.

7.2.2 Control Regions and Validation Regions

The region enriched in the $W(\rightarrow \tau\nu)$ +jets process is defined by requiring a single baseline muon. An uppercut is applied to the transverse mass (m_T) to filter out events from the $W \rightarrow \mu\nu$ process. The m_T is defined as

$$m_T = \sqrt{2p_T(\ell)E_T^{\text{miss}}(1 - \cos \Delta\phi(\ell, \mathbf{p}_T^{\text{miss}}))}, \quad (7.2)$$

where $p_T(\ell)$ corresponds to the p_T of the lepton. The m_T distribution is shown in Figure 7.7, where m_T is required to be less than 50 GeV to suppress the $W(\rightarrow \mu\nu)$ +jets process. In the $1\mu_{\text{base}}$ category, the same selection is applied to all physics objects and tracks as described in Section 6.5.1, except that $\mathbf{p}_T^{\text{recoil}}$ is used instead of $\mathbf{p}_T^{\text{miss}}$ for variables calculated using $\mathbf{p}_T^{\text{miss}}$. As discussed in Section 3.3.2, the E_T^{miss} trigger uses only the calorimeter information to determine the missing transverse energy. Since muons do not deposit substantial energy in the calorimeter, they are not considered in the E_T^{miss} trigger calculation. This means that events with a significant vectorial sum of missing transverse momentum and muon momentum appear as substantial missing transverse momentum in the E_T^{miss} trigger. As the $W(\rightarrow \tau\nu)$ +jets process produces a sizeable vectorial sum of missing transverse momentum and muon momentum, we require the E_T^{miss} trigger in the $1\mu_{\text{base}}$ category. Furthermore, it is essential to note that the track selection criteria employed in the $1\mu_{\text{base}}$ category are identical to the 0ℓ category.

To increase statistics, the track $S(d_0)$ requirement for the CRs is lowered to $S(d_0) > 3$. Although the $S(d_0)$ threshold differs from the SRs, the p_T^{recoil} requirement remains aligned. A single NF is applied to the τ decay tracks and is constrained by performing a simultaneous fit using the CRs in the 0ℓ and $1\mu_{\text{base}}$ categories. The CRs in the 0ℓ and $1\mu_{\text{base}}$ categories are denoted as CR- τ_h and CR- τ_ℓ , respectively.

To ensure that the extrapolation of the NF from the high- p_T range ($8 < p_T < 20$ GeV) to the low- p_T range ($2 < p_T < 5$ GeV) is valid, we have defined two additional VRs. These VRs have been defined by relaxing the track p_T requirement to a medium- p_T range ($5 < p_T < 8$ GeV). For both VRs, the p_T^{recoil} range has been reduced to $300 < p_T^{\text{recoil}} < 400$ GeV to minimize signal contamination. The two VRs in the $1\mu_{\text{base}}$ and 0ℓ categories are denoted as VR- τ_ℓ and VR- τ_h .

An additional NF is calculated for the extrapolation in the low- p_T^{recoil} range ($300 < p_T^{\text{recoil}} < 400$ GeV). The NF is measured in the high- p_T range of the low- p_T^{recoil} range and is then applied to the medium- p_T range of the low- p_T^{recoil} range. The NF calculated in the low- p_T^{recoil} range is only used to validate the extrapolation and is not applied to the SRs. Therefore, the names of the CRs are prefixed with ‘‘CR2-’’. The CRs in the high- p_T range of the $1\mu_{\text{base}}$ and 0ℓ categories are named CR2- τ_ℓ and CR2- τ_h , respectively.

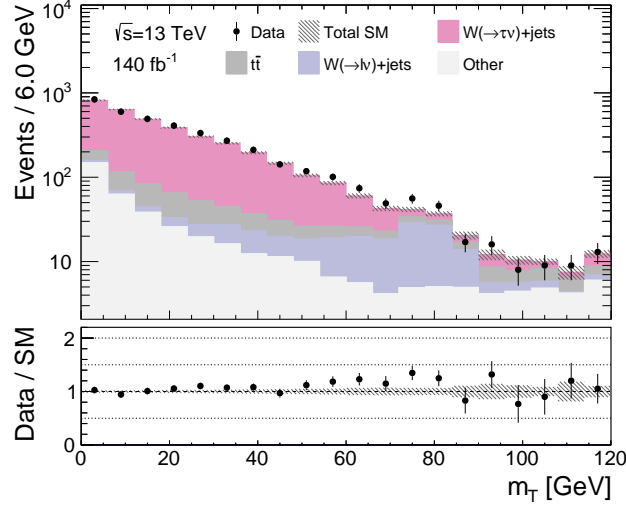


Figure 7.7: Distribution of m_T in the $1\mu_{\text{base}}$ category. Selections to signal tracks are not applied. The bottom panel shows the ratio of the observed data and background yield estimated directly from simulation samples. The “Other” category includes contributions from $Z(\rightarrow \nu\bar{\nu})+\text{jets}$, $Z(\rightarrow \tau\tau)+\text{jets}$, di-boson, single top, $\gamma+\text{jets}$ and multijet processes.

Table 7.1: Applied selections for each CR and VR for calculation and validation of NFs. Only selections orthogonal to the SR are listed. The track-level preselections are omitted from the table since they are identical in all categories. The selections in the parentheses represent the selection corresponding to the CRs for the VRs.

Category	0ℓ			$1\mu_{\text{base}}$	
	<i>Preselections</i>				
$N(\ell_{\text{base}})$	= 0			= 1	
m_T [GeV]	-			< 50	
Region	SR	CR- τ_h	VR(CR2)- τ_h	CR- τ_ℓ	VR(CR2)- τ_ℓ
<i>Additional selections to define SRs, CRs, and VRs</i>					
p_T^{recoil} [GeV]	> 600	> 600	[300, 400]	> 600	[300, 400]
Track p_T [GeV]	[2, 5]	[8, 20]	[5, 8] ([8, 20])	[8, 20]	[5, 8] ([8, 20])
Track $S(d_0)$	> 8		> 3		> 3

To summarize, the definition of the CRs and VRs for the normalization of τ decay tracks is provided in Table 7.1. The background composition in the CRs and VRs is illustrated in Figures 7.8 and 7.9, respectively.

Figure 7.8: Pie-charts showing the background composition in the CRs for τ decay tracks, estimated directly from simulation samples. τ decay tracks are categorized into leptonic and hadronic τ decay tracks, denoted as the τ_{lep} track and the τ_{had} track, respectively. Background processes other than the τ decay tracks are merged into the “Other” category.

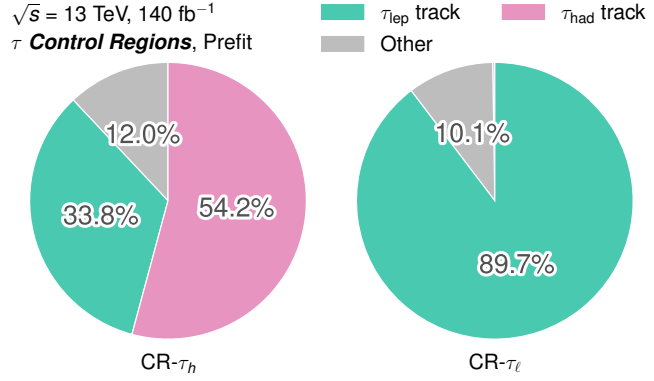
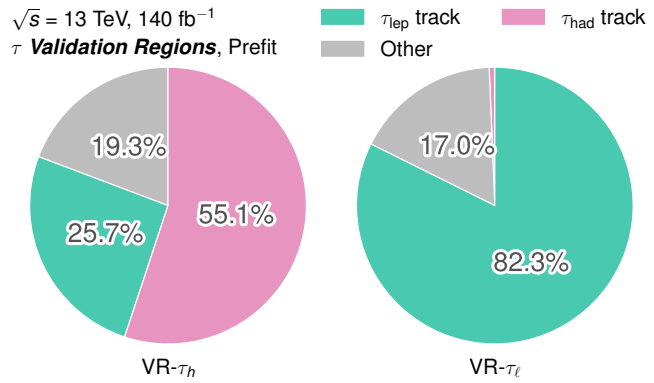


Figure 7.9: Pie-charts showing the background composition in the VRs for τ decay tracks, estimated directly from simulation samples. τ decay tracks are categorized into leptonic and hadronic τ decay tracks, denoted as the τ_{lep} track and the τ_{had} track, respectively. Background processes other than the τ decay tracks are merged into the “Other” category.



7.2.3 Fit results in Validation Regions

The yields in the VRs are estimated by multiplying the derived NFs by the yields of τ decay tracks obtained from MC simulation samples. The estimated yields and post-fit distributions in each VR are summarized in Table 7.2 and Figure 7.10, respectively. The observed data are in good agreement with the estimated numbers and distributions in all VRs. The track $S(d_0)$ distribution from the τ decay is well modeled for both hadronic and leptonic decays. Therefore, the measured NF in different track $S(d_0)$ ranges can be applied to the SR bins.

Furthermore, the extrapolation of the NF for τ decay tracks was validated using τ leptons generated from the top-pair production. The study resulted in the confirmation of the consistency between the estimated yields and the number of observed data. Supplementary information detailing the validation method utilizing top-pair production and the definitions of CRs and VRs are provided in Appendix G.

Table 7.2: Observed data and estimated yields using results from the background-only fit in the VRs. The errors include both statistical and systematic uncertainties.

Yields	VR- τ_h	VR- τ_ℓ
Observed	839	304
Fitted SM events	848 ± 24	308 ± 18
QCD track	75 ± 12	14 ± 14
W +jets (τ_{had} track)	449 ± 15	2.0 ± 1.0
W +jets (τ_{lep} track)	209 ± 7	244 ± 10
$t\bar{t}$	66 ± 12	24 ± 5
Other	50 ± 5	23.7 ± 2.9

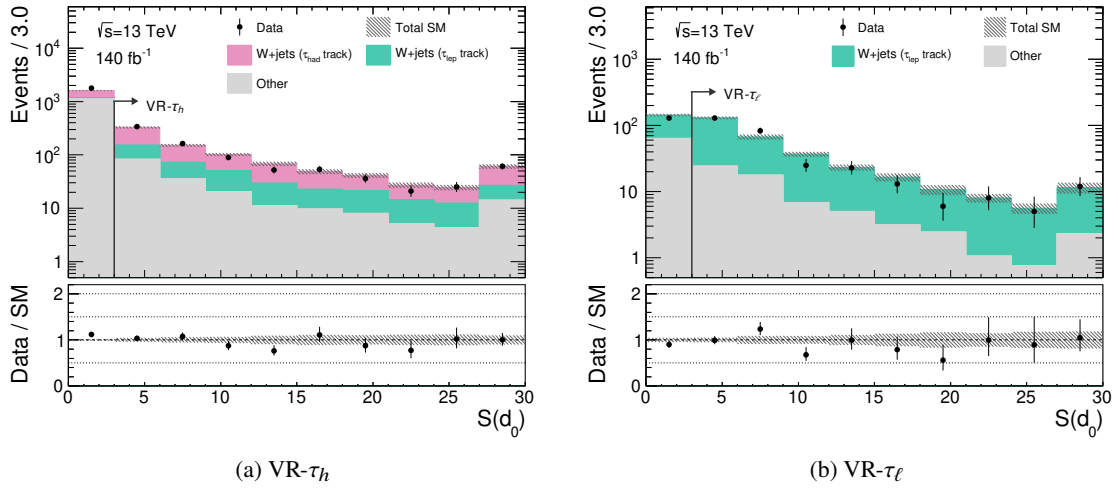


Figure 7.10: Post-fit track $S(d_0)$ distributions in VRs for estimating τ decay tracks. Each plot is drawn without applying selections to the illustrated variable. The bins enclosed by arrows indicate the respective regions. The dashed line illustrates signal simulation samples with different mass and mass differences. The hatched area corresponds to the combined systematic and MC statistical uncertainties. The bottom panel shows the ratio of the observed data yield and the estimated background yield. (a) Background processes other than the hadronic and leptonic τ decay tracks are merged into the “Other” category. (b) Background processes other than the leptonic τ decay tracks are merged into the “Other” category.

7.3 Full data-driven background estimation for QCD tracks

7.3.1 Overview

The contribution of QCD tracks in the $Z(\rightarrow \nu\bar{\nu})$ +jets and $W(\rightarrow \ell\nu)$ +jets processes is determined using a full data-driven approach. These processes involve the production of a single vector boson and are collectively known as the “V+jets” process. In the V+jets process, QCD tracks are not produced by the weak boson decay. Therefore, we can obtain equivalent distributions from other regions where the V+jets process dominates but with different decay topologies. Initially, the shape of the track $S(d_0)$ distribution is obtained from other V+jets processes and is referred to as the “ $S(d_0)$ template”. Once the $S(d_0)$ template is obtained, the number of events in the SRs is estimated by normalizing the $S(d_0)$ template in the low- $S(d_0)$ range ($S(d_0) < 8$), which is adjacent to the SRs. As discussed in Section 7.2, the $\mathbf{p}_T^{\text{recoil}}$ variable is also used for the estimation of QCD tracks, which represent the \mathbf{p}_T of the weak bosons.

The $Z(\rightarrow \ell\ell)$ +jets process is similar to the $Z(\rightarrow \nu\bar{\nu})$ +jets process, except that it contains two leptons and differs only in its decay mode. As a result, both processes exhibit the same weak boson kinematics at the truth level. However, the branching ratio of the $Z \rightarrow \ell\ell$ decay is smaller than the $Z \rightarrow \nu\bar{\nu}$ decay by a factor of five. This leads to fewer events and significant statistical errors on the extracted $S(d_0)$ template. To achieve sufficient statistics and reduce the uncertainty on the $S(d_0)$ template, we use regions dominated by the $W(\rightarrow \mu\nu)$ +jets process. We define a region enriched in the $W(\rightarrow \mu\nu)$ +jets process by requiring one signal muon, called the “1-muon category” (denoted as “1 μ ”). To validate the extrapolation of the $S(d_0)$ template from the 1 μ category, we use regions enriched in the $W(\rightarrow e\nu)$ +jets and $Z(\rightarrow \ell\ell)$ +jets processes. These regions require one signal electron, called the “1-electron category” (denoted as “1 e ”), and two signal leptons, referred to as the “2-lepton category” (denoted as “2 ℓ ”). To increase the statistics, we relax the selection for p_T^{recoil} to 300 GeV. As discussed in Section 8.3, the correlation between the $S(d_0)$ template and the weak boson p_T appears sufficiently small based on the MC simulations. This hypothesis is further validated using data.

The γ +jets process has a large production cross-section that produces an equivalent $S(d_0)$ template to those of events that produce a weak boson. To further validate that the $S(d_0)$ template is independent of the energy scale of the hard-scatter interaction, VRs enriched in the γ +jets process are constructed. Due to the larger cross-sections of the γ +jets process, these regions are expected to be predominantly populated by QCD tracks in the γ +jets process, which enables the validation of the $S(d_0)$ template in the high- p_T^{recoil} range. The new regions share the same p_T^{recoil} and $S(d_0)$ cuts used for the background estimation method but are defined as requiring the presence of precisely one signal photon, called the “1-photon category” (denoted as “1 γ ”).

For the estimation of QCD tracks, $\mathbf{p}_T^{\text{recoil}}$ is calculated by adding the \mathbf{p}_T of leptons and photons to the $\mathbf{p}_T^{\text{miss}}$. For each of the V+jets processes, the definition of $\mathbf{p}_T^{\text{recoil}}$ is shown in Table 7.3, and the topology of the events is illustrated in Figure 7.11.

Transfer Factors (TFs) are defined as the ratio between event yields in regions with $S(d_0) < 8$ (denoted as region “B”), and the $S(d_0)$ regions corresponding to the two SR bins (denoted as

Table 7.3: Definition of $\mathbf{p}_T^{\text{recoil}}$ in each category. $\mathbf{p}_T(\mu)$, $\mathbf{p}_T(e)$, and $\mathbf{p}_T(\gamma)$ represent the transverse momentum of the signal muon, electron, and photon, respectively. $\mathbf{p}_T(\ell_1)$ and $\mathbf{p}_T(\ell_2)$ represent the transverse momentum of the leading and sub-leading signal lepton, respectively.

Category	Purpose	Dominant process	Definition of $\mathbf{p}_T^{\text{recoil}}$
0ℓ	SRs	$Z(\rightarrow \nu\bar{\nu})+\text{jets}$	$\mathbf{p}_T^{\text{miss}}$
1μ	Measurement of TFs	$W(\rightarrow \mu\nu)+\text{jets}$	$\mathbf{p}_T^{\text{miss}} + \mathbf{p}_T(\mu)$
$1e$	Validation of TFs	$W(\rightarrow e\nu)+\text{jets}$	$\mathbf{p}_T^{\text{miss}} + \mathbf{p}_T(e)$
2ℓ	Validation of TFs	$Z(\rightarrow \ell\ell)+\text{jets}$	$\mathbf{p}_T^{\text{miss}} + \mathbf{p}_T(\ell_1) + \mathbf{p}_T(\ell_2)$
1γ	Validation of TFs	$\gamma+\text{jets}$	$\mathbf{p}_T^{\text{miss}} + \mathbf{p}_T(\gamma)$

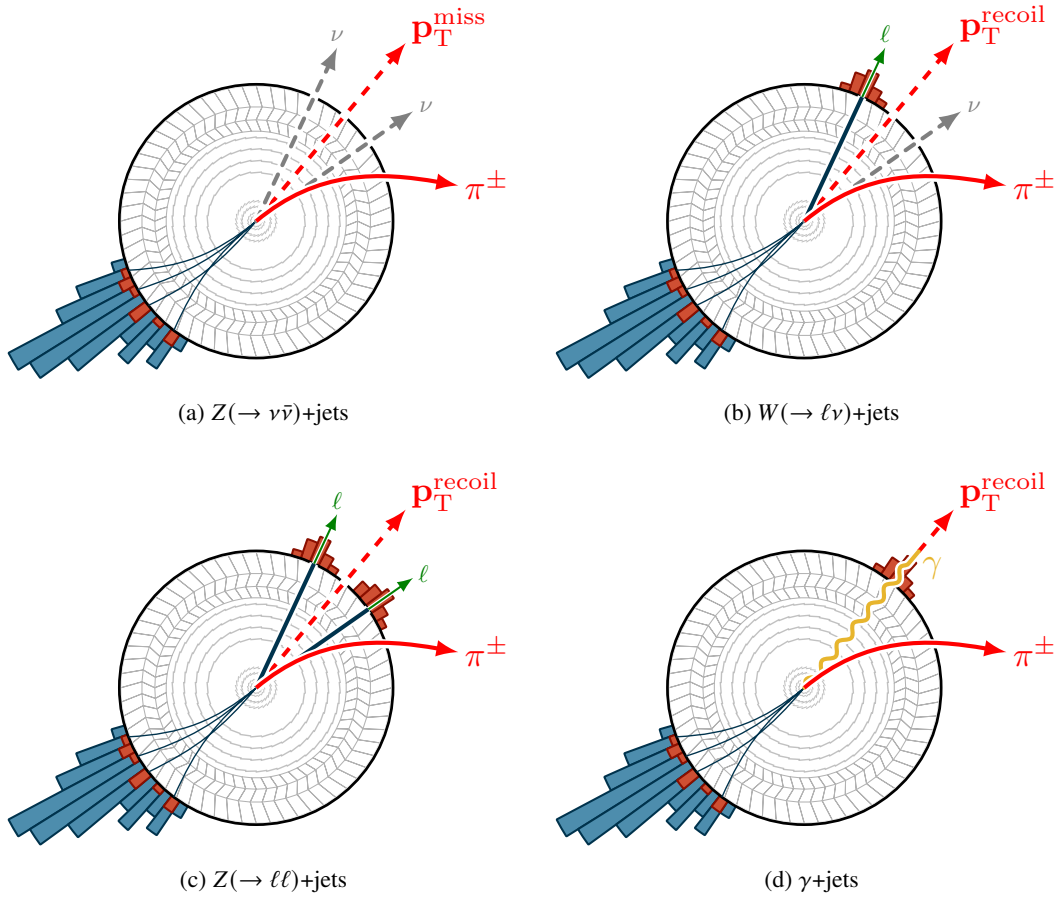
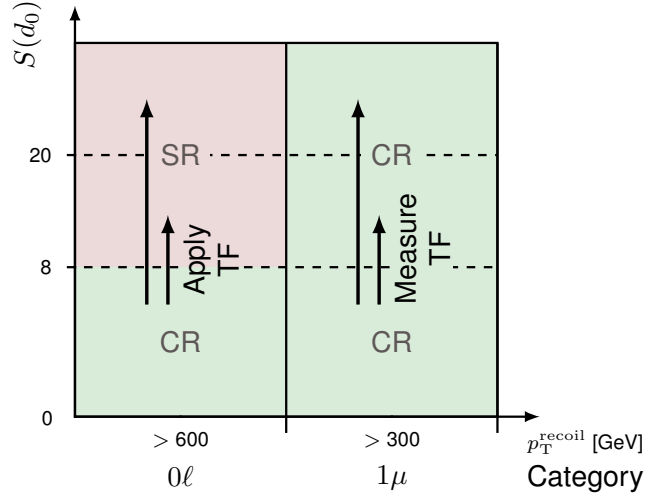


Figure 7.11: Schematic of the event topology among different $V+\text{jets}$ processes in the ATLAS detector. The outer part of the circle shows the calorimeter, while the inside part shows the ID. The red and blue bars represent the energy measured by the hadronic and electromagnetic calorimeters, respectively. The thick blue lines indicate tracks from leptons that must be removed from the event to ensure the same event topology across different $V+\text{jets}$ processes. Leptons and photons also deposit energy into the calorimeter but need not be removed since signal tracks are defined without using calorimeter information.

Figure 7.12: Schematic of the region definitions in the 0ℓ and 1μ category. The regions with $S(d_0) > 8$ are divided into two bins with an $S(d_0)$ threshold at 20. The red (green) area shows the SRs (CRs) used to estimate the QCD tracks. The TFs for each $S(d_0)$ bin are calculated by taking the ratio between the CRs in the 1μ category, as indicated by the two arrows. The TFs are then multiplied by the CR yield in the 0ℓ category to estimate the QCD track yields in the SRs.



region “A”). The shape of the $S(d_0)$ template is embedded in the TFs. The TFs for QCD tracks are measured in these CRs, defined as

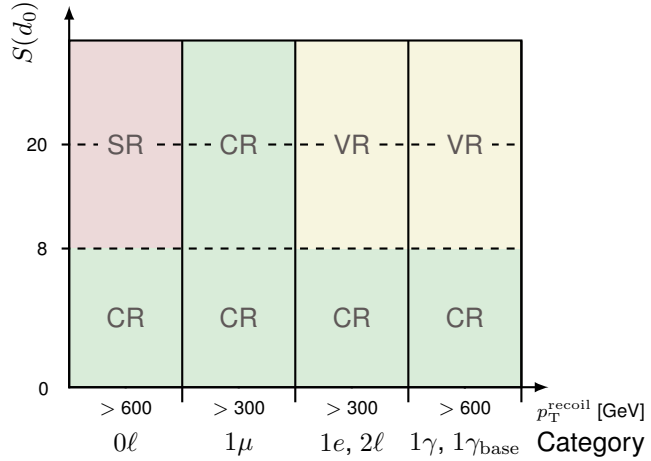
$$\text{TF}_{B \rightarrow A} = \frac{N_{\text{data}}^A - N_{\text{non-QCDtrack}}^A}{N_{\text{data}}^B - N_{\text{non-QCDtrack}}^B}, \quad (7.3)$$

where $N_{\text{data}}^{A(B)}$ represent the observed data in region A (B). $N_{\text{non-QCDtrack}}^{A(B)}$ represent the expected total yield from the non-QCD track background, including the signal process in region A (B). Figure 7.12 shows a schematic diagram of the background estimation strategy using the 1μ and 0ℓ categories, where the 0ℓ category is the region defined by applying the preselections discussed in Section 6.5.1. To estimate the number of QCD tracks in the SRs, the TFs measured in the 1μ category are multiplied by the number of data events, subtracting other processes estimated by simulation, in the low $S(d_0)$ region ($S(d_0) < 8$) adjacent to the SRs. Following the SR definitions discussed in Section 6.5.2, regions with $S(d_0) > 8$ are divided into two bins.

In the 1γ category, the purity of the γ +jets process is about 70% and the remaining 30% contribution is from the multijet process. Since we confirmed that the $S(d_0)$ templates for the γ +jets and multijet processes are equivalent using MC simulations, we can validate the TFs in the 1γ category. To verify that both the γ +jets and the multijet process have similar $S(d_0)$ templates with data, we defined additional regions enriched in the multijet process. These regions are defined by requiring a single baseline photon, which does not pass the signal requirement, referred to as the “1-baseline photon category” (denoted as “ $1\gamma_{\text{base}}$ ”).

In the CRs and VRs defined for the estimation of the QCD tracks, the contribution of the τ decay tracks is sufficiently small. Therefore, the yield of τ decay tracks is obtained directly from MC simulations. The background estimation strategy for QCD tracks discussed in this section is summarized below.

Figure 7.13: Schematic of the region definitions for validating the measured TFs. The regions with $S(d_0) > 8$ are divided into two bins with an $S(d_0)$ threshold at 20. The yellow area shows the VRs used to estimate the QCD tracks.



- The $S(d_0)$ template is extracted from data in the 1μ category, enriched in the $W(\rightarrow \mu\nu)$ +jets process, to calculate the TF for each SR bin.
- The TFs are validated in the $1e$ and 2ℓ category, enriched in the $W(\rightarrow e\nu)$ +jets and $Z(\rightarrow \ell\ell)$ +jets processes. The regions are defined in the low- p_T^{recoil} range to increase statistics.
- To validate the TFs in a high- p_T^{recoil} range, the 1γ category, enriched in the γ +jets process, is utilized.
- To verify that γ +jets and multijet processes have similar $S(d_0)$ templates, the $1\gamma_{\text{base}}$ category, enriched in the multijet process, is utilized.

Figure 7.13 shows a schematic diagram of the validation strategy for the measured TFs. The definition of each region used to measure and validate the TFs is described below.

7.3.2 Preselection

The same selection is applied to all physics objects and tracks as described in Section 6.5.1, except that $\mathbf{p}_T^{\text{recoil}}$ is used instead of $\mathbf{p}_T^{\text{miss}}$ for variables calculated using $\mathbf{p}_T^{\text{miss}}$. The $\mathbf{p}_T^{\text{recoil}}$ topology is expected to be similar between regions enriched in the $Z(\rightarrow \ell\ell)$ +jets, $W(\rightarrow \ell\nu)$ +jets, γ +jets, and multijet processes. The additional preselections applied to each category are summarized below. The preselections applied to each category introduced in this section are summarized in Table 7.4 compared to the 0ℓ category.

1-muon & 1-electron category The $W(\rightarrow \mu\nu)$ +jets ($W(\rightarrow e\nu)$ +jets) enriched region is defined by requiring a single signal (electron) with $p_T > 10$ GeV ($p_T > 30$ GeV) and m_T around the W boson mass, as illustrated in Figure 7.14. In the 1μ and $1e$ categories, $\mathbf{p}_T^{\text{recoil}}$ is defined as

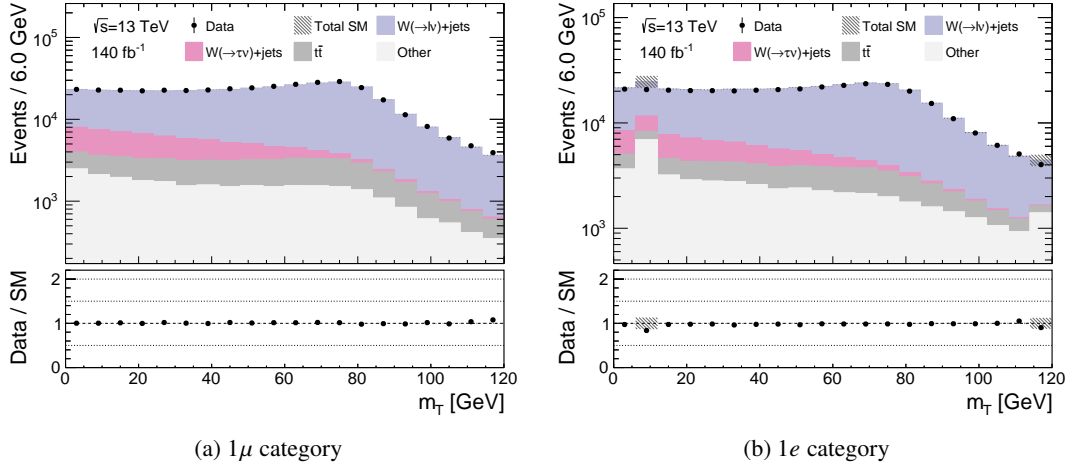


Figure 7.14: Distribution of m_T in the 1μ and $1e$ categories. Signal track selections are not applied. The bottom panel shows the ratio of the observed data to the background yield estimated directly from the simulation samples. The “Other” category includes contributions from Z +jets, di-boson, single top, γ +jets, and multijet processes.

the vector sum of the transverse momentum of the lepton and the missing transverse momentum. The E_T^{miss} (single-electron) trigger is required for events with signal muons (electrons).

2-lepton category The $Z(\rightarrow \ell\ell)$ +jets enriched region is defined by requiring two signal leptons and an invariant mass ($m_{\ell\ell}$) around the Z boson mass, as shown in Figure 7.15. In the 2ℓ category, $\mathbf{p}_T^{\text{recoil}}$ is defined as the vector sum of the transverse momentum of the dilepton system and the missing transverse momentum. The E_T^{miss} (single-electron) trigger is required for events with signal muons (electrons).

1-baseline(signal) photon category The γ +jets enriched region is defined by requiring a single signal photon. The multijet enriched region requires a single baseline photon that does not satisfy the signal photon criteria. Both regions require a photon with $p_T > 200$ GeV. In the 1γ and $1\gamma_{\text{base}}$ categories, $\mathbf{p}_T^{\text{recoil}}$ is defined as the vector sum of the transverse momentum of the photon and the missing transverse momentum. The single-photon trigger is required for events with photons.

Common selections In each category, tracks associated with leptons or photons are removed from the event to mimic the event topology in the 0ℓ category. Another difference between the 0ℓ category is from photon conversion tracks around the leptons. Leptons emit a photon by bremsstrahlung and can convert at any point in the ID, leading to tracks with significant impact parameters, especially from electrons as shown in Figure 7.16(a). With photon conversion tracks in the 1μ , $1e$, and 2ℓ categories, the TFs cannot be correctly calculated nor validated. By requiring

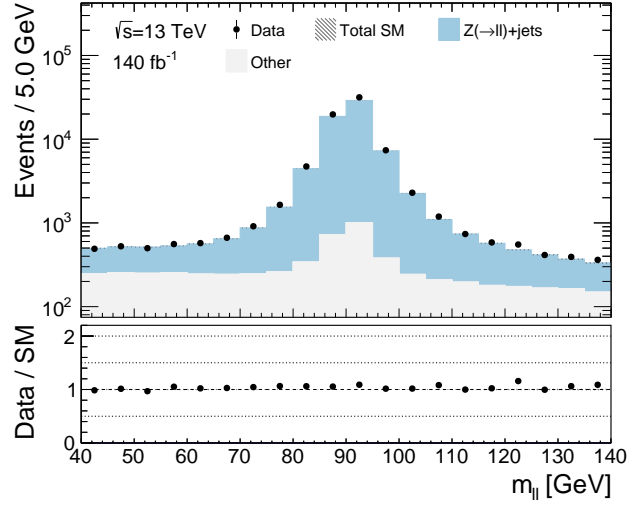


Figure 7.15: Distribution of $m_{\ell\ell}$ in the 2ℓ category. Selections to signal tracks are not applied. The bottom panel shows the ratio of the observed data and background yield estimated directly from simulation samples. The “Other” category includes contributions from W +jets, $Z(\rightarrow \tau\tau)$ +jets, di-boson, single top, γ +jets, and multijet processes.

a minimum ΔR of 0.04 between tracks and leptons, almost all photon conversion tracks in the 2ℓ category are eliminated, with a reduction rate of about 98%, as shown in Figure 7.16(b).

7.3.3 Control Regions and Validation Regions

Each category is divided into three $S(d_0)$ bins to measure and validate the TFs, equivalent to the $S(d_0)$ binning in the 0ℓ category. Due to the large statistics, the 1γ and $1\gamma_{\text{base}}$ categories are defined in the high- $p_{\text{T}}^{\text{recoil}}$ range ($p_{\text{T}}^{\text{recoil}} > 600$ GeV).

The TFs are measured by CRs in the 1μ category, referred to as CR- 1μ , CR- 1μ -Low, and CR- 1μ -High, where the additional suffix corresponds to the $S(d_0)$ range used to define SR-Low and SR-High. The TFs are applied to the data measured in the $S(d_0) < 8$ bin of the $1e$, 2ℓ , 1γ , and $1\gamma_{\text{base}}$ categories, referred to as CR- $1e$, CR- 2ℓ , CR- 1γ , CR- $1\gamma_{\text{base}}$, respectively. The expected background yields are extrapolated to the $8 < S(d_0) < 20$ ($20 < S(d_0)$) bin, referred to as VR- $1e$ -Low(-High), VR- 2ℓ -Low(-High), VR- 1γ -Low(-High), and VR- $1\gamma_{\text{base}}$ -Low(-High).

The background composition in the 1ℓ and 2ℓ (1γ and $1\gamma_{\text{base}}$) categories is illustrated in Figure 7.17(a) (Figure 7.17(b)). The definition of the CRs and VRs for the TFs of the QCD tracks is summarized in Table 7.4.

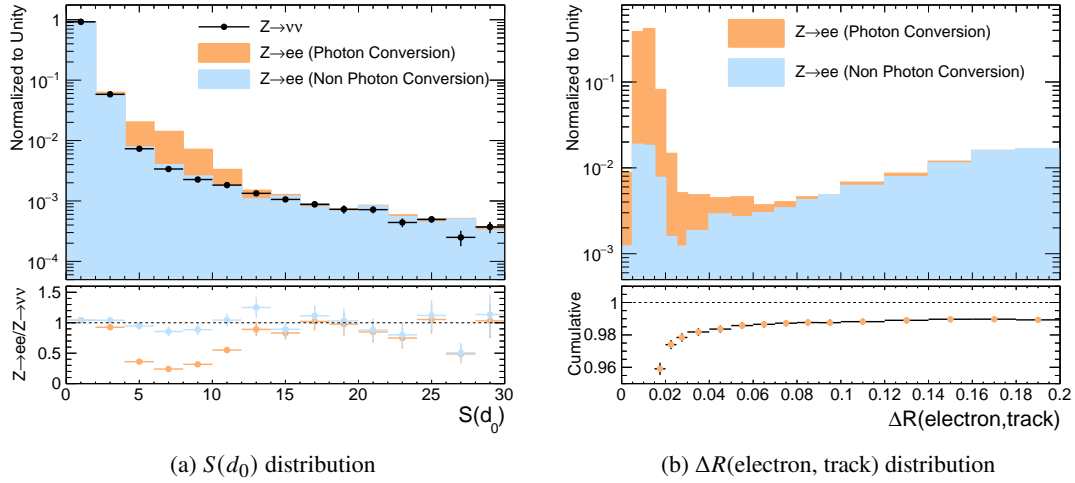
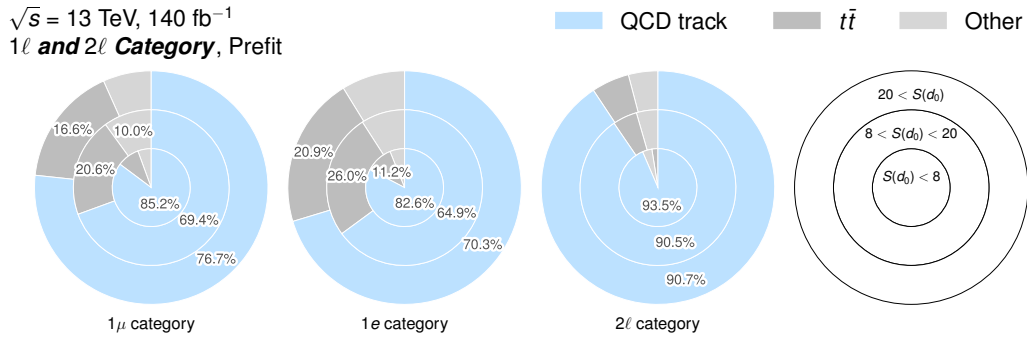


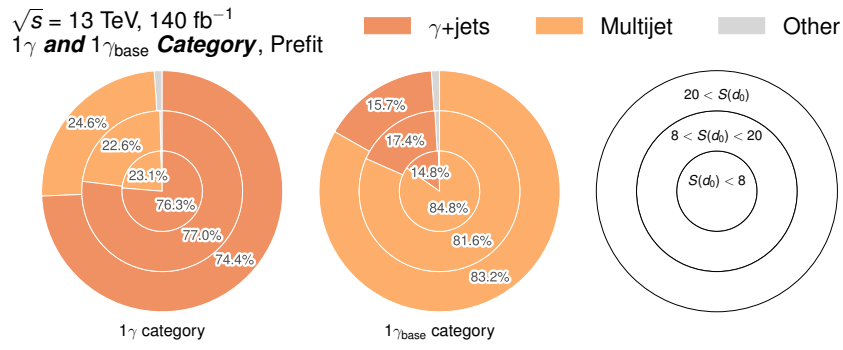
Figure 7.16: $S(d_0)$ and $\Delta R(\text{electron, track})$ distribution of tracks in the $2e$ category, categorized into photon conversion and non-photon conversion tracks. (a) The black dots in the upper plot represent the tracks $S(d_0)$ distribution from the $Z(\rightarrow \nu\bar{\nu})+\text{jets}$ process. The bottom plot shows the ratio between tracks from the $Z(\rightarrow \nu\bar{\nu})+\text{jets}$ and $Z(\rightarrow ee)+\text{jets}$ process. The red dots indicate where the ratio is taken, including the photon conversion tracks, and the blue dots indicate the case where it is not included. (b) The $\Delta R(\text{electron, track})$ distribution is produced by requiring $S(d_0) > 3$ for signal candidate tracks to highlight the impact of the photon conversion tracks. The bottom plot shows the accumulated fraction of photon conversion tracks from left to right.

Table 7.4: Applied selections for each CR and VR for the calculation and validation of the TFs. Only selections orthogonal to the SRs are listed. The track-level preselections are omitted from the table since they are identical in all categories. The selections in the parentheses represent the selection corresponding to the CRs.

Category	0ℓ	1μ	$1e$	2ℓ	1γ
<i>Preselections</i>					
Trigger	$E_T^{\text{miss}} = 0$	$E_T^{\text{miss}} = 1$	Single- e	E_T^{miss} or Single- e	Single- γ
$N(\ell)$	= 0	= 1	= 1	= 2	= 0
$N(\gamma)$	-	-	-	-	= 1
$p_T(\ell_1)$ [GeV]	-	> 10	> 30	$p_T(\mu) > 10$ ($p_T(e) > 30$)	-
$p_T(\ell_2)$ [GeV]	-	-	-	> 10	-
$p_T(\gamma)$ [GeV]	-	-	-	-	> 200
m_T [GeV]	-	[56, 106]	[56, 106]	-	-
m_{ll} [GeV]	-	-	-	[66.2, 116.2]	-
Region	SR(CR- 0ℓ)	CR- 1μ	VR(CR)- $1e$	VR(CR)- 2ℓ	VR(CR)- 1γ
<i>Additional selections to define SRs, CRs, and VRs</i>					
p_T^{recoil} [GeV]	> 600	> 300	> 300	> 300	> 600
Track $S(d_0)$	> 8 (< 8)	-	> 8 (< 8)	> 8 (< 8)	> 8 (< 8)



(a) Background composition in the 1μ , $1e$, and 2ℓ category



(b) Background composition in the 1γ , $1\gamma_{\text{base}}$ category

Figure 7.17: Pie-charts showing the background composition in the (a) 1μ , $1e$, and 2ℓ category and (b) 1γ , $1\gamma_{\text{base}}$ category, estimated directly from simulation samples. (a) The “Other” category includes contributions from $Z(\rightarrow \tau\tau)$ +jets, di-boson, single top, γ +jets, and multijet processes. (b) The “Other” category includes contributions from Z +jets, W +jets, di-boson, single top, and $t\bar{t}$ processes.

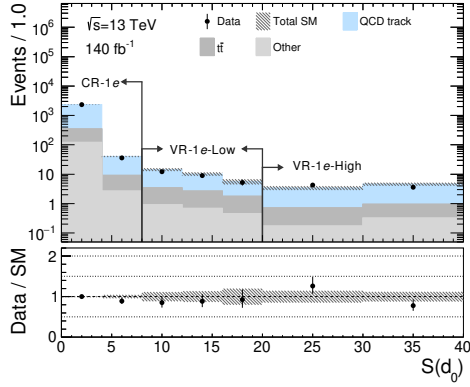
7.3.4 Fit results in Validation Regions

The yields in the VRs are estimated by multiplying the derived TFs with the observed data in the adjacent low $S(d_0)$ bin with $S(d_0) < 8$. The estimated yields and post-fit distributions in each VR are summarized in Table 7.5 and Figures 7.18 to 7.21. The observed data are in good agreement with the estimated numbers and distributions in all VRs.

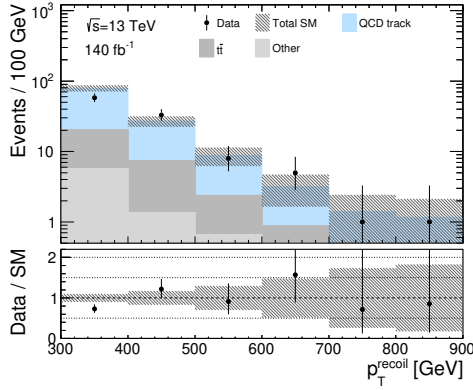
Table 7.5: Observed data and estimated yields using results from the background-only fit in the (a) High $S(d_0)$ and (b) Low $S(d_0)$ VRs. The suffixes -High and -Low representing the $S(d_0)$ bins are omitted from the naming convention. The errors include both statistical and systematic uncertainties.

(a) High $S(d_0)$ VRs for validation of the TFs				
Yields	VR-2 ℓ	VR-1 e	VR-1 γ	VR-1 γ_{base}
Observed	39	79	33	21
Fitted SM events	49 ± 7	80 ± 10	28 ± 4	20.5 ± 3.1
QCD track	46 ± 7	64 ± 10	28 ± 4	20.4 ± 3.1
W +jets (τ_{had} track)	–	0.16 ± 0.12	–	–
W +jets (τ_{lep} track)	–	< 0.1	–	–
$t\bar{t}$	1.5 ± 0.9	11.7 ± 2.8	–	< 0.1
Other	1.20 ± 0.35	4.7 ± 1.0	–	–

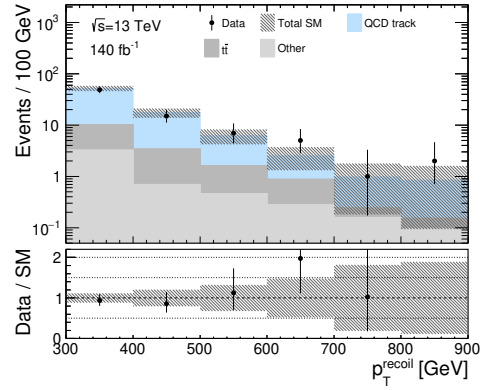
(b) Low $S(d_0)$ VRs for validation of the TFs				
Yields	VR-2 ℓ	VR-1 e	VR-1 γ	VR-1 γ_{base}
Observed	58	106	40	26
Fitted SM events	69 ± 7	121 ± 11	39 ± 5	28.5 ± 3.3
QCD track	65 ± 8	89 ± 11	39 ± 5	28.3 ± 3.3
W +jets (τ_{had} track)	–	< 1	< 0.1	–
W +jets (τ_{lep} track)	–	< 1	< 0.1	< 0.1
$t\bar{t}$	2.3 ± 1.1	23 ± 6	< 0.1	< 0.1
Other	2.1 ± 0.5	7.9 ± 1.5	< 0.1	0.14 ± 0.14



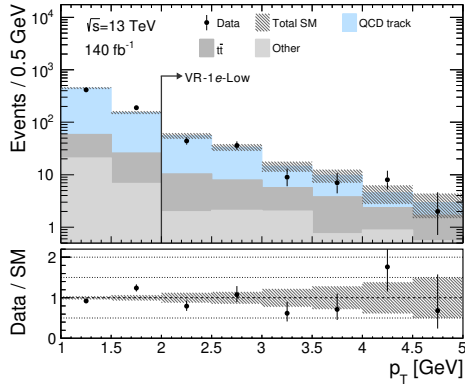
(a) Track $S(d_0)$ distribution



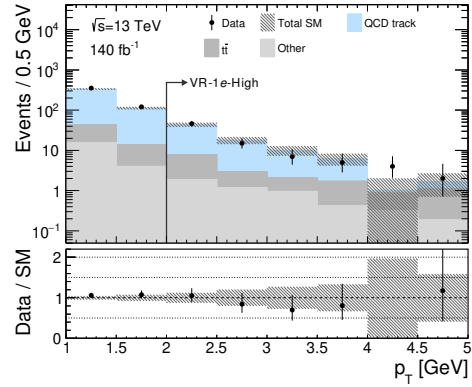
(b) p_T^{recoil} distribution (Low $S(d_0)$)



(c) p_T^{recoil} distribution (High $S(d_0)$)

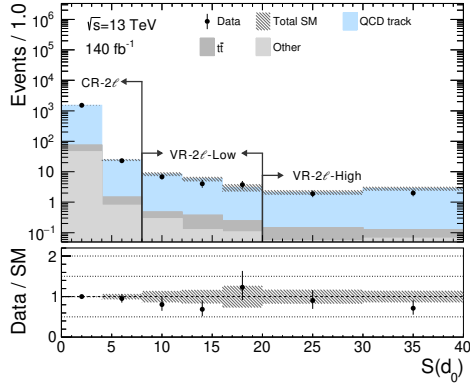


(d) Track p_T distribution (Low $S(d_0)$)

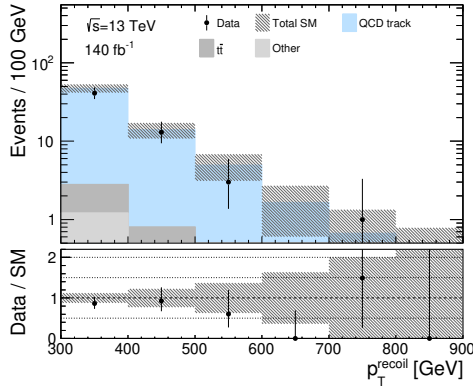


(e) Track p_T distribution (High $S(d_0)$)

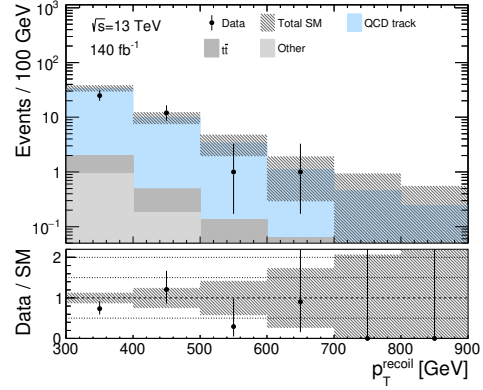
Figure 7.18: Post-fit distributions for VRs in the $1e$ category. Each plot is drawn without applying selections to the illustrated variable. The bins enclosed by arrows indicate the respective regions. The dashed line illustrates signal simulation samples with different mass and mass differences. The hatched area corresponds to the combined systematic and MC statistical uncertainties. The bottom panel shows the ratio of the observed data yield to the estimated background yield. The “Other” category includes contributions from Z +jets, di-boson, single top, γ +jets, and multijet processes.



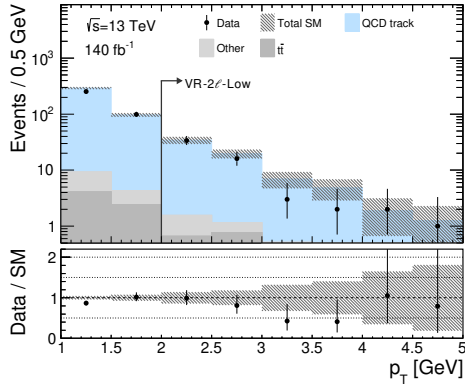
(a) Track $S(d_0)$ distribution



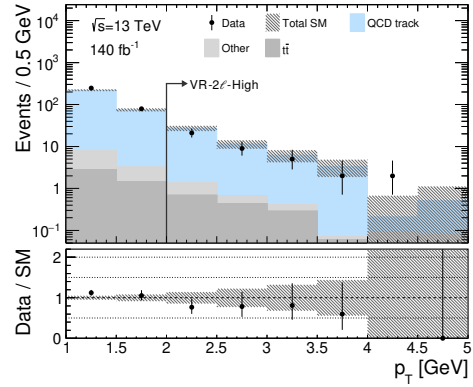
(b) p_T^{recoil} distribution (Low $S(d_0)$)



(c) p_T^{recoil} distribution (High $S(d_0)$)

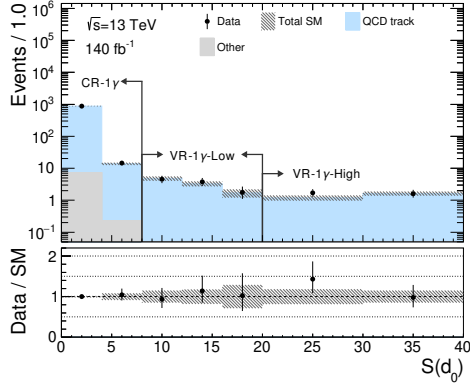


(d) Track p_T distribution (Low $S(d_0)$)

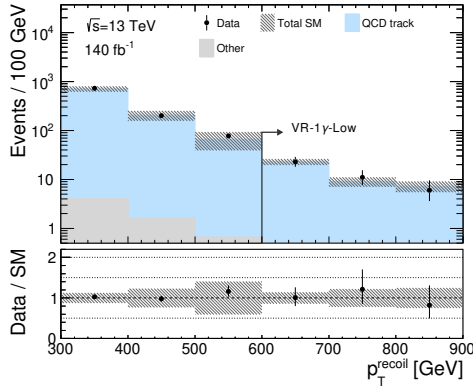


(e) Track p_T distribution (High $S(d_0)$)

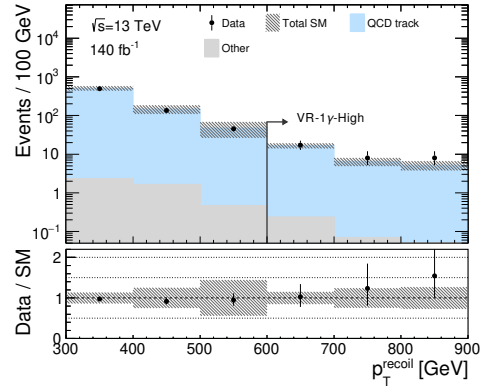
Figure 7.19: Post-fit distributions for VRs in the 2ℓ category. Each plot is drawn without applying selections to the illustrated variable. The bins enclosed by arrows indicate the respective regions. The dashed line illustrates signal simulation samples with different mass and mass differences. The hatched area corresponds to the combined systematic and MC statistical uncertainties. The bottom panel shows the ratio of the observed data yield to the estimated background yield. The “Other” category includes contributions from W +jets, di-boson, single top, γ +jets, and multijet processes.



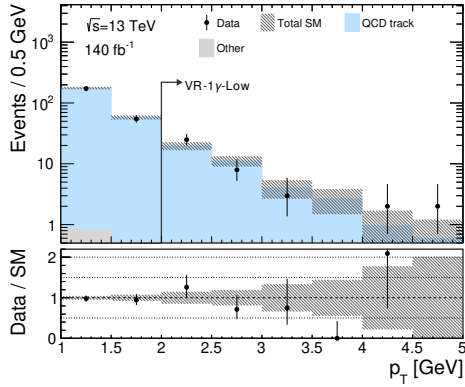
(a) Track $S(d_0)$ distribution



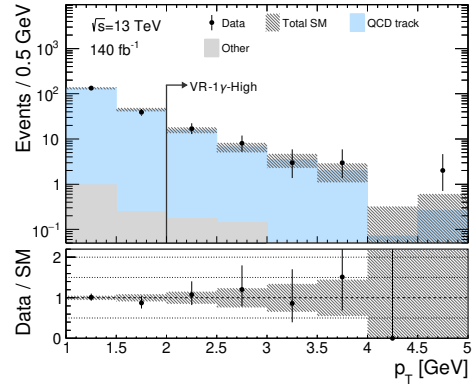
(b) p_T^{recoil} distribution (Low $S(d_0)$)



(c) p_T^{recoil} distribution (High $S(d_0)$)

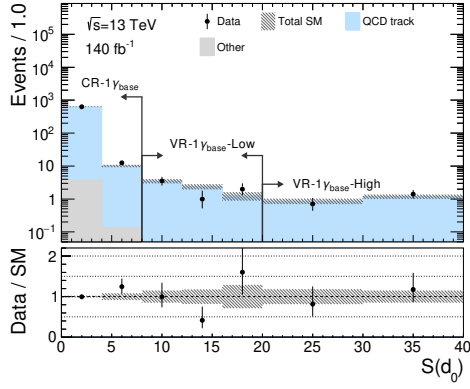


(d) Track p_T distribution (Low $S(d_0)$)

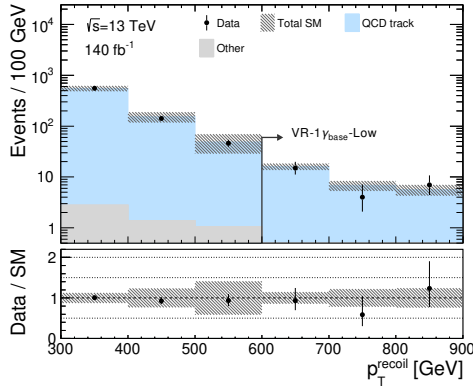


(e) Track p_T distribution (High $S(d_0)$)

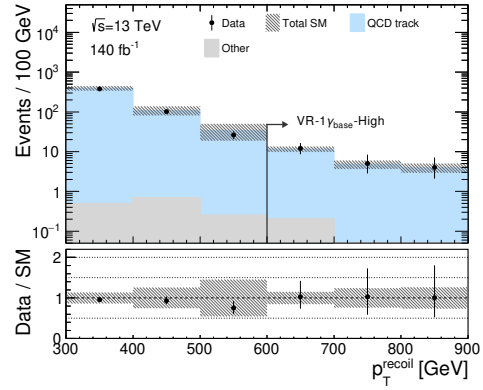
Figure 7.20: Post-fit distributions for VRs in the 1 γ category. Each plot is drawn without applying selections to the illustrated variable. The bins enclosed by arrows indicate the respective regions. The dashed line illustrates signal simulation samples with different mass and mass differences. The hatched area corresponds to the combined systematic and MC statistical uncertainties. The bottom panel shows the ratio of the observed data yield to the estimated background yield. The “Other” category includes contributions from Z +jets, W +jets, di-boson, single top, and $t\bar{t}$ processes.



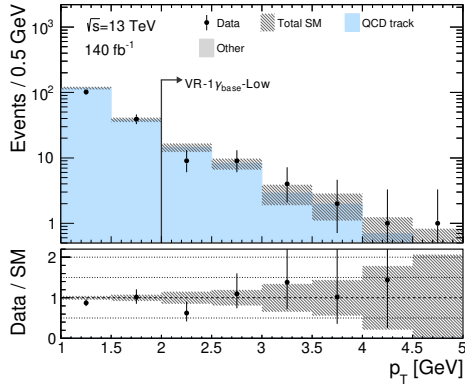
(a) Track $S(d_0)$ distribution



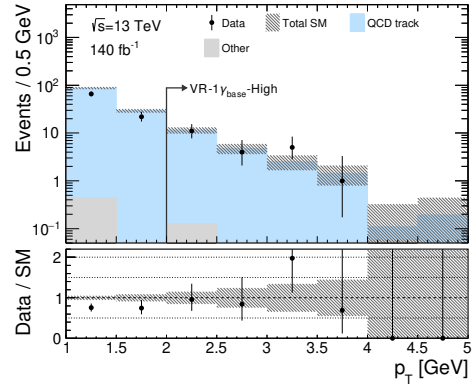
(b) p_T^{recoil} distribution (Low $S(d_0)$)



(c) p_T^{recoil} distribution (High $S(d_0)$)



(d) Track p_T distribution (Low $S(d_0)$)



(e) Track p_T distribution (High $S(d_0)$)

Figure 7.21: Post-fit distributions for VRs in the $1\gamma_{\text{base}}$ category. Each plot is drawn without applying selections to the illustrated variable. The bins enclosed by arrows indicate the respective regions. The dashed line illustrates signal simulation samples with different mass and mass differences. The hatched area corresponds to the combined systematic and MC statistical uncertainties. The bottom panel shows the ratio of the observed data yield to the estimated background yield. The “Other” category includes contributions from Z +jets, W +jets, di-boson, single top, and $t\bar{t}$ processes.

7.4 Validation of the combined estimation

As discussed in Sections 7.3 and 7.2, background estimation methods are validated using different boson production or decay modes for QCD tracks and adjusting at least two selections on kinematic variables for τ decay tracks. To validate the background estimation methods in a region with kinematics closer to the SRs, we defined a region where only the E_T^{miss} condition is slightly relaxed to $300 < E_T^{\text{miss}} < 400$ GeV with respect to the SRs, as illustrated in Figure 7.22. The background composition in the 0ℓ category is illustrated in Figure 7.23. The composition of the QCD tracks and τ decay tracks in these VRs, denoted as VR- 0ℓ -Low and VR- 0ℓ -High, are almost equal to the composition in the SRs. Therefore, we can verify the validity of each background estimation method in these VRs.

To estimate the number of QCD tracks, the TFs are applied to the number of observed data, subtracting the contribution of non-QCD track background events in the region with $S(d_0) < 8$, denoted as CR- 0ℓ -Low E_T^{miss} . τ decay tracks are estimated by multiplying the NF measured in CR2- τ_ℓ and CR2- τ_h .

The estimated yields and post-fit distributions in each VR are summarized in Table 7.6 and Figure 7.24, respectively. The observed data is in good agreement with the estimated numbers and distributions across all VRs.

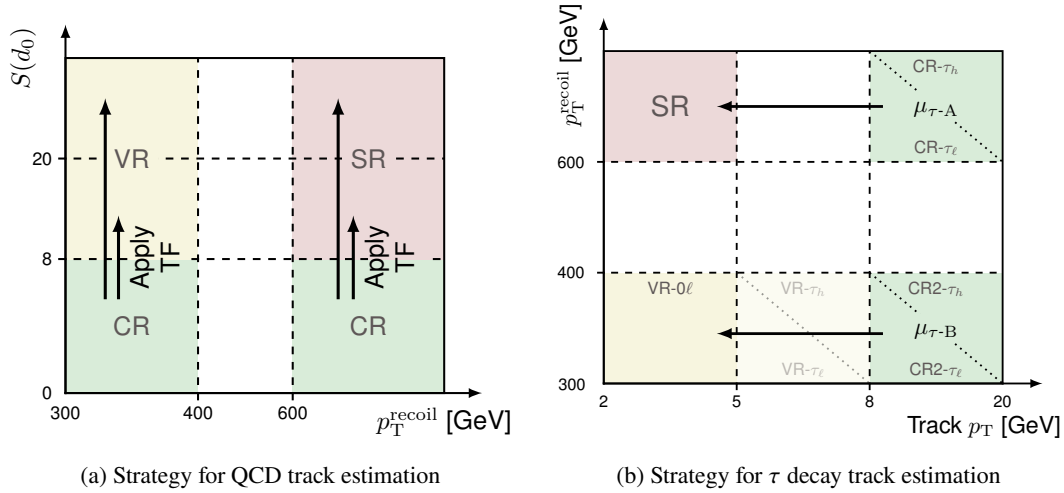


Figure 7.22: Schematic of the region definitions of VRs near the SRs, filled in yellow. The red (green) area shows the SRs (CRs) utilized for the estimation of the QCD tracks in Figure (a) and τ decay tracks in Figure (b). To reduce signal contamination, an upper limit on the p_T^{recoil} range is set at 400 GeV. (a) Regions with $S(d_0) > 8$ are divided into two bins with an $S(d_0)$ threshold at 20. The TFs for the QCD tracks are multiplied by the CR yield defined in the low- p_T^{recoil} range. (b) The NF for τ decay tracks are calculated in the low- p_T^{recoil} range and applied to the yields in the VRs.

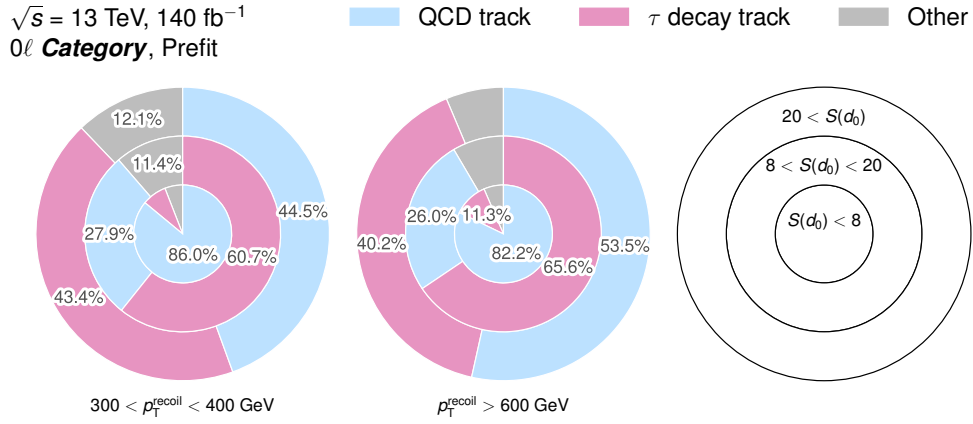
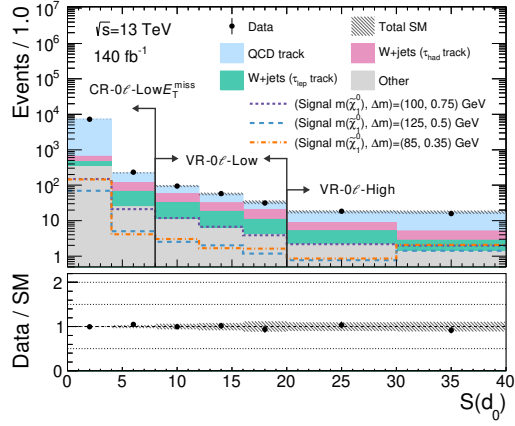


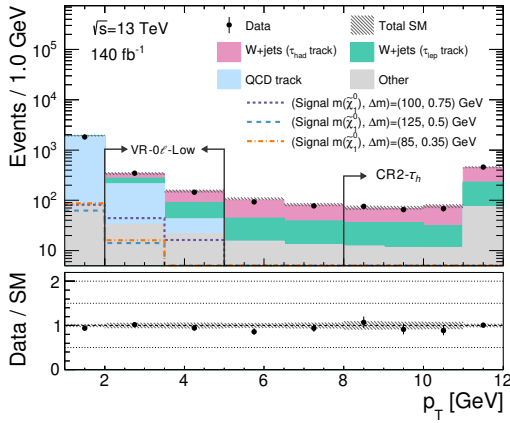
Figure 7.23: Pie-charts showing the background composition in the 0ℓ category, estimated directly from simulation samples. The “Other” category includes contributions from $Z(\rightarrow \tau\tau)$ +jets, γ +jets, QCD multijet, di-boson, single top and $t\bar{t}$ processes.

Table 7.6: Observed data and estimated yields using results from the background-only fit in the VRs. The errors include both statistical and systematic uncertainties.

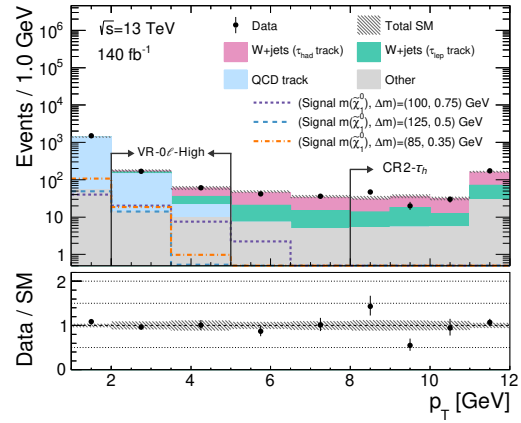
Yields	VR- 0ℓ -Low	VR- 0ℓ -High
Observed	736	343
Fitted SM events	740 ± 40	351 ± 33
QCD track	298 ± 35	213 ± 32
W +jets (τ_{had} track)	194 ± 10	59 ± 5
W +jets (τ_{lep} track)	165 ± 8	44.1 ± 3.4
$t\bar{t}$	45 ± 8	17.8 ± 3.5
Other	37 ± 4	17.2 ± 2.3



(a) Track $S(d_0)$ distribution



(b) Track p_T distribution (Low $S(d_0)$)



(c) Track p_T distribution (High $S(d_0)$)

Figure 7.24: Post-fit distributions for VRs near the SRs. Each plot is drawn without applying selections to the illustrated variable. The bins enclosed by arrows indicate the respective regions. The dashed line illustrates signal simulation samples with different mass and mass differences. The hatched area corresponds to the combined systematic and MC statistical uncertainties. The bottom panel shows the ratio of the observed data yield and the estimated background yield. The “Other” category includes contributions from $Z(\rightarrow \tau\tau)$ +jets, di-boson, single top, $t\bar{t}$, γ +jets, and multijet processes.

7.5 Summary

This section summarizes the results of the validation of the background estimation methods described in the previous sections. The significance quantifies the difference between the estimated background yields and the data, denoted as χ , and defined as

$$\chi = \frac{n_{\text{obs}} - n_{\text{exp}}}{\sigma_{\text{total}}}, \quad (7.4)$$

$$\sigma_{\text{total}} = \sqrt{\sigma_{\text{exp}}^2 + \sigma_{\text{obs}}^2}, \quad (7.5)$$

where n_{obs} and σ_{obs} are the observed yields and statistical uncertainties, n_{exp} and σ_{exp} are the expected yield and uncertainties derived from the systematic uncertainties discussed in Chapter 8. The yields and differences for each VR are visualized in Figure 7.25. In each VR, the expected and observed yields are consistent within the uncertainty.

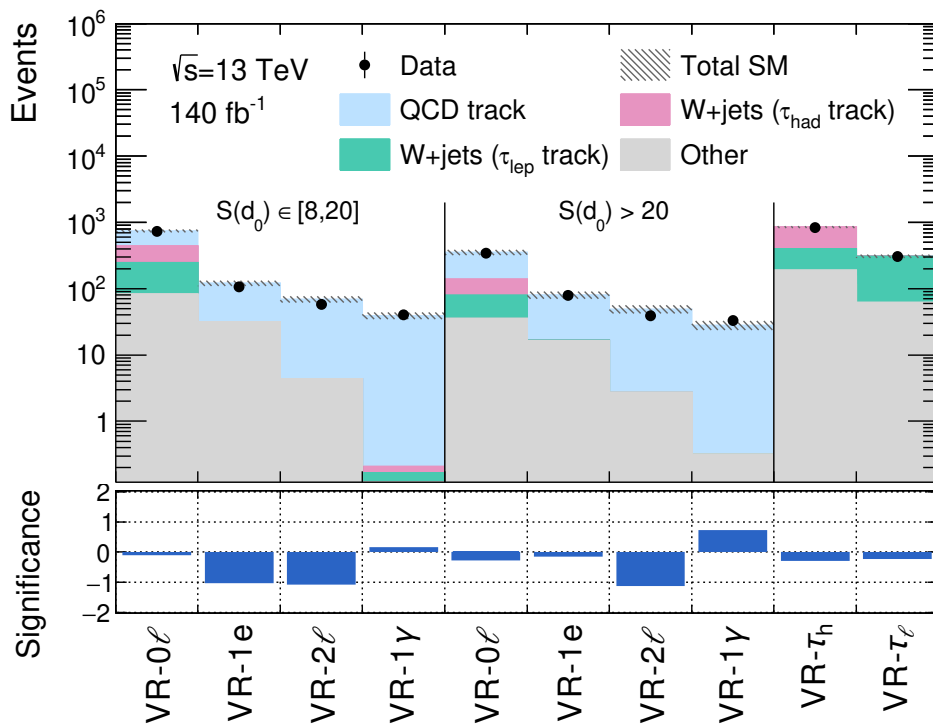


Figure 7.25: Overview of fit results in the VRs. The upper plot summarizes the observed and estimated yields for each VR, while the bottom plot illustrates the difference between the observed and estimated yields. The “Other” category includes contributions from $Z(\rightarrow \tau\tau)$ +jets, di-boson, single top, $t\bar{t}$, γ +jets, and multijet processes.

Chapter 8

Systematic Uncertainties

The uncertainty of the estimated background and signal yields is referred to as systematic uncertainties and is discussed in this chapter. This thesis considers three types of systematic uncertainties: theoretical modeling uncertainties, experimental uncertainties, and additional uncertainties arising from the adopted data-driven background estimation strategy discussed in Section 7.

8.1 Theoretical Uncertainty

Theoretical uncertainties arise from the choice of parameters used to generate MC simulation samples, as elaborated in Section 4.2. Varying the parameters has the effect of altering both the cross-section and the shape of the kinematic distribution. This analysis thoroughly evaluates the theoretical uncertainties for all signal and background processes.

As explained in Section 4.2.1, non-physical variables such as the factorization scale (μ_F) and the renormalization scale (μ_R) are set in the MC simulations. Uncertainties from μ_F and μ_R [111] are evaluated as the variation of the yields obtained by varying these parameters by a factor of 2.0 and 0.5. The PDF [112] and strong coupling constant (α_S) at a specific energy scale are obtained by extrapolating distributions from experiments to higher energy scales using the DGLAP evolution equation and the RGE, respectively. Therefore, experimental uncertainties and missing higher-order calculations in the equations are sources of uncertainties and are evaluated as the variation of the yields obtained using different PDFs and α_S values.

For $W(\rightarrow \tau\nu)+\text{jets}$, we also consider the following theoretical uncertainties. Since $W(\rightarrow \tau\nu)+\text{jets}$ is normalized using the control regions (CRs), the signal regions (SRs) and the validation regions (VRs) are only affected by the extrapolation of uncertainties from the CRs. In SHERPA, the energy scale to calculate the overlap between jets from matrix element calculation and parton shower is set to 20 GeV. The uncertainty is evaluated by comparing the yields obtained by varying the energy scale to 30 and 15 GeV. The resummation scale of soft gluon emissions is a potential source of uncertainty and is evaluated by varying the scale by a factor of 0.5 and 2.

$W(\rightarrow \tau\nu)+\text{jets}$ are calculated considering NLO QCD corrections, but the contribution of NLO EWK correction becomes more significant, especially in regions where the transverse momentum of weak bosons is high. Approximate NLO EW corrections are evaluated using the electroweak virtual approximation [113].

For signal samples, we also consider the following theoretical uncertainties. As discussed in Section 4.2.3, PYTHIA is tuned to match the distributions observed from the data, sensitive to underlying events, jet structure, and additional jet emissions. These uncertainties are considered by comparing the yields from samples generated by varying five types of parameters: one for underlying event effects, one for jet structure effects, and three for different aspects of extra jet production. In addition, theoretical uncertainties for the cross-section are also taken into account.

8.2 Experimental Uncertainty

Experimental uncertainty includes uncertainty in the calibration procedure to match physics objects to data and uncertainty in luminosity measurement and pileup. Sections 8.2.1 and 8.2.2 describe the uncertainties considered for jets and tracks. In the MC simulations, the pileup modeling is corrected to fit the data, and the uncertainty resulting from this procedure is explained in Section 8.2.3. Other uncertainties that contribute less than 1% to the yield of the SRs in this analysis are summarized in Section 8.2.4.

8.2.1 Jets

As explained in Section 5.3.1, the energy of the reconstructed jets is scaled to obtain the complete energy, and the resolution of the simulation samples is calibrated to match the data. Additionally, the jet vertex tagging algorithm is applied to mitigate pileup jets. For reconstructed jets, three types of uncertainty are taken into account: Jet Energy Scale (JES), Jet Energy Resolution (JER), and Jet Vertex Tagger (JVT) uncertainty. Only the uncertainty from JES contributes over 2% to the SRs. The remaining uncertainties are listed in Appendix H. More details are given in Ref. [101, 114].

Jet Energy Scale (JES) As discussed in Section 5.3.1, three types of in-situ calibrations are performed sequentially. To assess the total uncertainty of the in-situ calibration, systematic uncertainties from each step are propagated. Various potential sources of uncertainty are considered, as listed below.

- **Mis-modeling of physics processes :** Mis-modeling is evaluated by comparing results from different MC generators.
- **Uncertainties of reference objects :** The uncertainties of reference objects are evaluated by propagating the uncertainties for each reference object through the calibration step.

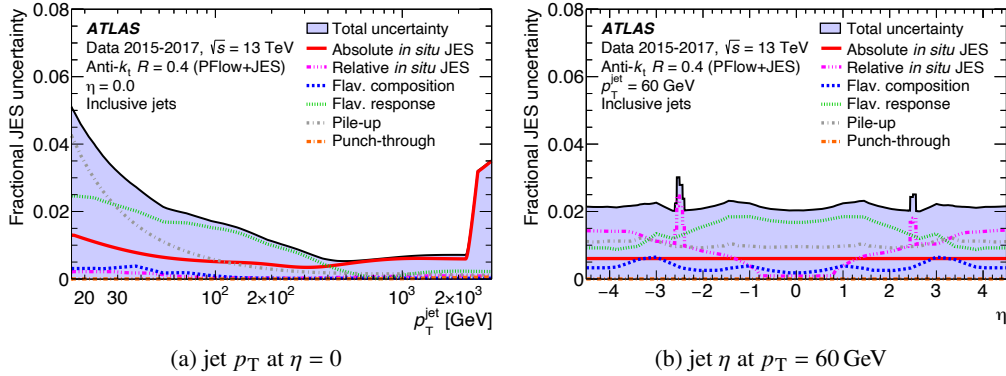


Figure 8.1: Fractional uncertainty on the jet energy scale as a function of jet p_T and η . The “Relative *in situ* JES” represents uncertainties arising from the η intercalibration, while uncertainties from other in-situ calibrations are categorized as “Absolute *in situ* JES”. Flavour composition and response uncertainties are assessed by comparing the difference between quark- and gluon-initiated jet responses and the response of gluon-initiated jets from two different generators with a multijet-like flavour composition. The punch-through uncertainty comes from inaccuracies in modeling the correction for energetic jets that escape the calorimeter and enter the MSs. The energy not absorbed by the calorimeter is estimated and complemented by the number of segments measured by the MS. The uncertainty is assessed by comparing the difference in jet response in the data and simulation. The filled area represents the total uncertainty, calculated by taking the quadrature sum of all the components in the figure. The figures are taken from Ref. [101].

- **Uncertainties of event topology** : Event topology uncertainties are evaluated by adjusting the event selections and examining how the response in the data and simulation varies.

The JES uncertainties are summarized in Figure 8.1.

8.2.2 Tracks

In this analysis, the resolution of the track impact parameter is essential to identify signal events. However, as shown in Figure 6.2, the distribution of the transverse and longitudinal impact parameter resolution reconstructed in the MC simulation and the data is inconsistent since the material description is imperfect. Since QCD tracks in the V +jets process are estimated using data, they are not affected by inconsistencies in impact parameter resolution between data and MC. On the contrary, τ decay tracks can be affected as they use MC simulations for estimation. To account for variations in the data, we assessed yield variation by one-sided systematic variations on the transverse and longitudinal impact parameter resolution. To determine these uncertainties, we replaced the nominal impact parameters with a random value taken from a Gaussian distribution. The central value of the distribution is the original MC impact parameter, while the standard deviation is determined by examining the discrepancies between the resolution of the MC simulation and the data.

8.2.3 Pileup

As discussed in Section 4.1, the distribution of the mean number of interactions per crossing in MC simulation samples is reweighted to match the distribution in the data. The uncertainty of the applied reweighting factor, evaluated with measured inelastic cross-sections [115], is included.

8.2.4 Other experimental uncertainties

In this analysis, other experimental uncertainties that affect the estimated background yields from muons [116], electrons [117], E_T^{miss} [102], triggers [116, 117], and luminosity measurement [66] have a negligible impact ($< 1\%$) and are summarized in Table 8.1. As discussed in Section 4.1, the uncertainty of the integrated luminosity is 0.83% [59].

Table 8.1: Impact from other minor experimental uncertainties. The numbers show the impact of systematics uncertainties on post-fit background yields in the SRs.

Objects	Systematic sources	Impact (%)
E_T^{miss}	Scale and resolution of soft term	< 1
Muons	Efficiency measurement	< 0.1
	Calibration of resolution and momentum scale	
Electrons	Efficiency measurement	< 0.1
	Calibration of resolution and momentum scale	
Photons	Calibration of resolution and momentum scale	< 0.1
Triggers	Correction of difference between data and simulation	< 0.1
Luminosity	Luminosity measurement	0.83

8.3 Uncertainty of Data-driven background estimation

As discussed in Section 7.3, the background estimation method for QCD tracks from the V +jets process assumes that the track $S(d_0)$ distributions are identical across different categories. To account for potential differences, the TFs calculated in the 0ℓ , 1μ , $1e$, 2μ , and $2e$ categories have been compared using MC simulation samples. Figure 8.2 summarizes the measured TFs in each category. The first (second) bin corresponds to the TF calculated by taking the ratio of yields in the range of $S(d_0) < 8$ and $8 < S(d_0) < 20$ ($S(d_0) > 20$). The difference in the measured TF between different categories can potentially lead to a misestimate of the QCD track yields in the SRs. As can be seen from the bottom plot, the ratio in each region is consistent with unity within the MC statistical errors. To address potential differences in the track $S(d_0)$ distribution between different regions, a conservative flat uncertainty of 5% (10%) is assigned in SR-Low (SR-High) to

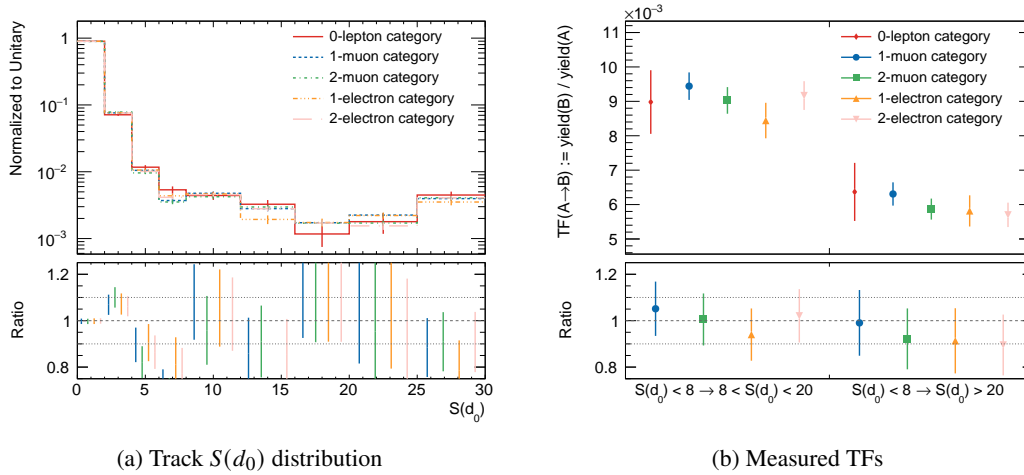


Figure 8.2: Comparison of the track $S(d_0)$ distribution and TFs calculated in the 0ℓ , 1μ , $1e$, 2μ , and $2e$ categories. The error bars indicate MC statistical errors. For the 0ℓ category, TFs are calculated in the high- p_T^{recoil} range. For other categories, the TFs are calculated in the low- p_T^{recoil} range due to lower statistics compared to the 0ℓ category. The bottom panel shows the ratio of the track $S(d_0)$ distribution and TFs between different categories. The 0ℓ category is taken as a reference and compared with other categories.

the samples estimated by the full data-driven background estimation method. This uncertainty is left uncorrelated between the two $S(d_0)$ bins defining the SRs in the fit.

8.4 Summary of Systematic Uncertainties

In addition to the uncertainties described above, two additional uncertainties are considered.

- **CR data statistics** : The uncertainty arising from the limited data statistics in CRs. This includes both the CR statistics for the background estimation of the τ decay tracks discussed in Section 7.2 and for extracting and normalizing the $S(d_0)$ template in the background estimation of the QCD tracks discussed in Section 7.3.
- **MC statistics** : The uncertainty arising from the limited number of MC simulation samples.

The total systematic uncertainty, along with the breakdown in each SR and VR, is visualized in Figure 8.3. In both SRs, the dominant source of uncertainties is the limited data statistics in the CRs, with MC statistics contributing as a secondary factor. In SR-High, the additional 10% uncertainty in the TF contributes at a level comparable to that of the MC statistics.

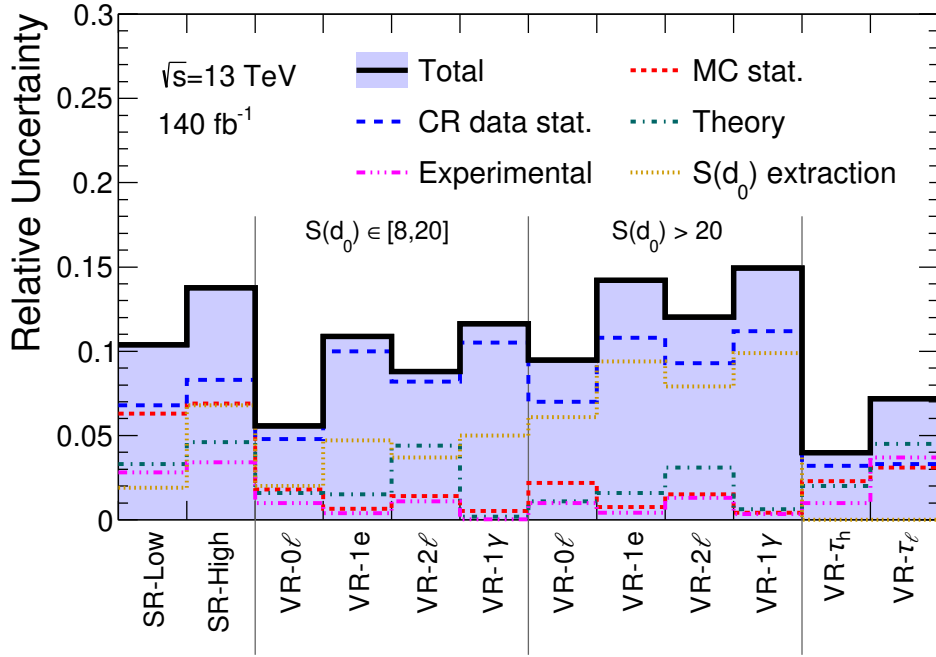


Figure 8.3: Systematic uncertainties on the post-fit background yields in the SRs, VRs for QCD tracks, and VRs for τ decay tracks. The CR data statistics category is the uncertainty that arises from the limited data statistics in CRs. The MC statistics category represents the uncertainty arising from the limited number of MC simulation samples. The experimental category indicates systematic uncertainties originating from the reconstruction, identification, isolation, and calibration of physics objects and tracks. The theory uncertainty category represents the uncertainty arising from the choice of parameters for generating MC simulation samples. The $S(d_0)$ extraction category corresponds to the uncertainty from the potential shape difference of the track $S(d_0)$ distribution between the 0ℓ and 1μ categories, discussed in Section 8.3. The solid line shows the sum of the errors but not necessarily the quadratic sum of the uncertainties since each uncertainty may be correlated.

Chapter 9

Results

This chapter reports the results of the search for mildly-displaced tracks from chargino and neutralino decays. To evaluate the robustness of the background estimation method outlined in Chapter 7, a simultaneous fit procedure, referred to as “background-only fit”, is performed in the control regions (CRs) without any signals. Following the evaluation of the background estimation method through the background-only fit, the resulting Normalization Factor (NF) and Transfer Factors (TFs) are extrapolated to the signal regions (SRs). The estimated yields and kinematic distributions in the SRs are reported in Section 9.1. A model-independent search, followed by a model-dependent interpretation, is conducted by performing a hypothesis test with the estimated yields and observed yields. The results are presented in Sections 9.2 and 9.3.

9.1 Background-only fit results in signal regions

The NF and TFs are derived by fitting the observed data in the CRs using a likelihood function defined as

$$L(x; (\mu_B, \theta)) = \prod_j^N \frac{(E_j(\mu_B, \theta))^{x_j}}{x_j!} e^{-E_j(\mu_B, \theta)}, \quad (9.1)$$

where μ_B is the NF and TFs, θ is the nuisance parameters defined in Section 8, x_j and $E_j(\mu_B, \theta)$ is the number of observed and estimated yields in region j .

The NF and TFs are obtained by performing a maximum likelihood fit using the MC simulation and the observed data in the CRs. A simultaneous fit is performed with all the CRs (CR- τ_h , CR- τ_ℓ , CR- 1μ , CR- 1μ -Low, CR- 1μ -High, and CR- 0ℓ) and the obtained factors are extrapolated to the validation regions (VRs) for validation. The derived NF and TFs are presented in Table 9.1. The observed and post-fit yields in the CRs are presented in Table 9.2.

Table 9.1: NF and TFs measured in the background-only fit. TFs are calculated according to the $S(d_0)$ binning of the SRs.

Background	$S(d_0)$ region	Factor	Value
τ decay track	-	Normalization	1.07 ± 0.11
QCD track	Low	Transfer	$(1.10 \pm 0.12) \times 10^{-2}$
	High	Transfer	$(7.9 \pm 0.9) \times 10^{-3}$

Table 9.2: Observed data and estimated yields using results from the background-only fit in the CRs. The CRs used to calculate the NF for τ decay tracks are located in the left two columns, while the remaining CRs are used to calculate the TFs for QCD tracks. The errors include both statistical and systematic uncertainties.

Yields	CR- τ_ℓ	CR- τ_h	CR- 0ℓ	CR- 1μ -Low	CR- 1μ -High	CR- 1μ
Observed	68	126	1461	183	120	14450
Fitted SM events	68 ± 6	126 ± 10	1460 ± 40	183 ± 14	120 ± 11	14450 ± 120
QCD track	0.28 ± 0.22	4.6 ± 1.3	1270 ± 40	140 ± 15	100 ± 11	12660 ± 230
W +jets (τ_{had} track)	0.16 ± 0.09	67 ± 6	69 ± 9	< 1	< 1	< 100
W +jets (τ_{lep} track)	59 ± 7	42 ± 5	42 ± 5	< 1	< 1	< 100
$t\bar{t}$	2.5 ± 0.4	4.9 ± 0.9	14.1 ± 2.7	29 ± 6	14.3 ± 2.9	1110 ± 190
Other	5.3 ± 3.1	8.5 ± 2.0	63 ± 11	13.8 ± 2.8	5.4 ± 1.1	670 ± 60

As discussed in Section 7.5, the difference between the observed and estimated yields in each VR is less than 1σ , and the distributions are consistent with the estimated ones. The robustness of the background estimation method has been demonstrated, and no additional systematic errors arising from the estimation method are applied.

Given the demonstrated robustness of the background estimation method, the NF and TFs are extrapolated to the SRs to estimate the yields within these regions. The observed and estimated yields in the SRs are summarized in Table 9.3 and Figure 9.1. The post-fit track $S(d_0)$ distribution overlaid with several signal simulation samples is illustrated in Figure 9.2. The observed data in both SRs match the estimated yields well, and no significant discrepancies were identified in the post-fit distributions. Post-fit kinematic plots for other variables are given in Figure 9.3. Figure 9.4 shows a display of an event categorized into SR-High.

Table 9.3: Observed data and estimated yields using results from the background-only fit in the SRs. The errors include both statistical and systematic uncertainties.

Yields	SR-Low	SR-High
Observed	35	15
Fitted SM events	37 ± 4	14.8 ± 2.0
QCD track	14.0 ± 1.7	10.0 ± 1.5
W +jets (τ_{had} track)	10.6 ± 2.0	1.9 ± 0.8
W +jets (τ_{lep} track)	9.6 ± 1.6	2.0 ± 0.6
$t\bar{t}$	1.3 ± 0.4	0.44 ± 0.14
Other	1.8 ± 0.6	0.32 ± 0.31

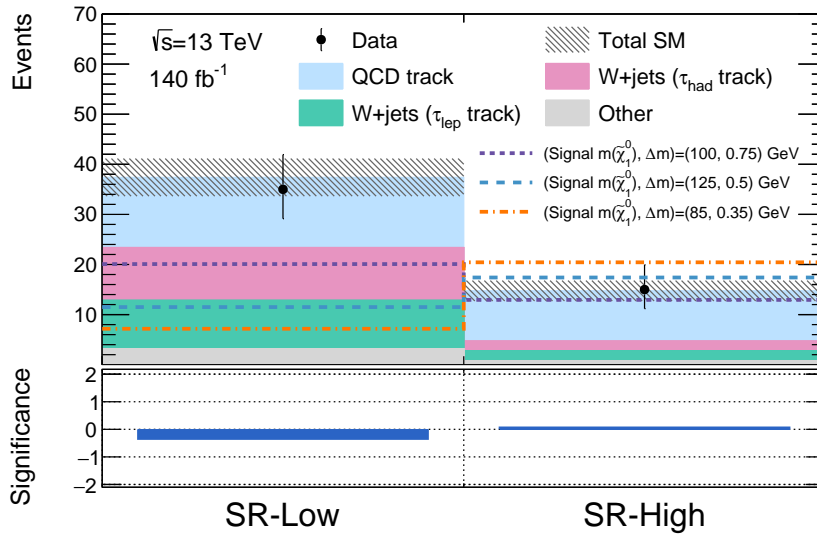


Figure 9.1: Overview of fit results in the SRs. The upper plot summarizes observed and estimated yields for each SR, while the bottom plot illustrates the difference between the observed and estimated yields. The dashed line illustrates signal simulation samples with different mass and mass differences. The “Other” category includes contributions from $Z(\rightarrow \tau\tau)$ +jets, di-boson, single top, $t\bar{t}$, γ +jets, and multijet processes.

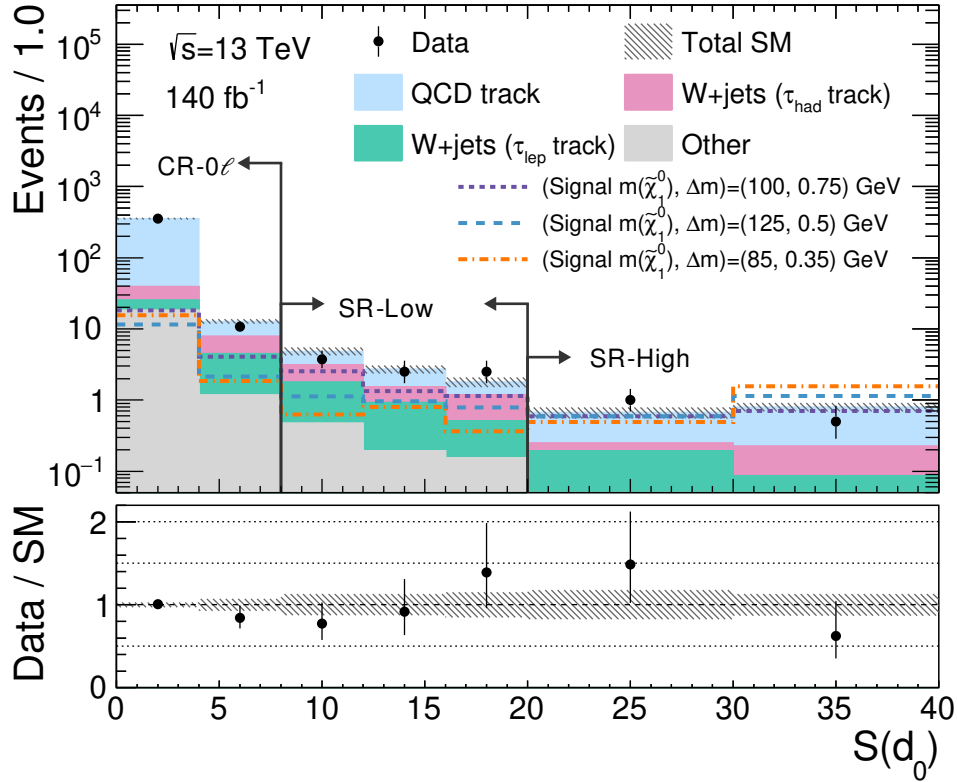


Figure 9.2: Post-fit track $S(d_0)$ distribution in the SR bins and CR- 0ℓ . The bins enclosed by arrows indicate the respective regions. The dashed line illustrates signal simulation samples with different mass and mass differences. The hatched area corresponds to the combined systematic and MC statistical uncertainties. The bottom panel shows the ratio of the observed data yield and estimated background yield. The “Other” category includes contributions from $Z(\rightarrow \tau\tau)$ +jets, di-boson, single top, $t\bar{t}$, γ +jets, and multijet processes.

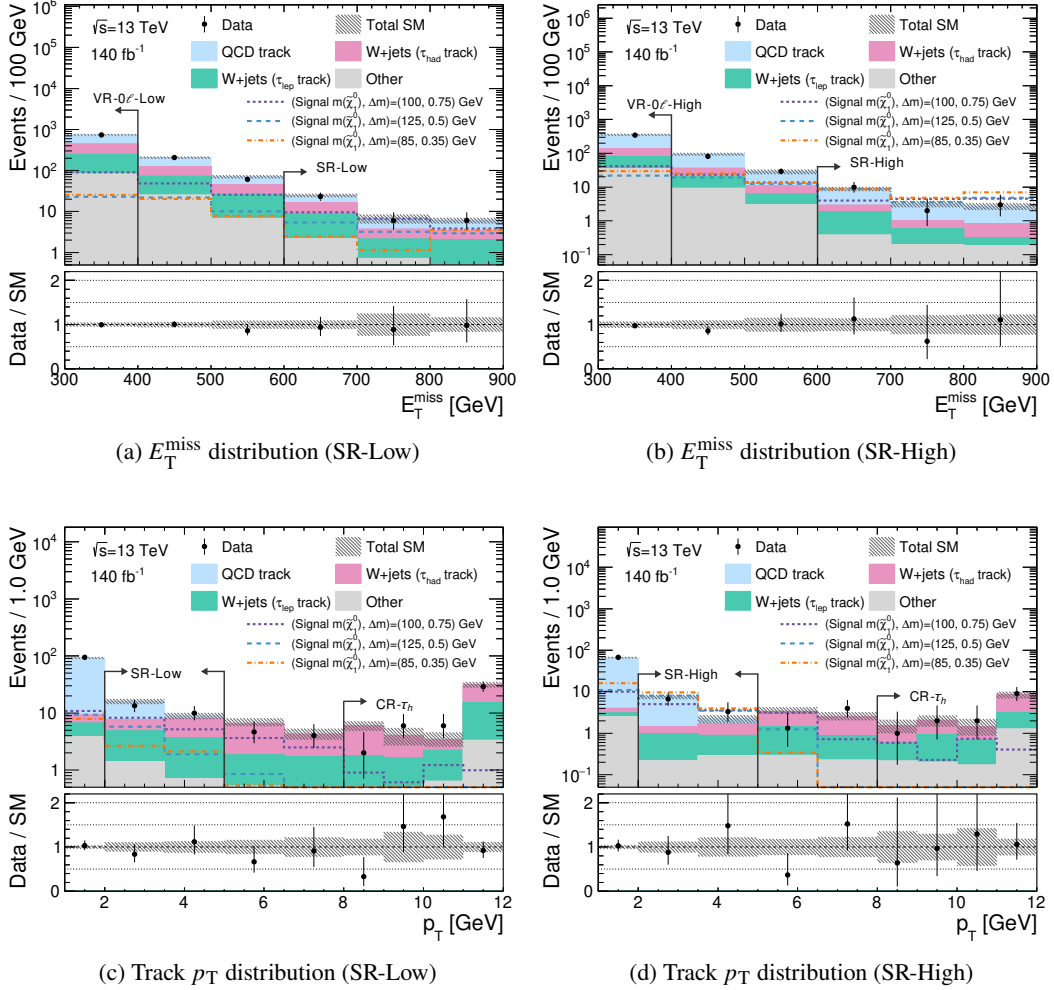


Figure 9.3: Post-fit distributions in the SR bins. Each plot is drawn without applying selections to the variable illustrated. The bins enclosed by arrows indicate the respective regions. The dashed line illustrates signal simulation samples with different mass and mass differences. The hatched area corresponds to the combined systematic and MC statistical uncertainties. The bottom panel shows the ratio of the observed data yield and the estimated background yield. The “Other” category includes contributions from $Z(\rightarrow \tau\tau)$ +jets, di-boson, single top, $t\bar{t}$, γ +jets, and multijet processes.

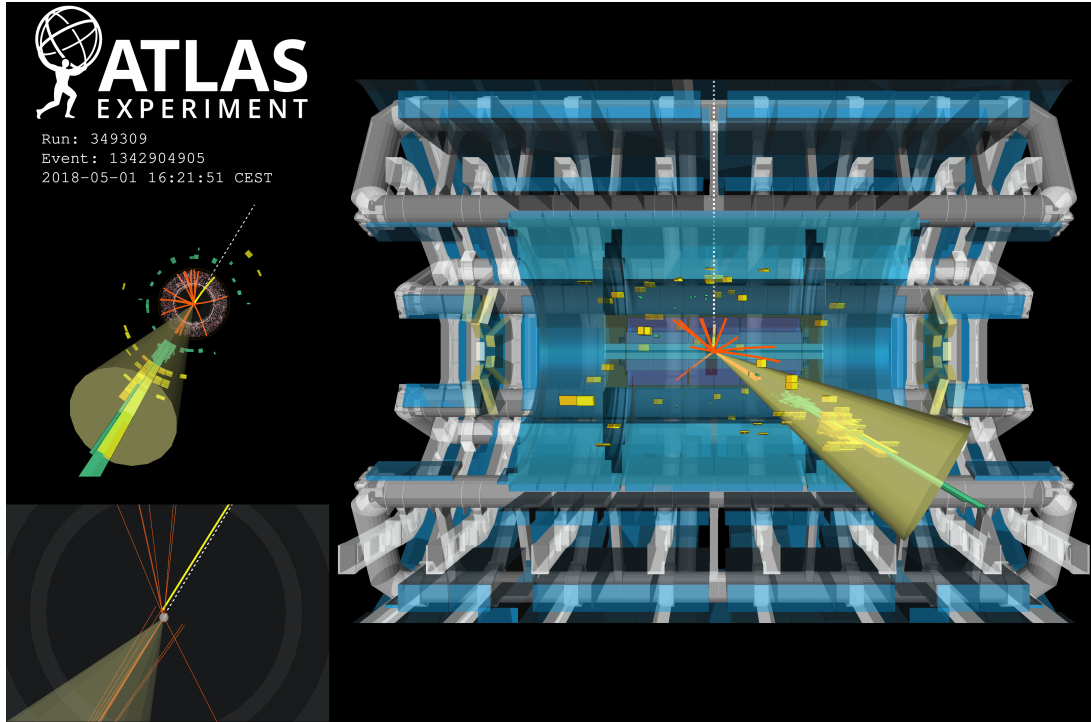


Figure 9.4: Event display of a data event recorded in 2018 data, categorized into SR-High. The two figures on the left show a cross-sectional view of the ATLAS detector from the beam axis direction, and the right shows a cross-sectional view perpendicular to the beam axis. Green and yellow bars in the ATLAS detector illustrate energy deposits in the electromagnetic and hadronic calorimeters, respectively. The jet reconstructed from energy deposits in the calorimeter is depicted as a yellow cone. The solid red lines in the ID indicate reconstructed tracks, with yellow indicating signal candidate tracks that passed the event selections. The white dashed line illustrates the missing transverse momentum, which points in the opposite direction of the reconstructed jet and is aligned with the signal candidate track. The lower left figure is a magnified view of the area near the beam axis, which shows that the signal candidate track is generated slightly away from the interaction point. The magnitude of the missing transverse momentum is $E_T^{\text{miss}} = 1001$ GeV, while the jet is reconstructed with $p_T = 1009$ GeV in the direction of $\eta = 1.16$. The signal candidate track is reconstructed with $p_T = 3.3$ GeV and $S(d_0) = 38.3$, in the direction of $\eta = 0.04$.

9.2 Model-independent search

Upper limits on the number of beyond the Standard Model (BSM) signal yields are established by performing a hypothesis test with the null hypothesis describing a background-only scenario. Both SRs are used individually to derive model-independent constraints, which are sensitive to a broader range of lifetimes compared to using a single SR bin or a merged region by both SR bins.

Signal yields are incorporated into the fit procedure by modifying the likelihood as

$$L(x; (\mu, \mu_B, \theta)) = \prod_j^N \frac{(E_j(\mu, \mu_B, \theta))^{x_j}}{x_j!} e^{-E_j(\mu, \mu_B, \theta)}. \quad (9.2)$$

$E_j(\mu, \mu_B, \theta)$ now includes the contribution from the signal samples as

$$E_j = \mu s_j(\theta) + b_j(\mu_B, \theta), \quad (9.3)$$

where s_j is the number of estimated signal yields in region j . The symbol μ represents a free parameter known as the signal strength, which scales the signal yields.

As no specific models are being considered for the signals, the signal yields are included exclusively in the SRs and not in the CRs.

The profile likelihood ratio is introduced to determine the ‘‘test statistic’’ for the hypothesis test, with the profile likelihood ratio defined as

$$\lambda(\mu) = \frac{L(\mu, \hat{\mu}_B, \hat{\theta})}{L(\hat{\mu}, \hat{\mu}_B, \hat{\theta})}. \quad (9.4)$$

In the equation, $\hat{\mu}$, $\hat{\mu}_B$, and $\hat{\theta}$ represent a set of parameters that maximize the likelihood, while $\hat{\mu}_B$ and $\hat{\theta}$ denote a set of parameters that maximize the likelihood for a given μ value. Using the profile likelihood ratio as defined, the test statistic is expressed as

$$q_\mu = -2 \ln \lambda(\mu). \quad (9.5)$$

The p -value, denoting the probability of observing the given data or more extreme data, assuming that the null hypothesis is true, can be defined as

$$p_\mu = \int_{q_{\mu, \text{obs}}}^{\infty} f(q_\mu | \mu) dq_\mu, \quad (9.6)$$

Table 9.4: 95% CL upper limits on the visible cross-section ($\langle\epsilon\sigma\rangle_{\text{obs}}^{95}$) and on the number of signal events (S_{obs}^{95}). The third column (S_{exp}^{95}) shows the 95% CL upper limit on the number of signal events, given the expected number (and $\pm 1\sigma$ excursions on the expectation) of background events. The last two columns indicate the CL_B value and the discovery p -value ($p(s=0)$). In cases where the observed yield is below the expected yield, the p -value is capped at 0.5. CL_B provides a measure of compatibility of the observed data with the signal strength hypothesis at the 95% CL limit relative to fluctuations of the background, and $p(s=0)$ measures compatibility of the observed data with the background-only hypothesis relative to fluctuations of the background.

Signal channel	N_{obs}	N_{exp}	$\langle\epsilon\sigma\rangle_{\text{obs}}^{95}$ [fb]	S_{obs}^{95}	S_{exp}^{95}	CL_B	$p(s=0)$ (Z)
SR-Low	35	37.39 ± 3.81	0.10	13.5	$15.1^{+6.3}_{-4.2}$	0.37	0.50 (0.00)
SR-High	15	14.76 ± 2.03	0.07	9.9	$9.6^{+4.4}_{-2.8}$	0.52	0.50 (0.01)

where $f(q_\mu|\mu)$ represents the probability density function of q_μ with a given μ value. Executing the hypothesis test involves obtaining $f(q_\mu|\mu)$ for each μ value by running pseudo experiments called “toy-experiments”, which requires a substantial amount of computing resources to obtain a distribution with sufficient statistics. Another method is to use the asymptotic formula, where the test statistic follows a chi-square distribution derived from Wald’s approximation. This thesis takes the asymptotic formula approach, given a sufficient number of events in both SRs.

The upper limit on the signal strength μ is set at the value that can be excluded with 95% confidence level (CL_s), defined as

$$CL_s = \frac{CL_{s+b}}{CL_b} = \frac{p_s}{p_{s=0}}. \quad (9.7)$$

The p -value from the combined signal and background hypothesis is divided by the p -value derived from the background-only hypothesis to avoid setting limits in regions of low experimental sensitivity. The upper limits derived using SR-Low and SR-High are summarized in Table 9.4. The expected number of events, labeled N_{exp} , is extracted from Table 9.3. An upper limit is placed on the visible cross-section, which is defined as the product of the cross-section and the acceptance. The equation describing this limit is

$$\langle\epsilon\sigma\rangle_{\text{obs}}^{95} = S_{\text{obs}}^{95} / (\text{Integrated luminosity} = 140 \text{ fb}^{-1}), \quad (9.8)$$

where S_{obs}^{95} is the upper limit placed on the number of observed signal events. Given the consistency between the observed and expected number of yields, the upper limits placed on S_{obs}^{95} and S_{exp}^{95} are also consistent.

9.3 Model-dependent interpretation

Exclusion limits for specific models are determined by performing a hypothesis test that incorporates signal yields estimated from simulation samples in both SRs and CRs into the likelihood. Both SRs are incorporated into the fitting procedure to calculate the CL_s value. The CL_s value is calculated for the $\mu = 1$ hypothesis for each signal point in the $m(\tilde{\chi}_1^0)$ and $\Delta m(\tilde{\chi}_1^\pm, \tilde{\chi}_1^0)$ plane. The CL_s values between each signal point are smoothly interpolated, and the points with $CL_s = 0.05$ are connected to form the exclusion limit.

The expected and observed exclusion limits for SR-Low and SR-High individually are presented in Figures 9.5(a) and 9.5(b), respectively. As illustrated in the figure, SR-High has good overall sensitivity, while SR-Low exhibits slightly better sensitivity for larger mass differences. The combined exclusion limit and a comparison with exclusion limits from previous analyses are shown in Figures 9.6(a) and 9.6(b), respectively. The higgsino mass was excluded up to about 170 GeV with mass differences of approximately 0.6 GeV. This analysis successfully explored the 0.3 – 1.0 GeV mass difference region for the first time at the LHC, which had been challenging to search with sensitivity beyond that of LEP.

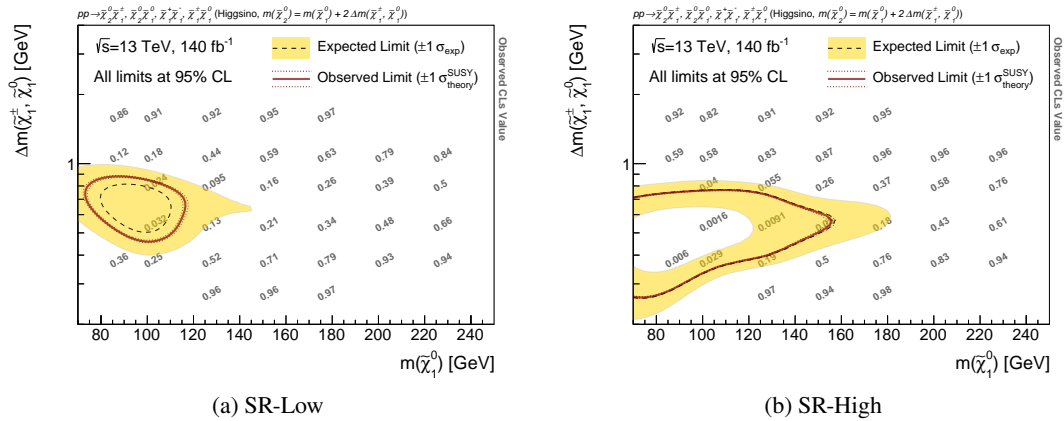


Figure 9.5: The expected and observed exclusion limits for SR-Low and SR-High individually are illustrated. The expected exclusion limits are depicted by black dashed lines, with the yellow band representing one standard deviation of the expected exclusion. Red lines represent the observed exclusion limits, and the gray numbers indicate the observed CL_s values. Figures 9.5(a) and 9.5(b) show the exclusion limits using only SR-Low and SR-High, respectively.

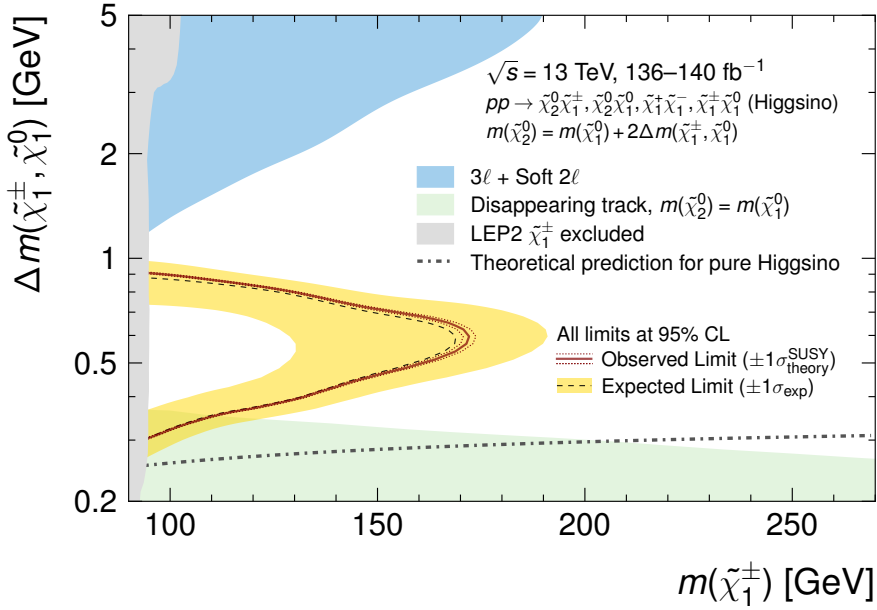
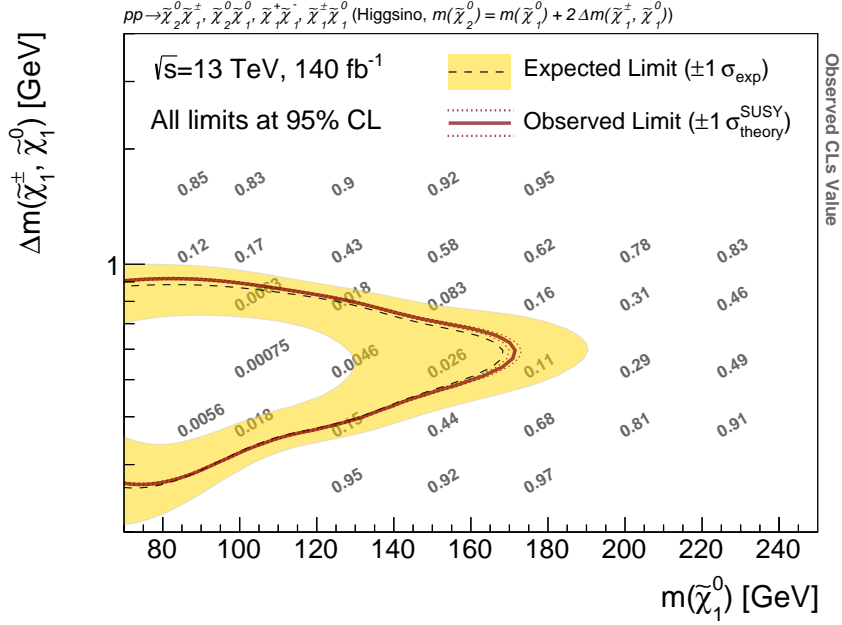


Figure 9.6: The expected and observed exclusion limits using all SRs. The expected exclusion limits are represented by black dashed lines, with the yellow band representing one standard deviation of the expected exclusion. Red lines represent the observed exclusion limits. (a) The gray numbers indicate the observed CL_s values. The values between each signal point are smoothly interpolated to form the observed exclusion limits. (b) The exclusion limits of this analysis are presented, along with existing experimental constraints on the higgsino states with compressed mass spectra.

Chapter 10

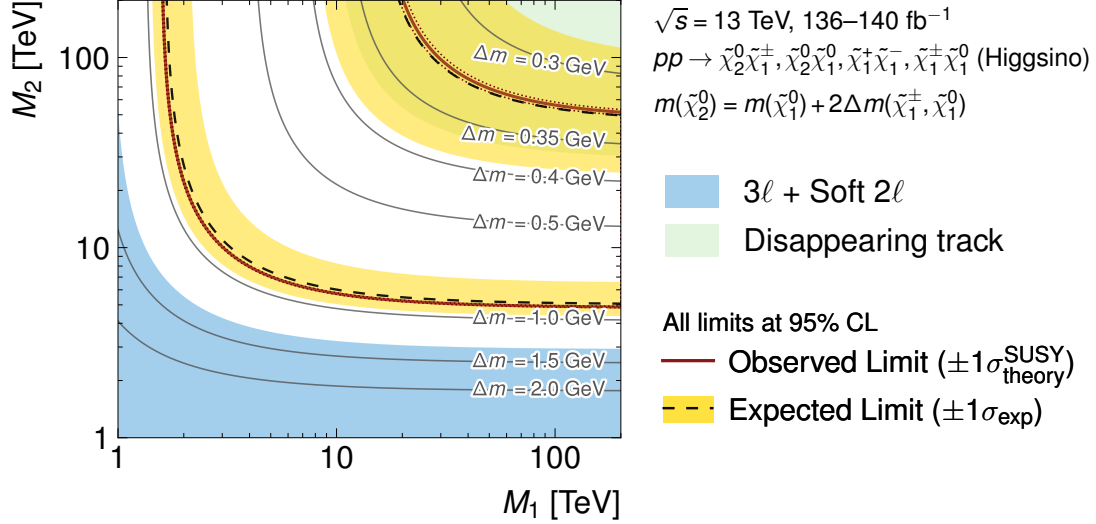
Discussion

As mentioned in Section 2.3.3, the higgsino mass difference shows significant variations depending on the bino and wino mass. Therefore, we will first discuss the limits imposed on the masses of bino and wino by this analysis.

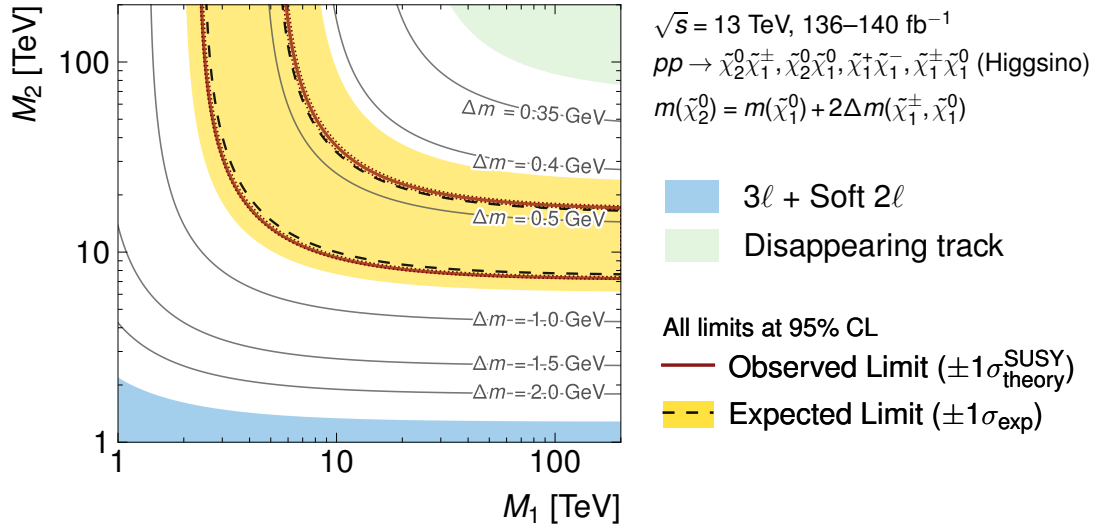
As discussed in Section 2.3.2, the higgsino mass is expected to be near the electroweak scale from electroweak naturalness. This analysis is sensitive to the light higgsino scenario, with the mass difference between the lightest chargino and neutralino in the range of 0.3–1.0 GeV. In Section 10.2, we will discuss the impact of this analysis on the light higgsino scenario. Finally, in Section 10.3, we discuss the sensitivity projection of this analysis with the data acquired in the future data-taking period at the LHC.

10.1 Limit on the Electroweakino masses

As discussed in Section 2.3.3, the masses of bino (M_1) and wino (M_2) and the mass difference between the lightest chargino and neutralino are related as in Equation 2.12. Therefore, this equation can be used to project the exclusion limit in Figure 9.6(b) into a limit on the wino and bino masses. At $\mu \approx m(\tilde{\chi}_1^\pm) = 100$ GeV, this analysis covers most of the higgsino mass difference regions that previous searches have not covered. Figure 10.1 shows the limits of the wino and bino masses in this analysis at $\mu = 100$ GeV. The rejection of $\Delta m(\tilde{\chi}_1^\pm, \tilde{\chi}_1^0) \approx 0.3–0.9$ GeV in this analysis indicates that the wino and bino masses can be rejected in the range of $\mathcal{O}(10)$ TeV. Although the exclusion of the mass difference weakens to $\Delta m(\tilde{\chi}_1^\pm, \tilde{\chi}_1^0) \approx 0.45–0.75$ GeV for $\mu \approx m(\tilde{\chi}_1^\pm) = 150$ GeV, as shown in Figure 10.1, still a substantial wino and bino mass parameter space is excluded by this analysis. The exclusion with different slices in $\tan\beta$ and the angle of the complex phase of M_1 and M_2 are shown in Appendix I.3.



(a) $\mu = 100 \text{ GeV}$



(b) $\mu = 150 \text{ GeV}$

Figure 10.1: The observed and expected exclusion limits at the 95% CL in the M_1 and M_2 plane for (a) $\mu = 100 \text{ GeV}$ and (b) $\mu = 150 \text{ GeV}$. The expected and observed limits in the displaced track analysis are overlaid with the observed limits from existing analyses.

10.2 Implication to Electroweak Naturalness

As discussed in Sections 2.4.2 and 2.4.4, the results of direct dark matter detection and electron EDM experiments impose strong limits on the electroweak gaugino mass. Figure 10.2(a) shows the exclusion limits for μ and M_2 obtained by this analysis overlaid with the results obtained by other collider searches, the direct dark matter detection, and electron EDM experiments. The projection of the limits to the gaugino mass from the results of the direct dark matter detection and the electron EDM experiment are approximated by Equation 2.16 and Equation 2.18, respectively. As can be seen in the figure, this analysis searched for a region with a very large gaugino mass of $\mathcal{O}(10)$ TeV, which had not been excluded by the direct dark matter detection nor by the electron EDM experiment. However, as shown in Equation 2.18, the magnitude of the electron EDM is highly dependent on $\tan\beta$ and the complex phase of the wino mass parameter (ϕ_2). Additional figures produced by varying $\tan\beta$ and the phase of the wino mass parameter (ϕ_2) are given in Figure 10.2(b).

Electroweak naturalness requires the higgsino mass to be at the electroweak scale, while the masses of other particles like wino and bino can have arbitrary values. This leads to a wide range of possible mass spectra for the higgsinos. Although the direct dark matter detection and electron EDM experiments provide stringent limits to the possible mass spectra, they are sensitive only when wino and bino are sufficiently light. This analysis, along with the results of other collider searches, the direct dark matter detection, and electron EDM experiments, has performed a comprehensive search for the light higgsino scenario. In particular, in the higgsino mass difference region in interest, to which only the LEP experiment has been sensitive, the constraint on the higgsino mass only runs up to 90 GeV. The present analysis allows us to search the mass region up to about 170 GeV, which is on the verge of surpassing the electroweak scale.

10.3 Future Prospects

As mentioned in Section 3.4, a new LHC data-taking period (Run 3) from 2022 to 2025 (planned), boosting the data statistics available for the analysis began in 2022. The HL-LHC, scheduled to start in 2029, will provide even higher statistics by increasing the instantaneous luminosity by a factor of 5–7.5 with respect to the nominal value of the current LHC. In the following, we will discuss the extended sensitivity of this and other analyses targeting the higgsino LSP scenarios using data obtained during Run 3 and HL-LHC.

10.3.1 Soft Lepton and Disappearing Track analysis

As discussed in Section 2.4.1, the soft lepton and disappearing track analysis successfully extended sensitivity to the region with the small higgsino mass difference using Run 2 data. The sensitivity of the soft lepton and the disappearing track analysis using 3000 fb^{-1} data acquired with the HL-LHC is presented in Figure 10.3. The soft lepton analysis is expected to increase the sensitivity

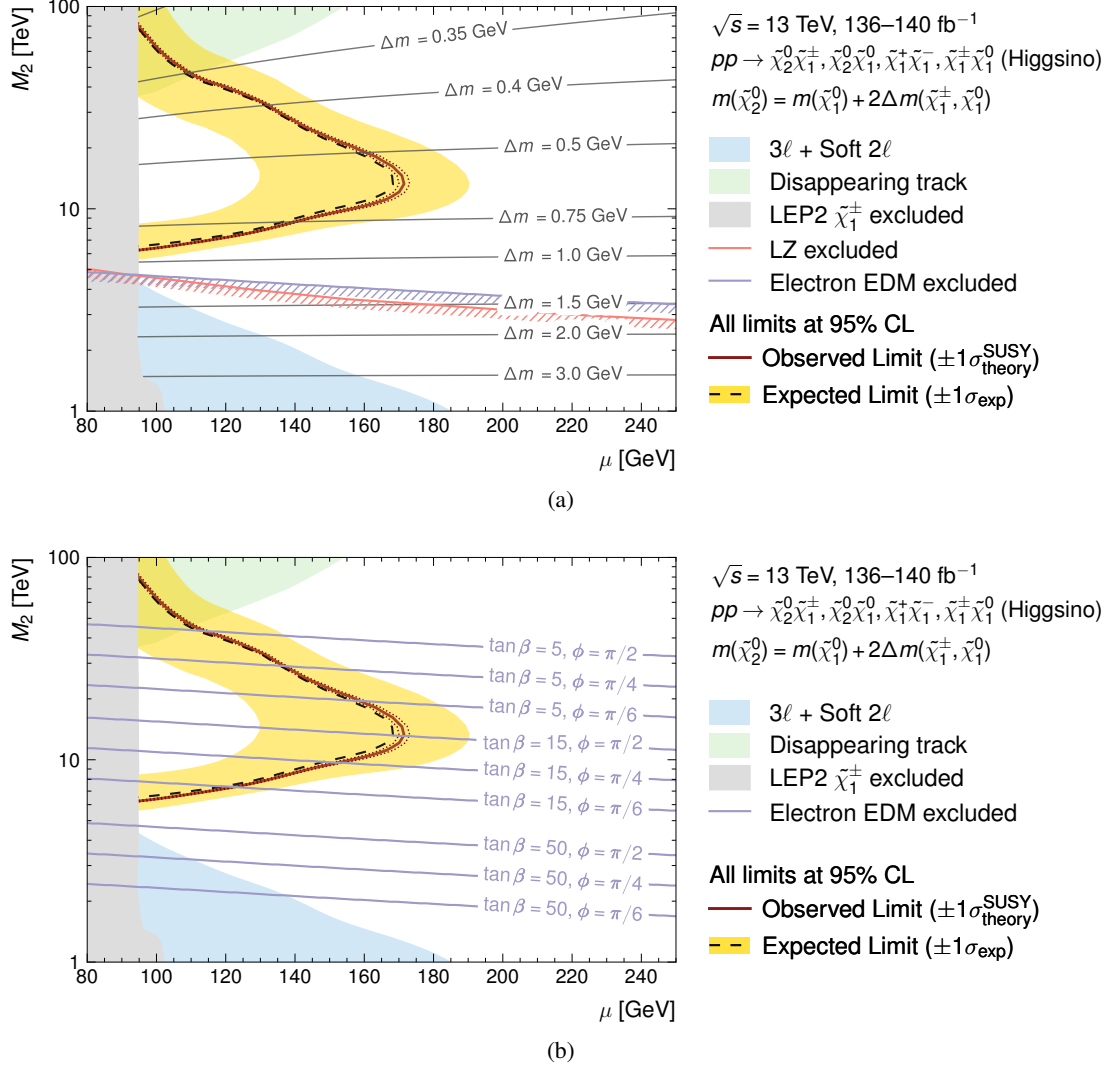
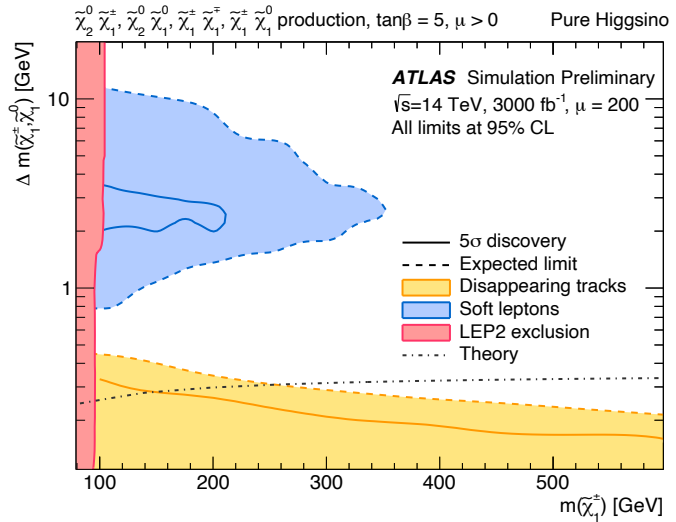


Figure 10.2: The observed and expected exclusion limits at the 95% CL in the μ and M_2 plane, with $M_1 = M_2$ and $\tan\beta = 50$. The expected exclusion limits are represented by black dashed lines, with the yellow band representing one standard deviation of the expected exclusion. Red lines represent the observed exclusion limits. The exclusion limits by the soft lepton analysis, disappearing track analysis, and the LEP experiment are overlaid. (a) The gray line shows the correlation between μ and M_2 that satisfies the described mass difference. The solid lines with hatched areas indicate regions excluded by direct dark matter detection (LZ experiment [21]) and electron EDM (JILA experiment [52]). (b) The solid lines indicate regions excluded by electron EDM (JILA experiment [52]) with different $\tan\beta$ and ϕ_2 values.

Figure 10.3: Future projection of exclusion limits by the soft lepton and disappearing track analysis using data collected during the HL-LHC, in the $m(\tilde{\chi}_1^\pm)$ and $\Delta m(\tilde{\chi}_1^\pm, \tilde{\chi}_1^0)$ plane. The blue (yellow) dashed line illustrates the expected exclusion limits at the 95% CL in the soft lepton (disappearing track) analysis. The red-filled area illustrates the observed exclusion limit at the 95% CL from LEP [20]. The solid blue and yellow lines illustrate the 5σ discovery potential of the analyses. The figure is taken from Ref. [118].



up to 350 GeV in the exclusion limit with higgsino mass differences of approximately 2.5 GeV. Compared to Figure 1.1, the sensitivity of the soft lepton search to the mass of the chargino is found to be extended by about 150 GeV with a higgsino mass difference of $O(1)$ GeV. In the pure higgsino limit, the disappearing track analysis is expected to increase the sensitivity to 250 GeV. Compared to Figure 1.1, the disappearing track analysis extends the sensitivity by about 60 GeV, limited by the increase of fake tracks (accidental alignment of hits within the ID) due to the increased number of pileup interactions. However, the new analysis methods used in the Run 2 analysis are not taken into account in this projection. Therefore, further improvement in sensitivity is expected in the HL-LHC by reducing the number of fake tracks by introducing the new analysis methods in the Run 2 analysis [15].

As can be seen from Figure 10.3, it is challenging to extend the sensitivity to the target higgsino mass difference region, even when using the large statistics of the HL-LHC. Figure 9.6(b) shows that the result from this analysis with Run 2 statistics already outperforms the soft lepton and disappearing track analysis at 3000 fb^{-1} , in the region where the higgsino mass difference is $O(100)$ MeV.

10.3.2 Displaced Track analysis

The sensitivity of the displaced track analysis was evaluated with the expected data statistics recorded during Run 3 and HL-LHC. The track reconstruction performance is expected to remain comparable between Run 2 and Run 3, as the Inner Detector (ID) remains unchanged and the instantaneous luminosity stays at a similar level. On the other hand, in the HL-LHC, it is necessary to consider that the environment for track reconstruction changes due to the replacement of the ID, and the mean number of interactions per crossing increases significantly. First, we will discuss the tracking performance in the HL-LHC and identify the types of background that are expected to

increase. Then, the expected sensitivity of this analysis for Run 3 and HL-LHC will be presented. Finally, we briefly summarize other search methods using the mildly-displaced track signature.

Tracking Performance in the HL-LHC Tracks can be classified into three categories: primary vertex tracks, pileup tracks, and fake tracks. Primary vertex tracks and pileup tracks are reconstructed by particles produced from primary and pileup vertices, respectively. Fake tracks are reconstructed by random combinations of hits from the ID. In the HL-LHC, the increase in instantaneous luminosity leads to a rise in fake and pileup tracks. This is caused by the significantly higher number of hits in the ITk and pileup vertices.

The tracking performance for the primary vertex tracks varies depending on the ITk geometry, reconstruction algorithms, and the environment that features a large number of interactions. Figure 10.4 shows the expected efficiency and resolution of the transverse impact parameter ($|d_0|$) of the tracks reconstructed by the ITk. As seen in the figure, while the efficiency is slightly worse in the central region of the ITk, it remains almost the same overall. The d_0 resolution slightly improves for tracks with low p_T as the pixel size becomes finer. Therefore, the tracking performance of HL-LHC can be reasonably approximated using the efficiency and d_0 resolution in the Run 2 analysis.

Figure 10.5 compares the number of tracks reconstructed with $p_T > 1$ GeV using the Run 3 geometry and reconstruction algorithm with that of the ITk geometry. As depicted in the figure, the number of tracks does not show a linear correlation with the number of interactions when it reaches around 60 with the Run 2 geometry and reconstruction algorithm. This is due to the presence of fake tracks. On the other hand, the reconstructed tracks obtained by the ITk geometry and reconstruction algorithm exhibit a clean linear correlation with the number of interactions, which implies that the amount of fake tracks can be significantly suppressed in the HL-LHC. Therefore, when evaluating the sensitivity of the HL-LHC, the fake track is treated as sufficiently negligible.

Figure 10.6 illustrates the correlation between the number of interactions and the fraction of pileup tracks present within the signal tracks. As shown in the figure, an increase in pileup tracks must be considered when evaluating the sensitivity of the analysis in the HL-LHC, as the number of pileup tracks is directly proportional to the number of pileup vertices. To account for the increase of pileup, in the HL-LHC sensitivity projection presented below, the simulated events are reweighted so that the pileup effect is comparable with the case of the number of interactions being 200.

Expected Sensitivity in Run 3 and HL-LHC Since a large increase in statistics is expected, especially for the HL-LHC, the E_T^{miss} selection is tightened from 600 GeV to 800 GeV to increase the signal-to-background ratio. Figure 10.7 shows the sensitivity of this analysis for data obtained by Run 3 and HL-LHC, overlaid with exclusion limits of existing analyses. Using the large statistics of 3000–4000 fb^{-1} expected in the HL-LHC, the sensitivity can be extended to about 250 GeV.

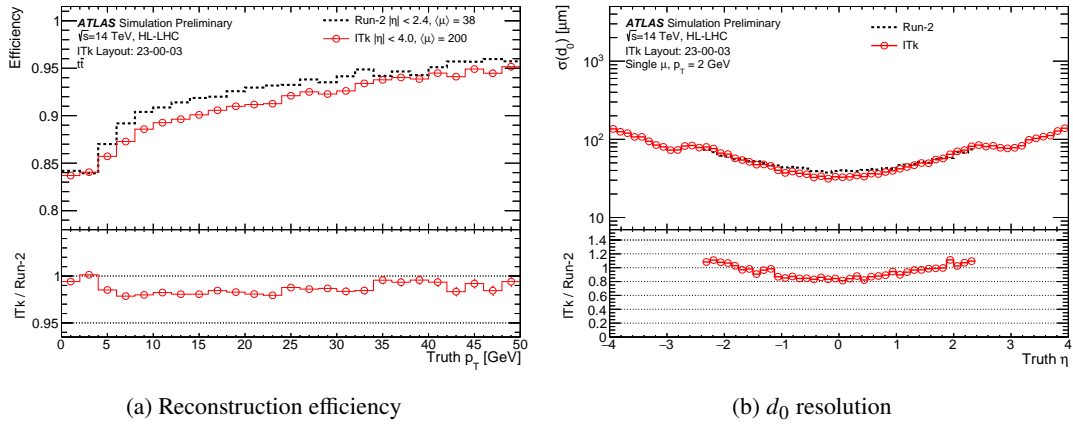


Figure 10.4: Expected performance of the track reconstruction with the ITk. (a) Comparison between the efficiency in the Run 2 and that expected in the HL-LHC assuming the ITk geometry using the $t\bar{t}$ samples. The ITk geometry assumes that the mean number of interactions per crossing, denoted as $\langle\mu\rangle$, is 200. Track reconstruction in the ITk geometry requires more hits than Run 2 in the region $|\eta| < 2.0$, but the performance remains at the same level. (b) Comparison between the d_0 resolution with the Run 2 and ITk geometry using single muon samples. The resolution is evaluated as a function of the η of truth muons with $p_T = 2$ GeV. The figures are taken from Ref. [119].

Figure 10.5: Comparison of the number of tracks reconstructed with $p_T > 1$ GeV utilizing the Run 2 geometry and reconstruction algorithm with that expected in the HL-LHC assuming the ITk geometry and reconstruction algorithm. The ITk geometry assumes that the mean number of interactions per crossing, denoted as $\langle\mu\rangle$, is 200. The figure is taken from Ref. [119].

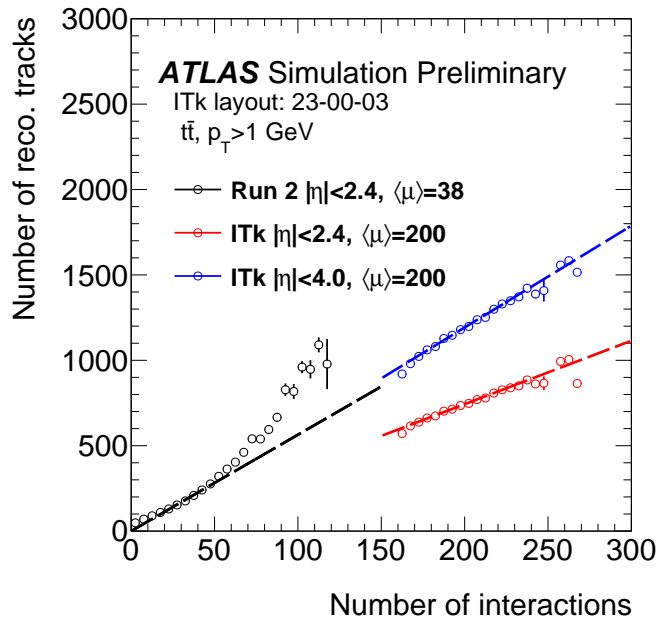
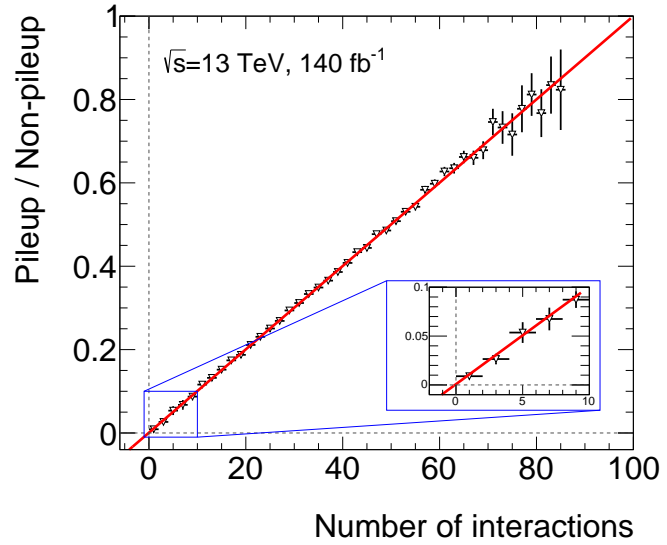


Figure 10.6: Correlation between the number of interactions and the fraction of pileup tracks present within the signal tracks. The distribution is fitted with a linear function expressed in the red line.



By combining the results of the soft lepton and disappearing track analyses shown in Figure 10.3, we can see that the HL-LHC statistics enable an extensive search for the target higgsino mass difference region using the current analyses alone.

Other search methods using the mildly-displaced track signature Since the number of signal events also increases significantly in the HL-LHC, a tighter selection can be applied using mildly-displaced tracks, as described below. This analysis only requires one mildly-displaced track, while requiring two from the $pp \rightarrow \tilde{\chi}_1^+ \tilde{\chi}_1^-$ process would further reduce the number of background events, especially for τ decay tracks. Another new channel that can be promising in the presence of larger statistics of data is the identification of the neutralino decay vertex with two mildly-displaced tracks. As can be seen in Figure 2.12(b), in the region where the mass difference between the two neutralinos is 1 GeV, the branching ratio of $\tilde{\chi}_2^0 \rightarrow \tilde{\chi}_1^0 \pi^\pm \pi^\mp$ is about 40%. In this higgsino mass difference region, the neutralino has a relatively long lifetime, resulting in the decay of the neutralino at a distance from the interaction point and the production of two tracks. Therefore, tracks from the neutralino decay can be identified by reconstructing a displaced vertex formed by a pair of oppositely charged tracks. In this case, strange hadrons can be the main background, as in this analysis, but they can be reduced by vetoing the vertex mass consistent with the strange hadron masses. Figure 10.8 shows the diagrams of the signals discussed above.

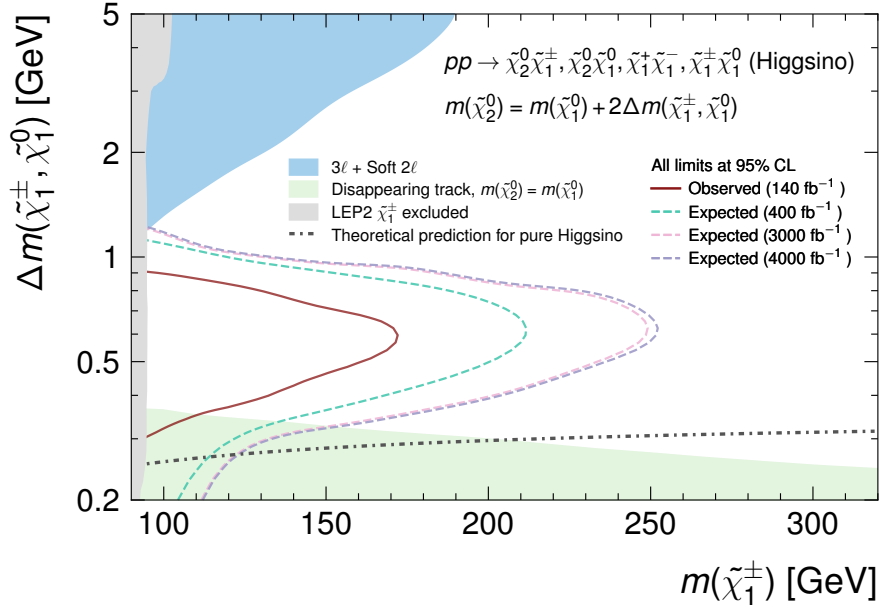


Figure 10.7: Future projection of the exclusion limits by the displaced track analysis using the data collected during the Run 3 and HL-LHC, shown in the $m(\tilde{\chi}_1^\pm)$ and $\Delta m(\tilde{\chi}_1^\pm, \tilde{\chi}_1^0)$ plane. The red solid line illustrates the observed exclusion limits at the 95% CL in the displaced track analysis using the Run 2 data. The dashed lines illustrate the expected exclusion limit at the 95% CL with integrated luminosity of 400 fb^{-1} , 3000 fb^{-1} , and 4000 fb^{-1} .

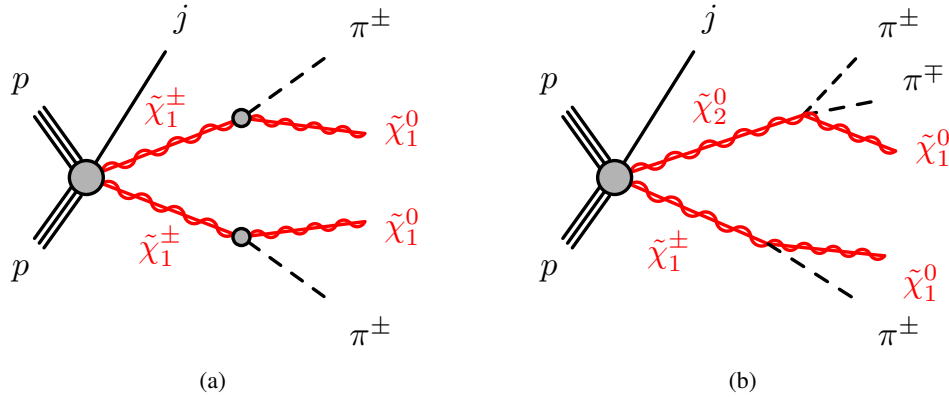


Figure 10.8: Diagrams of processes resulting in multiple mildly-displaced tracks. (a) The $pp \rightarrow \tilde{\chi}_1^+ \tilde{\chi}_1^-$ process produces two mildly-displaced tracks, which could be utilized to further reduce background events. (b) In $\Delta m(\tilde{\chi}_2^0, \tilde{\chi}_1^0) \sim 1 \text{ GeV}$, the neutralino decay produces two opposite charged pions at a distance from the interaction point. Tracks from the neutralino decay can be identified by reconstructing the displaced vertex by two opposite charge tracks.

Chapter 11

Conclusion

This thesis reports the search for higgsinos with compressed mass spectra using 140 fb^{-1} of $\sqrt{s} = 13 \text{ TeV}$ proton-proton collision data collected by the ATLAS detector at the Large Hadron Collider (LHC). In this search, we specifically targeted the region where the mass difference between the higgsinos is $0.3 - 1.0 \text{ GeV}$, which is a sensitivity blind spot for collider experiments since LEP. In addition, this region is highly challenging to search by the direct dark matter detection experiments due to the suppressed coupling between the higgsinos and the target nuclei. Because of the very small mass difference, higgsinos have a relatively long lifetime and decay at a distance of a few millimeters from the interaction point. Therefore, the charged particles produced by the decay leave a track in the detector with a subtle yet detectable impact parameter from the interaction point, referred to as “mildly-displaced tracks”. Since most Standard Model (SM) particles decay promptly on the collision, requiring a mildly-displaced track allows one to effectively select out the tracks originating from the higgsino decays.

In this search, events in interest are triggered by requiring hadronic activity from an initial-state radiation jet to boost higgsinos to the opposite direction and generate a significant missing transverse momentum. For each event, a single mildly-displaced track is selected and classified into two signal regions (SRs) according to the magnitude of the impact parameter. SM backgrounds from particles with relatively long lifetimes were estimated using various data-driven approaches.

The observed data and the SM predictions are consistent in both SRs, allowing us to set a 95% CL limit on the higgsino mass as a function of the higgsino mass difference. In the higgsino mass difference region of $0.3 - 1.0 \text{ GeV}$, the higgsino mass is excluded up to about 170 GeV . This result allows us to exceed the LEP limit in the corresponding higgsino mass difference for the first time.

The novel analysis approach used in this search allowed us to enter the gap where increasing sensitivity in collider and direct dark matter detection experiments has been challenging. Even with the high statistics of the High-Luminosity LHC (HL-LHC) ($\sqrt{s} = 14 \text{ TeV}$, $\mathcal{L} = 3000 \text{ fb}^{-1}$), this search is by far the most effective approach that can extend the sensitivity to a region with a small mass difference, and the sensitivity can be extended to about 250 GeV for the higgsino mass. This analysis, along with other searches conducted by ATLAS and direct dark matter detection

experiments, paves the way towards a comprehensive search up to about 250 GeV irrespective of the assumption of the higgsino mass difference. This allows us to examine the simple consequence of the naturalness argument that the higgsino mass should be about the electroweak scale.

Bibliography

- [1] R. Barbieri and G. Giudice, *Upper bounds on supersymmetric particle masses*, *Nucl. Phys. B* **306** (1988) 63 (cit. on p. 13).
- [2] B. de Carlos and J. Casas, *One-loop analysis of the electroweak breaking in supersymmetric models and the fine-tuning problem*, *Phys. Lett. B* **309** (1993) 320, arXiv: [hep-ph/9303291](https://arxiv.org/abs/hep-ph/9303291) (cit. on p. 13).
- [3] V. C. Rubin and J. Ford W. Kent, *Rotation of the Andromeda Nebula from a Spectroscopic Survey of Emission Regions*, *The Astrophysical Journal* **159** (1970) 379 (cit. on pp. 13, 19).
- [4] V. C. Rubin, J. Ford W. K. and N. Thonnard, *Rotational properties of 21 SC galaxies with a large range of luminosities and radii, from NGC 4605 ($R=4kpc$) to UGC 2885 ($R=122kpc$).*, *The Astrophysical Journal* **238** (1980) 471 (cit. on pp. 13, 19).
- [5] R. Massey, T. Kitching and J. Richard, *The dark matter of gravitational lensing*, *Reports on Progress in Physics* **73** (2010) 086901, URL: <https://dx.doi.org/10.1088/0034-4885/73/8/086901> (cit. on pp. 13, 19).
- [6] D. Clowe et al., *A Direct Empirical Proof of the Existence of Dark Matter**, *The Astrophysical Journal* **648** (2006) L109, URL: <https://dx.doi.org/10.1086/508162> (cit. on pp. 13, 19).
- [7] Y. Golfand and E. Likhtman, *Extension of the Algebra of Poincare Group Generators and Violation of P Invariance*, *JETP Lett.* **13** (1971) 323, [*Pisma Zh. Eksp. Teor. Fiz.* **13** (1971) 452] (cit. on p. 13).
- [8] D. Volkov and V. Akulov, *Is the neutrino a goldstone particle?*, *Phys. Lett. B* **46** (1973) 109 (cit. on p. 13).
- [9] J. Wess and B. Zumino, *Supergauge transformations in four dimensions*, *Nucl. Phys. B* **70** (1974) 39 (cit. on p. 13).
- [10] J. Wess and B. Zumino, *Supergauge invariant extension of quantum electrodynamics*, *Nucl. Phys. B* **78** (1974) 1 (cit. on p. 13).
- [11] S. Ferrara and B. Zumino, *Supergauge invariant Yang-Mills theories*, *Nucl. Phys. B* **79** (1974) 413 (cit. on p. 13).

- [12] A. Salam and J. Strathdee, *Super-symmetry and non-Abelian gauges*, *Phys. Lett. B* **51** (1974) 353 (cit. on p. 13).
- [13] G. R. Farrar and P. Fayet, *Phenomenology of the production, decay, and detection of new hadronic states associated with supersymmetry*, *Phys. Lett. B* **76** (1978) 575 (cit. on p. 13).
- [14] S. P. Martin, *A Supersymmetry Primer*, *Adv. Ser. Direct. High Energy Phys.* **18** (1998) 1, arXiv: [hep-ph/9709356](https://arxiv.org/abs/hep-ph/9709356) (cit. on pp. 13, 21–23).
- [15] ATLAS Collaboration, *Search for long-lived charginos based on a disappearing-track signature using 136fb^{-1} of pp collisions at $\sqrt{s} = 13\text{ TeV}$ with the ATLAS detector*, *Eur. Phys. J. C* **82** (2022) 606, arXiv: [2201.02472](https://arxiv.org/abs/2201.02472) [[hep-ex](#)] (cit. on pp. 14, 129, 157).
- [16] CMS Collaboration, *Search for disappearing tracks in proton–proton collisions at $\sqrt{s} = 13\text{ TeV}$* , *Phys. Lett. B* **806** (2020) 135502, arXiv: [2004.05153](https://arxiv.org/abs/2004.05153) [[hep-ex](#)] (cit. on pp. 14, 28).
- [17] ATLAS Collaboration, *Searches for electroweak production of supersymmetric particles with compressed mass spectra in $\sqrt{s} = 13\text{ TeV}$ pp collisions with the ATLAS detector*, *Phys. Rev. D* **101** (2020) 052005, arXiv: [1911.12606](https://arxiv.org/abs/1911.12606) [[hep-ex](#)] (cit. on p. 14).
- [18] ATLAS Collaboration, *Search for chargino–neutralino pair production in final states with three leptons and missing transverse momentum in $\sqrt{s} = 13\text{ TeV}$ pp collisions with the ATLAS detector*, *Eur. Phys. J. C* **81** (2021) 1118, arXiv: [2106.01676](https://arxiv.org/abs/2106.01676) [[hep-ex](#)] (cit. on p. 14).
- [19] CMS Collaboration, *Search for electroweak production of charginos and neutralinos in proton–proton collisions at $\sqrt{s} = 13\text{ TeV}$* , *JHEP* **04** (2021) 147, arXiv: [2106.14246](https://arxiv.org/abs/2106.14246) [[hep-ex](#)] (cit. on p. 14).
- [20] ALEPH, DELPHI, L3 and O. Experiments, *Combined LEP Chargino Results, up to 208 GeV for low DM*, LEPSUSYWG/02-04.1, 2022, URL: https://lepsusy.web.cern.ch/lepsusy/www/inoslowdmsummer02/charginolowdm_pub.html (cit. on pp. 14, 28, 129).
- [21] J. Aalbers et al., *First Dark Matter Search Results from the LUX-ZEPLIN (LZ) Experiment*, *Phys. Rev. Lett.* **131** (4 2023) 041002, URL: <https://link.aps.org/doi/10.1103/PhysRevLett.131.041002> (cit. on pp. 14, 29, 30, 128).
- [22] *SUSY August 2023 Summary Plot Update*, tech. rep., All figures including auxiliary figures are available at <https://atlas.web.cern.ch/Atlas/GROUPS/PHYSICS/PUBNOTES/ATL-PHYS-PUB-2023-025>: CERN, 2023, URL: <https://cds.cern.ch/record/2871728> (cit. on p. 14).
- [23] P. Fayet, *Supersymmetry and weak, electromagnetic and strong interactions*, *Phys. Lett. B* **64** (1976) 159 (cit. on p. 17).

- [24] P. Fayet, *Spontaneously broken supersymmetric theories of weak, electromagnetic and strong interactions*, *Phys. Lett. B* **69** (1977) 489 (cit. on p. 17).
- [25] *Measurement and QCD analysis of neutral and charged current cross sections at HERA*, *The European Physical Journal C* **30** (2003) 1, ISSN: 1434-6052, URL: <http://dx.doi.org/10.1140/epjc/s2003-01257-6> (cit. on p. 17).
- [26] *An NLO QCD analysis of inclusive cross-section and jet-production data from the ZEUS experiment*, *The European Physical Journal C* **42** (2005) 1, ISSN: 1434-6052, URL: <http://dx.doi.org/10.1140/epjc/s2005-02293-x> (cit. on p. 17).
- [27] H1 and Z. Collaborations, *Combination of Measurements of Inclusive Deep Inelastic $e^\pm p$ Scattering Cross Sections and QCD Analysis of HERA Data*, 2015, arXiv: [1506.06042](https://arxiv.org/abs/1506.06042) [hep-ex] (cit. on p. 17).
- [28] K. Abe et al., *Precise Measurement of the Left-Right Cross Section Asymmetry in Z Boson Production by e^+e^- Collisions*, *Phys. Rev. Lett.* **73** (1 1994) 25, URL: <https://link.aps.org/doi/10.1103/PhysRevLett.73.25> (cit. on p. 18).
- [29] *Electroweak parameters of the Z0 resonance and the standard model*, *Physics Letters B* **276** (1992) 247, ISSN: 0370-2693, URL: <https://www.sciencedirect.com/science/article/pii/037026939290572L> (cit. on p. 18).
- [30] F. Abe et al., *Evidence for top quark production in p^-p collisions at $\sqrt{s}=1.8$ TeV*, *Phys. Rev. Lett.* **73** (2 1994) 225, URL: <https://link.aps.org/doi/10.1103/PhysRevLett.73.225> (cit. on p. 18).
- [31] F. Englert and R. Brout, *Broken Symmetry and the Mass of Gauge Vector Mesons*, *Phys. Rev. Lett.* **13** (9 1964) 321, URL: <https://link.aps.org/doi/10.1103/PhysRevLett.13.321> (cit. on p. 18).
- [32] P. W. Higgs, *Broken Symmetries and the Masses of Gauge Bosons*, *Phys. Rev. Lett.* **13** (16 1964) 508, URL: <https://link.aps.org/doi/10.1103/PhysRevLett.13.508> (cit. on p. 18).
- [33] ATLAS Collaboration, *Observation of a new particle in the search for the Standard Model Higgs boson with the ATLAS detector at the LHC*, *Phys. Lett. B* **716** (2012) 1, arXiv: [1207.7214](https://arxiv.org/abs/1207.7214) [hep-ex] (cit. on p. 18).
- [34] CMS Collaboration, *Observation of a new boson at a mass of 125 GeV with the CMS experiment at the LHC*, *Phys. Lett. B* **716** (2012) 30, arXiv: [1207.7235](https://arxiv.org/abs/1207.7235) [hep-ex] (cit. on p. 18).
- [35] TEXample.net, *Standard model of physics*, URL: <http://www.texample.net/tikz/examples/model-physics/> (cit. on p. 18).
- [36] Planck Collaboration et al., *Planck 2018 results - VI. Cosmological parameters*, *A&A* **641** (2020) A6, URL: <https://doi.org/10.1051/0004-6361/201833910> (cit. on p. 19).

- [37] T. Bringmann, F. Calore, A. Galea and M. Garny, *Electroweak and Higgs boson internal bremsstrahlung. General considerations for Majorana dark matter annihilation and application to MSSM neutralinos*, *Journal of High Energy Physics* **2017** (2017) 41, URL: [https://doi.org/10.1007/JHEP09\(2017\)041](https://doi.org/10.1007/JHEP09(2017)041) (cit. on p. 23).
- [38] P. Ciafaloni et al., *On the importance of electroweak corrections for Majorana dark matter indirect detection*, *Journal of Cosmology and Astroparticle Physics* **2011** (2011) 018, ISSN: 1475-7516, URL: <http://dx.doi.org/10.1088/1475-7516/2011/06/018> (cit. on p. 23).
- [39] *ATLAS Run 2 searches for electroweak production of supersymmetric particles interpreted within the pMSSM*, All figures including auxiliary figures are available at <https://atlas.web.cern.ch/Atlas/GROUPS/PHYSICS/CONFNOTES/ATLAS-CONF-2023-055>: CERN, 2023, URL: <https://cds.cern.ch/record/2870222> (cit. on pp. 24, 158, 159).
- [40] J. A. Casas, J. M. Moreno, S. Robles, K. Rolbiecki and B. Zaldívar, *What is a natural SUSY scenario?*, *Journal of High Energy Physics* **2015** (2015) 70, URL: [https://doi.org/10.1007/JHEP06\(2015\)070](https://doi.org/10.1007/JHEP06(2015)070) (cit. on p. 25).
- [41] M. Papucci, J. T. Ruderman and A. Weiler, *Natural SUSY endures*, *Journal of High Energy Physics* **2012** (2012) 35, URL: [https://doi.org/10.1007/JHEP09\(2012\)035](https://doi.org/10.1007/JHEP09(2012)035) (cit. on p. 25).
- [42] H. Fukuda, N. Nagata, H. Oide, H. Otono and S. Shirai, *Cornering Higgsinos Using Soft Displaced Tracks*, *Phys. Rev. Lett.* **124** (10 2020) 101801, URL: <https://link.aps.org/doi/10.1103/PhysRevLett.124.101801> (cit. on pp. 25, 26, 29).
- [43] H. Zhou and N. Liu, *Probing compressed higgsinos with forward protons at the LHC*, 2022, arXiv: [2208.10406](https://arxiv.org/abs/2208.10406) [hep-ph] (cit. on p. 25).
- [44] S. P. Martin, *Implications of purity constraints on light higgsinos*, 2024, arXiv: [2403.19598](https://arxiv.org/abs/2403.19598) [hep-ph] (cit. on p. 25).
- [45] M. Ibe, Y. Nakayama and S. Shirai, *Precise estimate of charged Higgsino/Wino decay rate*, *Journal of High Energy Physics* **2024** (2024), ISSN: 1029-8479, URL: [http://dx.doi.org/10.1007/JHEP03\(2024\)012](http://dx.doi.org/10.1007/JHEP03(2024)012) (cit. on p. 25).
- [46] ATLAS Collaboration, *Search for new phenomena in events with an energetic jet and missing transverse momentum in pp collisions at $\sqrt{s} = 13$ TeV with the ATLAS detector*, *Phys. Rev. D* **103** (2021) 112006, arXiv: [2102.10874](https://arxiv.org/abs/2102.10874) [hep-ex] (cit. on p. 27).
- [47] CMS Collaboration, *Search for new particles in events with energetic jets and large missing transverse momentum in proton–proton collisions at $\sqrt{s} = 13$ TeV*, *JHEP* **11** (2021) 153, arXiv: [2107.13021](https://arxiv.org/abs/2107.13021) [hep-ex] (cit. on p. 27).

- [48] CMS Collaboration, *Search for supersymmetry in final states with two or three soft leptons and missing transverse momentum in proton–proton collisions at $\sqrt{s} = 13$ TeV*, *JHEP* **04** (2021) 091, arXiv: 2111.06296 [hep-ex] (cit. on p. 28).
- [49] N. Nagata and S. Shirai, *Higgsino dark matter in high-scale supersymmetry*, *Journal of High Energy Physics* **2015** (2015) 29, URL: [https://doi.org/10.1007/JHEP01\(2015\)029](https://doi.org/10.1007/JHEP01(2015)029) (cit. on pp. 29–31).
- [50] C. Dessert, J. W. Foster, Y. Park, B. R. Safdi and W. L. Xu, *Higgsino Dark Matter Confronts 14 Years of Fermi γ -Ray Data*, *Phys. Rev. Lett.* **130** (20 2023) 201001, URL: <https://link.aps.org/doi/10.1103/PhysRevLett.130.201001> (cit. on p. 30).
- [51] Y. Li, S. Profumo and M. Ramsey-Musolf, *Bino-driven electroweak baryogenesis with highly suppressed electric dipole moments*, *Physics Letters B* **673** (2009) 95, ISSN: 0370-2693, URL: <https://www.sciencedirect.com/science/article/pii/S037026930900149X> (cit. on p. 31).
- [52] T. S. Roussy et al., *An improved bound on the electron’s electric dipole moment*, *Science* **381** (2023) 46, eprint: <https://www.science.org/doi/pdf/10.1126/science.adg4084>, URL: <https://www.science.org/doi/abs/10.1126/science.adg4084> (cit. on pp. 31, 32, 128).
- [53] V. A. Beylin, V. I. Kuksa, G. M. Vereshkov and R. S. Pasechnik, *Neutralino-nucleon interaction in the Split Higgsino scenario of the Dark Matter*, *Int. J. Mod. Phys. A* **24** (2009) 6051, arXiv: 0903.4201 [hep-ph] (cit. on p. 33).
- [54] ATLAS Collaboration, *The ATLAS Experiment at the CERN Large Hadron Collider*, *JINST* **3** (2008) S08003 (cit. on pp. 34, 36–41).
- [55] CMS Collaboration, *The CMS Experiment at the CERN LHC*, *JINST* **3** (2008) S08004 (cit. on p. 34).
- [56] T. A. Collaboration et al., *The ALICE experiment at the CERN LHC*, *Journal of Instrumentation* **3** (2008) S08002, URL: <https://dx.doi.org/10.1088/1748-0221/3/08/S08002> (cit. on p. 34).
- [57] T. L. Collaboration et al., *The LHCb Detector at the LHC*, *Journal of Instrumentation* **3** (2008) S08005, URL: <https://dx.doi.org/10.1088/1748-0221/3/08/S08005> (cit. on p. 34).
- [58] E. Mobs, *The CERN accelerator complex - August 2018. Complexe des accélérateurs du CERN - Août 2018*, (2018), General Photo, URL: <https://cds.cern.ch/record/2636343> (cit. on p. 35).
- [59] ATLAS Collaboration, *Luminosity determination in pp collisions at $\sqrt{s} = 13$ TeV using the ATLAS detector at the LHC*, (2022), arXiv: 2212.09379 [hep-ex] (cit. on pp. 35, 45, 112).

- [60] F. Huegging, *The ATLAS Pixel Insertable B-Layer (IBL)*, tech. rep., CERN, 2010, URL: <https://cds.cern.ch/record/1303015> (cit. on p. 38).
- [61] ATLAS Collaboration, *Alignment of the ATLAS Inner Detector in Run-2*, *Eur. Phys. J. C* **80** (2020) 1194, arXiv: 2007.07624 [hep-ex] (cit. on p. 38).
- [62] ATLAS Collaboration, *ATLAS Liquid Argon Calorimeter: Technical Design Report*, ATLAS-TDR-2; CERN-LHCC-96-041, 1996, URL: <https://cds.cern.ch/record/331061> (cit. on p. 40).
- [63] ATLAS Collaboration, *Performance of the ATLAS trigger system in 2015*, *Eur. Phys. J. C* **77** (2017) 317, arXiv: 1611.09661 [hep-ex] (cit. on p. 42).
- [64] ATLAS Collaboration, *Performance of the missing transverse momentum triggers for the ATLAS detector during Run-2 data taking*, *JHEP* **08** (2020) 080, arXiv: 2005.09554 [hep-ex] (cit. on pp. 43, 66).
- [65] ATLAS Collaboration, *ATLAS data quality operations and performance for 2015–2018 data-taking*, *JINST* **15** (2020) P04003, arXiv: 1911.04632 [physics.ins-det] (cit. on p. 45).
- [66] G. Avoni et al., *The new LUCID-2 detector for luminosity measurement and monitoring in ATLAS*, *Journal of Instrumentation* **13** (2018) P07017, URL: <https://dx.doi.org/10.1088/1748-0221/13/07/P07017> (cit. on pp. 45, 112).
- [67] A. Collaboration, *LuminosityPublicResultsRun2*, URL: <https://twiki.cern.ch/twiki/bin/view/AtlasPublic/LuminosityPublicResultsRun2> (cit. on p. 46).
- [68] T. Gleisberg et al., *Event generation with SHERPA 1.1*, *JHEP* **02** (2009) 007, arXiv: 0811.4622 [hep-ph] (cit. on pp. 46, 48).
- [69] P. Skands, *QCD for Collider Physics*, 2012, arXiv: 1104.2863 [hep-ph] (cit. on p. 46).
- [70] G. Altarelli and G. Parisi, *Asymptotic freedom in parton language*, *Nuclear Physics B* **126** (1977) 298, ISSN: 0550-3213, URL: <https://www.sciencedirect.com/science/article/pii/0550321377903844> (cit. on p. 47).
- [71] V. Gribov and L. Lipatov, *Deep inelastic electron scattering in perturbation theory*, *Physics Letters B* **37** (1971) 78, ISSN: 0370-2693, URL: <https://www.sciencedirect.com/science/article/pii/0370269371905764> (cit. on p. 47).
- [72] Y. L. Dokshitzer, *Calculation of the Structure Functions for Deep Inelastic Scattering and e^+e^- Annihilation by Perturbation Theory in Quantum Chromodynamics.*, *Sov. Phys. JETP* **46** (1977) 641 (cit. on p. 47).

- [73] B. Andersson, G. Gustafson, G. Ingelman and T. Sjöstrand, *Parton fragmentation and string dynamics*, *Physics Reports* **97** (1983) 31, ISSN: 0370-1573, URL: <https://www.sciencedirect.com/science/article/pii/0370157383900807> (cit. on p. 47).
- [74] ATLAS Collaboration, *The ATLAS Simulation Infrastructure*, *Eur. Phys. J. C* **70** (2010) 823, arXiv: [1005.4568](https://arxiv.org/abs/1005.4568) [[physics.ins-det](https://arxiv.org/archive/physics)] (cit. on p. 47).
- [75] S. Agostinelli et al., *GEANT4 – a simulation toolkit*, *Nucl. Instrum. Meth. A* **506** (2003) 250 (cit. on p. 47).
- [76] W. Lukas, *Fast Simulation for ATLAS: Atfast-II and ISF*, *J. Phys. Conf. Ser.* **396** (2012) 022031, ed. by M. Ernst, D. Düllmann, O. Rind and T. Wong (cit. on p. 47).
- [77] The NNPDF Collaboration, R. D. Ball et al., *Parton distributions for the LHC run II*, *JHEP* **04** (2015) 040, arXiv: [1410.8849](https://arxiv.org/abs/1410.8849) [[hep-ph](https://arxiv.org/archive/hep)] (cit. on p. 48).
- [78] S. Catani, L. Cieri, G. Ferrera, D. de Florian and M. Grazzini, *Vector Boson Production at Hadron Colliders: A Fully Exclusive QCD Calculation at Next-to-Next-to-Leading Order*, *Phys. Rev. Lett.* **103** (8 2009) 082001, URL: <https://link.aps.org/doi/10.1103/PhysRevLett.103.082001> (cit. on p. 48).
- [79] S. Frixione, G. Ridolfi and P. Nason, *A positive-weight next-to-leading-order Monte Carlo for heavy flavour hadroproduction*, *JHEP* **09** (2007) 126, arXiv: [0707.3088](https://arxiv.org/abs/0707.3088) [[hep-ph](https://arxiv.org/archive/hep)] (cit. on p. 48).
- [80] P. Nason, *A new method for combining NLO QCD with shower Monte Carlo algorithms*, *JHEP* **11** (2004) 040, arXiv: [hep-ph/0409146](https://arxiv.org/abs/hep-ph/0409146) (cit. on p. 48).
- [81] S. Frixione, P. Nason and C. Oleari, *Matching NLO QCD computations with parton shower simulations: the POWHEG method*, *JHEP* **11** (2007) 070, arXiv: [0709.2092](https://arxiv.org/abs/0709.2092) [[hep-ph](https://arxiv.org/archive/hep)] (cit. on p. 48).
- [82] S. Alioli, P. Nason, C. Oleari and E. Re, *A general framework for implementing NLO calculations in shower Monte Carlo programs: the POWHEG BOX*, *JHEP* **06** (2010) 043, arXiv: [1002.2581](https://arxiv.org/abs/1002.2581) [[hep-ph](https://arxiv.org/archive/hep)] (cit. on p. 48).
- [83] T. Sjöstrand et al., *An introduction to PYTHIA 8.2*, *Comput. Phys. Commun.* **191** (2015) 159, arXiv: [1410.3012](https://arxiv.org/abs/1410.3012) [[hep-ph](https://arxiv.org/archive/hep)] (cit. on p. 48).
- [84] ATLAS Collaboration, *ATLAS Pythia 8 tunes to 7 TeV data*, ATL-PHYS-PUB-2014-021, 2014, URL: <https://cds.cern.ch/record/1966419> (cit. on p. 48).
- [85] D. J. Lange, *The EvtGen particle decay simulation package*, *Nuclear Instruments and Methods in Physics Research Section A: Accelerators, Spectrometers, Detectors and Associated Equipment* **462** (2001) 152, BEAUTY2000, Proceedings of the 7th Int. Conf. on B-Physics at Hadron Machines, ISSN: 0168-9002, URL: <https://www.sciencedirect.com/science/article/pii/S0168900201000894> (cit. on p. 49).

- [86] M. Czakon and A. Mitov, *Top++: A program for the calculation of the top-pair cross-section at hadron colliders*, *Comput. Phys. Commun.* **185** (2014) 2930, arXiv: [1112.5675 \[hep-ph\]](#) (cit. on p. 49).
- [87] J. Alwall et al., *The automated computation of tree-level and next-to-leading order differential cross sections, and their matching to parton shower simulations*, *JHEP* **07** (2014) 079, arXiv: [1405.0301 \[hep-ph\]](#) (cit. on p. 49).
- [88] B. Fuks, M. Klasen, D. R. Lamprea and M. Rothering, *Precision predictions for electroweak superpartner production at hadron colliders with RESUMMINO*, *Eur. Phys. J. C* **73** (2013) 2480, arXiv: [1304.0790 \[hep-ph\]](#) (cit. on p. 49).
- [89] S. Frixione, E. Laenen, P. Motylinski and B. R. Webber, *Angular correlations of lepton pairs from vector boson and top quark decays in Monte Carlo simulations*, *JHEP* **04** (2007) 081, arXiv: [hep-ph/0702198](#) (cit. on p. 49).
- [90] P. Artoisenet, R. Frederix, O. Mattelaer and R. Rietkerk, *Automatic spin-entangled decays of heavy resonances in Monte Carlo simulations*, *JHEP* **03** (2013) 015, arXiv: [1212.3460 \[hep-ph\]](#) (cit. on p. 49).
- [91] A. Collaboration, *Summary plots from the ATLAS Standard Model physics group*, URL: <https://atlas.web.cern.ch/Atlas/GROUPS/PHYSICS/CombinedSummaryPlots/SM> (cit. on p. 51).
- [92] L. S. C. S. W. Group, *SUSYCrossSections*, URL: <https://twiki.cern.ch/twiki/bin/view/LHCPhysics/SUSYCrossSections> (cit. on p. 51).
- [93] ATLAS Collaboration, *Performance of the ATLAS track reconstruction algorithms in dense environments in LHC Run 2*, *Eur. Phys. J. C* **77** (2017) 673, arXiv: [1704.07983 \[hep-ex\]](#) (cit. on p. 54).
- [94] R. Frühwirth, *Application of Kalman filtering to track and vertex fitting*, *Nuclear Instruments and Methods in Physics Research Section A: Accelerators, Spectrometers, Detectors and Associated Equipment* **262** (1987) 444, ISSN: 0168-9002, URL: <https://www.sciencedirect.com/science/article/pii/0168900287908874> (cit. on p. 54).
- [95] ATLAS Collaboration, *Reconstruction of primary vertices at the ATLAS experiment in Run 1 proton–proton collisions at the LHC*, *Eur. Phys. J. C* **77** (2017) 332, arXiv: [1611.10235 \[hep-ex\]](#) (cit. on p. 56).
- [96] W. Waltenberger, *Adaptive vertex reconstruction*, (2008) (cit. on p. 56).
- [97] ATLAS Collaboration, *Jet reconstruction and performance using particle flow with the ATLAS Detector*, *Eur. Phys. J. C* **77** (2017) 466, arXiv: [1703.10485 \[hep-ex\]](#) (cit. on pp. 56, 57, 172).
- [98] M. Cacciari, G. P. Salam and G. Soyez, *The anti- k_t jet clustering algorithm*, *JHEP* **04** (2008) 063, arXiv: [0802.1189 \[hep-ph\]](#) (cit. on p. 57).

- [99] ATLAS Collaboration, *Performance of pile-up mitigation techniques for jets in pp collisions at $\sqrt{s} = 8$ TeV using the ATLAS detector*, *Eur. Phys. J. C* **76** (2016) 581, arXiv: [1510.03823](https://arxiv.org/abs/1510.03823) [[hep-ex](#)] (cit. on p. 57).
- [100] ATLAS Collaboration, *ATLAS flavour-tagging algorithms for the LHC Run 2 pp collision dataset*, (2022), arXiv: [2211.16345](https://arxiv.org/abs/2211.16345) [[physics.data-an](#)] (cit. on p. 57).
- [101] ATLAS Collaboration, *Jet energy scale and resolution measured in proton–proton collisions at $\sqrt{s} = 13$ TeV with the ATLAS detector*, *Eur. Phys. J. C* **81** (2020) 689, arXiv: [2007.02645](https://arxiv.org/abs/2007.02645) [[hep-ex](#)] (cit. on pp. 58, 110, 111, 201).
- [102] ATLAS Collaboration, *Performance of missing transverse momentum reconstruction with the ATLAS detector using proton–proton collisions at $\sqrt{s} = 13$ TeV*, *Eur. Phys. J. C* **78** (2018) 903, arXiv: [1802.08168](https://arxiv.org/abs/1802.08168) [[hep-ex](#)] (cit. on pp. 60, 112).
- [103] ATLAS Collaboration, *E_T^{miss} performance in the ATLAS detector using 2015–2016 LHC pp collisions*, ATLAS-CONF-2018-023, 2018, URL: <https://cds.cern.ch/record/2625233> (cit. on p. 61).
- [104] A. Collaboration, *Impact Parameter Resolution Using 2016 MB Data*, URL: <https://atlas.web.cern.ch/Atlas/GROUPS/PHYSICS/PLOTS/IDTR-2016-018/> (cit. on p. 65).
- [105] ATLAS Collaboration, *Selection of jets produced in 13 TeV proton–proton collisions with the ATLAS detector*, ATLAS-CONF-2015-029, 2015, URL: <https://cds.cern.ch/record/2037702> (cit. on p. 66).
- [106] ATLAS Collaboration, *Early Inner Detector Tracking Performance in the 2015 Data at $\sqrt{s} = 13$ TeV*, ATL-PHYS-PUB-2015-051, 2015, URL: <https://cds.cern.ch/record/2110140> (cit. on pp. 68, 69).
- [107] A. Collaboration, *Number of tracks vs. mu with full 2016 data*, URL: <https://atlas.web.cern.ch/Atlas/GROUPS/PHYSICS/PLOTS/IDTR-2016-015/> (cit. on p. 69).
- [108] ATLAS Collaboration, *K_S^0 and Λ production in pp interactions at $\sqrt{s} = 0.9$ and 7 TeV measured with the ATLAS detector at the LHC*, *Phys. Rev. D* **85** (2012) 012001, arXiv: [1111.1297](https://arxiv.org/abs/1111.1297) [[hep-ex](#)] (cit. on p. 71).
- [109] ATLAS Collaboration, *Performance of the reconstruction of large impact parameter tracks in the inner detector of ATLAS*, ATL-PHYS-PUB-2017-014, 2017, URL: <https://cds.cern.ch/record/2275635> (cit. on p. 71).
- [110] ATLAS Collaboration, *Formulae for Estimating Significance*, ATL-PHYS-PUB-2020-025, 2020, URL: <https://cds.cern.ch/record/2736148> (cit. on p. 76).

- [111] ATLAS Collaboration, *Multi-boson simulation for 13 TeV ATLAS analyses*, ATL-PHYS-PUB-2016-002, 2016, URL: <https://cds.cern.ch/record/2119986> (cit. on p. 109).
- [112] J. Butterworth et al., *PDF4LHC recommendations for LHC Run II*, *J. Phys. G* **43** (2016) 023001, arXiv: [1510.03865](https://arxiv.org/abs/1510.03865) [hep-ph] (cit. on p. 109).
- [113] S. Kallweit, J. M. Lindert, P. Maierhöfer, S. Pozzorini and M. Schönherr, *NLO electroweak automation and precise predictions for W+multijet production at the LHC*, 2015, arXiv: [1412.5157](https://arxiv.org/abs/1412.5157) [hep-ph] (cit. on p. 110).
- [114] ATLAS Collaboration, *Tagging and suppression of pileup jets with the ATLAS detector*, ATL-CONF-2014-018, 2014, URL: <https://cds.cern.ch/record/1700870> (cit. on pp. 110, 201).
- [115] ATLAS Collaboration, *Measurement of the Inelastic Proton–Proton Cross Section at $\sqrt{s} = 13$ TeV with the ATLAS Detector at the LHC*, *Phys. Rev. Lett.* **117** (2016) 182002, arXiv: [1606.02625](https://arxiv.org/abs/1606.02625) [hep-ex] (cit. on p. 112).
- [116] ATLAS Collaboration, *Muon reconstruction and identification efficiency in ATLAS using the full Run 2 pp collision data set at $\sqrt{s} = 13$ TeV*, *Eur. Phys. J. C* **81** (2021) 578, arXiv: [2012.00578](https://arxiv.org/abs/2012.00578) [hep-ex] (cit. on pp. 112, 172, 174).
- [117] ATLAS Collaboration, *Electron reconstruction and identification in the ATLAS experiment using the 2015 and 2016 LHC proton–proton collision data at $\sqrt{s} = 13$ TeV*, *Eur. Phys. J. C* **79** (2019) 639, arXiv: [1902.04655](https://arxiv.org/abs/1902.04655) [hep-ex] (cit. on p. 112).
- [118] ATLAS sensitivity to winos and higgsinos with a highly compressed mass spectrum at the HL-LHC, tech. rep., All figures including auxiliary figures are available at <https://atlas.web.cern.ch/Atlas/GROUPS/PHYSICS/PUBNOTES/ATL-PHYS-PUB-2018-031>: CERN, 2018, URL: <https://cds.cern.ch/record/2647294> (cit. on p. 129).
- [119] ATLAS Collaboration, *Expected tracking and related performance with the updated ATLAS Inner Tracker layout at the High-Luminosity LHC*, ATL-PHYS-PUB-2021-024, 2021, URL: <https://cds.cern.ch/record/2776651> (cit. on p. 131).
- [120] B. Abi et al., *Measurement of the Positive Muon Anomalous Magnetic Moment to 0.46 ppm*, *Phys. Rev. Lett.* **126** (14 2021) 141801, URL: <https://link.aps.org/doi/10.1103/PhysRevLett.126.141801> (cit. on p. 156).
- [121] R. L. Workman et al., *Review of Particle Physics*, *PTEP* **2022** (2022) 083C01 (cit. on p. 155).
- [122] D. P. Aguillard et al., *Measurement of the Positive Muon Anomalous Magnetic Moment to 0.20 ppm*, *Phys. Rev. Lett.* **131** (16 2023) 161802, URL: <https://link.aps.org/doi/10.1103/PhysRevLett.131.161802> (cit. on p. 155).

- [123] J. Zhao, J. Zhu, P. Zhu and R. Zhu,
Light Higgsino scenario confronted with the muon $g - 2$,
Phys. Rev. D **107** (5 2023) 055030,
URL: <https://link.aps.org/doi/10.1103/PhysRevD.107.055030>
(cit. on p. 156).
- [124] S. Iwamoto, T. T. Yanagida and N. Yokozaki,
Wino-Higgsino dark matter in MSSM from the $g-2$ anomaly,
Physics Letters B **823** (2021) 136768, ISSN: 0370-2693, URL: <https://www.sciencedirect.com/science/article/pii/S0370269321007085>
(cit. on p. 156).
- [125] S. Profumo, T. Stefaniak and L. Stephenson-Haskins, *Not-so-well-tempered neutralino,*
Phys. Rev. D **96** (5 2017) 055018,
URL: <https://link.aps.org/doi/10.1103/PhysRevD.96.055018>
(cit. on p. 157).
- [126] ATLAS Collaboration,
ATLAS Muon Spectrometer Phase-II Upgrade: Technical Design Report,
ATLAS-TDR-026; CERN-LHCC-2017-017, 2017,
URL: <https://cds.cern.ch/record/2285580> (cit. on p. 163).
- [127] A. Collaboration, *Level-0 TGC trigger performance of trigger algorithms in software and firmware implementations,* URL: <https://twiki.cern.ch/twiki/bin/view/AtlasPublic/L0MuonTriggerPublicResults> (cit. on p. 170).
- [128] ATLAS Collaboration, *Electron and photon performance measurements with the ATLAS detector using the 2015–2017 LHC proton–proton collision data,*
JINST **14** (2019) P12006, arXiv: [1908.00005](https://arxiv.org/abs/1908.00005) [hep-ex] (cit. on pp. 174, 179).
- [129] A. Hoecker et al., *TMVA - Toolkit for Multivariate Data Analysis,* 2007,
arXiv: [physics/0703039](https://arxiv.org/abs/physics/0703039) [physics.data-an] (cit. on p. 175).
- [130] A. Collaboration,
Electron and photon efficiencies in LHC Run 2 with the ATLAS experiment, 2023,
arXiv: [2308.13362](https://arxiv.org/abs/2308.13362) [hep-ex] (cit. on pp. 177, 178).
- [131] ATLAS Collaboration, *ATLAS Inner Tracker Pixel Detector: Technical Design Report,*
ATLAS-TDR-030; CERN-LHCC-2017-021, 2017,
URL: <https://cds.cern.ch/record/2285585> (cit. on p. 188).
- [132] ATLAS Collaboration, *Characterisation and mitigation of beam-induced backgrounds observed in the ATLAS detector during the 2011 proton–proton run,*
JINST **8** (2013) P07004, arXiv: [1303.0223](https://arxiv.org/abs/1303.0223) [hep-ex] (cit. on p. 191).

List of Figures

1.1	Existing experimental constraints on the higgsino states with compressed mass spectra, established by the ATLAS experiment.	14
1.2	The masses and lifetimes of metastable particles in the SM.	15
1.3	Schematics of the mildly-displaced track signature.	15
2.1	Particles constituting the SM.	18
2.2	Diagram of a proton decay mediated by a strange squark.	21
2.3	Renormalization group evolution of the inverse gauge couplings $\alpha_a^{-1}(Q)$ ($a = 1, 2, 3$), calculated up to two-loop effects.	22
2.4	Scatter plot of the neutralino mass points that pass through the pMSSM scan and the resulting relic density.	24
2.5	Schematic of the mass spectra of electroweakinos in the higgsino LSP scenario with the gauginos decoupled in mass.	26
2.6	Dependence of the chargino lifetime ($c\tau$) on the mass difference between the chargino and neutralino (Δm_{\pm}).	27
2.7	Diagrams of processes targeted by the existing searches for electroweakino-pair production with compressed mass spectra of higgsinos.	28
2.8	Diagrams inducing elastic and inelastic scattering between neutralinos and quarks.	30
2.9	Dependence of the SI elastic scattering cross-section on the gaugino mass.	30
2.10	Barr-Zee diagrams induced by charginos contributing to the electron EDM.	31
2.11	Dependence of the electron EDM on the gaugino mass.	32
2.12	Branching ratio and higgsino mass difference dependence for $\tilde{\chi}_1^{\pm}$ and $\tilde{\chi}_2^0$	33
3.1	Overall view of the LHC accelerator system.	35
3.2	Cross-section view and coordinate system of the ATLAS detector.	36
3.3	Layout of the superconducting magnets in the ATLAS detector.	37
3.4	Schematic of the ID in the barrel region.	38
3.5	Schematic of the ID in the endcap region.	39
3.6	Layout of the calorimeters and MSs in the ATLAS detector.	40
3.7	Overview of the trigger and data acquisition system in Run 2.	42
4.1	Mean number of interactions per crossing for each data-taking year.	46

4.2	Illustration of the event generation step of a $t\bar{t}h$ event.	46
4.3	Feynman diagrams illustrating single boson and di-boson productions.	48
4.4	Feynman diagrams illustrating top-quark pair and single top productions.	49
4.5	Feynman diagrams illustrating QCD multijet productions.	49
4.6	Feynman diagrams illustrating pair productions of electroweakinos.	50
4.7	Production cross-section of SM background processes and signal processes. . .	51
5.1	Schematic view of various particles passing through the ATLAS detector, leaving characteristic signals in the detector.	53
5.2	Schematic of the event reconstruction flow utilized in this thesis.	53
5.3	Schematics of the track reconstruction process.	55
5.4	Schematics of the track parameters viewed from both the beam axis and a viewpoint perpendicular to the beam axis.	55
5.5	Dependence of the calibrated jet relative energy resolution on jet p_T	58
5.6	E_T^{miss} and soft term distributions in data and simulation for $Z \rightarrow \mu\mu$ events. . .	61
6.1	Feynman diagram of the higgsinos pair-production process targeted by this analysis. .	64
6.2	Resolution of transverse and longitudinal impact parameters.	65
6.3	Schematic of the analysis strategy.	65
6.4	E_T^{miss} trigger efficiency for each data-taking period during Run 2.	66
6.5	Distribution of ϕ direction of E_T^{miss} before and after applying the <i>Tight</i> jet cleaning. .	67
6.6	Distributions for track performance.	69
6.7	Schematic of tracks from the primary vertex and pileup vertices in an event. . .	70
6.8	Shape comparison of track $ \eta $ and $ \Delta z_0 \sin \theta $ distributions after requiring the <i>Tight Primary</i> working point.	70
6.9	Decay topology of chargino decay, 1-prong τ decay, 3-prong τ decay, B meson decay, and K_S^0 decay.	71
6.10	Distribution of track p_T after requiring the “jets+ E_T^{miss} ” signature and signal track selections.	72
6.11	Distribution of $\min(\Delta\phi(\mathbf{p}_T^{\text{jets}}, \mathbf{p}_T^{\text{miss}}))$ after requiring the “jets+ E_T^{miss} ” signature. .	74
6.12	Shape comparison of $ \Delta\phi(\mathbf{p}_T^{\text{track}}, \mathbf{p}_T^{\text{miss}}) $ distributions after requiring all preselections and displacement for signal tracks.	75
6.13	Shape comparison of E_T^{miss} , track p_T , and track $S(d_0)$ distributions after requiring all preselections.	77
6.14	Track $S(d_0)$ distribution after applying $E_T^{\text{miss}} > 600$ GeV and track $p_T \in [2, 5]$ GeV .	78
6.15	Proportion and efficiency of signal tracks after each selection.	79
6.16	E_T^{miss} and track p_T distributions.	80
7.1	Pie-charts showing the background composition in each SR.	81
7.2	Composition of signal candidate tracks in SR-Low and SR-High from $W(\rightarrow \tau\nu)$ +jets process.	83
7.3	Composition of signal candidate tracks in SR-Low and SR-High from $Z(\rightarrow \nu\bar{\nu})$ +jets process	84
7.4	Pre-fit track p_T distribution without applying the track p_T selection.	86

7.5	Distribution of $S(d_0)$ of the leading muon.	86
7.6	Schematic views of region definition for τ decay track background estimation.	87
7.7	Distribution of m_T in the $1\mu_{\text{base}}$ category.	89
7.8	Pie-charts showing the background composition in the CRs for τ decay tracks.	90
7.9	Pie-charts showing the background composition in the VRs for τ decay tracks.	90
7.10	Post-fit track $S(d_0)$ distributions in VRs for estimating τ decay tracks.	91
7.11	Schematic of the event topology among different V +jets processes in the ATLAS detector.	93
7.12	Schematic of the region definitions in the 0ℓ and 1μ category.	94
7.13	Schematic of the region definitions for validation of the measured TFs.	95
7.14	Distribution of m_T in the 1μ and $1e$ categories.	96
7.15	Distribution of $m_{\ell\ell}$ in the 2ℓ category.	97
7.16	$S(d_0)$ and $\Delta R(\text{electron, track})$ distribution of tracks in the $2e$ category.	98
7.17	Pie-charts showing the background composition in the 1μ , $1e$, 2ℓ , 1γ , and $1\gamma_{\text{base}}$ category.	99
7.18	Post-fit distributions for VRs in the $1e$ category.	101
7.19	Post-fit distributions for VRs in the 2ℓ category.	102
7.20	Post-fit distributions for VRs in the 1γ category.	103
7.21	Post-fit distributions for VRs in the $1\gamma_{\text{base}}$ category.	104
7.22	Schematic of the region definitions of VRs near the SRs.	105
7.23	Pie-charts showing the background composition in the 0ℓ category.	106
7.24	Post-fit distributions for VRs near the SRs.	107
7.25	Overview of fit results in the VRs.	108
8.1	Fractional uncertainty on the jet energy scale as a function of jet p_T and η	111
8.2	Comparison of the track $S(d_0)$ distribution and TFs calculated in the 0ℓ , 1μ , $1e$, 2μ and $2e$ category.	113
8.3	Systematic uncertainties on the post-fit background yields in the SRs, VRs for QCD tracks, and VRs for τ decay tracks.	114
9.1	Overview of fit results in the SRs.	117
9.2	Post-fit track $S(d_0)$ distribution in the SR bins and CR- 0ℓ	118
9.3	Post-fit distributions in the SR bins.	119
9.4	Event display of a data event recorded in 2018 data, categorized into SR-High.	120
9.5	The expected and observed exclusion limits for SR-Low and SR-High individually.	123
9.6	The expected and observed exclusion limits using all SRs.	124
10.1	The observed and expected exclusion limits at the 95% CL in the M_1 and M_2 plane for (a) $\mu = 100$ GeV and (b) $\mu = 150$ GeV	126
10.2	The observed and expected exclusion limits at the 95% CL in the μ and M_2 plane, with $M_1 = M_2$ and $\tan\beta = 50$	128
10.3	Future projection of exclusion limits by the soft lepton and disappearing track analysis using data collected during the HL-LHC, in the $m(\tilde{\chi}_1^\pm)$ and $\Delta m(\tilde{\chi}_1^\pm, \tilde{\chi}_1^0)$ plane.	129

10.4	Expected performance of the track reconstruction with the ITk.	131
10.5	Comparison of the number of tracks reconstructed with $p_T > 1$ GeV	131
10.6	Correlation between the number of interactions and the fraction of pileup tracks present within the signal tracks.	132
10.7	Future projection of the exclusion limits by the displaced track analysis using the data collected during the Run 3 and HL-LHC, shown in the $m(\tilde{\chi}_1^\pm)$ and $\Delta m(\tilde{\chi}_1^\pm, \tilde{\chi}_1^0)$ plane.	133
10.8	Diagrams of processes resulting in multiple mildly-displaced tracks.	133
A.1	Representative loop contributions to the muon $g-2$	156
A.2	wino-higgsino-smuon(sneutrino) loop contributing to the muon $g-2$	156
A.3	Current constraints on the well-tempered bino-higgsino and bino-wino neutralino scenarios.	157
A.4	Scatter plot of points passing through the pMSSM scan.	158
A.5	Excluded models before and after applying the constraints from ATLAS Run 2 analyses.	159
B.1	Overview of the endcap muon trigger logic.	161
B.2	The structure of the TGC EI chambers.	163
B.3	Schematics of the muon segment reconstruction in the TGC BW.	165
B.4	The angular resolution of tracks obtained from muons with $p_T = 20$ GeV	166
B.5	An example of a coincidence window that is used to evaluate the muon p_T	166
B.6	Muon efficiency for each p_T threshold after the wire-strip coincidence.	167
B.7	The layout of the muon spectrometers for the HL-LHC.	168
B.8	Performance of the developed trigger logic in the endcap region	168
B.9	Muon efficiency for p_T threshold at 20 GeV in the very-forward region.	169
B.10	Trigger efficiency and trigger rate of the trigger logic developed in the endcap and forward region.	170
C.1	Schematic of the PFlow algorithm.	172
C.2	Muon identification and isolation efficiency.	174
C.3	Electron identification and isolation efficiency.	177
C.4	Photon identification efficiency.	178
C.5	Photon isolation efficiency.	179
E.1	The lifetime of τ leptons, strange hadrons, and B/D mesons.	185
F.1	Distribution of time information of the leading jet passing and failing the <i>Tight</i> jet cleaning.	190
F.2	Schematic view of region definition for the non-collision background estimation.	190
F.3	Event display of a non-collision background event.	191
G.1	Feynman diagram of the $t\bar{t}$ process, where the two W decays to 1μ and 1τ	192
G.2	Schematic of the region definitions of $t\bar{t}$ VRs.	194
G.3	Pie-charts showing the background composition in the $t\bar{t}$ category.	195

G.4	Systematic uncertainties on the post-fit background yields in the $t\bar{t}$ VRs.	197
G.5	Overview of fit results in the $t\bar{t}$ VRs.	197
G.6	Post-fit distributions in the 2μ category.	198
G.7	Post-fit distributions in the 1μ category.	199
H.1	Absolute uncertainty on the relative jet energy resolution as a function of jet p_T at $\eta = 0.2$	201
H.2	JVT efficiency as a function of the reconstructed Z boson p_T (p_T^{ref}).	201
I.1	Signal acceptance of each signal production mode combining all SRs.	203
I.2	Signal efficiency of each signal production mode in SR-Low.	204
I.3	Signal efficiency of each signal production mode in SR-High.	205
I.4	The expected and observed upper limits on the cross-section for each signal grid point.	206
I.5	The observed and expected exclusion limits at the 95% CL in the M_1 and M_2 plane for $\mu = 100$ GeV	207
I.6	The observed and expected exclusion limits at the 95% CL in the M_1 and M_2 plane for $\mu = 150$ GeV	208

List of Tables

2.1	Chiral supermultiplets in the MSSM.	21
2.2	Vector supermultiplets in the MSSM.	21
3.1	Selected LHC parameters of $\sqrt{s} = 13$ TeV proton-proton collision during 2015–2018	35
3.2	Coverage and performance of the beam pipe and each inner detector.	38
3.3	Coverage and performance of each MS.	41
4.1	Summary of generator setup for SM background and signal samples.	50
5.1	The order of overlaps removed between reconstructed objects.	60
5.2	Summary of object definitions utilized in this thesis.	62
6.1	Summary of the E_T^{miss} trigger configuration for each data-taking period.	66
6.2	The selection criteria to define signal track objects.	72
6.3	Selections applied to define the 0ℓ category and SRs.	79
7.1	Applied selections for each CR and VR for calculation and validation of NFs.	89
7.2	Observed data and estimated yields using results from the background-only fit in the VRs.	91
7.3	Definition of $\mathbf{p}_T^{\text{recoil}}$ in each category.	93
7.4	Applied selections for each CR and VR for the calculation and validation of the TFs.	98
7.5	Observed data and estimated yields using results from the background-only fit in the High $S(d_0)$ and Low $S(d_0)$ VRs.	100
7.6	Observed data and estimated yields using results from the background-only fit in the VRs.	106
8.1	Impact from other minor experimental uncertainties.	112
9.1	NF and TFs measured in the background-only fit.	116
9.2	Observed data and estimated yields using results from the background-only fit in the CRs.	116

9.3	Observed data and estimated yields using results from the background-only fit in the SRs.	117
9.4	Breakdown of upper limits.	122
C.1	Definitions of isolation working point of electrons and photons.	176
D.1	Background yields after applying each event kinematic selection.	181
D.2	Background yields after applying each track kinematic selection.	182
D.3	Background yields after applying each track kinematic selection for SR-Low and SR-High.	183
D.4	Cutflows for signal samples with $m(\tilde{\chi}_1^0) = 150$ GeV , $\Delta m(\tilde{\chi}_1^\pm, \tilde{\chi}_1^0) = 1.5, 1.0,$ and 0.75 GeV	184
D.5	Cutflows for signal samples with $m(\tilde{\chi}_1^0) = 150$ GeV , $\Delta m(\tilde{\chi}_1^\pm, \tilde{\chi}_1^0) = 0.5, 0.35,$ and 0.25 GeV	184
E.1	Number of tracks in SR-Low and SR-High estimated from the $W(\rightarrow \tau\nu)$ +jets sample for each decay mode.	186
E.2	Number of tracks in SR-Low and SR-High estimated from the $Z(\rightarrow \nu\bar{\nu})$ +jets sample for each decay mode.	187
F.1	Number of observed and estimated tracks ($N_{\text{track}}^{\text{obs}}$ and $N_{\text{track}}^{\text{est}}$) in each region used to estimate the number of tracks from non-collision background near the SR.	191
G.1	Applied selections for each CR and VR for leptonic τ decay tracks.	194
G.2	Applied selections for each CR and VR for hadronic τ decay tracks.	195
G.3	NFs measured in the background-only fit.	196
G.4	Observed data and estimated yields using results from the background-only fit in the CRs.	196

Appendices

Appendix A

Supplements of Theoretical Background

A.1 Muon Anomalous Magnetic Moment

The muon anomalous magnetic moment is still a controversial candidate for an anomaly, but if it exists, it is a phenomenon that cannot be explained by the SM. The muon magnetic moment is one of the quantities measured with great precision and is a key quantity in validating the SM. A 5σ discrepancy has been observed between the prediction by the SM and the experimental measurements, referred to as the “muon $g-2$ anomaly”. The muon magnetic moment (\vec{M}) can be described using the muon spin (\vec{S}) as

$$\vec{M} = g_\mu \left(\frac{q}{2m_\mu} \right) \vec{S}, \quad (\text{A.1})$$

where g_μ is the gyromagnetic ratio, m_μ and q is the mass and charge of the muon. From the Dirac equation, g_μ is derived as 2, although the quantum loop correction causes slight deviations, referred to as the anomalous magnetic moment (“muon $g-2$ ”). The anomalous magnetic moment is described as

$$a_\mu = \frac{g_\mu - 2}{2}. \quad (\text{A.2})$$

Figure A.1 shows representative loop contributions to the anomalous magnetic moment.

The predicted value of a_μ in the SM is [121]

$$a_\mu(\text{SM}) = 116591810(1)(40)(18) \times 10^{-11}, \quad (\text{A.3})$$

where the numbers in brackets show uncertainties from electroweak, lowest-order hadronic, and higher-order hadronic contributions. The combined experimental average of a_μ from BNL and FNAL is [122]

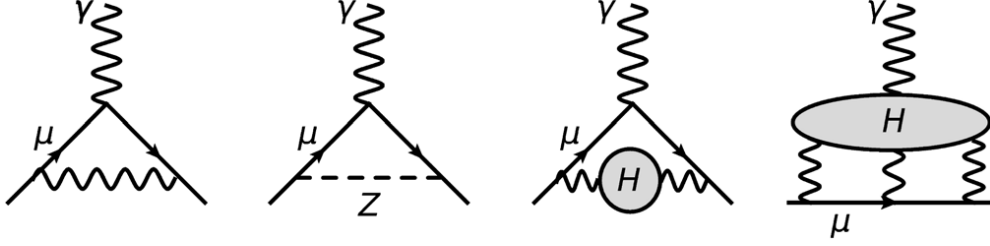
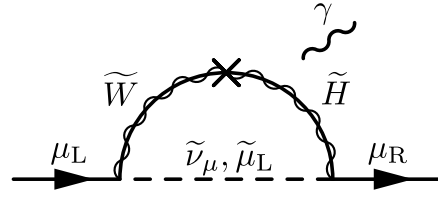


Figure A.1: Representative loop contributions to the muon $g-2$. Feynman diagrams of first-order QED and weak processes, leading-order hadronic vacuum polarization, and hadronic light-by-light contributions are arranged from left to right. The figure is taken from Ref. [120].

Figure A.2: wino-higgsino-smuon(sneutrino) loop contributing to the muon $g-2$. The external photon line can be attached to any charged internal line in the diagram. The figure is taken from Ref. [124].



$$a_\mu(\text{Exp.}) = 116592059(22) \times 10^{-11}, \quad (\text{A.4})$$

where the numbers in brackets show the combined uncertainties.

In the Minimal Supersymmetric Standard Model (MSSM), additional loop corrections to the muon $g-2$ arise from electroweakino and sleptons. To explain the observed $g-2$ at the 2σ level with light higgsinos at the range of 100–400 GeV, the mass of winos and sleptons is upper bound by 3 TeV and 800 GeV, as discussed in Ref. [123]. Figure A.2 shows one of the diagrams with winos, higgsinos, and smuons (sneutrinos) in the loop corrections. Similar loops are induced by bino, winos, higgsinos, smuons, and sneutrinos, and the magnitude strongly depends on the masses of the particles and $\tan\beta$.

A.2 Mechanisms to enhance the annihilation cross-section of bino-like LSP

As discussed in Section 2.2, the annihilation cross-section of a bino-like lightest SUSY particle (LSP) is too small to account for the observed relic density. To enhance the annihilation cross-section, we consider the case where bino and higgsino or wino are mixed to form an LSP. This allows the bino-like LSP to co-annihilate with other neutralinos and charginos with degenerate mass, referred to as the “well-tempered neutralino”. However, achieving this requires a fine-tuning of the mass parameters, with $M_1 \sim \mu$ for the bino-higgsino scenario and $M_1 \sim M_2$ for the bino-wino scenario. Figures A.3(a) and A.3(b) show the current constraints in the well-tempered bino-higgsino and bino-wino neutralino scenarios, respectively.

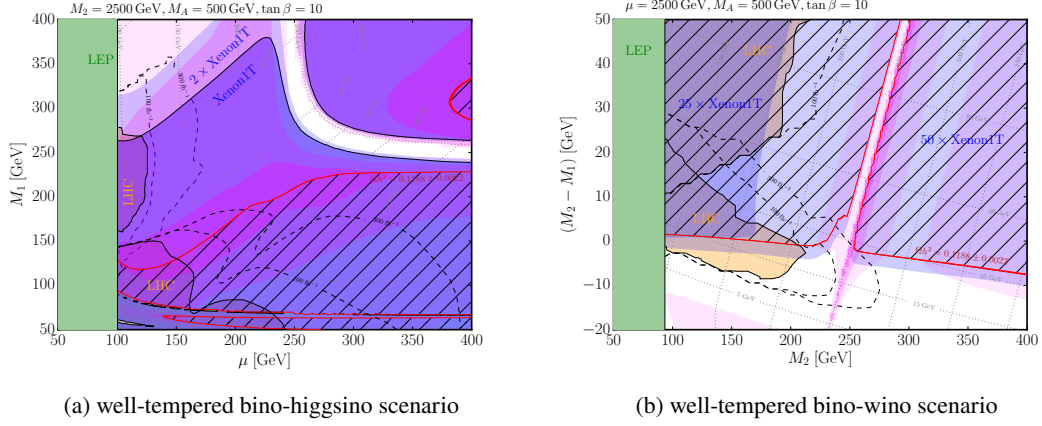


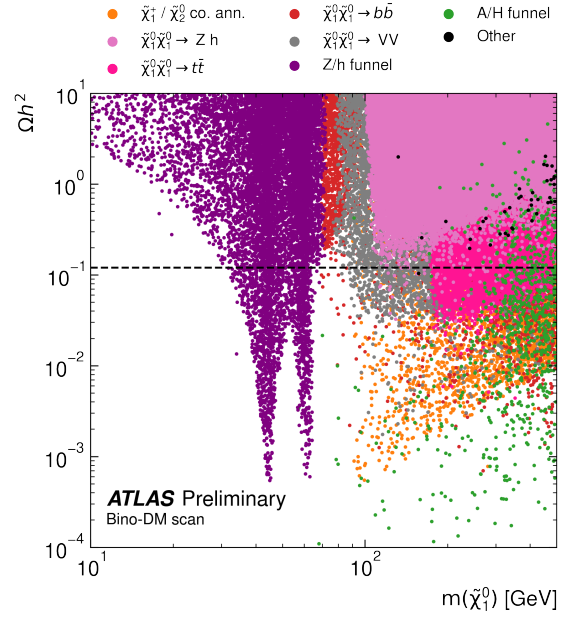
Figure A.3: Current constraints on the well-tempered bino-higgsino and bino-wino neutralino scenarios. The pseudo-scalar Higgs boson mass and $\tan\beta$ are fixed to $M_A = 500$ GeV and $\tan\beta = 10$, respectively. The orange (green) regions represent the parameter space excluded by LHC (LEP) searches. Exclusion limits from the direct dark matter detection experiment are shown as regions filled with blue. The red line shows the region that explains the observed relic density of the dark matter, and the shaded regions surrounded by the red line show the region where the dark matter would be overabundant. (a) Constraints on the well-tempered bino-higgsino in the μ and M_1 plane. The diagonal and hyperbolic-shaped dotted gray lines represent the mass difference and LSP mass, respectively. (b) Constraints on the well-tempered bino-wino in the M_2 and $M_2 - M_1$ plane. The horizontal and vertical dotted gray lines represent the mass difference and the LSP mass, respectively. The figures are taken from Ref. [125].

Although achieving the “well-tempered neutralino” requires a fine-tuning of the mass parameters, certain cases avoid this requirement. For instance, the “ Z/H funnel” mechanism enhances the annihilation cross-section by annihilation to Z or Higgs boson when the LSP mass is approximately half the mass of the Z or Higgs boson. Figure A.4 shows the neutralino mass points and the resulting relic density that pass through the phenomenological MSSM (pMSSM) scan, which focuses on the bino-like LSP case. The figure indicates that the bino-like LSP can have a relatively low mass and still meet the relic density criteria, thanks to the Z/H funnel mechanism.

A.3 Limits to electroweakinos as a dark matter candidate

Many searches for electroweak gauginos have been conducted in the LHC, providing various limits on the supersymmetry (SUSY) parameters. Scans of the pMSSM parameters have been performed using the results of ATLAS Run 2 analyses and external constraints. Figure A.5(a) shows the number of models before and after applying the constraints of ATLAS Run 2 analyses for each LSP component. Compared to other scenarios, the wino-like LSP scenario is highly excluded by the disappearing track analysis [15]. Models with bino-like and higgsino-like LSP are not excluded by Run 2 analyses. However, most of the bino-like LSP models are further

Figure A.4: Scatter plot of points passing through the pMSSM scan. The horizontal dashed line corresponds to the observed relic density. The color of each point corresponds to the dominant annihilation mechanism. The pMSSM scan focuses on the bino-like LSP. The figure is taken from Ref. [39].



excluded by requiring the constraint from the observed relic density. To oversample the additional annihilation mechanisms for the Bino-like LSP model, an extra scan has been performed with only Bino-like LSP models. Figure A.5(b) shows the number of models before and after applying the constraints of ATLAS Run 2 analyses for bino-like LSP. Most models with LSP mass in the Z/h funnel region are excluded by Run 2 analyses.

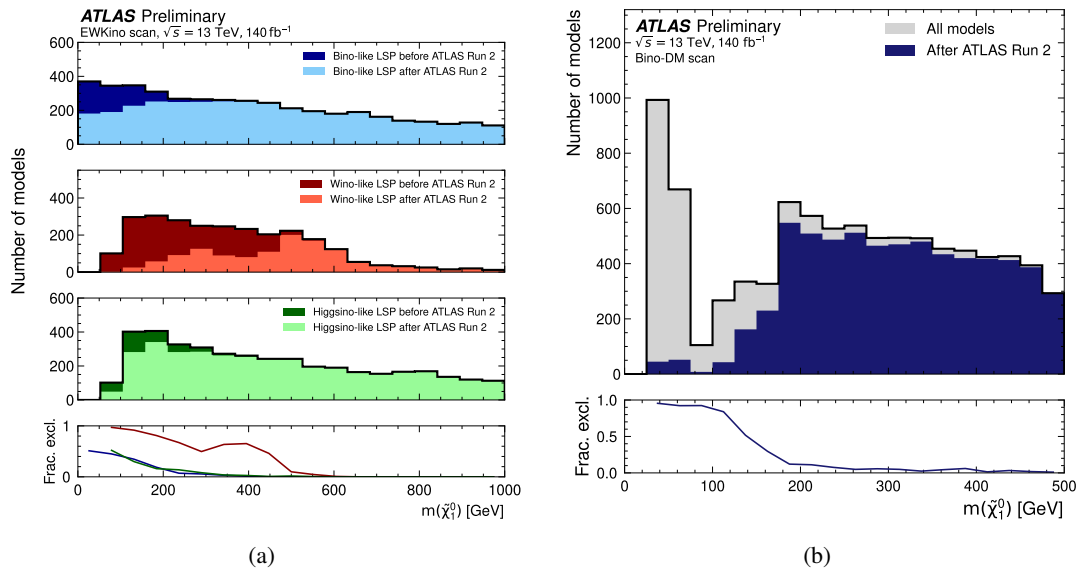


Figure A.5: (a) Number of models before and after applying the constraints from ATLAS Run 2 analyses for each LSP component. The bottom plot shows the fraction of excluded models for each LSP component. (b) Number of bino-like LSP models before and after applying the constraints from ATLAS Run 2 analyses. The peak on the left side shows models in the Z/h funnel region, and most of the models are excluded by ATLAS Run 2 analyses. The bottom plot shows the fraction of excluded models. The figures are taken from Ref. [39].

Appendix B

Muon Trigger Upgrade for the HL-LHC

The muon trigger in the ATLAS detector is divided into the barrel region using the Resistive Plate Chamber (RPC) detector and the endcap region using the Thin Gap Chamber (TGC) detector. This chapter focuses on the upgrade of the muon system in the endcap region for the HL-LHC. First, Section B.1 gives an overview of the TGC detector installed outside the magnetic field and the current trigger logic to reconstruct muon segments. Section B.2 explains the sources of the increased trigger rate and describes the trigger logic using muon detectors inside the magnetic field to mitigate it. Section B.3 provides an overview of the upgrades of the trigger system towards the HL-LHC in the endcap region to reduce the trigger rate. Section B.4 describes the new trigger logic that can be implemented with the upgrade and personal contributions to the development. Finally, Section B.4.3 summarizes the performance achieved by the developed trigger logic.

B.1 Overview of the Thin Gap Chamber

Three TGC stations, called M1, M2, and M3 from the inside, are located outside the magnetic field. The M1 station consists of a TGC Triplet, which has three layers of wires and two layers of strips. The M2 and M3 stations consist of TGC Doublets with two layers of wires and strips. Each wire and strip layer is slightly shifted in the η and ϕ direction, which provides improved position resolution by taking the coincidence between each layer. M1, M2, and M3 have disk-like structures, and the three stations are called the TGC Big Wheel (TGC BW). The location of the muon segment reconstruction is determined using the positional information provided by M3, and this criterion will remain unchanged in the HL-LHC.

The region with $1.05 < |\eta| < 1.9$ is referred to as the endcap region, while the region with $1.9 < |\eta| < 2.4$ is known as the forward region. Each region is divided into 48 and 24 units in the ϕ direction, respectively, and these units are called the “trigger sectors”. The trigger decision is made separately on the A- and C-sides, using only the information within the same trigger sector.

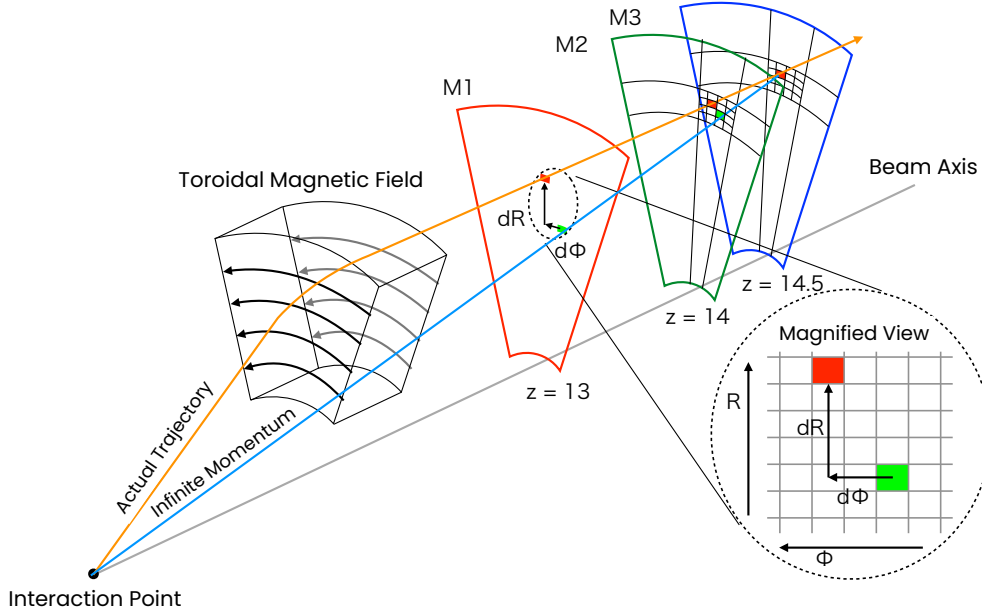


Figure B.1: Overview of the endcap muon trigger logic. The p_T is measured by calculating the difference in R -position at M1 relative to M3 between the hit positions at M1, M2, and M3 and the trajectory of a muon that passes through with infinite momentum.

Muons produced from the interaction point pass the toroidal magnetic field applied in the ϕ direction and bent in the η direction. Furthermore, muons are also bent in the ϕ direction by the magnetic field component in the z direction generated by the solenoid magnet near the collision point and the magnetic field component in the R direction generated near the toroidal magnet. The curvature of the muon track depends on the p_T . Therefore, it is possible to calculate the p_T of a muon by measuring its change in position in the R and ϕ directions compared to when it passes through with infinite momentum. The trigger decision is performed by setting a threshold on the calculated p_T . Figure B.1 shows a schematic of the trigger logic for Run 2 and Run 3.

In the current trigger system, the on-detector boards require that the wire (strip) has a hit on at least 2-out-of-3 (1-out-of-2) layers at M1 and at least 3-out-of-4 layers at M2 and M3. The difference between the positions of M1 and M3 in the R (ϕ) direction is sent to the off-detector boards to calculate the p_T , referred to as the ‘‘Sector Logic Board’’ (SL board). The average efficiency of the TGC detector in each layer is 92.7% for wires and 92.1% for strips, and the limited combination of layers limits the detection efficiency of muons in the current system to 91.8%.

B.2 Trigger Logic using Muon Detectors inside the Magnetic Field

Two primary sources cause the increase in the trigger rate. First, low-momentum secondary particles, which are produced by elastic or inelastic scattering of the proton beam with residual gas in the beam pipe, are bent by the magnetic field and enter the TGC BW, where they appear as muons with high momentum. These events are called “fake muons” and are the main reason for the increase in the trigger rate. Secondly, the accuracy of determination of the muon p_T causes the trigger rate to increase by triggering muons with a low p_T below the threshold value. To reduce the trigger rate, four types of detectors are placed inside the magnetic field.

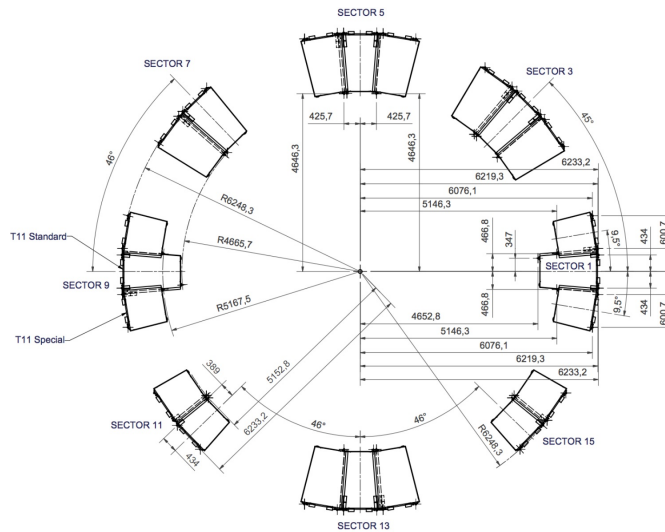
In the region of $1.05 < |\eta| < 1.3$, the RPC and TGC detectors with limited coverage are placed, and the area not covered by these two detectors is supplemented by the Tile Calorimeter (TileCal) that covers the entire ϕ region. In the Run 3, a new detector called the New Small Wheel (NSW) was introduced in the region $1.3 < |\eta| < 2.7$ to measure the position and angle information of the muon segment with high accuracy. As for the fake muon, since it is not from the interaction point, it can be significantly reduced by taking the coincidence between the TGC BW and the muon detectors inside the magnetic field. Detectors such as the TileCal can measure position, whereas the NSW detector measures both position and angle. By combining these measurements with position information in the TGC BW, p_T determination can be performed with even higher accuracy, reducing muons with low p_T . Combining the information from the TGC BW with the information from the detectors inside the magnetic field is called the “Inner Coincidence”.

B.3 Upgrade of the Endcap Muon Trigger System

To accommodate the increased trigger rate, all trigger logic and readout boards will be replaced, except for the ASD board, which is installed on the TGC chamber. This board converts analog signals to digital signals and is designed to operate in the HL-LHC environment. Therefore, it does not need to be replaced. The TGC EI chamber, the TGC detector installed inside the magnetic field, will also be replaced with a new TGC detector. Each upgrade will be described in detail below.

TGC electronics upgrade The TGC trigger logic and readout boards must meet certain conditions. First, all TGC hit information processed by the ASD board should be sent to the SL board, which performs the trigger decision using all hit information at once. Additionally, the SL board should handle all data readouts. Since the SL board must be capable of processing vast amounts of data compared to the Run 3, a large-scale FPGA called XCVU13P of the Virtex UltraScale+ FPGA series will be used. The XCVU13P is equipped with standard Block RAM and a large-capacity memory called the “UltraRAM”, which can be used to perform large-scale computations.

Figure B.2: The structure of the TGC EI chambers. The TGC EI consists of two types of TGC chambers: a chamber called T11 Standard and a slightly shorter TGC chamber in the R direction called T11 Special. TGC chambers are installed to avoid interference with the toroidal magnet and calorimeter in the barrel section and support structures of the detector. The figure is taken from Ref. [126].



TGC EI chamber upgrade The TGC EI chambers installed in the $1.0 < |\eta| < 1.3$ region have a complicated structure to avoid interference with the toroidal magnet and calorimeter in the barrel section and support structures of the detector. As shown in Figure B.2, the TGC EI consists of several TGC chambers of different sizes. The current TGC EI chamber has a two-layer (doublet) structure and requires that at least one of the two layers have a hit. However, in environments with high luminosity, the hit rate in the TGC EI is also high, and the current system cannot suppress the increase in trigger rate due to fake muons. Furthermore, if one of the two layers becomes non-functional, the TGC EI cannot be used for the Inner Coincidence, leading to a significant increase in the trigger rate caused by fake muons.

To address this situation, the TGC Doublet will be replaced by a TGC Triplet with a three-layer structure with a higher resolution. It is possible to require at least two of the three layers to have hits by introducing the TGC triplet. This results in improved reduction performance against noise and accidental hits. Furthermore, the three-layer configuration ensures robustness when one layer becomes inoperative.

B.4 Development of the New Endcap Trigger Logic

In the upgrade towards the HL-LHC, the latency of the trigger decision will increase from $2.5 \mu\text{s}$ to $10 \mu\text{s}$ due to the larger buffer size that retains detector information during the trigger decision. In addition to receiving all hit information, the longer latency allows the incorporation of more sophisticated trigger logic for reconstructing muon segments with greater precision. The new endcap muon trigger logic for the HL-LHC is divided into three stages.

- The HL-LHC muon system will be able to reconstruct muon segments using a process called “pattern matching algorithm”. This algorithm will utilize the hit data from all

seven layers of the TGC BW, which will be transferred to the SL board. This method reconstructs tracks with higher efficiency and higher positional and angular resolution than conventional methods. The reconstructed angle information is used to perform a highly accurate determination of p_T .

- By combining the position and angle information obtained from the track reconstructed by the TGC BW with the precise position and angle information of multiple detectors present within the magnetic field, p_T determination can be performed with greater accuracy. The trigger rate caused by fake muons is reduced by requiring a hit in the detector inside the magnetic field as in the current system. The trigger rate caused by fake muons will also be reduced by requiring a hit in the detector inside the magnetic field as in the current system.
- In the current system, the MDT detector is used only for software-based precise trigger decisions. However, the MDT detector will also be available for hardware-based fast trigger decisions in the HL-LHC.

In the following, we would like to present the method developed for reconstructing muon segments in the TGC BW. Furthermore, we will discuss the coincidence logic between the detectors located inside the magnetic field.

B.4.1 Muon Segment Reconstruction in the TGC BW

In the HL-LHC, all hit information is sent to the SL. Therefore, we can require that the wire (strip) has a hit on at least 5-out-of-7 (4-out-of-6) layers. This will result in a muon detection efficiency of 96.0% at the TGC BW, an improvement of 4.2% over the current system. In the initial stage of the muon segment reconstruction, segments are reconstructed separately in the $\Delta\theta$ and $\Delta\phi$ directions using wire and strip information. After this step, the angle information of the wire and strip segments is combined to determine the muon p_T . Below are further explanations of these two steps.

Pattern Matching Algorithm In the pattern matching algorithm, the angle and position information of the muon segments corresponding to each TGC BW hit combination is calculated in advance, and a pattern list is created that corresponds the TGC hit information to the segment information on a one-to-one basis. The position and angle information of the wire and strip segments is represented by 18 bits. The created pattern list is stored in the large memory of the FPGA, and p_T threshold values corresponding to the input hit combinations are output at high speed. If we intend to store all the patterns for the seven TGC layers in the trigger sector, the pattern list can consume a substantial amount of memory. For example, the pattern list in the forward region, with approximately 2^7 wire channels per layer, would require about $(2^7)^7 \times 18 \text{ bit} \sim 8 \text{ Pb}$ of memory, which is impractical. To address this issue, we define the overlapping part between layers for each M1, M2, and M3 station as the representative point. This approach enables us to store only the combination of three representative points for each station, significantly reducing

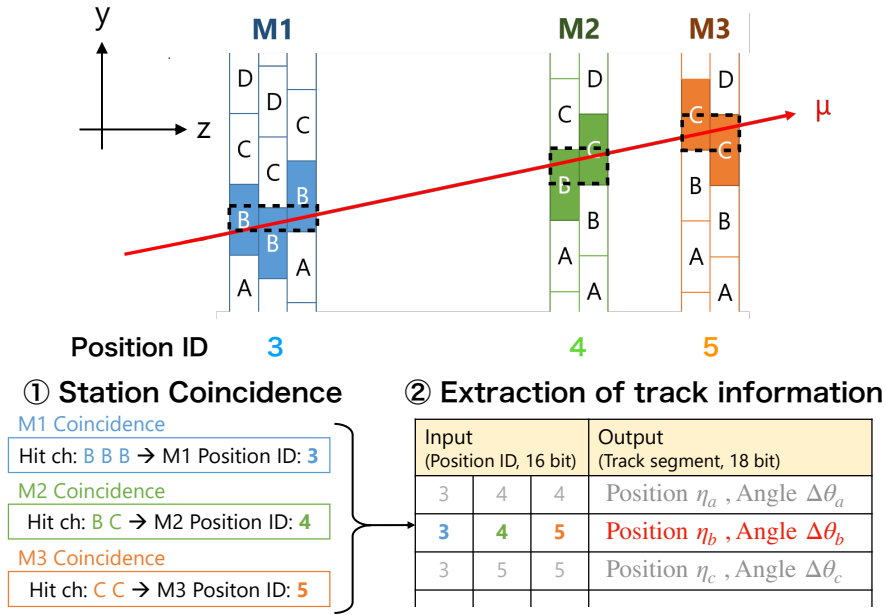


Figure B.3: Schematics of the muon segment reconstruction in the TGC BW. The first step is to define representative points that overlap between the layers of each station, referred to as the “Station Coincidence”. The angle and position information of the muon segments is extracted from the pattern list using the combination of the representative points at each station.

the necessary memory for the pattern list. Schematics of the pattern matching algorithm are illustrated in Figure B.3.

Pattern lists have been developed for each TGC BW trigger sector, considering the difference in the magnetic field depending on the ϕ position. If a single muon produces multiple hits within a station, this may result in various output patterns. Therefore, it is necessary to determine a method to select a single pattern when multiple candidates are produced. There are two possible methods: one is to prioritize outputs with larger p_T , and the other is to prioritize outputs with a large number of matched layers. In prioritizing the highest p_T output, even if the reconstructed track angle is incorrect, the one with the highest p_T is selected, leading to a systematic deviation in the angle information. Figure B.4 shows the method that prioritizes the highest number of matched layers. This method provides good angular resolution while not producing any systematic deviations in relation to the correct angular information.

Coincidence between Wire and Strip Segments TGC BW uses the pattern matching algorithm using wires and strips independently to determine the angle and position information of muon segments in the η and ϕ directions, respectively. In addition to the magnetic field in the R direction, a magnetic field in the ϕ direction is produced in the transition region between the barrel and endcap toroidal magnet. Therefore, depending on the region, the $\Delta\theta$ and $\Delta\phi$ of the muon segment are correlated as shown in Figure B.5. The relationship between the angles of the

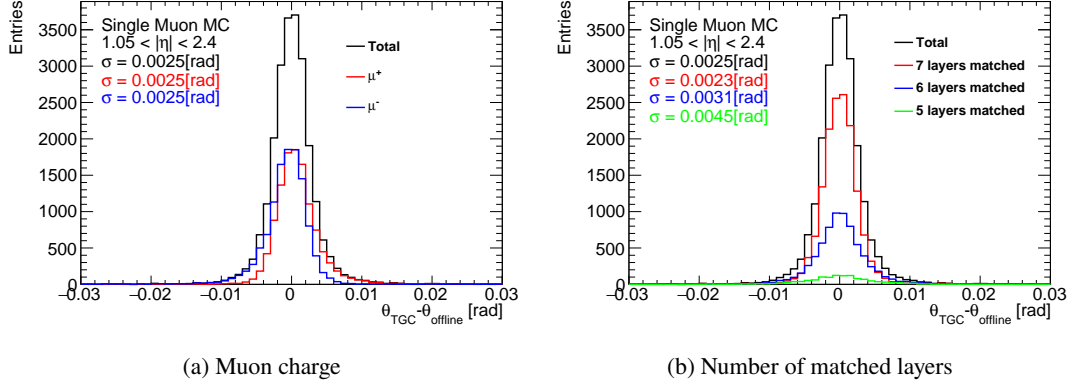
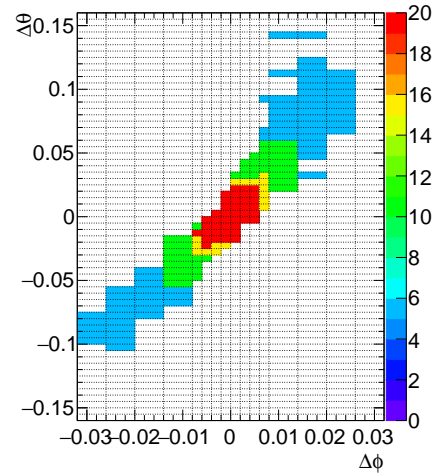


Figure B.4: The angular resolution of tracks obtained from muons with $p_T = 20$ GeV. The angular resolution is evaluated using a single muon sample, which produces only one muon during each event. (a) The angular resolution of each charge is shown. The figure illustrates that the angular resolution remains consistent across different charges. (b) The angular resolution is shown for each number of matched layers. The figure indicates that increasing the number of matched layers results in an improved angular resolution.

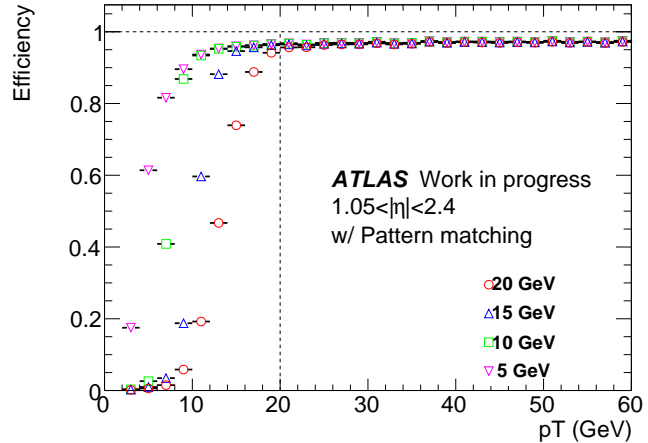
Figure B.5: An example of a coincidence window that is used to evaluate the muon p_T . In the coincidence window, red, yellow, green, and blue cells represent muons that pass the p_T threshold for 20, 15, 10, and 5 GeV. Information on the angular difference ($\Delta\theta$ and $\Delta\phi$) calculated by wire and strip segment reconstruction is used to evaluate the p_T threshold the muon passes. The $\Delta\phi$ axis is divided non-uniformly to provide higher resolution for muons with higher p_T .



muon segment ($\Delta\theta$ and $\Delta\phi$) and p_T in each region is called the “Coincidence Window”, which is stored in the large memory of the FPGA. The coincidence window represents $\Delta\theta$ in 7 bits and $\Delta\phi$ in 4 bits. Since a higher p_T requires higher resolution, the $\Delta\phi$ axis is divided non-uniformly, as shown in the figure.

Figure B.6 shows the efficiency of muons with the developed coincidence window. It can be seen that muons with p_T below the threshold are reduced while maintaining a high efficiency of about 97% in the plateau region.

Figure B.6: Muon efficiency for each p_T threshold after the wire-strip coincidence. The efficiency is evaluated using a single muon sample, which produces only one muon during each event.



B.4.2 Coincidence with detectors inside the magnetic field

In the ATLAS detector, fake muons that do not originate from the collision point cause the increase in the trigger rate. To reduce the trigger rate, the position and angle of the track reconstructed by the TGC BW are combined with the information from the detector inside the magnetic field. Four types of detectors are installed inside the magnetic field, as shown in Figure B.7, and each detector covers different areas. Therefore, it is necessary to properly select the detector inside the magnetic field with which position and angle information should be combined according to the position of the muon segment reconstructed by the TGC BW. It is possible for muon segments in the same position of the TGC BW to be detected by different detectors based on the charge and p_T due to different directions and magnitude of the curvature. To address this, we optimized the detectors to be combined based on the charge and p_T information obtained by the sign of the $\Delta\theta$ information of the muon segment reconstructed in the TGC BW. The logic of the Inner Coincidence in the endcap ($1.05 < |\eta| < 1.3$), forward ($1.3 < |\eta| < 2.4$), and very-forward ($2.4 < |\eta| < 2.7$) regions is briefly explained below.

Endcap region ($1.05 < |\eta| < 1.3$) Three types of detectors are installed in the endcap region: TGC, RPC, and TileCal. Since the TGC and RPC detectors can measure positional information, muons with low p_T can be reduced by the difference between the positional information of the muon segment reconstructed by the TGC BW. As the TileCal cannot determine precise position information, it can only detect the presence of a muon passing through it. When a muon segment is reconstructed in the TGC BW, a significant reduction in fake muons can be achieved by requiring the corresponding TileCal cell to have a substantial energy deposit. The performance of the developed trigger logic at p_T threshold 20 GeV in the endcap region is given in Figure B.8 for each detector. The figure shows that the efficiency at the plateau is about 2% lower when using the TileCal. This is because the TileCal has modules that cover the entire ϕ direction, but there is a dead zone between each module.

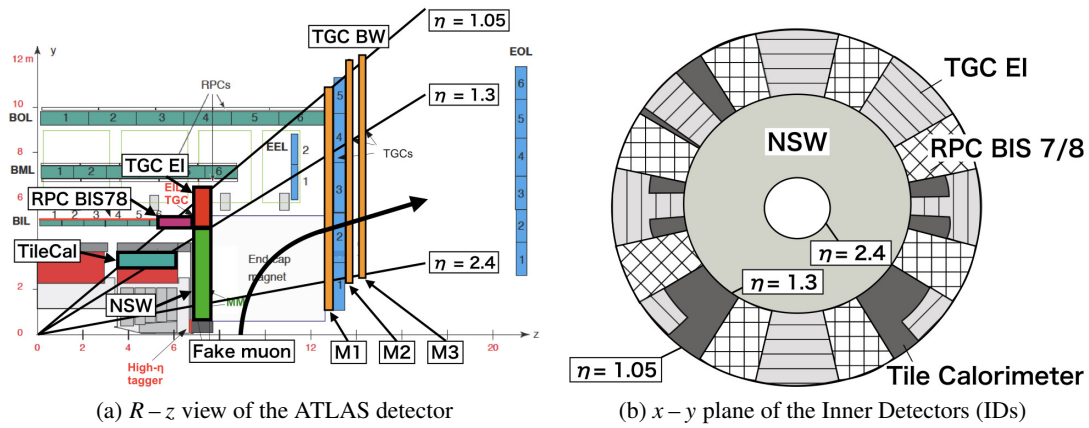


Figure B.7: The layout of the muon spectrometers for the HL-LHC.

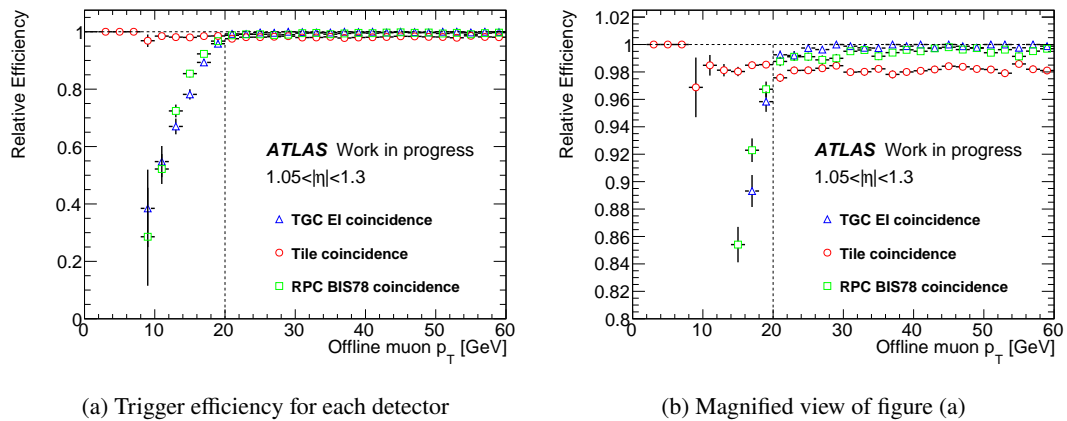
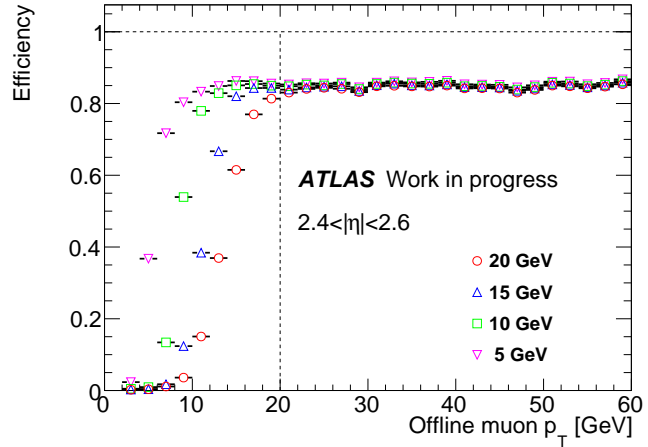


Figure B.8: Performance of the developed trigger logic at p_T threshold 20 GeV in the endcap region. The TileCal has a lower positional resolution, resulting in a lower reduction of low- p_T muons compared to the TGC and the RPC. The efficiency is evaluated using a single muon sample, which produces only one muon during each event.

Figure B.9: Muon efficiency for p_T threshold at 20 GeV in the very-forward region. The efficiency is evaluated using a single muon sample, which produces only one muon during each event.



Forward region ($1.3 < |\eta| < 2.4$) The forward region is covered by the NSW, which can measure position and angle information with high accuracy. Therefore, combining the angular information of the muon segment in the TGC BW and the NSW position and angle information can significantly reduce low- p_T muons. The performance of the trigger logic developed in the forward region is given in Section B.4.3 along with the performance in the endcap region.

Very-forward region ($2.4 < |\eta| < 2.7$) NSW covers up to a region of $|\eta| < 2.7$, which allows the muon trigger region to be extended to more forward regions. On the other hand, as shown in Figure B.7, M2 and M3 of the TGC BW only cover the region of $|\eta| < 2.4$, and therefore muon segment reconstruction cannot be performed in the TGC BW. Decreasing the trigger rate solely by relying on the M1 station would be difficult. However, achieving an acceptable trigger rate is possible by using the NSW in combination with the Monitored Drift Tube (MDT), increasing the accuracy of the p_T measurement. The muon p_T is measured by comparing the hit position in the NSW and the M1 station. In addition, setting a threshold value for the angle information of the NSW reduces triggers caused by charged particles not originating from the collision point. Since only three layers of wires and two layers of strips are available at the M1 station, the trigger rate increases significantly due to noise. Despite the lower detection efficiency, the total number of layers of wires and strips with hits in the M1 station must be more than four layers, and the hits must be on the same layer for both wires and strips. The performance of the developed trigger logic in the very-forward region is given in Figure B.9. Although tight conditions are applied to the number of layers in the M1 station, the efficiency of the plateau is about 85%. Despite the high trigger rate expected at the p_T threshold of 20 GeV within the HL-LHC, which currently stands at approximately 83 kHz, a further reduction is anticipated with the MDT in the future.

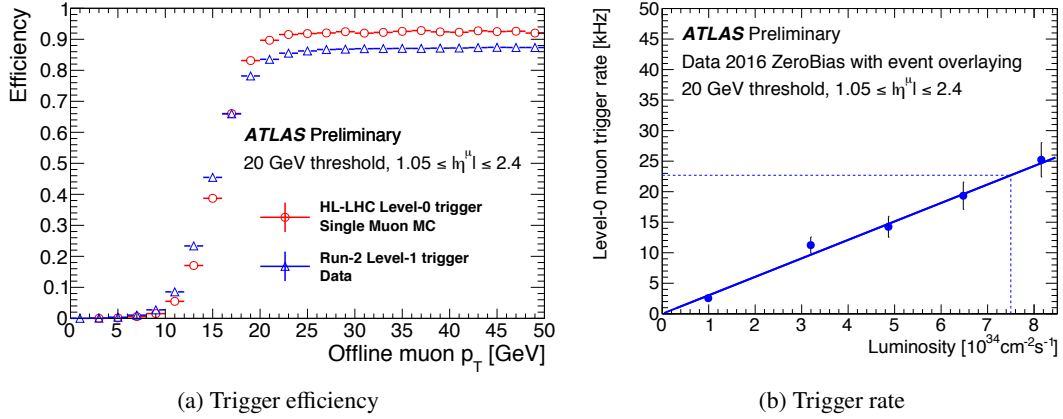


Figure B.10: Trigger efficiency and trigger rate of the trigger logic developed in the endcap and forward region. (a) For the HL-LHC trigger logic, the trigger efficiency is evaluated using a single muon sample, which produces only one muon during each event. The trigger efficiency for the Run 2 trigger logic is evaluated using data taken in 2018. The plateau efficiency of the HL-LHC is relatively high compared to Run 2 since all hit information is sent to the SL board, allowing more loose conditions to be imposed on the number of hits. (b) The trigger rate for the nominal luminosity ($1 \times 10^{34} \text{ cm}^{-2} \text{ s}^{-1}$) is obtained using the Run 2 data taken in 2016 with the zero-bias trigger. To estimate the trigger rate at higher luminosity, the events in these data are overlaid. The solid blue line shows the result of fitting the points with a linear function. The figures are taken from Ref. [127].

B.4.3 Summary of the Endcap Muon Trigger Logic

The efficiency and trigger rate evaluated for the trigger logic developed in the endcap and forward region are summarized in Figure B.10. The figure also shows the trigger efficiency of the trigger logic in Run 2, which indicates that the trigger logic in the HL-LHC can further reduce low- p_T muons while maintaining a high efficiency above the p_T threshold. The trigger rate for the p_T threshold of 20 GeV at the luminosity of the HL-LHC is approximately 23 kHz. The trigger rate is expected to be further reduced by using the MDT for more accurate p_T determination.

Appendix C

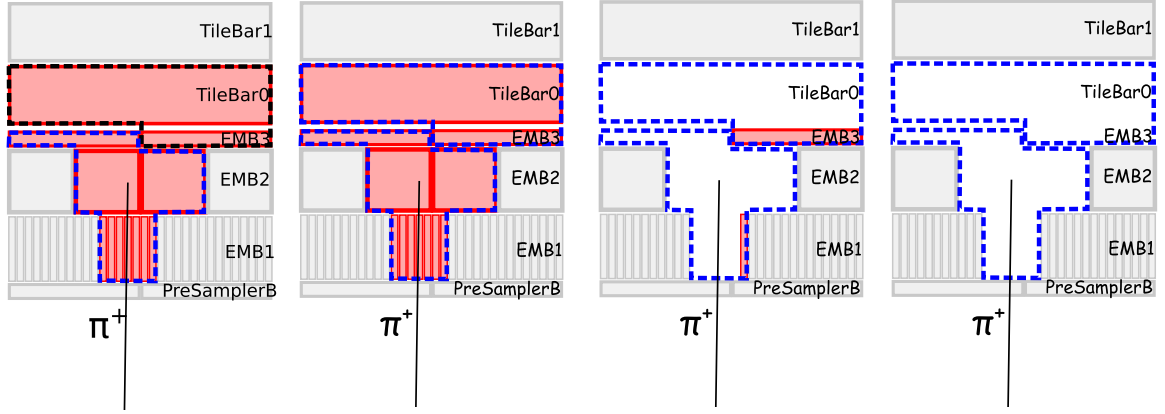
Supplements of Event Reconstructions

C.1 Jets

Particle Flow (PFlow) algorithm The energy deposit that has been double-counted is subtracted from the topo-clusters through the following procedure.

- **Track selection** : The reconstructed tracks undergo various selection criteria to mitigate the impact of poorly measured tracks. However, tracks are not required to be associated with the primary vertex during this stage. Additionally, tracks associated with reconstructed leptons are excluded from the subtraction process.
- **Track/topo-cluster matching** : Tracks are matched to a single topo-cluster based on the positional difference. To minimize the matching of incorrect topo-clusters, a permissive criterion is applied to the energy and momentum ratio of calorimeters and tracks, defined as $E^{\text{clus}} / p^{\text{trk}} > 0.1$.
- **Split shower recovery** : A single particle may leave energy deposits in multiple topo-clusters. To identify cases where topo-clusters are divided into multiple topo-clusters from a single particle, the discrepancy between the anticipated and matched topo-cluster energy is used as a discriminant. When the discriminant falls below a specific threshold, topo-clusters within a cone size of $\Delta R = 0.2$ around the track are merged.
- **Energy subtraction** : The expected energy deposit from charged particles associated with the track is assessed through simulation samples. The energy deposit estimated from tracks is then subtracted from the matched topo-clusters on a cell-by-cell basis.
- **Remnant removal** : The remaining topo-clusters are discarded if the energy is consistent with the shower fluctuations.

The schematic of the Particle Flow (PFlow) algorithm is given in Figure [C.1](#).



(a) Track/topo-cluster matching (b) Split shower recovery (c) Energy subtraction (d) Remnant removal

Figure C.1: Schematic of the PFlow algorithm in the case of two topo-clusters are reconstructed by a charged pion. The red cells represent energy deposits by the charged pion, and the dotted lines show the reconstructed topo-clusters. In step (a), the reconstructed track is matched to the topo-cluster represented with a blue dotted line. In step (b), the other topo-cluster is merged to recover a single shower split into multiple topo-clusters. In steps (c) and (d), the topo-clusters matched to the track are subtracted on a cell-by-cell basis, and the remaining topo-clusters are discarded. The figures are taken from Ref. [97].

C.2 Muons

Muon objects are formed with the following four steps, which are briefly described. More details can be found in Ref. [116].

Reconstruction This thesis uses two types of algorithms for reconstruction: “combined” and “standalone” algorithms.

- **Combined algorithm** : Muons are reconstructed by combining information from the ID and Muon spectrometer (MS) to form muons called combined muons (CB muons). Track candidates reconstructed in the MS are extrapolated to the ID to find the corresponding track.
- **Standalone algorithm** : To recover efficiency in the forward region ($2.5 < |\eta| < 2.7$) due to the limited ID coverage, muons are reconstructed using only the MS information called standalone muons (SA muons).

Identification Additional selection criteria are applied to suppress muon candidates from in-flight decays of charged mesons, such as strange mesons or pions. Muons from in-flight decays are expected to have “kink” topology, and this characteristic can be discerned by assessing the

compatibility between the momentum measurements obtained from the ID and the MS. For CB muons, the “ q/p significance” is used to quantify the “kink” topology, defined as

$$\frac{|(q/p)_{\text{ID}} - (q/p)_{\text{ME}}|}{\sqrt{\sigma_{\text{ID}}^2 + \sigma_{\text{ME}}^2}}, \quad (\text{C.1})$$

where σ corresponds to the momentum resolution and subscripts represent the detectors used for measurement.

In this thesis, the *Medium* working point is used for muon identification. Additional requirements on the number of MDT or Cathode Strip Chamber (CSC) stations with at least three hits, denoted as “precision stations”, are applied. In the $|\eta| < 0.1$ region, where the MS is not fully equipped, the number of MDT or CSC stations with less than three hits and lacks at least three hits anticipated based on its trajectory, denoted as “precision hole station”, is also used. CB muons are required to pass q/p significance < 7 and at least two precision stations, except for the $|\eta| < 0.1$ region. In the $|\eta| < 0.1$ region, CB muons with at least one precision station and at most one precision hole station are also allowed. SA muons in the forward regions ($2.5 < |\eta| < 2.7$) are required to have at least three precision stations.

Isolation Muons from semi-leptonic decay of hadronic sources can be suppressed by measuring hadronic activities around the muons using track and calorimeter information. The PFlow algorithm is used to remove the overlap of activities of charged particles, as discussed in Subsection 5.3.1.

In this thesis, the *PflowLoose_VarRad* working point is used for muon isolation. The track-based isolation variable, denoted as $p_{\text{T}}^{\text{varcone30}}$, is defined as the scalar sum of the p_{T} of tracks with $p_{\text{T}} > 1$ GeV and within a variable cone size around the muon. The radius of the cone is adjusted based on the momentum of the muon, as muons decaying from high-momentum hadronic sources tend to be closely aligned with other decay particles. The radius used for $p_{\text{T}}^{\text{varcone30}}$ is defined as $\min(0.3, 10/p_{\text{T}})$. The calorimeter-based isolation variable, denoted as $E_{\text{T}}^{\text{neflow20}}$, is defined as the scalar sum of neutral particle-flow objects within $\Delta R < 0.2$ of the muon. Combining the track-based and calorimeter-based isolation variables, muons are required to pass the selection described as

$$(p_{\text{T}}^{\text{varcone30}} + 0.4 \times E_{\text{T}}^{\text{neflow20}}) < 0.16 \times p_{\text{T}}^{\mu}. \quad (\text{C.2})$$

The efficiencies for muon identification and isolation are summarized in Figures C.2(a) and C.2(b), respectively.

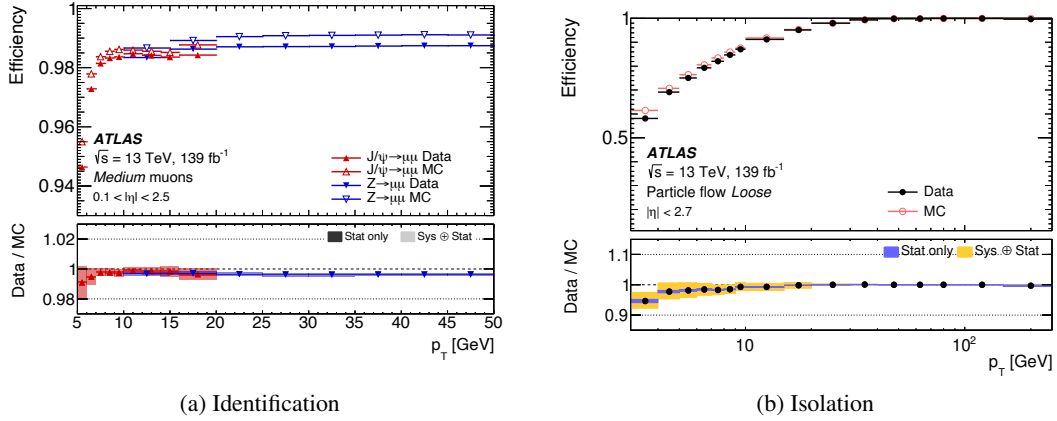


Figure C.2: (a) Muon identification efficiency for the *Medium* working point as a function of muon p_T measured in $J/\psi \rightarrow \mu\mu$ and $Z \rightarrow \mu\mu$ events. (b) Muon isolation efficiency for the *PflowLoose_VarRad* working point as a function of muon p_T measured in $Z \rightarrow \mu\mu$ events. In both figures, the bottom panel shows the ratio of data and simulation with the combined systematic and Monte Carlo (MC) statistical uncertainties. The figures are taken from Ref. [116].

Momentum Calibration The momenta of muons in data and simulation samples do not perfectly match due to incomplete knowledge of the alignment of detectors and energy deposits in calorimeters or detector material. Therefore, the momenta are calibrated using the invariant mass ($m_{\mu\mu}$) of $J/\psi \rightarrow \mu\mu$ and $Z \rightarrow \mu\mu$ processes for low and high p_T , respectively. Correction factors are measured for the momentum of the CB muons, as well as the ID and MS tracks associated with the CB muon. The calibration step is validated by comparing the corrected CB muon momentum with the momentum combined from measurements in the ID and MS.

C.3 Electrons and Photons

Electron and photon objects are formed with the following four steps described briefly. More details can be found in Ref. [128].

Reconstruction The reconstruction of electrons and photons begins with the following common steps.

1. **Track and topo-cluster matching** : Tracks reconstructed in the ID are matched to topo-clusters. Matched tracks are re-fitted to account for energy losses by bremsstrahlung.
2. **Conversion vertex reconstruction** : Tracks matched to topo-clusters are used to reconstruct conversion vertices from conversion photons. Tracks with hits in the silicon detectors and hits exclusively in the TRT detectors are used as inputs. Two types of vertices are reconstructed: two-track and single-track conversion vertices. Two-track conversion vertices

are reconstructed from tracks with opposite signs. In contrast, single-track conversion vertices are reconstructed from a single track with no hits in the innermost ID layers. The tracks are required to have a high probability of being electrons based on Transition Radiation Tracker (TRT) hit information.

“Superclusters” with variable sizes are formed by combining topo-clusters using the objects mentioned above. The size is dynamically adjusted to incorporate energy from bremsstrahlung photons or electrons generated through photon conversions. For electrons, the formation of superclusters extends to include topo-clusters that share the matched track with those already added to the superclusters. In the case of conversion photons, topo-clusters matched with tracks associated with the conversion vertex are added.

Identification Electron identification is performed using a likelihood discriminant with the following inputs.

- Variables of the primary track associated with the electron
- Lateral and longitudinal shower shape in the electromagnetic calorimeter
- Information regarding the alignment of the track and calorimeter

The likelihood discriminant is formed by probability density functions (pdfs) measured in $Z \rightarrow ee$ for ($E_T > 15$ GeV) and $J/\psi \rightarrow ee$ (for $E_T > 15$ GeV) events for signals and backgrounds. Separate pdfs are derived from electrons in data events for each E_T and η range to incorporate the energy and position dependence. The likelihood discriminant is formed using the signal and background pdfs as

$$L_{S(B)}(\mathbf{x}) = \prod_{i=1}^n P_{S(B),i}(x_i). \quad (\text{C.3})$$

This thesis uses the *LooseAndBLayerLLH* and *MediumLLH* working points for electron identification. The *LooseAndBLayerLLH* working point requires a threshold to the likelihood discriminant to achieve a detection efficiency of 93% for electrons with $E_T = 40$ GeV, and additionally requires a hit in the Insertable B-Layer (IBL) to suppress electrons from photon conversions. The *Medium* working point requires a slightly strict threshold to the likelihood discriminant to achieve a detection efficiency of 88% for electrons with $E_T = 40$ GeV.

Photon identification is performed by applying cuts to shower-shape variables of photons to suppress hadronic jet backgrounds. Energy deposit in the first layer of the EM calorimeter is particularly effective in suppressing photons from neutral pion decays. This thesis uses the *Tight* working point for photon identification. The applied cuts are optimized using TMVA [129] for both converted and unconverted photons.

Isolation This thesis uses the *Loose_VarRad* working point for electron isolation. The track-based isolation variable for electrons, denoted as $p_T^{\text{varcone30}}$, is defined as the scalar sum of the p_T of tracks with $p_T > 1$ GeV and within a variable cone size around the electron. The calorimeter-based isolation variable for electrons, denoted as $E_T^{\text{topoetcone20}}$, is defined as the scalar sum of topo-clusters within $\Delta R < 0.2$ of the electron.

This thesis uses the *FixedCutTight* working point for photon isolation. The track-based isolation variable for photons, denoted as p_T^{cone20} , is defined as the scalar sum of the p_T of tracks with $p_T > 1$ GeV and within a cone size of $\Delta R = 0.2$ around the photon. The calorimeter-based isolation variable for photons, denoted as $E_T^{\text{topoetcone40}}$, is defined as the scalar sum of topo-clusters within $\Delta R < 0.4$ of the photon.

The selections applied to track-based isolation variables and calorimeter-based isolation variables are summarized in Table C.1.

Table C.1: Definitions of isolation working point of electrons and photons.

Object	Working point	Track-based isolation	Calorimeter-based isolation
Electron	<i>Loose_VarRad</i>	$p_T^{\text{varcone30}}/p_T < 0.15$	$E_T^{\text{topoetcone20}}/p_T < 0.2$
Photon	<i>FixedCutTight</i>	$p_T^{\text{cone20}}/p_T < 0.05$	$E_T^{\text{topoetcone40}} < 0.022 \times p_T + 2.45$

The electron identification and isolation efficiencies are summarized in Figures C.3(a) and C.3(b), respectively. The efficiencies for converted and unconverted photon identification and isolation are summarized in Figures C.4(a) and C.4(b) and Figures C.5(a) and C.5(b), respectively.

Energy Calibration The energy scale and resolution of electrons and photons are calibrated using the $Z \rightarrow ee$ process. The correction factor for the energy scale applied to the data is denoted as α_i , where i represents the η region. Similarly, the correction factor for the energy resolution applied to the simulation is denoted as c_i . The two correction factors are defined as

$$E^{\text{data, corr}} = \frac{E^{\text{data}}}{(1 + \alpha_i)}, \quad (\text{C.4})$$

$$\left(\frac{\sigma_E}{E}\right)^{\text{MC, corr}} = \left(\frac{\sigma_E}{E}\right)^{\text{MC}} \oplus c_i, \quad (\text{C.5})$$

where α_i and c_i are derived by minimizing the difference between the invariant mass distribution in data and simulation.

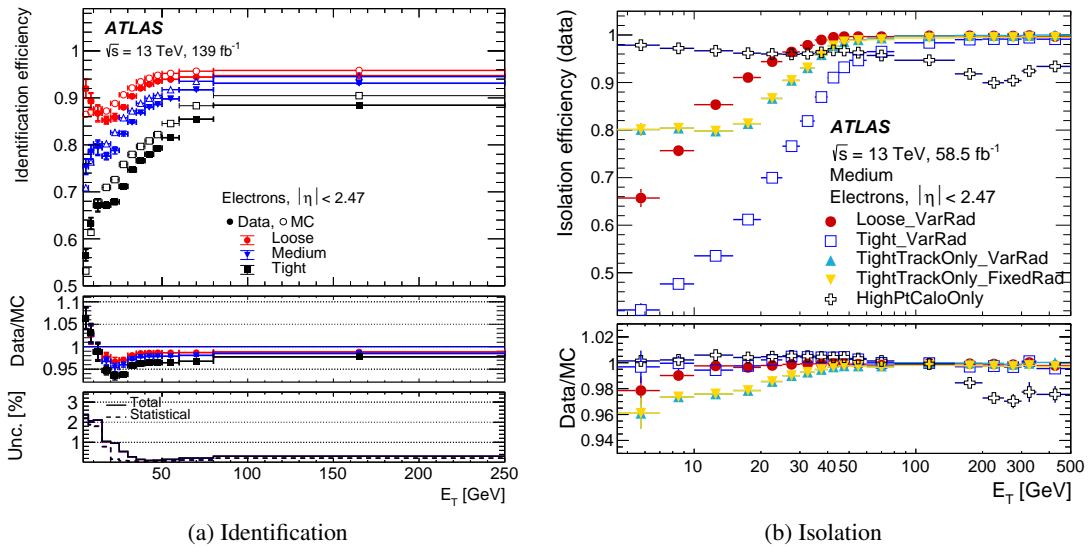


Figure C.3: (a) Electron identification efficiency for multiple working points as a function of electron E_T measured in $Z \rightarrow ee$ events. The middle panel shows the ratio of data and simulation, and the combined systematic and MC statistical uncertainties are illustrated in the bottom panel. (b) Electron isolation efficiency for the multiple working points as a function of electron E_T measured in $Z \rightarrow ee$ events. The bottom panel shows the ratio of data and simulation with the combined systematic and MC statistical uncertainties. The figures are taken from Ref. [130].

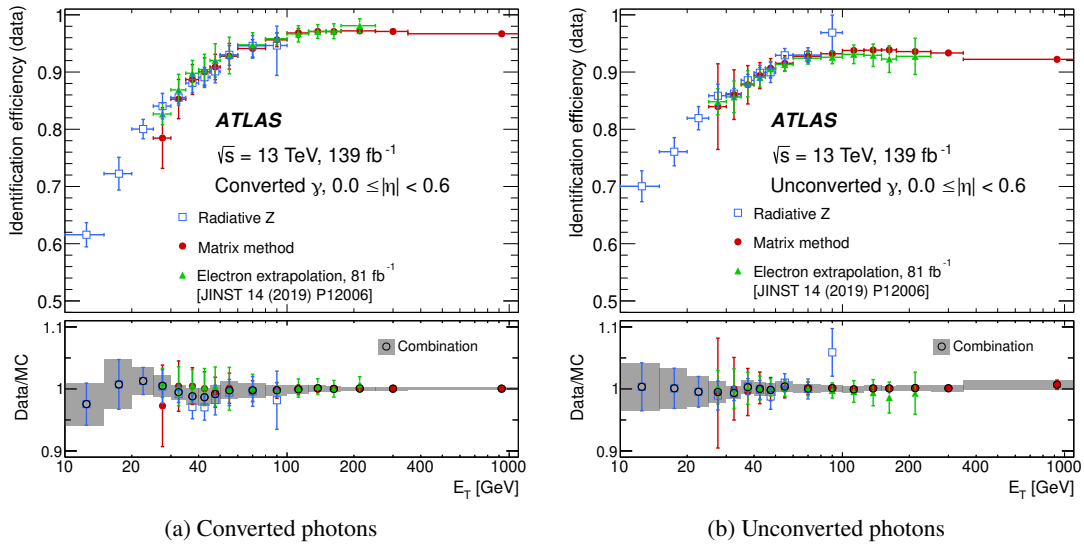
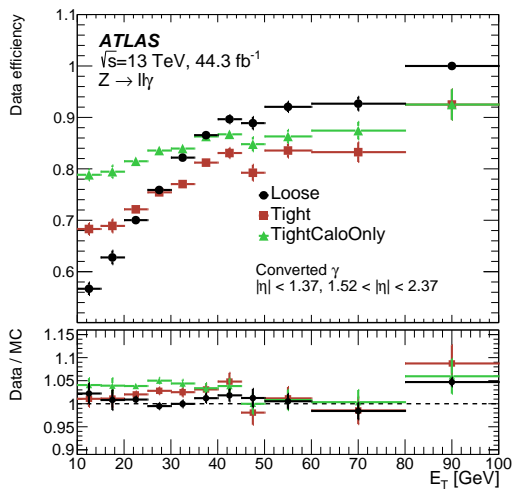
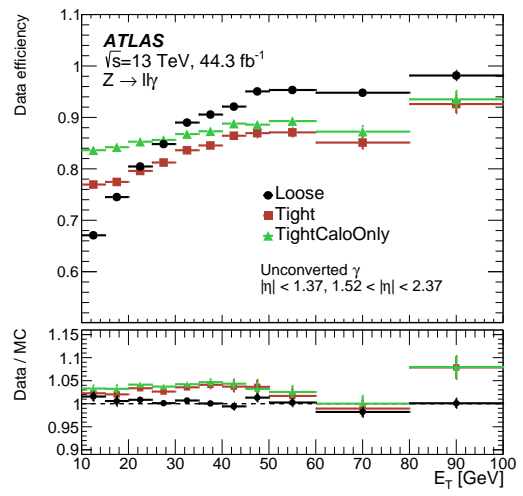


Figure C.4: Photon identification efficiency for converted and unconverted photons as a function of photon E_T . The “Radiative Z” method collects $Z \rightarrow \ell\ell\gamma$ events to measure the photon identification in low E_T ranges. The “Matrix method” utilizes inclusive photon events collected by single-photon triggers, providing large data statistics in the high E_T range. The “Electron extrapolation” method is used to complement the measurements in the medium E_T range using $Z \rightarrow ee$ events. The shower shape from electrons is transformed to match the properties of photon showers estimated by simulation. The bottom panel shows the ratio of data and simulation with the combined systematic and MC statistical uncertainties. The figures are taken from Ref. [130].



(a) Converted photons



(b) Unconverted photons

Figure C.5: Photon isolation efficiency for converted and unconverted photons as a function of photon E_T , measured in $Z \rightarrow \ell\ell\gamma$ events for multiple working points. The bottom panel shows the ratio of data and simulation with the combined systematic and MC statistical uncertainties. The figures are taken from Ref. [128].

Appendix D

Expected yields and efficiency for each selection

This chapter summarizes the expected yield and efficiency after applying selections described in Chapter 6.

The yields of the background process after each selection are summarized in Tables D.1 to D.3. Table D.1 shows the yields after applying selections to satisfy the “jets+ E_T^{miss} ” signature such as the event cleaning and leading jet selections, and Table D.2 shows the yields after applying selections to the track kinematics. Table D.3 shows the yields after selections applied to define the SRs described in Section 6.5.2.

For the signal process, expected yields for each mass difference are summarized in Tables D.4 and D.5 for all selections.

Table D.1: Background yields after applying each event kinematic selection. The efficiency for each selection is also presented.

Variable	$Z(\rightarrow \nu\bar{\nu})+\text{jets}$	$Z(\rightarrow \ell\ell)+\text{jets}$	$Z(\rightarrow \tau\tau)+\text{jets}$
–	3.5×10^5	1.2×10^6	9.6×10^4
Trigger	3.5×10^5 (99.7%)	1.1×10^5 (9.3%)	3.2×10^4 (32.7%)
Leading jet p_T [GeV]	3.5×10^5 (99.8%)	6.4×10^4 (58.3%)	2.1×10^4 (66.1%)
Leading jet $ \eta $	3.5×10^5 (100.0%)	6.4×10^4 (99.8%)	2.1×10^4 (99.8%)
Leading jet cleaning working point	3.5×10^5 (99.6%)	6.4×10^4 (99.5%)	2.1×10^4 (99.3%)
E_T^{miss} [GeV]	3.5×10^5 (99.5%)	1.7×10^3 (2.6%)	7.7×10^3 (37.1%)
Number of leptons	3.4×10^5 (97.5%)	512.2 (30.6%)	3.4×10^3 (44.3%)
Number of jets	3.2×10^5 (93.4%)	479.5 (93.6%)	2.7×10^3 (78.6%)
$\min(\Delta\phi(\mathbf{p}_T^{\text{jets}}, \mathbf{p}_T^{\text{miss}}))$	2.9×10^5 (91.0%)	423.9 (88.4%)	756.7 (28.3%)

Variable	$W(\rightarrow \ell\nu)+\text{jets}$	$W(\rightarrow \tau\nu)+\text{jets}$	$t\bar{t}$
–	2.2×10^6	3.9×10^5	3.2×10^6
Trigger	1.0×10^6 (47.0%)	3.3×10^5 (84.2%)	2.2×10^6 (70.8%)
Leading jet p_T [GeV]	7.8×10^5 (76.8%)	3.0×10^5 (92.2%)	5.0×10^5 (22.1%)
Leading jet $ \eta $	7.8×10^5 (99.9%)	3.0×10^5 (100.0%)	4.9×10^5 (98.4%)
Leading jet cleaning working point	7.8×10^5 (99.5%)	3.0×10^5 (99.5%)	4.9×10^5 (99.8%)
E_T^{miss} [GeV]	2.7×10^5 (34.9%)	2.3×10^5 (76.8%)	1.3×10^5 (26.5%)
Number of leptons	6.0×10^4 (22.1%)	1.7×10^5 (72.1%)	4.8×10^4 (37.4%)
Number of jets	5.5×10^4 (91.1%)	1.5×10^5 (87.6%)	2.0×10^4 (42.4%)
$\min(\Delta\phi(\mathbf{p}_T^{\text{jets}}, \mathbf{p}_T^{\text{miss}}))$	4.7×10^4 (85.2%)	8.7×10^4 (60.1%)	9.1×10^3 (44.3%)

Variable	Single top	Di-boson	$\gamma+\text{jets}$
–	1.1×10^6	1.4×10^5	1.7×10^6
Trigger	3.7×10^5 (32.4%)	8.1×10^4 (59.7%)	5.0×10^4 (2.9%)
Leading jet p_T [GeV]	9.5×10^4 (26.1%)	6.7×10^4 (82.7%)	4.6×10^4 (92.4%)
Leading jet $ \eta $	9.4×10^4 (98.2%)	6.7×10^4 (99.9%)	4.6×10^4 (100.0%)
Leading jet cleaning working point	9.3×10^4 (99.6%)	6.7×10^4 (99.6%)	2.6×10^4 (56.4%)
E_T^{miss} [GeV]	2.5×10^4 (26.3%)	3.8×10^4 (56.1%)	3.8×10^3 (14.8%)
Number of leptons	9.4×10^3 (38.2%)	1.9×10^4 (49.3%)	3.7×10^3 (96.7%)
Number of jets	5.5×10^3 (58.9%)	1.4×10^4 (77.8%)	3.2×10^3 (85.7%)
$\min(\Delta\phi(\mathbf{p}_T^{\text{jets}}, \mathbf{p}_T^{\text{miss}}))$	2.6×10^3 (47.7%)	1.1×10^4 (74.1%)	24.6 (0.8%)

Variable	Multijet	Total MC	Data
–	7.4×10^6	1.8×10^7	2.2×10^7
Trigger	9.2×10^5 (12.5%)	5.5×10^6 (31.1%)	7.6×10^6 (34.3%)
Leading jet p_T [GeV]	7.0×10^5 (75.4%)	2.9×10^6 (53.1%)	3.8×10^6 (49.6%)
Leading jet $ \eta $	6.9×10^5 (99.8%)	2.9×10^6 (99.6%)	3.8×10^6 (99.5%)
Leading jet cleaning working point	6.2×10^5 (89.7%)	2.8×10^6 (96.5%)	2.7×10^6 (71.3%)
E_T^{miss} [GeV]	3.0×10^5 (48.4%)	1.4×10^6 (48.3%)	1.2×10^6 (44.2%)
Number of leptons	2.5×10^5 (84.3%)	9.0×10^5 (66.7%)	7.9×10^5 (66.7%)
Number of jets	1.7×10^5 (67.4%)	7.4×10^5 (81.4%)	6.8×10^5 (86.4%)
$\min(\Delta\phi(\mathbf{p}_T^{\text{jets}}, \mathbf{p}_T^{\text{miss}}))$	1.0×10^3 (0.6%)	4.5×10^5 (60.8%)	4.8×10^5 (69.9%)

Table D.2: Background yields after applying each track kinematic selection. The efficiency for each selection is also presented.

Variable	$Z(\rightarrow \nu\bar{\nu})+\text{jets}$		$Z(\rightarrow \ell\ell)+\text{jets}$		$Z(\rightarrow \tau\tau)+\text{jets}$	
–	3.5×10^6		5.3×10^3		1.0×10^4	
Track quality	3.1×10^6	(86.5%)	4.5×10^3	(86.2%)	8.9×10^3	(85.3%)
N_{IBL}	2.9×10^6	(95.9%)	4.4×10^3	(95.8%)	8.5×10^3	(95.5%)
p_{T} [GeV]	1.2×10^6	(41.5%)	1.8×10^3	(41.4%)	3.5×10^3	(41.7%)
η	9.3×10^5	(75.9%)	1.4×10^3	(75.2%)	2.7×10^3	(75.5%)
$ d_0 $ [mm]	9.3×10^5	(100.0%)	1.4×10^3	(100.0%)	2.7×10^3	(100.0%)
$ \Delta z_0 \sin \theta $ [mm]	7.5×10^5	(81.2%)	1.1×10^3	(80.7%)	2.1×10^3	(80.2%)
$ \Delta\phi(p_{\text{T}}^{\text{track}}, E_{\text{T}}^{\text{miss}}) $	2.2×10^5	(29.8%)	328.0	(30.0%)	665.5	(31.1%)
Track-based isolation	1.5×10^5	(67.8%)	219.8	(67.0%)	434.9	(65.3%)
Secondary vertex veto	1.5×10^5	(99.9%)	219.6	(99.9%)	434.6	(99.9%)
Leading $S(d_0)$ selection	1.1×10^5	(74.4%)	164.8	(75.0%)	324.1	(74.6%)

Variable	$W(\rightarrow \ell\nu)+\text{jets}$		$W(\rightarrow \tau\nu)+\text{jets}$		$t\bar{t}$	
–	5.9×10^5		1.1×10^6		1.9×10^5	
Track quality	5.1×10^5	(86.2%)	9.6×10^5	(86.1%)	1.6×10^5	(86.6%)
N_{IBL}	4.9×10^5	(95.8%)	9.2×10^5	(95.7%)	1.6×10^5	(95.4%)
p_{T} [GeV]	2.0×10^5	(41.2%)	3.8×10^5	(41.5%)	6.9×10^4	(44.2%)
η	1.5×10^5	(76.0%)	2.9×10^5	(75.9%)	5.4×10^4	(79.0%)
$ d_0 $ [mm]	1.5×10^5	(100.0%)	2.9×10^5	(100.0%)	5.4×10^4	(100.0%)
$ \Delta z_0 \sin \theta $ [mm]	1.2×10^5	(81.0%)	2.4×10^5	(80.9%)	4.7×10^4	(86.7%)
$ \Delta\phi(p_{\text{T}}^{\text{track}}, E_{\text{T}}^{\text{miss}}) $	3.7×10^4	(29.6%)	7.1×10^4	(30.1%)	1.2×10^4	(26.1%)
Track-based isolation	2.4×10^4	(66.3%)	4.8×10^4	(67.7%)	6.3×10^3	(51.5%)
Secondary vertex veto	2.4×10^4	(99.9%)	4.8×10^4	(99.9%)	6.3×10^3	(99.9%)
Leading $S(d_0)$ selection	1.8×10^4	(74.9%)	3.6×10^4	(74.5%)	4.5×10^3	(71.3%)

Variable	Single top		Di-boson		$\gamma+\text{jets}$	
–	4.9×10^4		1.4×10^5		543.3	
Track quality	4.2×10^4	(86.4%)	1.2×10^5	(86.3%)	451.1	(83.0%)
N_{IBL}	4.0×10^4	(95.5%)	1.1×10^5	(95.7%)	418.0	(92.7%)
p_{T} [GeV]	1.8×10^4	(43.6%)	4.7×10^4	(41.8%)	157.1	(37.6%)
η	1.4×10^4	(77.7%)	3.7×10^4	(77.1%)	142.6	(90.8%)
$ d_0 $ [mm]	1.4×10^4	(100.0%)	3.7×10^4	(100.0%)	142.6	(100.0%)
$ \Delta z_0 \sin \theta $ [mm]	1.2×10^4	(85.5%)	3.0×10^4	(82.1%)	144.3	(101.2%)
$ \Delta\phi(p_{\text{T}}^{\text{track}}, E_{\text{T}}^{\text{miss}}) $	3.1×10^3	(26.6%)	8.6×10^3	(28.6%)	53.3	(36.9%)
Track-based isolation	1.8×10^3	(56.3%)	5.5×10^3	(64.6%)	13.7	(25.7%)
Secondary vertex veto	1.7×10^3	(99.9%)	5.5×10^3	(99.9%)	13.7	(100.0%)
Leading $S(d_0)$ selection	1.3×10^3	(72.2%)	4.1×10^3	(74.2%)	11.1	(81.3%)

Variable	Multijet		Total MC		Data	
–	1.8×10^4		5.7×10^6		7.7×10^6	
Track quality	1.5×10^4	(84.8%)	4.9×10^6	(86.4%)	6.6×10^6	(85.0%)
N_{IBL}	1.4×10^4	(94.2%)	4.7×10^6	(95.8%)	6.2×10^6	(95.0%)
p_{T} [GeV]	6.2×10^3	(43.7%)	2.0×10^6	(41.6%)	2.7×10^6	(42.8%)
η	4.9×10^3	(78.6%)	1.5×10^6	(76.1%)	2.0×10^6	(75.0%)
$ d_0 $ [mm]	4.9×10^3	(100.0%)	1.5×10^6	(100.0%)	2.0×10^6	(100.0%)
$ \Delta z_0 \sin \theta $ [mm]	3.9×10^3	(80.1%)	1.2×10^6	(81.4%)	1.6×10^6	(81.0%)
$ \Delta\phi(p_{\text{T}}^{\text{track}}, E_{\text{T}}^{\text{miss}}) $	1.4×10^3	(36.1%)	3.6×10^5	(29.7%)	4.7×10^5	(28.8%)
Track-based isolation	630.9	(44.5%)	2.4×10^5	(66.8%)	3.1×10^5	(67.3%)
Secondary vertex veto	630.8	(100.0%)	2.4×10^5	(99.9%)	3.1×10^5	(99.9%)
Leading $S(d_0)$ selection	476.9	(75.6%)	1.8×10^5	(74.4%)	2.2×10^5	(71.4%)

Table D.3: Background yields after applying each track kinematic selection for SR-Low and SR-High. The efficiency for each selection is also presented.

Variable	$Z(\rightarrow \nu\bar{\nu})+\text{jets}$		$Z(\rightarrow \ell\ell)+\text{jets}$		$Z(\rightarrow \tau\tau)+\text{jets}$	
Preselection	1.1×10^5	–	194.9	–	400.9	–
E_T^{miss} [GeV]	4319.2	(3.8%)	2.7	(1.4%)	7.3	(1.8%)
Track p_T [GeV]	801.1	(18.5%)	0.2	(7.0%)	1.3	(17.6%)
SR-Low	7.1	(0.9%)	-0.0	(-0.3%)	0.1	(6.1%)
SR-High	5.1	(0.6%)	0.0	(0.1%)	0.0	(2.1%)

Variable	$W(\rightarrow \ell\nu)+\text{jets}$		$W(\rightarrow \tau\nu)+\text{jets}$		$t\bar{t}$	
Preselection	2.1×10^4	–	4.1×10^4	–	5068.3	–
E_T^{miss} [GeV]	618.1	(2.9%)	1099.1	(2.7%)	88.3	(1.7%)
Track p_T [GeV]	69.3	(11.2%)	246.2	(22.4%)	15.9	(18.0%)
SR-Low	0.7	(1.0%)	20.8	(8.5%)	1.3	(8.5%)
SR-High	0.5	(0.7%)	4.5	(1.8%)	0.4	(2.8%)

Variable	Single top		Di-boson		$\gamma+\text{jets}$	
Preselection	1466.3	–	4362.0	–	1.5	–
E_T^{miss} [GeV]	51.9	(3.5%)	299.1	(6.9%)	0.0	(0.1%)
Track p_T [GeV]	6.7	(12.8%)	55.3	(18.5%)	0.0	(0.0%)
SR-Low	0.4	(5.8%)	1.3	(2.4%)	0.0	(0.0%)
SR-High	0.0	(0.0%)	0.3	(0.5%)	0.0	(0.0%)

Variable	Multijet		Total MC	
Preselection	467.9	–	1.9×10^5	–
E_T^{miss} [GeV]	4.2	(0.9%)	6489.7	(3.5%)
Track p_T [GeV]	1.9	(45.6%)	1197.8	(18.5%)
SR-Low	0.0	(0.0%)	31.7	(2.6%)
SR-High	0.0	(0.0%)	10.8	(0.9%)

Table D.4: Cutflows for signal samples with $m(\tilde{\chi}_1^0) = 150$ GeV, $\Delta m(\tilde{\chi}_1^\pm, \tilde{\chi}_1^0) = 1.5, 1.0,$ and 0.75 GeV.

Variable	$\Delta m(\tilde{\chi}_1^\pm, \tilde{\chi}_1^0) = 1.5$ GeV		$\Delta m(\tilde{\chi}_1^\pm, \tilde{\chi}_1^0) = 1.0$ GeV		$\Delta m(\tilde{\chi}_1^\pm, \tilde{\chi}_1^0) = 0.75$ GeV	
Initial number of event ($\mathcal{L} \times \sigma$)	1.4×10^5		1.4×10^5		1.4×10^5	
Preliminary event reduction	4.3×10^4	(30.5%)	4.4×10^4	(30.6%)	4.4×10^4	(30.6%)
Trigger selection and event cleaning	3.8×10^4	(88.6%)	3.8×10^4	(88.4%)	3.9×10^4	(88.3%)
Leading jet $p_T > 250$ GeV	8164.87	(21.3%)	8140.66	(21.2%)	8210.42	(21.2%)
Leading jet $ \eta < 2.4$	8041.61	(98.5%)	8015.01	(98.5%)	8086.68	(98.5%)
Leading jet cleaning working point	8000.66	(99.5%)	7972.63	(99.5%)	8046.44	(99.5%)
Lepton veto	7582.11	(94.8%)	7773.71	(97.5%)	7901.84	(98.2%)
Photon veto	7499.56	(98.9%)	7691.53	(98.9%)	7818.10	(98.9%)
$n_{\text{jet}} \leq 4$	7283.93	(97.1%)	7474.93	(97.2%)	7593.55	(97.1%)
$\min(\Delta\phi(\text{any jet}, \mathbf{p}_T^{\text{miss}})) > 0.4$	6613.79	(90.8%)	6804.89	(91.0%)	6912.05	(91.0%)
$n(\text{signal track candidate}) \geq 1$	3492.72	(52.8%)	3572.95	(52.5%)	3565.01	(51.6%)
$E_T^{\text{miss}} > 600$ GeV	215.71	(6.2%)	232.93	(6.5%)	232.32	(6.5%)
Track $p_T \in [2, 5]$ GeV	60.71	(28.1%)	69.03	(29.6%)	75.74	(32.6%)
SR-Low						
$S(d_0) \in [8, 20]$	0.30	(0.5%)	4.14	(6.0%)	10.31	(13.6%)
SR-High						
$S(d_0) \in [20, \infty)$	0.09	(0.1%)	1.20	(1.7%)	6.16	(8.1%)

 Table D.5: Cutflows for signal samples with $m(\tilde{\chi}_1^0) = 150$ GeV, $\Delta m(\tilde{\chi}_1^\pm, \tilde{\chi}_1^0) = 0.5, 0.35,$ and 0.25 GeV.

Variable	$\Delta m(\tilde{\chi}_1^\pm, \tilde{\chi}_1^0) = 0.5$ GeV		$\Delta m(\tilde{\chi}_1^\pm, \tilde{\chi}_1^0) = 0.35$ GeV		$\Delta m(\tilde{\chi}_1^\pm, \tilde{\chi}_1^0) = 0.25$ GeV	
Initial number of event ($\mathcal{L} \times \sigma$)	1.4×10^5		1.4×10^5		1.4×10^5	
Preliminary event reduction	4.4×10^4	(30.7%)	4.4×10^4	(30.8%)	4.5×10^4	(30.8%)
Trigger selection and event cleaning	3.9×10^4	(88.3%)	3.9×10^4	(88.3%)	3.9×10^4	(88.3%)
Leading jet $p_T > 250$ GeV	8237.52	(21.2%)	8195.16	(21.0%)	8308.96	(21.1%)
Leading jet $ \eta < 2.4$	8110.38	(98.5%)	8065.29	(98.4%)	8184.73	(98.5%)
Leading jet cleaning working point	8070.78	(99.5%)	8024.51	(99.5%)	8142.57	(99.5%)
Lepton veto	7955.52	(98.6%)	7912.68	(98.6%)	8028.68	(98.6%)
Photon veto	7870.36	(98.9%)	7827.72	(98.9%)	7940.17	(98.9%)
$n_{\text{jet}} \leq 4$	7655.47	(97.3%)	7604.84	(97.2%)	7712.77	(97.1%)
$\min(\Delta\phi(\text{any jet}, \mathbf{p}_T^{\text{miss}})) > 0.4$	6966.32	(91.0%)	6943.76	(91.3%)	7016.04	(91.0%)
$n(\text{signal track candidate}) \geq 1$	3366.59	(48.3%)	3140.10	(45.2%)	3104.41	(44.2%)
$E_T^{\text{miss}} > 600$ GeV	222.97	(6.6%)	193.03	(6.1%)	179.76	(5.8%)
Track $p_T \in [2, 5]$ GeV	62.75	(28.1%)	36.45	(18.9%)	29.39	(16.4%)
SR-Low						
$S(d_0) \in [8, 20]$	8.99	(14.3%)	2.55	(7.0%)	0.62	(2.1%)
SR-High						
$S(d_0) \in [20, \infty)$	11.28	(18.0%)	3.45	(9.5%)	0.57	(1.9%)

Appendix E

Composition of Background Events

As discussed in Section 7.1, the τ decay track and QCD track are the main backgrounds in this analysis. These backgrounds are reconstructed as displaced tracks due to the lifetime of τ leptons, strange hadrons, and B/D mesons, as illustrated in Figure E.1. In this chapter, more details of the background composition than those shown in the main text are provided in Tables E.1 and E.2. We also briefly explain how the tracks and truth particles in MC simulations are associated, which is crucial for understanding the background composition.

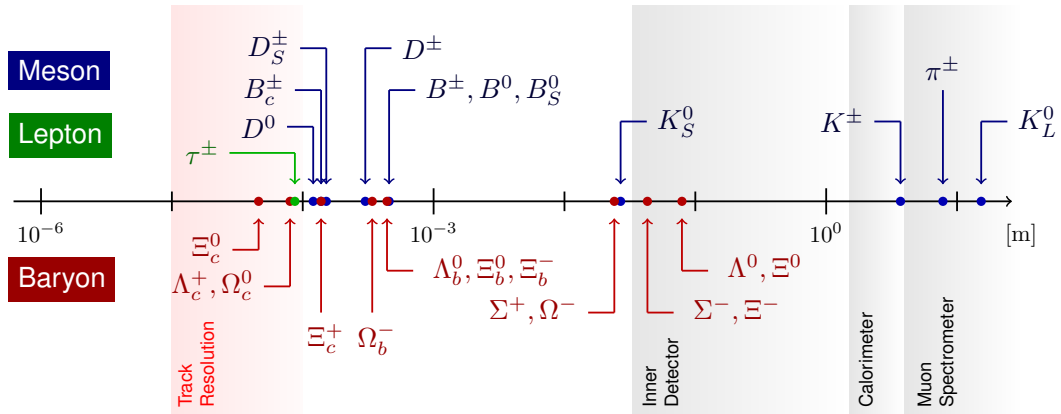


Figure E.1: The lifetime of τ leptons, strange hadrons, and B/D mesons. The gray areas indicate the location of the ID, the calorimeter, and the MS. The red region represents the resolution of the track reconstruction in the ATLAS detector. If a particle's lifetime is longer than this red region, it can be distinguished from particles produced promptly. Strange hadrons have significant lifetimes that reach the ATLAS detector, unlike τ leptons and B/D mesons, which have lifetimes close to the track resolution.

Table E.1: The table shows the number of tracks in SR-Low and SR-High estimated from the $W(\rightarrow \tau\nu)+\text{jets}$ sample for each decay mode. Decay modes from τ leptons are highlighted in blue. The first particle after the arrow corresponds to the particle producing the track.

(a) Composition in SR-Low			(b) Composition in SR-High		
Decay Mode	Count	Ratio [%]	Decay Mode	Count	Ratio [%]
$\tau^+ \rightarrow e^+ + \bar{\nu}_\tau + \dots$	3.90	23.77	$\tau^+ \rightarrow \pi^+ + \bar{\nu}_\tau$	2.36	31.77
$\tau^+ \rightarrow \pi^+ + \pi^0 + \dots$	2.42	14.75	$\tau^- \rightarrow e^- + \nu_\tau + \dots$	1.52	20.48
Pileup	2.12	12.93	Pileup	0.89	11.91
$\tau^+ \rightarrow \mu^+ + \bar{\nu}_\tau + \dots$	1.30	7.95	$\tau^+ \rightarrow e^+ + \bar{\nu}_\tau + \dots$	0.86	11.59
$\tau^- \rightarrow \pi^- + \nu_\tau$	1.15	7.04	$\tau^+ \rightarrow \mu^+ + \bar{\nu}_\tau + \dots$	0.57	7.66
$\tau^+ \rightarrow \pi^+ + \bar{\nu}_\tau$	0.97	5.91	$\tau^+ \rightarrow \pi^+ + \pi^0 + \dots$	0.46	6.14
$\tau^- \rightarrow \pi^- + \pi^0 + \dots$	0.94	5.76	$\bar{\Sigma}^- \rightarrow \bar{p} + \pi^0$	0.15	2.06
$\tau^+ \rightarrow \pi^+ + \bar{\nu}_\tau + \dots$	0.72	4.37	$\tau^- \rightarrow \pi^- + \pi^0 + \dots$	0.15	2.00
$\tau^+ \rightarrow e^+ + \bar{\nu}_\tau + \dots$	0.65	3.94	$\tau^- \rightarrow \pi^- + \nu_\tau$	0.14	1.91
other	2.23	13.59	other	0.33	4.49
Total	16.40	-	Total	7.44	-

Table E.2: The table shows the number of tracks in SR-Low and SR-High estimated from the $Z(\rightarrow \nu\bar{\nu})$ +jets sample for each decay mode. Decay modes from strange hadrons are highlighted in blue. The first particle after the arrow corresponds to the particle producing the track. *NoParticle* corresponds to particles with missing information due to low momentum. The notation “jets” indicates that the tracks are from jets and are classified according to the type of particle reconstructed as the track.

(a) Composition in SR-Low			(b) Composition in SR-High		
Decay Mode	Count	Ratio [%]	Decay Mode	Count	Ratio [%]
Pileup	1.57	18.64	Pileup	1.87	33.98
$\bar{\Sigma}^- \rightarrow \bar{p} + \pi^0$	0.57	6.83	$\Sigma^+ \rightarrow p + \pi^0$	0.39	7.16
$\Sigma^+ \rightarrow p + \pi^0$	0.50	5.97	$\rho(770)^- \rightarrow \pi^- + \pi^0$	0.34	6.21
$\bar{\Lambda} \rightarrow \bar{p} + \pi^+$	0.49	5.78	$\rho(770)^0 \rightarrow \pi^- + \pi^+$	0.30	5.42
$K_S^0 \rightarrow \pi^+ + \pi^-$	0.33	3.96	$K_S^0 \rightarrow \pi^- + \pi^+$	0.20	3.71
$b_1(1235)^+ \rightarrow \pi^+ + \omega(782)$	0.29	3.46	$\Lambda \rightarrow p + \pi^-$	0.18	3.29
$\rho(770)^+ \rightarrow \pi^+ + \pi^0$	0.27	3.21	$K_S^0 \rightarrow \pi^+ + \pi^-$	0.16	2.96
<i>jets</i> $\rightarrow \bar{p} + \dots$	0.23	2.74	$\bar{\Sigma}^- \rightarrow \bar{p} + \pi^0$	0.14	2.58
$\bar{\Lambda} \rightarrow \bar{p} + \text{NoParticle}$	0.20	2.37	$B^- \rightarrow \pi^- + D^*(2010)^+ + \dots$	0.14	2.51
$\Lambda \rightarrow p + \pi^-$	0.19	2.26	$\bar{\Lambda} \rightarrow \bar{p} + \pi^+$	0.12	2.21
$\rho(770)^- \rightarrow \pi^- + \pi^0$	0.19	2.24	$\rho(770)^0 \rightarrow \pi^+ + \pi^-$	0.12	2.18
$\Sigma^+ \rightarrow p + \text{NoParticle}$	0.13	1.51	$\rho(770)^+ \rightarrow \pi^+ + \pi^0$	0.11	1.93
$\bar{\Sigma}^- \rightarrow \bar{p} + \text{NoParticle}$	0.12	1.47	$\bar{\Sigma}^- \rightarrow \bar{p} + \text{NoParticle}$	0.09	1.61
$D^- \rightarrow \pi^- + \phi(1020) + \dots$	0.12	1.43	$\Delta(1232)^{++} \rightarrow p + \pi^+$	0.06	1.14
$K^*(892)^- \rightarrow K^- + \pi^0$	0.12	1.41	$\bar{\Delta}(1232)^- \rightarrow \bar{p} + \pi^0$	0.06	1.11
$K_S^0 \rightarrow \pi^- + \pi^+$	0.12	1.40	$\Sigma^+ \rightarrow p + \text{NoParticle}$	0.06	1.06
$\rho(770)^0 \rightarrow \pi^+ + \pi^-$	0.12	1.38	$\bar{K}_2^*(1430)^0 \rightarrow K^- + \pi^+$	0.06	1.06
$\bar{D}^0 \rightarrow \pi^- + K^+ + \dots$	0.11	1.27	$D^- \rightarrow e^- + K^0 + \dots$	0.06	1.02
$B^0 \rightarrow e^+ + D^*(2010)^- + \dots$	0.11	1.26	$B^- \rightarrow \mu^- + D_1(2430)^0 + \dots$	0.05	0.89
$K_S^0 \rightarrow \pi^+ + \text{NoParticle}$	0.10	1.15	<i>Unknown</i> $\rightarrow \bar{p} + \pi^0$	0.05	0.87
$\bar{B}_s^0 \rightarrow \pi^- + D_s^{*+} + \dots$	0.09	1.03	$B^- \rightarrow \mu^- + D^*(2007)^0 + \dots$	0.05	0.86
$K_S^0 \rightarrow \pi^- + \text{NoParticle}$	0.08	0.91	$D^0 \rightarrow \pi^- + K^+$	0.05	0.83
<i>jets</i> $\rightarrow \pi^- + \dots$	0.08	0.90	$\omega(782) \rightarrow \pi^- + \pi^+ + \dots$	0.04	0.81
$D^+ \rightarrow \mu^+ + \bar{K}^0 + \dots$	0.07	0.87	$\Sigma_c(2520)^0 \rightarrow \pi^- + \Lambda_c^+$	0.04	0.80
$B^- \rightarrow \mu^- + D^*(2007)^0 + \dots$	0.07	0.84	$a_1(1260)^0 \rightarrow \pi^- + \rho(770)^+$	0.04	0.77
$K^*(892)^0 \rightarrow K^+ + \pi^-$	0.07	0.83	$\bar{\Delta}(1232)^{-} \rightarrow \bar{p} + \pi^-$	0.04	0.76
$B^+ \rightarrow \mu^+ + \bar{D}^*(2007)^0 + \dots$	0.07	0.83	$\bar{\Lambda}_c^- \rightarrow \pi^- + \bar{\Lambda}$	0.04	0.76
$D^+ \rightarrow \pi^+ + \bar{K}^0 + \dots$	0.07	0.79	<i>jets</i> $\rightarrow \bar{p} + \dots$	0.04	0.75
$D^+ \rightarrow K^+ + \bar{K}^*(892)^0$	0.07	0.78	$D^+ \rightarrow \pi^+ + \bar{K}^0 + \dots$	0.04	0.72
other	1.89	22.47	other	0.55	10.05
Total	8.40	-	Total	5.50	-

Random combinations of hits may reconstruct tracks, or tracks may not be reconstructed due to a lack of hits caused by the detector's inefficiency. Therefore, it is essential to associate the tracks and MC simulation truth particles with high accuracy to understand the tracking performance in this analysis. The following quantity is defined as the probability that the reconstructed track and truth particle are identical [131]:

$$P_{\text{match}} = \frac{2N_{\text{common}}^{\text{pix}} + N_{\text{common}}^{\text{strip}}}{2N_{\text{track}}^{\text{pix}} + N_{\text{track}}^{\text{strip}}}, \quad (\text{E.1})$$

where $N_{\text{track}}^{\text{pix}}$ ($N_{\text{track}}^{\text{strip}}$) is the number of Pixel (Strip) detector clusters used for reconstruction of tracks. $N_{\text{common}}^{\text{pix}}$ ($N_{\text{common}}^{\text{strip}}$) is the number of Pixel (Strip) detector clusters used for reconstruction of tracks which the interaction of the truth particle and the ID has produced. A factor of 2 is applied to the number of pixel hits because the pixel measures 2-dimensional position information at each layer while the strip measures only 1-dimensional information at each layer. If a track has a truth particle that satisfies $P_{\text{match}} > 0.5$ (50% of the clusters used to reconstruct the track are from truth particles), the track and its truth particle are associated with each other.

Appendix F

Full data-driven estimation of Non-collision background

The contribution of non-collision background is estimated using the number of data in regions where their contribution is dominant. The reconstructed time of objects in the ATLAS detector is calibrated by considering the time-of-flight from the interaction point. Therefore, the time of objects from the interaction point is approximately zero. On the other hand, since jets produced by non-collision backgrounds do not originate from the interaction point, the time deviates from zero when calibrated by the time of flight from the interaction point. Figure F.1(a) shows the time of the leading jet ($|t_{\text{jet}}|$), which passed the *Tight* jet cleaning, indicating that a region dominated by non-collision background can be defined by requiring $|t_{\text{jet}}| > 5$ ns. As seen in Figure F.1(b), the non-collision background is dominant for events with leading jets that fail the *Tight* jet cleaning. Since the *Tight* jet cleaning applied to the leading jet does not use the time information of the jet, the reduction rate of non-collision background is not correlated with time information. And since *Tight* jet cleaning does not use the time information of jets, the reduction rate of non-collision background does not correlate with the time information. Therefore, the reduction rate of non-collision background by *Tight* jet cleaning for $|t_{\text{jet}}| > 5$ ns is first calculated from the ratio of the number of data in the region where the leading jet fails the tight jet cleaning to the number of data in the region where it passes. Assuming that the reduction rate is the same for $|t_{\text{jet}}| < 5$ ns, the contribution of non-collision background in the region where the leading jet with $|t_{\text{jet}}| < 5$ ns passing the *Tight* jet cleaning can be estimated by multiplying by the number of data in the region where the leading jet fails the *Tight* jet cleaning. Finally, the number of non-collision backgrounds in the region close to the SRs is obtained by adding the number estimated for $|t_{\text{jet}}| < 5$ ns and the number observed for $|t_{\text{jet}}| > 5$ ns.

Figure F.2 shows a schematic view of regions used for background estimation of non-collision background. Figure F.3 shows the event display of a non-collision background event. The results show a contribution at the per-mile level in the 0ℓ category, defined with $E_{\text{T}}^{\text{miss}} > 300$ GeV, $S(d_0) > 2$ and inclusive of jet timing (Table F.1). Since the SRs require $E_{\text{T}}^{\text{miss}} > 600$ GeV and $S(d_0) > 8$, it can be concluded that the contribution of non-collision background in the SRs is sufficiently small.

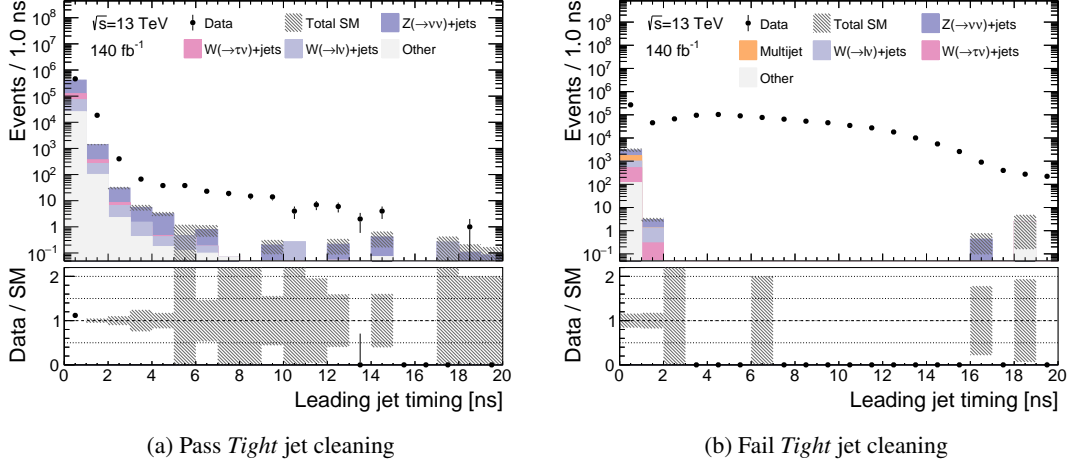
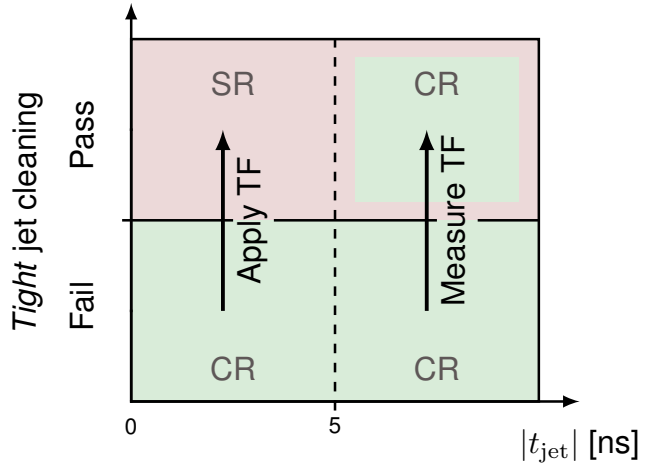


Figure F.1: Distribution of time information of the leading jet passing and failing the *Tight* jet cleaning. (a) The *Tight* jet cleaning effectively removes the non-collision background but remains in the area with high jet timing ($|t_{\text{jet}}| > 5$ ns). (b) In the region where the leading jet fails *Tight* jet cleaning, the contribution from MC simulation is negligible, indicating that the non-collision background is dominant.

Figure F.2: Schematic view of region definition for the non-collision background estimation. The green area shows the regions utilized for the estimation of non-collision background. The Transfer Factor (TF) is calculated by taking the ratio between the upper-right and lower-right region, as indicated by an arrow. The TF is then multiplied by the yield in the lower-left region to estimate the non-collision background yield in the upper-left region. The total contribution near the SRs is estimated by taking the sum of the observed yield in the upper-right region and the estimated yield in the lower-left region.



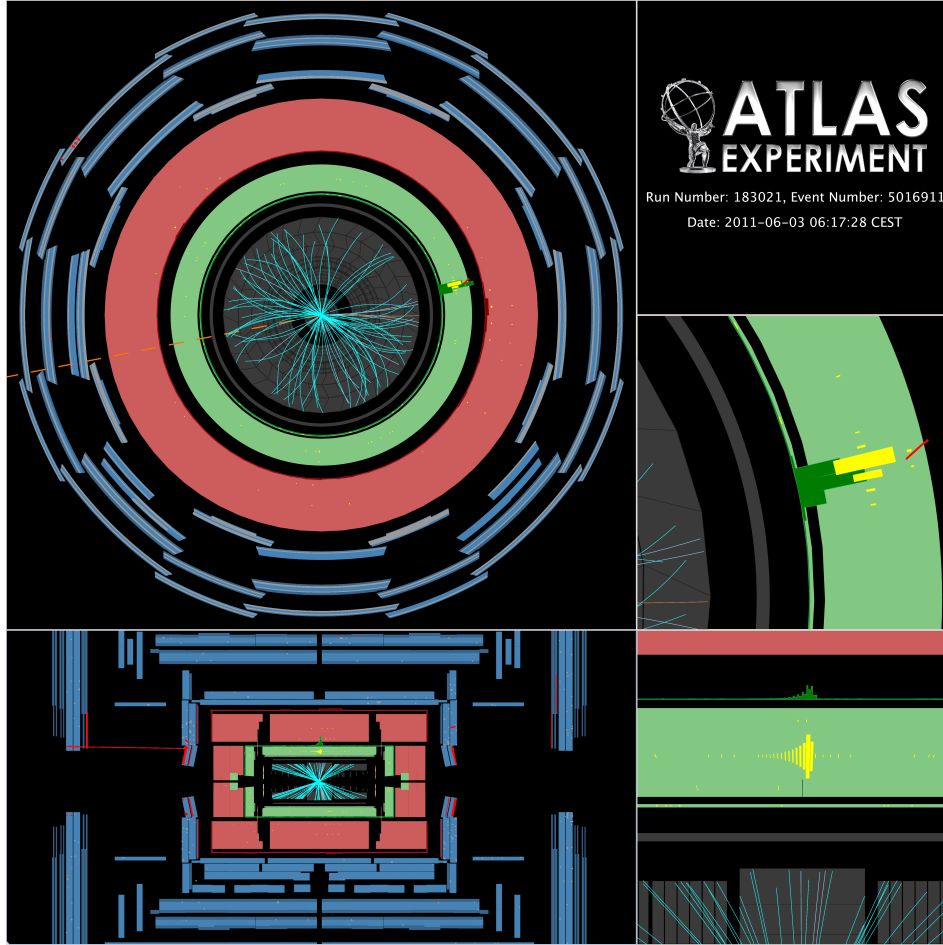


Figure F.3: Event display of a non-collision background event. The red areas represent hits in the muon spectrometers, and the horizontal red line is the reconstructed muon segment by the beam-induced muon. The horizontally produced muon passes through the calorimeter and leaves energy deposits in the calorimeter cells, illustrated as yellow rectangles. The upper-left plot shows no tracks associated with the reconstructed jets in the non-collision background event. The figure is taken from Ref. [132].

Table F.1: Number of observed and estimated tracks ($N_{\text{track}}^{\text{obs}}$ and $N_{\text{track}}^{\text{est}}$) in each region used to estimate the number of tracks from non-collision background near the SR.

Working point	Jet timing ($ t_{\text{jet}} $)	$N_{\text{track}}^{\text{obs}}$	$N_{\text{track}}^{\text{est}}$
Loose	> 5 ns	27721	-
Loose	< 5 ns	38601	-
Tight	> 5 ns	8	-
Tight	< 5 ns	-	11
Tight	-	-	19

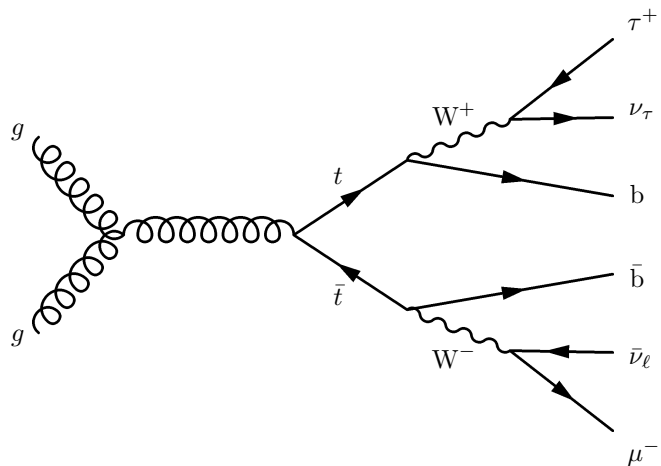
Appendix G

Validation of τ decay track estimation with $t\bar{t}$ process

G.1 Overview

As discussed in Section 7.2, the estimation strategy for the τ decay tracks was validated using the $W(\rightarrow \tau\nu)$ +jets process. Meanwhile, there are other processes in which τ decay tracks are generated, such as the $Z(\rightarrow \tau\tau)$ +jets and $t\bar{t}$ processes. Among them, the decay mode shown in Figure G.1 is characterized by two b -jets from the top decay, a muon from the leptonic decay of the W boson, and a large E_T^{miss} from two neutrinos, which are produced in the decay of the two W bosons. Therefore, defining a region enriched in the $t\bar{t}$ process is relatively easy compared to other methods that generate τ leptons in the final state. To validate the extrapolation of Normalization Factors (NFs) to different p_T ranges, in addition to the $W(\rightarrow \tau\nu)$ +jets process, the $t\bar{t}$ process is used.

Figure G.1: Feynman diagram of the $t\bar{t}$ process, where the two W boson decays to a single muon and a single τ lepton. The process is characterized by the production of a large E_T^{miss} , two b -jets, and a single muon. The validation of the leptonic τ decay track uses the decay of the τ lepton into a muon, while the validation of the hadronic τ decay track uses the decay of the τ lepton into a hadron. The remaining τ lepton is used as the “probe” to validate the extrapolation of NFs to different p_T ranges.



To enhance the purity of the $t\bar{t}$ process with di-leptonic decays, exactly two b -jets and a single signal muon from one of the W boson decays are required, as shown in Figure G.1. The hadronic decay of W bosons has a sizeable branching ratio that needs to be reduced by requiring exactly two b -jets. Two regions enriched in leptonic and hadronic τ decay tracks from one of the W bosons are defined to validate the NFs. For the τ lepton from the other W boson decay, the leptonic and hadronic τ decay track requires one baseline muon or one track with opposite charge of the signal muon. These regions are referred to as the “2 muon category” (denoted as “ 2μ ”) and the “1 muon category” (denoted as “ 1μ ”). These regions are divided into three categories according to the track p_T : low- p_T ($2 < p_T < 5$ GeV), medium- p_T ($5 < p_T < 8$ GeV), and high- p_T ($8 < p_T < 20$ GeV) range as defined in Section 7.2.

By requiring an additional baseline muon with an opposite-sign charge with the signal muon, a region dominated by the $t\bar{t}$ process, where the τ leptonically decays, is defined. By requiring an additional track with a large $S(d_0)$ and opposite-sign charge with the signal muon, a region dominated by the $t\bar{t}$ process, which the τ hadronically decay, is defined. Compared to the 2μ category, there are more QCD tracks not related to the τ decay tracks as backgrounds, especially in the low- p_T range. To extract the background template of the QCD tracks, we define a control region (CR) with an additional track with a large $S(d_0)$ and same-sign charge with the signal muon. This CR is dominated by QCD tracks. QCD tracks from the $t\bar{t}$ process are normalized in the same-sign charge region for each track p_T range and are extrapolated to the opposite-sign charge regions.

The region name depends on whether the signal muon charge is the same as or different from the baseline muon or track charge. If the charges are opposite, the category name is followed by OS (Opposite sign), and if they are the same, it is followed by SS (Same sign). Furthermore, the names of the regions are suffixed with -Low, -Med, or -High, depending on the p_T range of the track. The background estimation strategy using the $t\bar{t}$ process is summarized below.

- NFs for hadronic and leptonic decay tracks are measured in the high- p_T range in the 1μ and 2μ categories, respectively.
- The measured NFs are applied to the yields in the medium- p_T and low- p_T range to validate the extrapolation.
- In the low- p_T range, the QCD track has a particularly large effect in the 1μ category. To accurately estimate the contribution of the QCD track, the SS region of the 1μ category is defined to normalize the QCD tracks in each p_T region.

Figure G.2 shows a schematic picture of the definitions of the CR and the validation region (VR).

G.2 Control Regions and Validation Regions

To validate the extrapolation of the NF from the high- p_T range to the lower p_T ranges, the low- p_T and medium- p_T ranges are used as VRs for leptonic τ decay tracks, named as VR- 2μ OS-Low and

Figure G.2: Schematic of the region definitions of $t\bar{t}$ VRs, filled in yellow. The green area shows the CRs utilized for estimating the QCD tracks and τ decay tracks in the $t\bar{t}$ process. The regions in the middle row are used to normalize the QCD tracks in each p_T range.

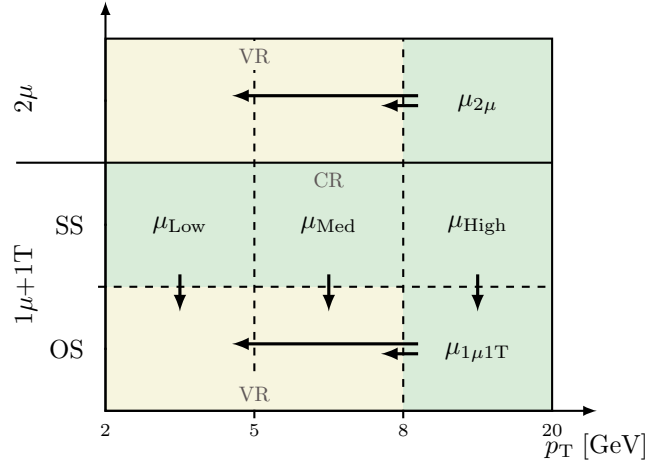


Table G.1: Applied selections for each CR and VR for leptonic τ decay tracks. The selections in the parentheses represent the selection corresponding to different p_T ranges.

Variable	CR-2 μ OS-High	VR-2 μ OS-Med(Low)
Trigger		Single- μ
$N_{\text{b-jets}}$		= 2
N_{jet}		= 2
$N(\ell_{\text{sig}})$		= 1
$N(\ell_{\text{base}})$		= 2
$Q(\mu) \times Q(\mu_{\text{base}})$		< 0
Track p_T	[8,20]	[5,8] ([2,5])

VR-2 μ OS-Med, respectively. To account for the mis-modeling of $t\bar{t}$ kinematics, the $t\bar{t}$ MC in VR-2 μ OS-Low and VR-2 μ OS-Med is normalized in the high- p_T range, named CR-2 μ OS-High. Definition of the CRs and VRs using the $t\bar{t}$ process to validate the leptonic τ decay tracks are summarized in Table G.1.

In the 1 μ category, we require E_T^{miss} and transverse mass (m_T) greater than 100 GeV and no additional jets to suppress the $t\bar{t} \rightarrow WWbb \rightarrow \ell\nu jbb (= \mu, e)$ process. The low- p_T and medium- p_T range is used as VRs for hadronic τ decay tracks, named VR-1 μ OS-Low and VR-1 μ OS-Med, respectively. The QCD tracks from the $t\bar{t}$ process are normalized in the same-sign charge region, named CR-1 μ SS-Low, CR-1 μ SS-Med, and CR-1 μ SS-High for each track p_T range. Definition of the CRs and VRs using the $t\bar{t}$ process to validate the hadronic τ decay tracks are summarized in Table G.2.

The background composition in the $t\bar{t}$ category is illustrated in Figure G.3.

Table G.2: Applied selections for each CR and VR for hadronic τ decay tracks. The selections in the parentheses represent the selection corresponding to the same-sign charge region. The selections in the curly brackets represent the selection corresponding to different p_T ranges.

Region	VR(CR)-1 μ OS(SS)-Low{Med}	CR-1 μ OS(SS)-High
Trigger		Single- μ
$N_{b\text{-jets}}$		= 2
N_{jet}		= 2
$N(\ell)$		= 1
E_T^{miss} [GeV]		> 100
m_T [GeV]		> 100
Track p_T [GeV]	[2,5] {[5,8]}	[8,20]
$Q(\mu) \times Q(\text{track})$		< 0 (> 0)

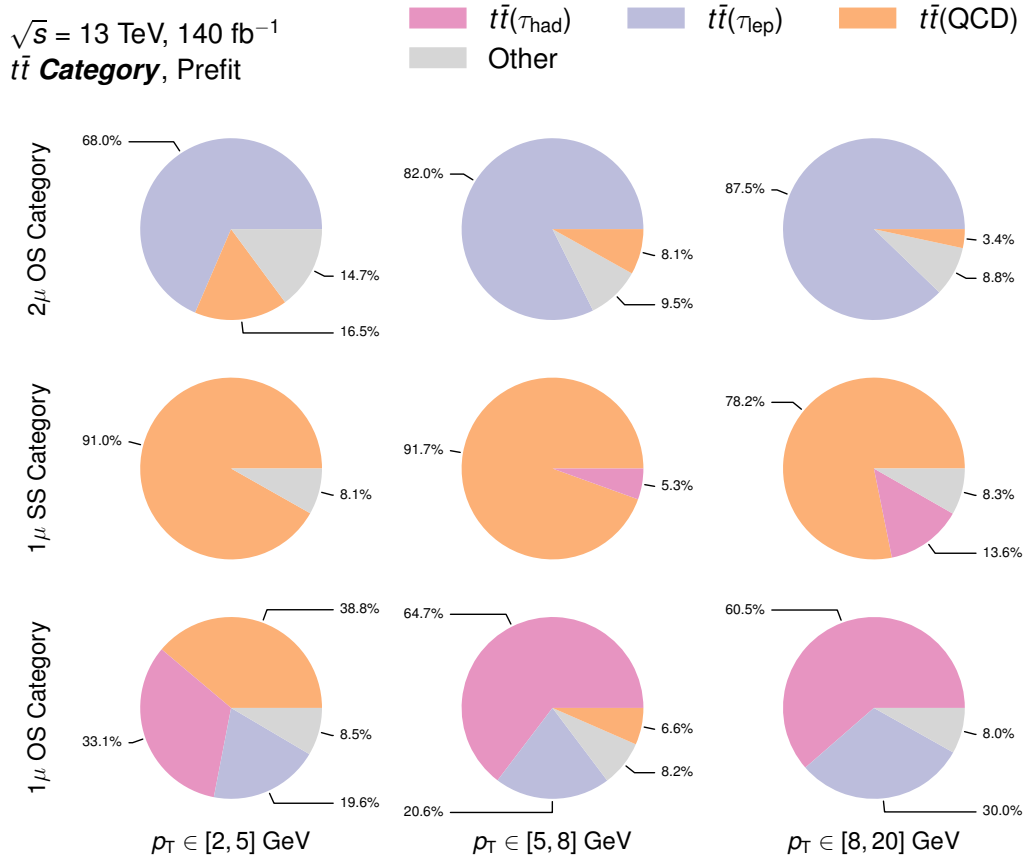


Figure G.3: Pie-charts showing the background composition in the $t\bar{t}$ category, estimated directly from simulation samples. Background processes with contributions smaller than 2% are not included in the pie charts.

Table G.3: NFs measured in the background-only fit.

Background	Track p_T range	Value
Leptonic τ decay track	–	1.03 ± 0.05
Hadronic τ decay track	–	0.97 ± 0.06
QCD track	Low ($2 < p_T < 5$ GeV)	1.58 ± 0.13
	Medium ($5 < p_T < 8$ GeV)	1.4 ± 0.5
	High ($8 < p_T < 20$ GeV)	0.7 ± 0.5

Table G.4: Observed data and estimated yields using results from the background-only fit in the CRs. The CRs used to calculate the NF for QCD tracks are located in the left three columns, while the remaining CRs are used to calculate the NFs for τ decay tracks. W_{lep} track indicates muon and electron tracks produced by the W boson decays. The errors include both statistical and systematic uncertainties. The “Other” category includes contributions from V +jets and single top processes.

Yields	CR-1 μ SS-High	CR-1 μ SS-Med	CR-1 μ SS-Low	CR-1 μ OS-High	CR-2 μ OS-High
Observed	5	14	267	415	709
Fitted SM events	5.0 ± 2.3	14 ± 4	267 ± 16	415 ± 20	709 ± 27
$t\bar{t}$ (τ_{had} track)	0.7 ± 0.4	0.7 ± 0.4	1.5 ± 0.6	251 ± 14	2.07 ± 0.09
$t\bar{t}$ (τ_{lep} track)	–	–	< 1	125 ± 7	621 ± 28
$t\bar{t}$ (W_{lep} track)	–	–	< 1	21 ± 4	12.8 ± 2.3
$t\bar{t}$ (QCD track)	3.9 ± 2.3	13 ± 4	243 ± 17	5.9 ± 1.3	24 ± 4
Other	0.41 ± 0.21	0.41 ± 0.21	22 ± 5	12.2 ± 2.3	50 ± 7

G.3 Fit results in Validation Regions

The NFs are obtained by performing a maximum likelihood fit using six CRs (CR-1 μ SS-High, CR-1 μ SS-Med, CR-1 μ SS-Low, CR-1 μ OS-High, and CR-2 μ OS-High). The derived factors are presented in Table G.3. The observed and post-fit yields in the CRs are presented in Table G.4.

The total systematic uncertainty, along with the breakdown in each VR, is visualized in Figure G.4. The yields and differences for each VR are visualized in Figure G.5. In each VR, the expected and observed yields are consistent within the uncertainty. This allowed us to verify the extrapolation of the NF for τ decay tracks from the high- p_T to the medium- p_T and low- p_T range using τ leptons produced in the $t\bar{t}$ process. Some kinematic distributions are shown in Figures G.6 and G.7.

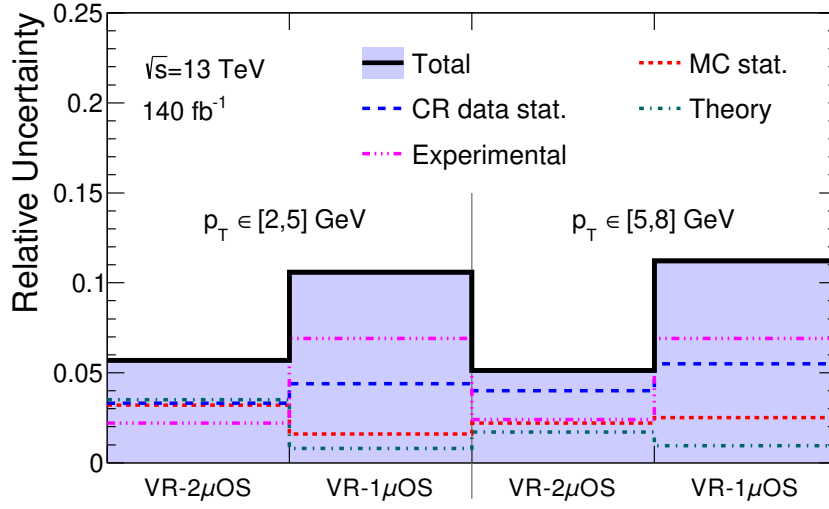


Figure G.4: Systematic uncertainties on the post-fit background yields in the $t\bar{t}$ VRs. The CR data statistics category is the uncertainty that arises from the limited data statistics in CRs. The MC statistics category represents the uncertainty arising from the limited number of MC simulation samples. The experimental category indicates systematic uncertainties originating from the reconstruction, identification, isolation, and calibration of physics objects and tracks. The theory uncertainty category represents the uncertainty that arises from the choice of parameters used to generate MC simulation samples. The solid line shows the sum of the errors but not necessarily the quadratic sum of the uncertainties since each uncertainty may be correlated.

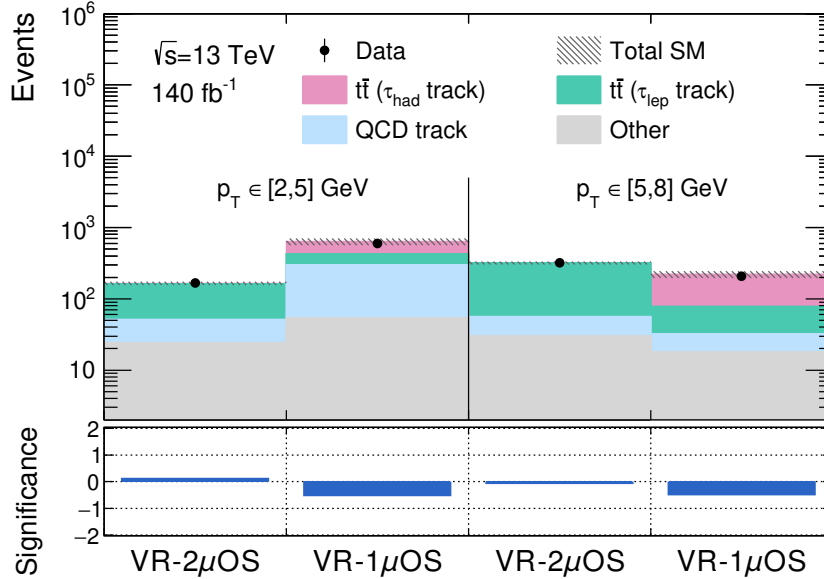
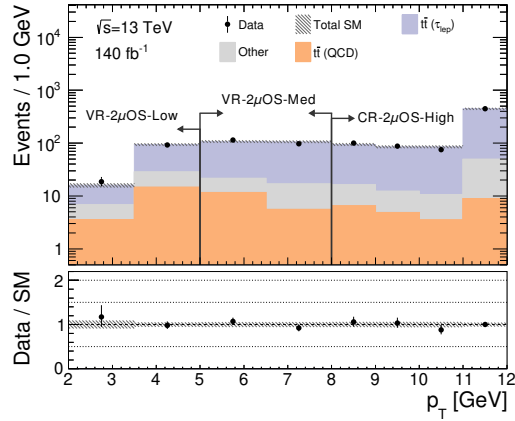
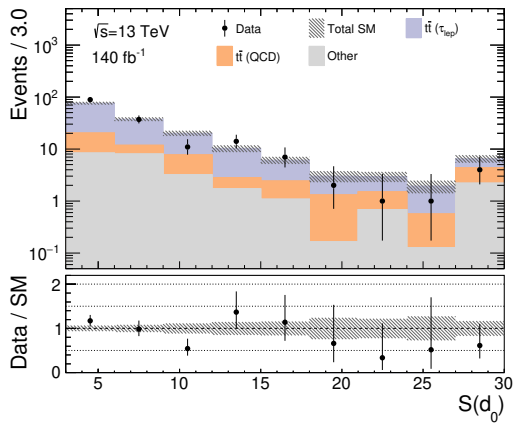


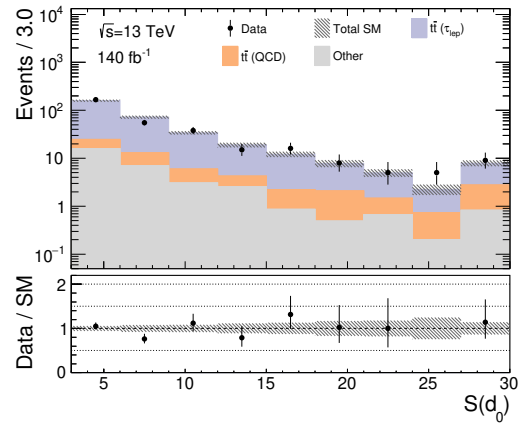
Figure G.5: Overview of fit results in the $t\bar{t}$ VRs. The upper plot summarizes observed and estimated yields for each VR, while the bottom plot illustrates the difference between the observed and estimated yields. The “Other” category includes contributions from V +jets and single top processes.



(a) Track p_T distribution

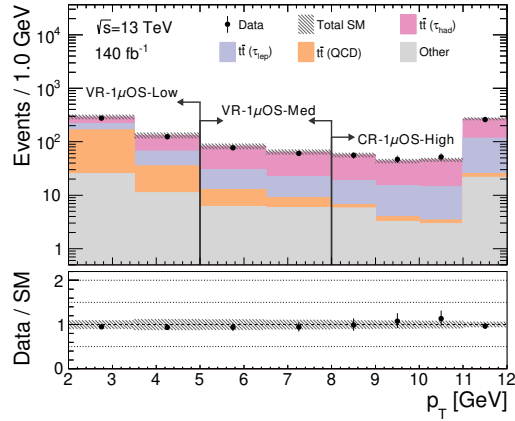


(b) Track $S(d_0)$ distribution (Low p_T)

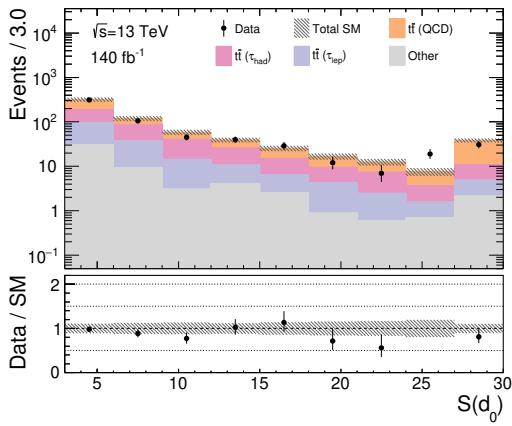


(c) Track $S(d_0)$ distribution (Medium p_T)

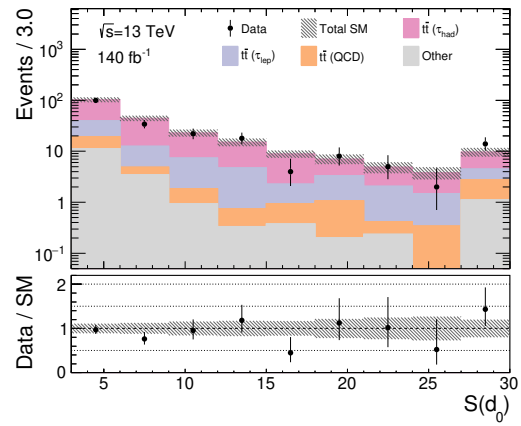
Figure G.6: Post-fit distributions in the 2μ category. Each plot is drawn without applying selections to the illustrated variable. The bins enclosed by arrows indicate the respective regions. The hatched area corresponds to the combined systematic and MC statistical uncertainties. The bottom panel shows the ratio of the observed data yield and the estimated background yield. The “Other” category includes contributions from V +jets and single top processes.



(a) Track p_T distribution



(b) Track $S(d_0)$ distribution (Low p_T)



(c) Track $S(d_0)$ distribution (Medium p_T)

Figure G.7: Post-fit distributions in the 1μ category. Each plot is drawn without applying selections to the illustrated variable. The bins enclosed by arrows indicate the respective regions. The hatched area corresponds to the combined systematic and MC statistical uncertainties. The bottom panel shows the ratio of the observed data yield and the estimated background yield. The “Other” category includes contributions from V +jets and single top processes.

Appendix H

Minor Experimental Uncertainties

Jet Energy Resolution (JER) Understanding the resolution of the reconstructed jet energy is crucial for making precise measurements of events involving jets. The impact on the overall JER uncertainty can be broken down into three terms.

- **Noise term** : Contribution from the electronic noise of the front-end electronics of the calorimeters, which is independent of the jet energy.
- **Stochastic term** : Statistical fluctuation of the deposited energy.
- **Constant term** : Contribution from mis-modeling of energy deposit in passive materials and energy response of calorimeters.

Contributions from the stochastic and constant terms are assessed in multijet events using an energetic jet as a reference (“multijet balance”). In contrast, the noise term is measured using the “random cones” method. The random cones method utilizes data collected by random unbiased triggers, comparing the energy deposits between two randomly selected cones with $R = 0.4$ to evaluate the noise term. The JER uncertainties are summarized in Figure [H.1](#).

Jet Vertex Tagging (JVT) To account for the difference between data and simulation for Jet Vertex Tagger (JVT), hard-scatter jets in $Z(\rightarrow \mu\mu)+\text{jets}$ events are used. The reconstructed Z boson p_T is used as a probe for the jet p_T . Figure [H.2](#) shows the JVT efficiency with different thresholds, measured by data and simulation. The JVT uncertainty is assessed by comparing the difference between data and simulation for different working points.

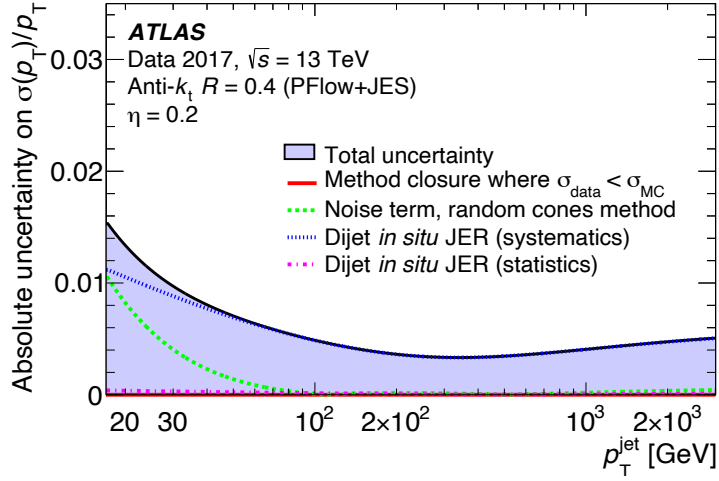


Figure H.1: Absolute uncertainty on the relative jet energy resolution as a function of jet p_T at $\eta = 0.2$. The red line represents the closure uncertainties, which are assessed by comparing the uncertainties using simulation samples for the multijet balance and random cones method. Uncertainties from the multijet balance are categorized into systematic and statistical terms, where the former includes uncertainties related to the energy scale of the reference jet, physics modeling, and event topology. The latter term corresponds to limitations in statistics from the collected data, which are negligible given the large production cross-section of the multijet process. The filled area represents the total uncertainty, calculated by taking the quadrature sum of all components in the figure. The figure is taken from Ref. [101].

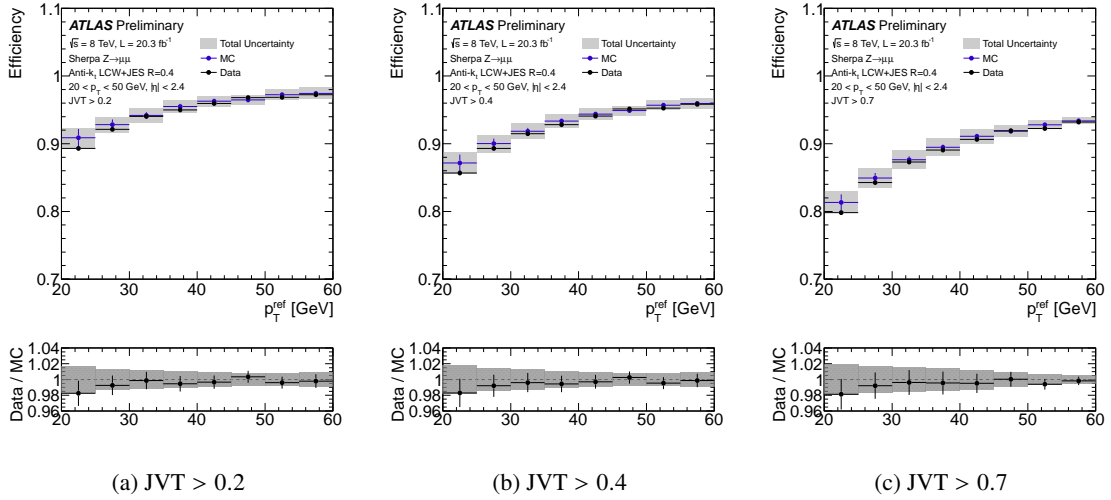


Figure H.2: JVT efficiency as a function of the reconstructed Z boson p_T (p_T^{ref}). The bottom plot shows the difference between the measured efficiency by data and simulation. The gray band represents the total uncertainty evaluated using the quadrature sum of statistical and systematic uncertainties. The figures are taken from Ref. [114].

Appendix I

Auxiliary Materials

I.1 Acceptance and Efficiency

Signal acceptance is the ratio of weighted events passing the SR selections applied to truth-level particle information without the $S(d_0)$ selection. The signal acceptance for each production mode is summarized in Figure I.1.

Signal efficiency is the ratio of the yield obtained after applying selection to truth-level particle information and the yield obtained by applying selection to the actual physics object at the reconstruction level. Therefore, it shows the efficiency when actual reconstruction efficiency and $S(d_0)$ selection are considered. The signal efficiency for each production mode in SR-Low and SR-High is summarized in Figures I.2 and I.3, respectively.

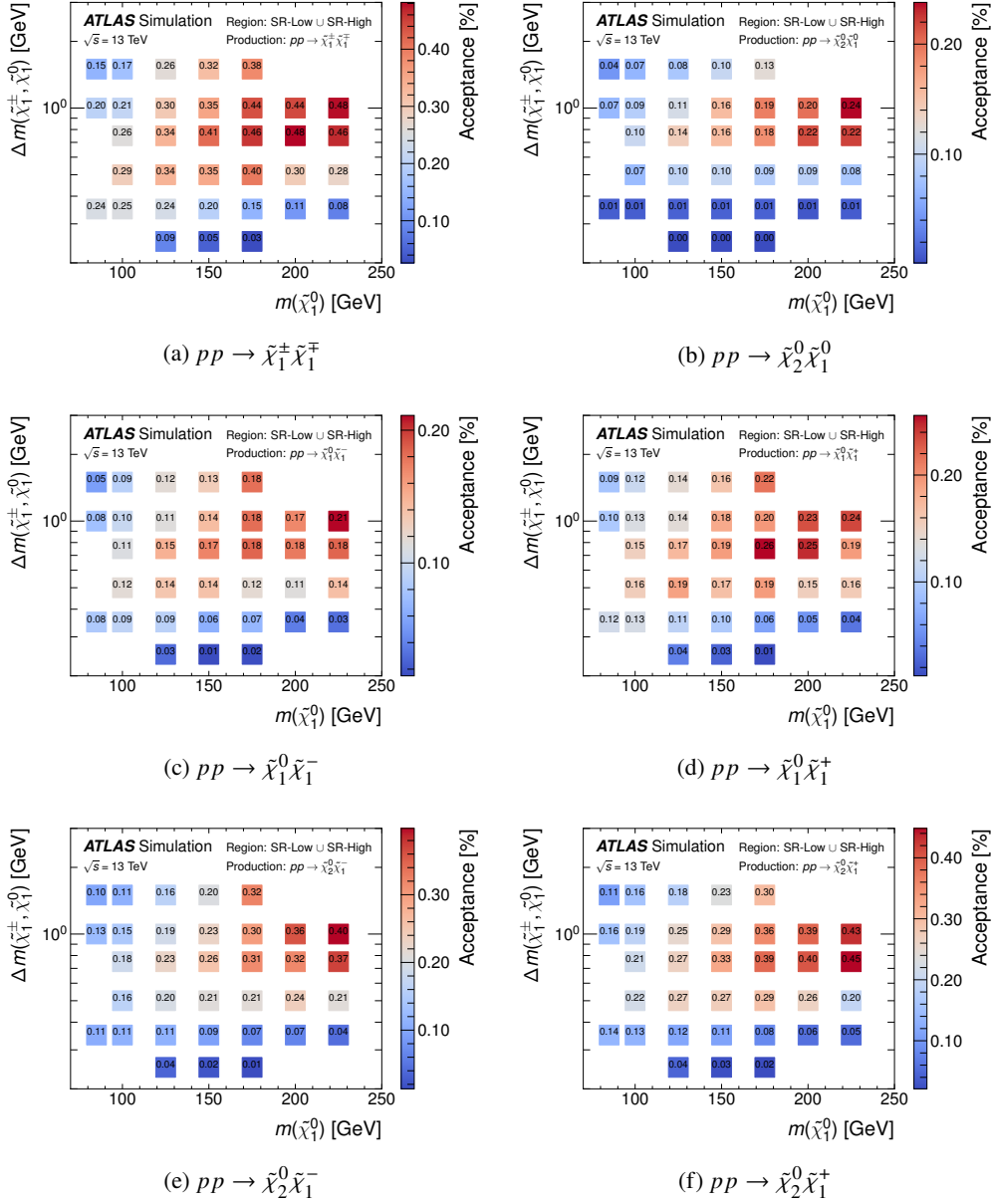


Figure I.1: Signal acceptance of each signal production mode combining all SRs.

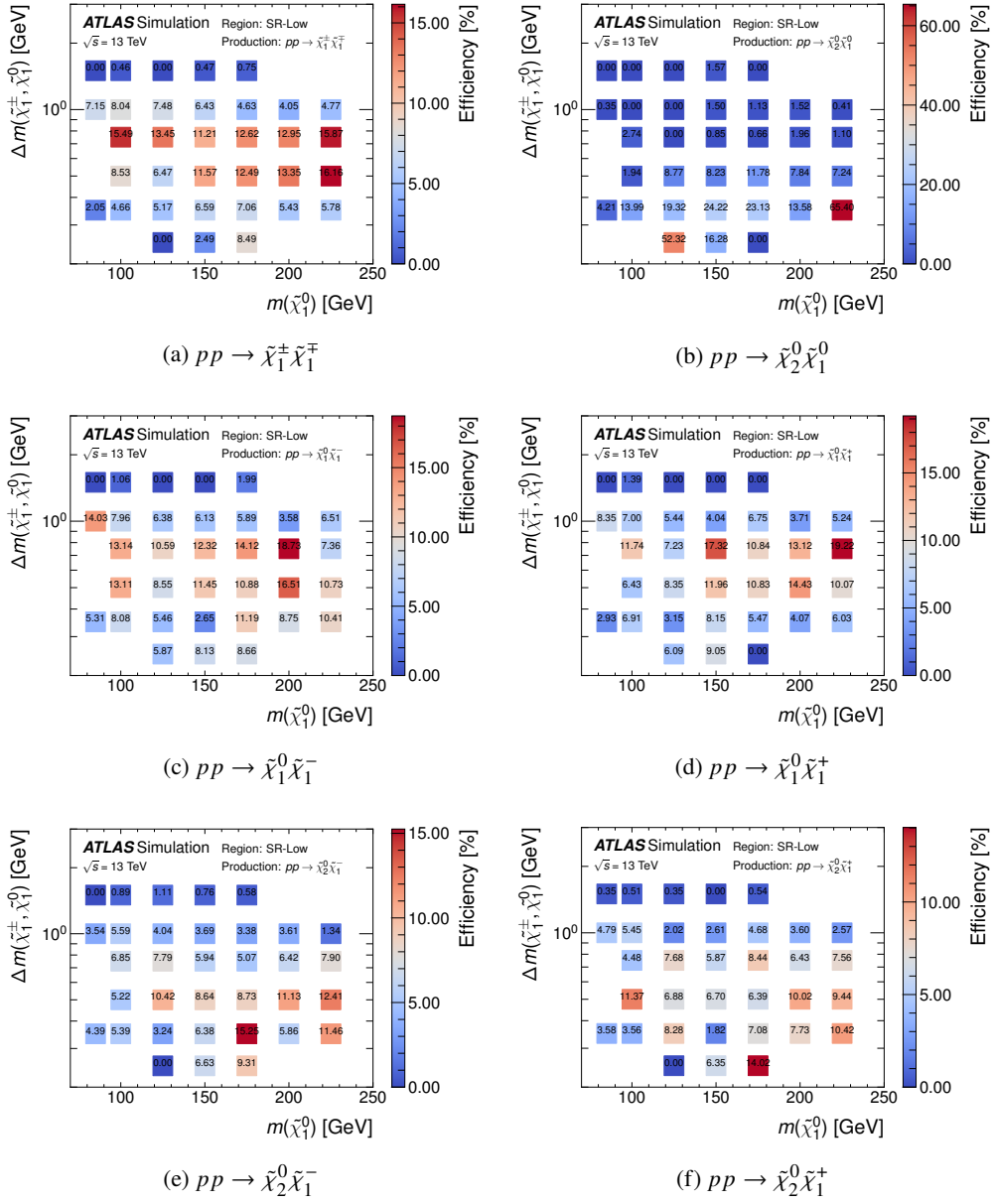


Figure I.2: Signal efficiency of each signal production mode in SR-Low.

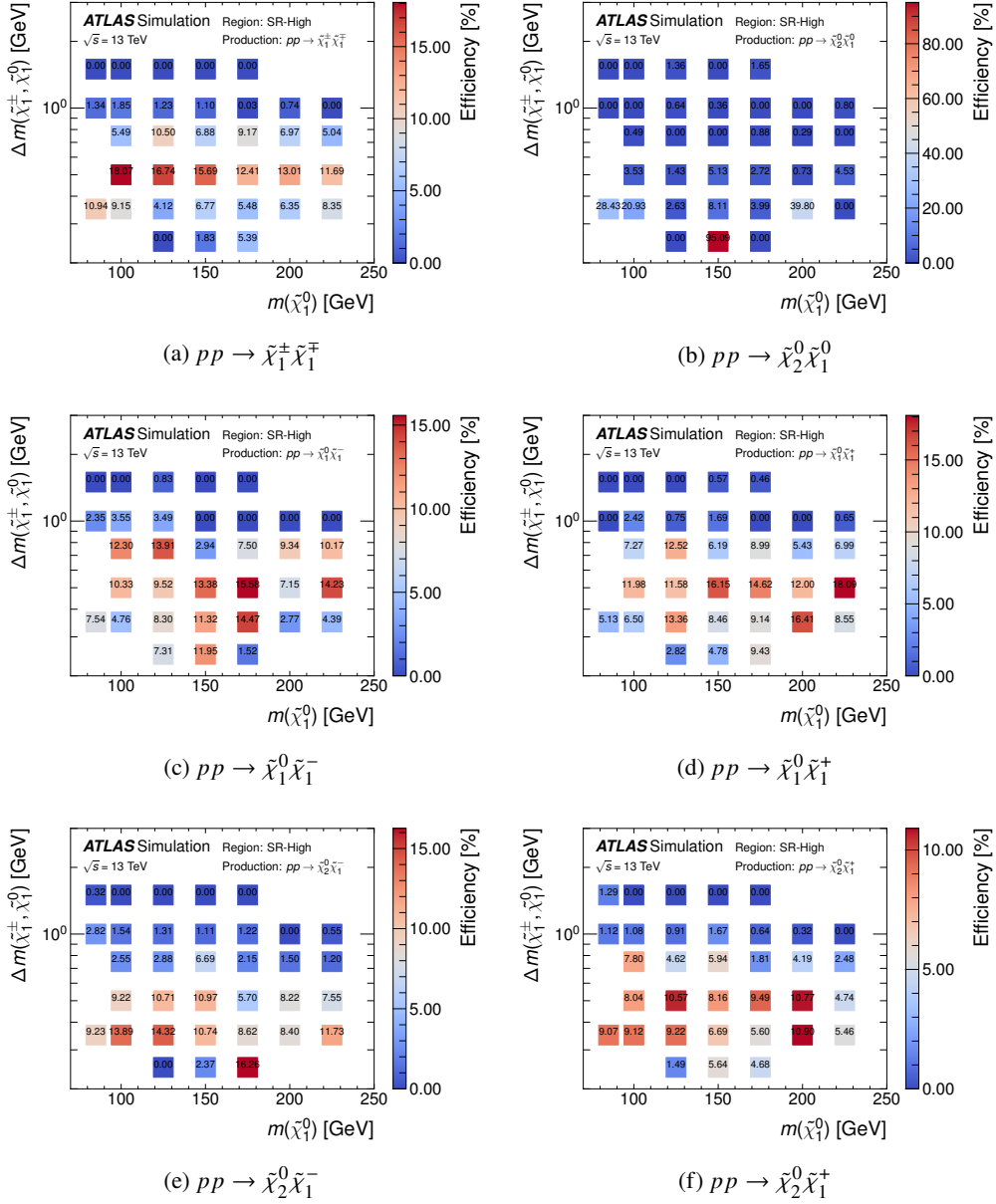
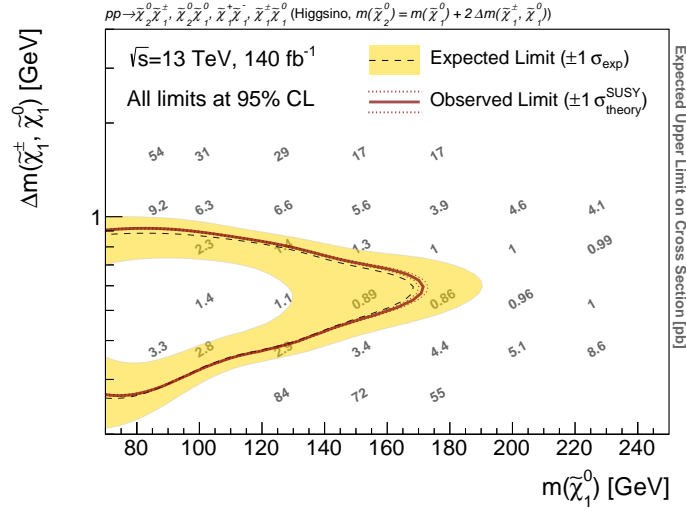


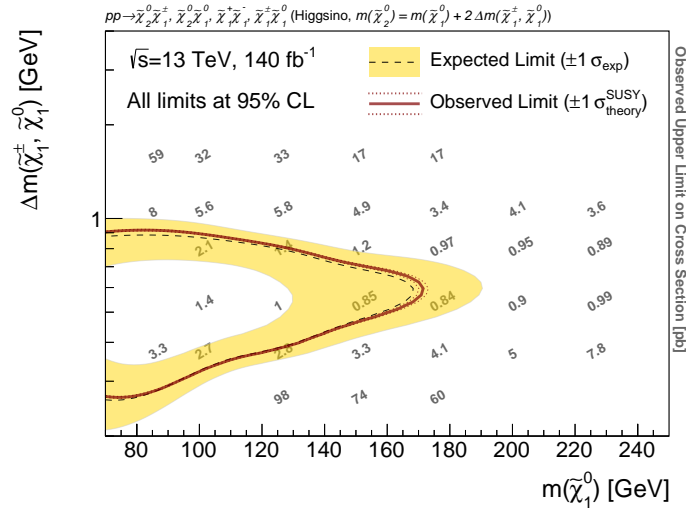
Figure I.3: Signal efficiency of each signal production mode in SR-High.

I.2 Cross-section Upper Limits

The expected and observed upper limits on the cross-section are given in Figures I.4(a) and I.4(b), respectively.



(a) Expected upper limits



(b) Observed upper limits

Figure I.4: The expected and observed upper limits on the cross-section for each signal grid point. The gray numbers represent the values. The expected (dashed) and observed (solid) 95% CL exclusion limits are overlaid.

I.3 Limit on Electroweakino masses

In Section 2.4.4, we have discussed that the bino and wino mass parameters may have complex phases, which can affect the mass difference between the lightest chargino and neutralino. Moreover, the value of $\tan\beta$ also impacts the mass difference, as explained in Equation 2.12. Therefore, this section provides exclusion limits for gaugino masses with varied $\tan\beta$ and complex phases. Figures I.5 and I.6 show the limits of the wino and bino masses at $\mu \approx m(\tilde{\chi}_1^\pm) = 100$ GeV and $\mu \approx m(\tilde{\chi}_1^\pm) = 150$ GeV, respectively.

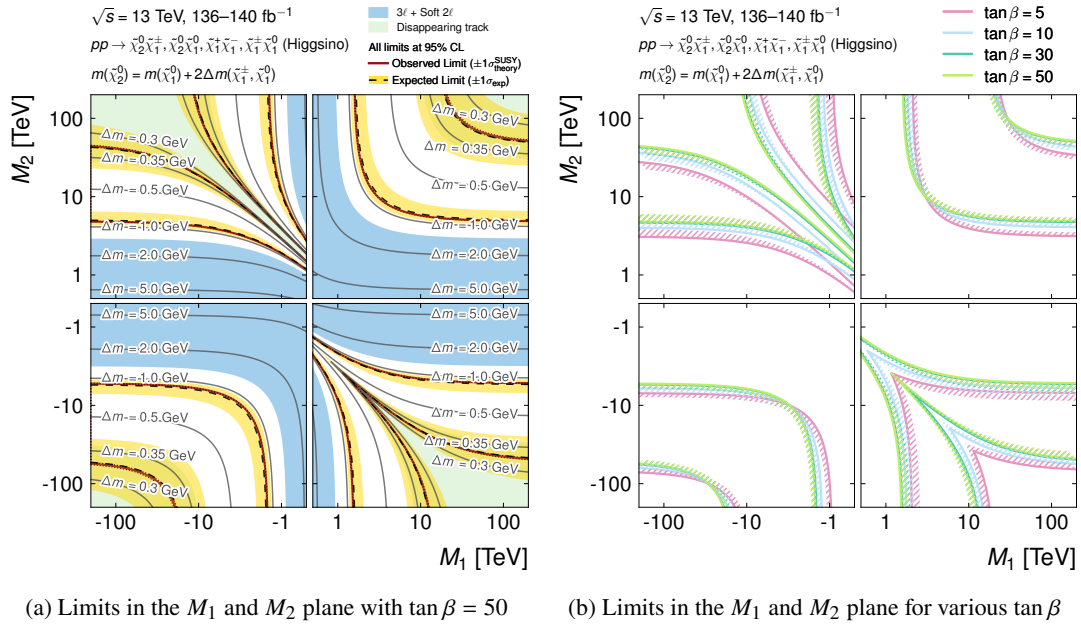
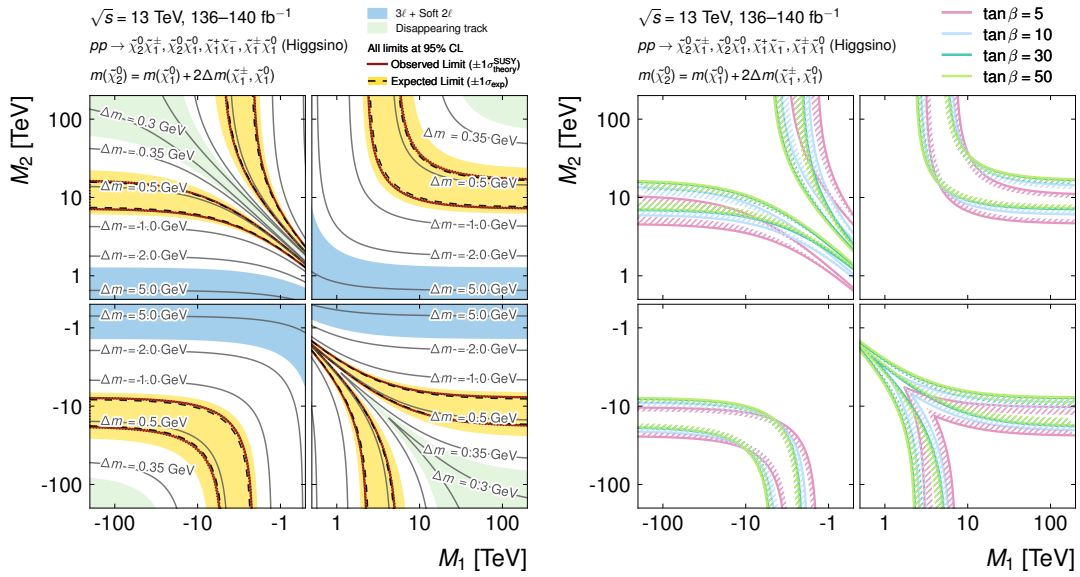


Figure I.5: The observed and expected exclusion limits at the 95% CL in the M_1 and M_2 plane for $\mu = 100$ GeV. (a) The expected and observed limits in the displaced track analysis overlaid with observed limits from existing analyses. (b) The expected and observed limits in the displaced track analysis for various $\tan\beta$. The hatched side indicates the area being excluded.



(a) Limits in the M_1 and M_2 plane with $\tan \beta = 50$

(b) Limits in the M_1 and M_2 plane for various $\tan \beta$

Figure I.6: The observed and expected exclusion limits at the 95% CL in the M_1 and M_2 plane for $\mu = 150 \text{ GeV}$. (a) The expected and observed limits in the displaced track analysis overlaid with observed limits from existing analyses. (b) The expected and observed limits in the displaced track analysis for various $\tan \beta$. The hatched side indicates the area being excluded.